

Air-Guard

Final Report

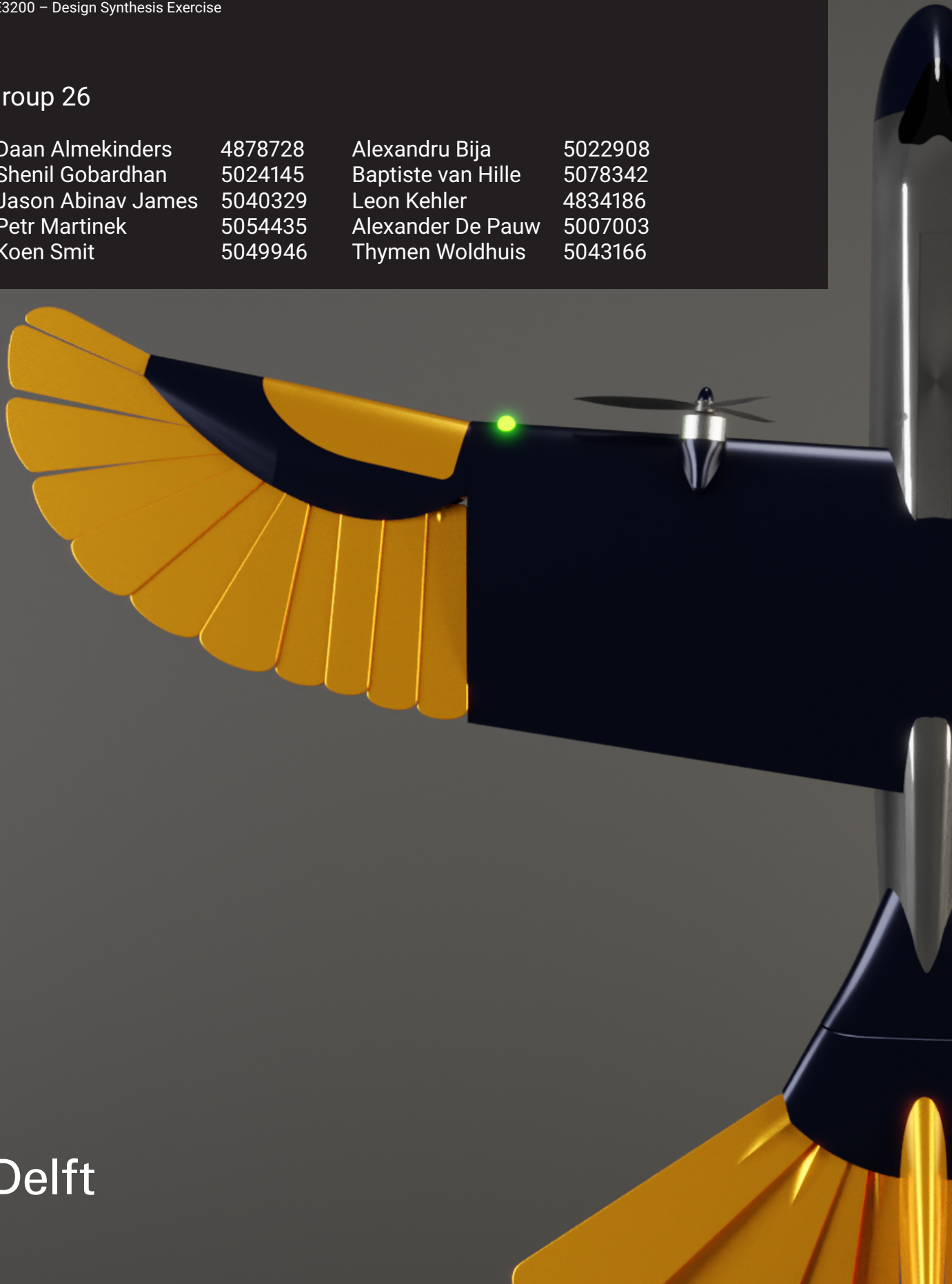
Report Version No. 1.0

June 21, 2022 | Delft, The Netherlands

AE3200 – Design Synthesis Exercise

Group 26

Daan Almekinders	4878728	Alexandru Bija	5022908
Shenil Gobardhan	5024145	Baptiste van Hille	5078342
Jason Abinav James	5040329	Leon Kehler	4834186
Petr Martinek	5054435	Alexander De Pauw	5007003
Koen Smit	5049946	Thymen Woldhuis	5043166



This page is intentionally left blank

Acknowledgements

We would like to thank our tutor Xuerui Wang and coaches Satya Ammu and Mike Zoutendijk for their clear guidance and help during the DSE. They provided us with an interesting design exercise and gave a lot of insights into their respective fields. In addition, we would like to thank Joris Melkert and Erwin Mooij for their weekly DSE videos which helped us get a clear overview of what needed to be done every week. As for external experts, we would like to thank Tomas Sinnige for his help with the propeller aerodynamics, Rob McDonald for insightful help on the use of OpenVSP, and lastly Alexander in 't Veld for helping with creating the flight dynamics model.

Summary

The drone market has been steadily growing over the last decades, resulting in drones becoming more and more common¹. For the majority of the time, the drones provide valuable services, from inspection work and deliveries to applications in emergencies, such as search and rescue, or rapid deliveries of medical supplies. Unfortunately, because drones are available to everyone, misuse cannot be fully prevented. They can cause significant disruptions to aviation, violate privacy, or transport illegal substances, leading to financial losses, or more serious consequences. A notable incident, that caused the delay of close to 1,000 flights affecting approximately 140,000 passengers, took place in 2018 at London Gatwick Airport, where 2 drones caused the airport to shut down for over 24 hours [1]. Additionally, it has been reported by Dubai International Airport, that the estimated costs of halting airport operations due to drones resulted in losses of close to \$100,000 per minute of downtime².

To counteract these hazardous situations, current anti-drone methods on the market include drone guns, quadcopters using catching systems, and radio frequency jamming systems. However, all of these methods come with their disadvantages. They either involve human interaction, have high operational costs, or cannot intercept quickly over a large area, leaving a large gap in the market for an efficient anti-drone system. The Air-Guard drone introduced in this report aims to fill this market gap, by providing a quick response time to a threat, while not compromising on neutralizing capabilities. It is a fixed-wing drone capable of autonomous visual tracking and catching unlicensed drones via a shooting net mechanism integrated with a parachute. Compared to multi-rotor drones, the Air-Guard drone concept has a longer range and higher efficiency, allowing it to be readily in the air until an unlicensed drone is detected. This is achieved thanks to its unique design inspired by bird morphology. Birds can actively morph their wings and tail surfaces to actively alter their aspect ratio, wing loading, and stability to achieve the most efficient flight configuration over a wide variety of flight profiles. Similarly, the Air-Guard drone morphs its wing and tail such that the drone can be stable while loitering, to then transition into high-g maneuvers in under a second. This allows the drone to more closely follow unlicensed drones in restricted areas and immobilize these drones in a matter of minutes autonomously. The morphing concept of the drone uses multiple actuators and elastic tendons in combination with specially designed artificial feathers to emulate bird morphology. The design also considers previously neglected areas of bird wing anatomy and incorporates bio-inspired aerodynamic surfaces to delay stall and increase the maneuverability of the drone.

This report is a follow-up of the midterm report, where the general configuration of the drone was set up. It aims to describe the progress on the Air-Guard project, mostly from a technical point of view, but also economic and operational aspects are covered. The UAV design is multidisciplinary and is influenced by many disciplines related to aerospace engineering. Aerodynamics, performance, structures, stability, control, and electronics considerations were combined to make the design possible. It was an iterative process, requiring careful coordination and communication between all the different departments. The result of this work translates into the design of a dual engine, 3.5 kg drone that is capable of loitering for an hour, with a maximum speed of 48 m/s. The wing span in extended configuration is 1.34 m, with a total length of 1.05 m. To neutralize the threat, the Air-Guard chases the unlicensed drone with the help of its high maneuverability, then fires a net equipped with a parachute from the nose to capture it. The materials used are balsa wood for the fuselage and fixed-wing, while the morphing surfaces are made of aluminum and 3D-printable Celanese VECTRA A950LCP. A great emphasis was put on the sustainability aspect of the drone, which lead to an electrically powered UAV, having a structure that is 99% recyclable.

¹<https://uavcoach.com/professional-drones/> [Accessed: 28/04/2022]

²[https://www.arabianbusiness.com/industries/transport/375851-drone-costs-100000-minute-loss-to-uae-airports#:~:text=Shutting%20down%20Dubai%20International%20Airport%20due%20to%20a%20drone%20costs%20%24100%2C000%20a%20minute,-%E2%80%9CIt%20is%20roughly&text=Airports%20in%20the%20UAE%20suffer,and%20Metrology%20\(ESMA\)%20estimates](https://www.arabianbusiness.com/industries/transport/375851-drone-costs-100000-minute-loss-to-uae-airports#:~:text=Shutting%20down%20Dubai%20International%20Airport%20due%20to%20a%20drone%20costs%20%24100%2C000%20a%20minute,-%E2%80%9CIt%20is%20roughly&text=Airports%20in%20the%20UAE%20suffer,and%20Metrology%20(ESMA)%20estimates) [Accessed: 29/04/2022]

Contents

Acknowledgements	iii	6.2 Requirements	46
Summary	iv	6.3 Wing Aerodynamics	46
Executive Overview	1	6.4 Morphing Wing	54
0.1 Problem Statement	1	6.5 Structures	57
0.2 Mission Need Statement	1	7 Tail Design	65
0.3 Design Setup	1	7.1 A Study into Avian Tail Morphology	65
0.4 Detailed Design	2	7.2 Design Process	65
0.5 Operations	5	7.3 Tail Aerodynamics	70
0.6 Conclusion and Recommendations	5	7.4 Tail Morphing	72
1 Introduction	6	7.5 Structures	76
2 Project Set-Up	7	8 Propulsion Design	78
2.1 Project Objectives	7	8.1 Requirements	78
2.2 RAMS Analysis	7	8.2 Propulsion System Design Process	78
2.3 Technical Risk Assessment	9	8.3 Propeller Influence on Lift	80
2.4 Contingency Management	14	9 Flight Dynamics	82
2.5 Project Sustainable Development Strategy	16	9.1 Linear Flight Dynamics Model	82
2.6 Resource Allocation	20	9.2 Non-linear Flight Dynamics Model	82
2.7 Market Analysis	22	9.3 Analysis of UAV Flight Dynamics	87
3 Design Overview	25	9.4 Controller Design	91
3.1 Design Approach	25	9.5 Recommendations	95
3.2 Technology Background	26	10 Performance	97
3.3 Functional Diagrams	26	10.1 Mass Performance	97
3.4 Requirements and Compliance Matrix	27	10.2 Analytical Performance Calculations	98
3.5 Summary of Trade-Offs	27	10.3 Results and Discussion	100
4 Fuselage Design	32	11 Operations	102
4.1 Electronics	32	11.1 Air Traffic Management	102
4.2 Fuselage Configuration	36	11.2 Manufacturing, Assembly & Integration Plan	107
4.3 Structures	37	11.3 Cost Analysis	112
5 Payload Design	40	11.4 Project Design & Development Logic	115
5.1 Requirements	40	11.5 Post-DSE Gantt Chart	116
5.2 Component Description	40	11.6 Return on Investment	117
6 Main Wing Design	45	11.7 Software Diagram	119
6.1 A Study into Avian Wing Morphology	45	12 Sensitivity Analysis	120
		12.1 Structures	120

12.2 Payload	121	13.4 Aerodynamics.	126
12.3 Aerodynamics.	121	13.5 Flight Dynamics Model	128
12.4 Flight Dynamics Model	122	14 Conclusion and Recommendations	130
13 Verification & Validation	123	Bibliography	132
13.1 Structures.	123	A Requirements and Compliance Matrix	134
13.2 Payload	125	B Functional Diagrams	138
13.3 Propulsion	126		

List of Symbols

			A_b	Barrel cross-section	m^2
α	Angle of attack	deg	AR	Aspect ratio	-
β	Sideslip	rad	B	Bandwidth	Hz
χ	Aerodynamic heading angle	rad	B	Boom area	m^2
δ_t	Tail deflection	deg	b	Wing span	m
$\delta_{e\ell}$	Left engine thrust setting	-	C	Channel capacity	bits/s
δ_{e_r}	Right engine thrust setting	-	C	Clamping coefficient	-
$\delta_{m\ell}$	Left wing morph	deg	c	Chord length	m
δ_{m_r}	Right wing morph	deg	c	Speed of light	m/s
δ_{m_t}	Tail morph	deg	c_f	Friction coefficient	-
γ	Climb angle	deg	c_l	Roll coefficient	-
γ_{CO_2}	Specific heat ratio of CO ₂	-	c_r	Chord length at root	m
λ_h	Horizontal tail taper ratio	-	c_t	Chord length at tip	m
$\Lambda_{0.25h}$	Horizontal tail quarter chord sweep	deg	$C_{dev.}$	Development cost	€
Ω	Aircraft angular velocity vector	rad / s	$C_{dir.op.}$	Direct operational cost	€
μ	Aerodynamic bank angle	rad	$C_{L_{max}}$	Maximum lift coefficient of the wing	-
μ	Dynamic viscosity	kg/m/s	$C_{l_{max}}$	Maximum lift coefficient of the airfoil	-
ν	Poisson ratio	-	C_{mac}	Pitching moment around the aerodynamic center	-
ν	Virtual control input	-	$C_{manf.}$	Manufacturing cost	€
ϕ	Aircraft roll angle	rad	D	Drag force	N
ψ	Aircraft heading angle	rad	D	Propeller Diameter	ft
ρ	Density	kg/m ³	E	Young's modulus	Pa
σ	Stress	Pa	f	Frequency	Hz
θ	Aircraft pitch angle	rad	F_D	Drag force	N
			G_{amp}	Amplifier gain	dB
			G_{ant}	Antenna gain	dB
\mathbb{T}	Transformation matrix	-	h	Height in earth reference frame	m
\mathbf{C}_F	Aerodynamic force coefficient vector	-	I	Moment of inertia	kg m ²
\mathbf{C}_M	Aerodynamic moment coefficient vector	-	J	Advance Ratio	-
\mathbf{F}_A	Aerodynamic force vector	N	k	Boltzmann constant	$m^2 \text{ kg s}^{-2} \text{ K}^{-1}$
\mathbf{G}	Control effectiveness matrix	-	k	Drag parameter	kg/m
\mathbf{M}_A	Aerodynamic moment vector	Nm	L	Lift force	N
\mathbf{X}	Position vector	m	l	Length	m
a	Speed of sound	m/s	L_b	Barrel length	m
			L_{FS}	Free-space path loss	dB

List of Symbols

M	Moment	Nm	t	Thickness	m
m	Mass	kg	t	Time	s
m_{pl}	Ejected payload mass	m	T_{sys}	Equivalent system noise temperature	K
MAC	Mean aerodynamic chord	m	u	Velocity in body frame x-direction	m/s
n	Revolutions per second	s^{-1}	u_d	Velocity of drone in body frame x-direction	m/s
P	Power	W	V	Shear force	N
p	Roll rate	rad/s	v	Velocity in body frame y-direction	m/s
P_0	Reservoir pressure	Pa	V_0	Reservoir volume	m^3
P_{atm}	Atmospheric pressure	Pa	V_m	Muzzle speed	m/s
P_{unit}	Unit price	€	V_{market}	Market volume	-
q	Pitch rate	rad/s	w	Velocity in body frame z-direction	m/s
q	Shear flow	N/m	X_E	East position in earth reference frame	m
R	Data rate	bits/s	X_N	North position in earth reference frame	m
r	Yaw rate	rad/s	X_{LEMAC}	X-location of the mean aerodynamic chord	m
S	Side force	N	\mathbf{F}	Force vector	N
S	Total wing surface area	m^2	\mathbf{I}	Inertia Tensor	$kg\ m^2$
S/N	Signal to noise ratio	-	\mathbf{V}	Aircraft velocity vector	m/s

List of Abbreviations

ABS Acrylonitrile Butadiene Styrene. 108	IP Ingress Protection. 7
AMS Achievable market share. 117	LCP Liquid Crystal Polymer. 62
ATM Air Traffic Management. 32	MAC Mean Aerodynamic Chord. 66
BMS Battery Management System. 35	NDI Nonlinear Dynamic Inversion. 91
CAD Computer Aided Design. 124	OPER Operation. 8
CDHS Command and Data Handling System. 34, 35	PAYL Payload. 40
CFD Computational Fluid Dynamics. 51	PLA PolyLactic Acid. 108
CFRP Carbon-Fiber-Reinforced Polymers. 59	RAMS Reliability, Availability, Maintainability and Safety. 7
CUAS Counter Unmanned Aerial System. 6	REQ Requirement. 7
DSE Design Synthesis Exercise. 5	ROI Return on Investment. 117
EOM Equations of Motion. 84	RX Receiver. 32
EOM Equations of Motion. 84	SLA StereoLithography Apparatus. 125
EPFL École Polytechnique Fédérale de Lausanne. 2	TRL Technology Readiness Level. 7
FBS Functional Breakdown Structure. 27	TX Transmitter. 32
FDM Fused Deposition Modeling. 125	UAV Unmanned Aerial Vehicle. 4
FEM Finite Element Method. 124	VLM Vortex Lattice Method. 47
GNSS Global Navigation Satellite System. 32	
HDPP High Density PolyPropylene. 108	
IMU Inertia Measurement Unit. 34	
INDI Incremental Nonlinear Dynamic Inversion. 91	

Executive Overview

In this chapter, a general overview of the report will be given. The aim here is to provide an extensive look into the final results of the project.

0.1. Problem Statement

Over the years, recreational drones have made large advances in terms of technology and the proliferation of these recreational drones means that they are now more accessible than ever. The increase in drone use and the inability to effectively counter drones that enter restricted/private airspace have resulted in large financial losses for airports, breaches in privacy and in some cases have facilitated the transport of drugs. A notable incident that caused the delays of close to 1,000 flights affecting approximately 140,000 passengers took place in 2018 at London Gatwick airport where 2 drones caused the shut down of the airport for over 24 hours [1][2]. Additionally, it has been reported by Dubai International Airport that halting airport operations due to drones results in losses close to 100,000 per minute of downtime [3].

0.2. Mission Need Statement

The Air-Guard system provides a counter-drone system with an autonomous, agile, reliable, affordable and sustainable aerial vehicle in order to efficiently protect sensitive airspace against the threat of unlicensed drones. The Air-Guard system aims to be implemented at Schiphol airport monitoring an area of 28 km² with the main design focus of the system for this project being the drone.

0.3. Design Setup

Before the detailed design process could be started, a thorough understanding of the design space needed to be created. This consisted of doing market research, studying the sustainability of the design, setting up a requirement list and doing preliminary research on how we want to tackle innovative design choices like morphing.

0.3.1. Market Analysis

Current anti-drone methods on the market include drone guns, quad-copter based net catching systems and radio jamming systems, however, these methods involve human interaction, have high operational costs, lack robustness and most importantly they lack the agility to chase and counter fast-moving drones leaving a large gap in the market for an efficient anti-drone system.

0.3.2. Sustainable Development Strategy

An important consideration throughout the design process is the sustainability of the system, once deployed in the real world. This does not consider only the environmental aspect, but also social, economic and operational sustainability.

The first step in achieving sustainable design is defining a philosophy that allows continuous implementation of sustainable principles by all team members and any other stakeholders involved in the project. The implemented philosophy in this project is the so-called lean manufacturing method. While this philosophy does not directly aim for sustainability as a primary goal, one of the results of successful implementation is the reduction of wasteful activities, increase in customer satisfaction and improvement of efficiency, all of which directly relate to sustainability.

However, this is a general idea that still has to be translated into a specific analysis of the morphing drone project. For this purpose, a sustainability model is created which allows to map and evaluate individual aspects and parties of the project. The model is based on a division of all sustainability aspects into four categories (environmental, social, economic and operational) which are then developed and discussed in detail. Based on this model, precise steps and actions are developed for each of the four categories to ensure a successful implementation of the defined sustainability philosophy.

0.3.3. Morphing

The concept of the manipulation of control surfaces has been investigated in detail by researchers at Stanford University in California and at École Polytechnique Fédérale de Lausanne (EPFL) in Lausanne [4] [5]. The extent to which morphing wings aid in increased maneuverability can be seen in the flight demonstrations of both designs, specifically the EPFL design shows a greater degree of maneuverability due to the inclusion of a morphing tail surface. To achieve the high maneuverability and range that the market lacks, morphing wings and tails will be used to increase these properties. Just copying the designs from Stanford or EPFL is not feasible since they are not built for the flight conditions that Air-Guard will encounter and it is not built for carrying a payload.

0.4. Detailed Design

The final design is presented in Figure 1. Further attention will be given to the different subsystems which are fuselage, payload, wing, tail, and propulsion. In addition, the performance was compared against the requirements, and the dynamic behavior of the drone was analyzed.

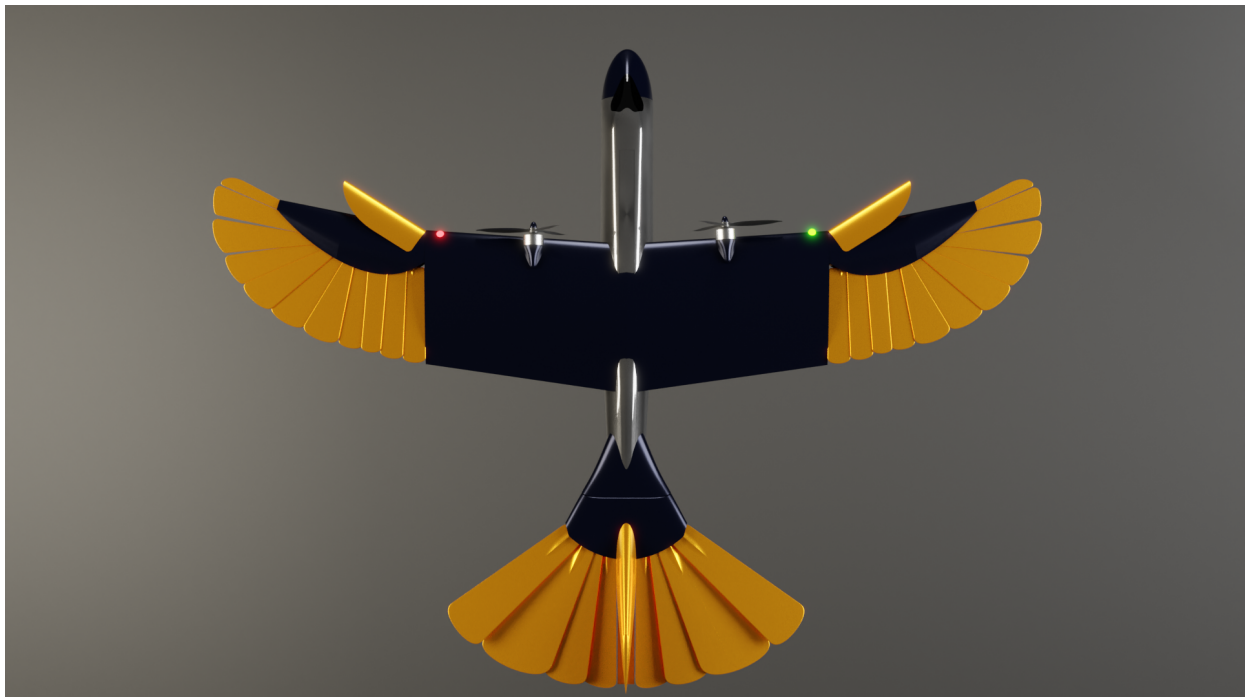


Figure 1: Top view of the final design

0.4.1. Fuselage

The fuselage is the central structure of the drone which houses all the electronics, payloads and internal structures to carry the loads from the wing and tail. The components inside the fuselage are shown in Figure 2.

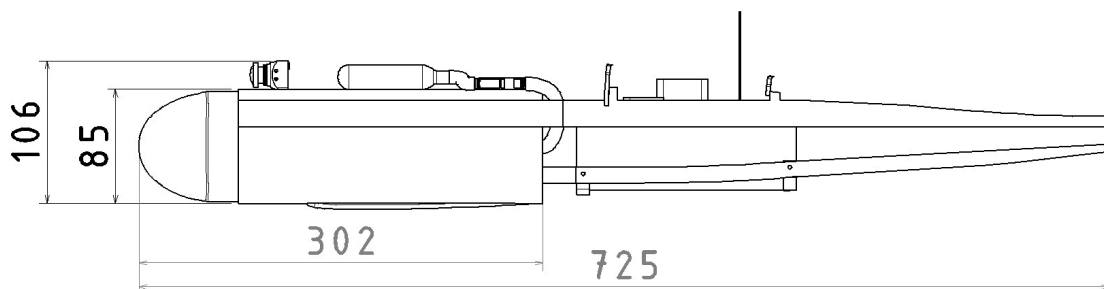


Figure 2: Fuselage internal dimensions (mm)

0.4.2. Payload

As mentioned before, the main objective of the drone is to catch unlicensed drones. To do this, the drone carries an in-house developed net shooting mechanism that functions on a pneumatic system. A gas canister will create a large internal pressure and after opening a solenoid valve it will exert its force on the capsule, thus shooting it outwards. Inside the capsule there is a parachute, net and weights. Figure 3 displays how this capsule will function once it is deployed. Afterwards, a pseudo nose will cover the fuselage such that the disturbance of the airflow is limited.

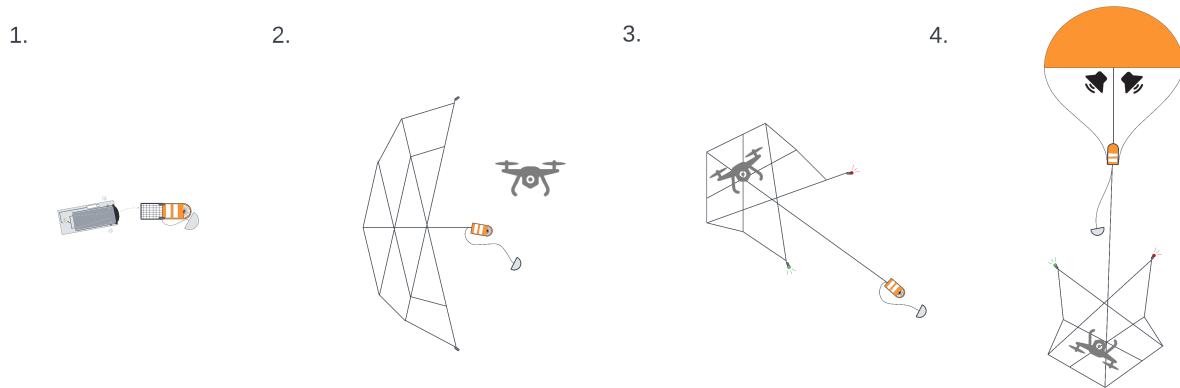


Figure 3: Deployment of the payload system

0.4.3. Wing

The wings were modeled using OpenVSP to simulate their behavior and estimate the required dimensions. The wings consist of an internal fixed-wing part, a transition section to house the morphing mechanisms and an outer, feather-like, section. When morphing the wings backwards, the lift on that side decreases such that the drone can roll. Another effect this has is moving the aerodynamic center backwards, thus making the drone more stable, which is necessary for the center of gravity shift the payload causes. Following from the study into avian morphology, it was found that birds use an alula to increase their maximum lift [6][7][8]. This is a feather located at the leading edge of the wing that essentially functions as a slat (as seen in normal aircraft). This is also included in the drone.

The morphing wing is actuated by a servo that rotates a hinge such that the leading edge of the outer wing moves backwards. To ensure the platelets' movement is dictated by the movement of the spar the outermost feather is rigidly connected to the spar itself. Each subsequent platelet is attached to the elastic tendon running from fixed outer platelet to the inner platelet. Structurally, both the inner wing and morphing wing were analyzed for the stress and sized such that the material and dimensions were optimized for performance.

0.4.4. Tail

From the study into morphology, it was found that a tail that can increase its size increases maneuverability and allows for a broader range of flight conditions. Using the most forward and most aft center of gravity position, the tail was sized such that it can make the drone neutrally stable with the aft center of gravity and both stable and unstable with the most forward center of gravity to achieve high maneuverability when in pursuit of an unlicensed drone. This has been verified by aerodynamic simulations, Figure 4, which shows the pitching moment around the center of gravity. Here, it can be seen that the pitching moment slope changes direction when morphing the wing and tail, which indicates a change in stability.

0.4. Detailed Design

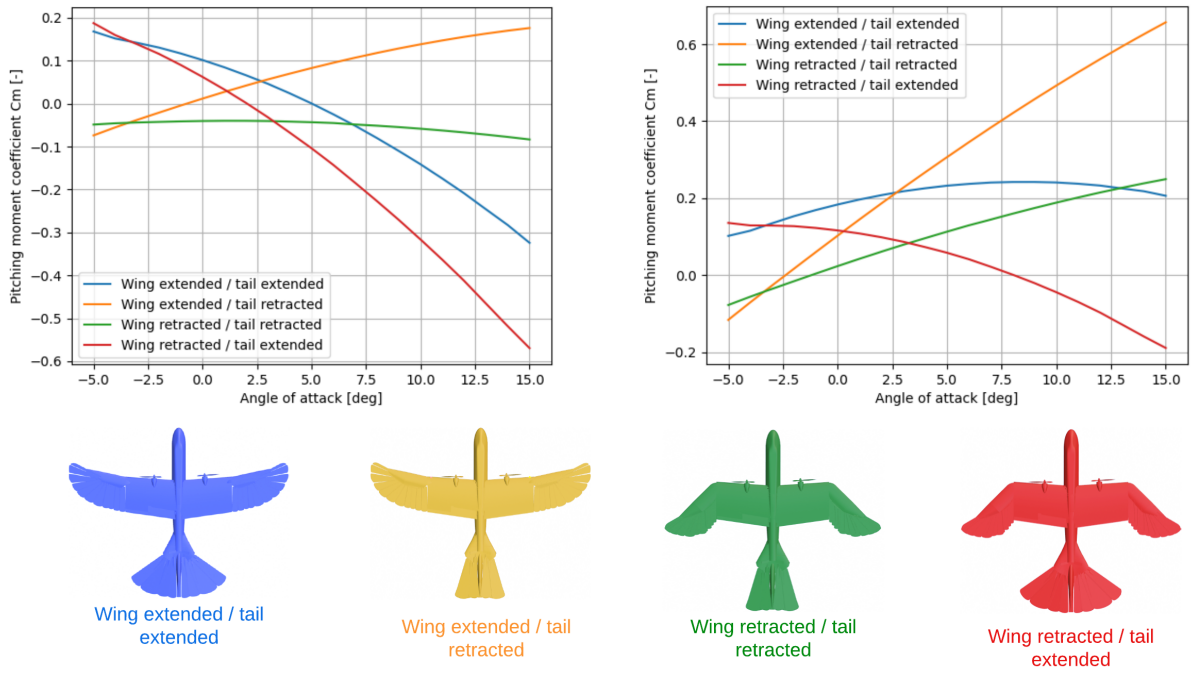


Figure 4: Pitching moment vs angle of attack for different morphing states with payload (left) and without payload (right)

To accommodate this change in tail size, a morphing mechanism had to be designed that can reliably morph the tail platelets outwards. The technical drawing can be found in [Figure 5](#)



Figure 5: Detailed view of the tail morphing mechanism, in extended position

0.4.5. Propulsion

Designing the propulsion system was done by taking into account the efficiency, the integration within the UAV and the effect on maneuverability. This resulted in the use of two wing-mounted propellers. The engine that was selected for this is the T-motor F100 with the Gemfan GF7040 propeller.

0.4.6. Flight Dynamics

With all the subsystems designed, a dynamic flight simulation was made to analyze the behavior of the UAV. A model was made with Matlab and Simulink, with which it was found that the UAV is indeed highly maneuverable. When deflecting the tail outwards and up and down, a large change in longitudinal stability was seen which matches the expectations. Also when morphing the main wing asymmetrically, a high rolling moment was found. Since the maneuverability is so high it was necessary to make a flight controller that operates the morphing actuators to achieve steady and straight flight.

0.4.7. Performance Analysis

Various requirements have been given by the customer regarding the flight performance of the UAV. With the design phase finished, these requirements were verified. This verification was done using a flight dynamics simulation and analytical calculations using aerodynamic, propulsion and structural parameters of the UAV. Using these methods, it was found that the drone should be able to meet all the performance requirements. The only exception are the minimum turn and minimum pull-up radii (required to be below 1 meters by REQ-UAV-PERF-015 and 1.5 m by REQ-UAV-PERF-016 respectively). These maneuvers would use a complex combination of wing and tail morphing, tail deflection, differential thrust and would probably be so-called super-maneuvers, that is maneuvers involving stall and thrust-to-weight ratio above 1, which is a too complex combination to be analyzed by the mentioned methods. These requirements should then be verified by a flight test.

0.5. Operations

After all research and development has been done, the drone also needs to be operated, which is why a careful study was performed in the manufacturing and integration process, the cost analysis and return on investments.

0.5.1. Manufacturing, Assembly and Integration Plan

Whilst designing the systems of the drone, the manufacturing, assembly, and integration plan has been a living document. By keeping the manufacturability and assembly of the components in mind, they will be able to be produced. For manufacturing, the methods for using the materials are documented and worked out. For final assembly, the assembly plans for the fuselage, wing, tail, and payload have been set up. Then, these plans have been combined to create the complete assembly order.

0.5.2. Cost Analysis and Return on Investment

A cost analysis of the project has been split up into development costs, manufacturing costs and direct operational costs. The first discussed, is the cost that should be accounted for when developing the UAV. The second one discusses the costs of one unit, based on the labour and material cost. Lastly, the direct operational costs contain the facilities the team needs to continue working on this after the DSE. All in all, this results in a total cost of 1.6 million euros. Assuming a market share of 42% and the numbers of airports to be served is 347 this would mean that the return on investment comes to 87%, which is above average for a start-up.

0.6. Conclusion and Recommendations

All calculations in this report have been done using simulation software. However, even the best simulation tools differ from real-life, so it is advised that in the next phase prototypes will be used to simulate the aerodynamic behavior and stress behavior as opposed to CFD and FEM. In addition, a prototype can be used to verify whether the morphing mechanisms and net shooting mechanism function as expected.

1. Introduction

During the month of December 2018, a number of drone sightings near the runway of the Gatwick airport provoked major disruptions in air traffic. As a result of the three-day incident, 140000 passengers, and 1000 flights were affected, which resulted in the loss of 61.3 million euros for airport authorities [1]. In order to solve this crisis, a large police force, and the military, were deployed in order to find and arrest the operators of the rogue drone. However, the efforts put in place did not lead to any arrests. This incident may have been prevented if a more robust prevention system had been put in place, to protect the runway from rogue drones. Furthermore, the size of the commercial drone market is increasing by 9.2% every year¹. This means that the likelihood of such events occurring again in the future is very high. This is why the team behind project Air-Guard has set the goal of designing a drone-catching system that can prevent such events from occurring again.

The purpose of this report is to present the results of the development of the counter unmanned aerial system (CUAS). The steps described in this report were carried out by ten students of aerospace engineering at TU Delft as part of the DSE project. The structure of the report is summarized in Figure 1.1;

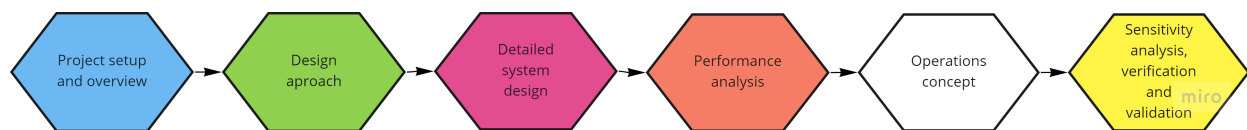


Figure 1.1: Final report structure

In Chapter 1, an overview of the project scope, and development was given. After that, a detailed project setup and market overview are documented in Chapter 2. An overview of the design approach follows in Chapter 3. This leads to the detailed design of the different drone systems, from Chapter 4 to Chapter 9. The final design is then analysed technically in Chapter 10, and operationally in Chapter 11. Finally, verification and validation of the design processes are performed in Chapter 13. Structural and control algorithms developed during the course of this project are available in the team's GitLab repository.

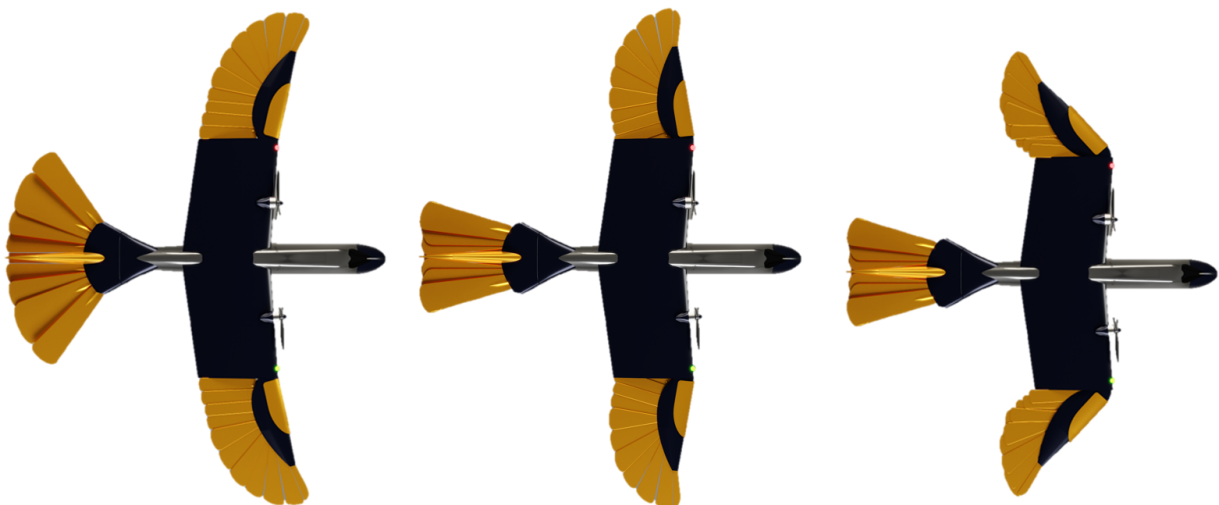


Figure 1.2: Wing and tail configurations of the final design

¹<https://www.statista.com/outlook/cmo/consumer-electronics/drones/europe?currency=EUR> [Accessed: 14/06/2022]

2. Project Set-Up

This chapter will discuss the set-up of the DSE project, and the deliverables associated with it. First, the project objectives will be given in [Section 2.1](#). Then the RAMS analysis and technical risk assessment will be discussed in [Section 2.2](#) and [Section 2.3](#). [Section 2.4](#) will discuss the contingency management during the project. The approach with respect to sustainability will be elaborated upon in [Section 2.5](#). In [Section 2.6](#) the resource allocation for the project will be discussed. Finally, a market analysis is done in [Section 2.7](#).

2.1. Project Objectives

Project objectives are used to guide the design team in a certain direction as to what the system needs to accomplish, these objectives were derived from the general problem the project aims to solve coupled with the expectations of the group and the various stakeholders in the project. The four main objectives that drive the design of the system are:

- Demonstrate the increased agility and efficiency of bio-inspired morphing drones as compared to traditional quad rotor drones
- Loiter, detect and engage with unlicensed drones in restricted air spaces
- Demonstrate the viability of sustainable operations and production of a bio-inspired morphing drone

2.2. RAMS Analysis

RAMS analyses are performed to ensure that a product is capable of fulfilling its mission, at all stages, under the conditions of reliability, availability, maintainability and safety¹. To properly assess the RAMS, the concepts should be unambiguously defined. Reliability refers to the probability of a product being able to perform its intended function and is usually described by its failure rate. Availability is a measure of how often a (sub-)system is fully operational within a given time frame. Its measure is typically given by the ratio of its up time to lifetime. Maintainability refers to the ability of a system to be repaired in a given time frame [9]. Lastly, safety refers to 'freedom from hazards to humans and equipment' [10].

2.2.1. Reliability

The systems and data used for the design of the drone have been proven in the operative environment. The net gun mechanism is available for consumers, and the morphing mechanism and belly landing have been proven to work by EPFL and Stanford University [4] [5]. In addition, the pneumatic take-off method is readily available on the market. Therefore, the data behind the design is considered to be of Technology Readiness Level (TRL) 9. As a result of the above, the reliability of the current drone design is high.

In addition to the Technology Readiness Level, four requirements have been set up to ensure the drone design will comply with the expected reliability level. The requirements are listed below and will all be tested by demonstration.

- REQ-UAV-RAMS-004: The morphing mechanism of the UAV shall be able to operate with 95% reliability
- REQ-UAV-RAMS-005: The UAV shall have a maximum lifetime of 5 years or 2000 flight cycles depending on which is reached first.
- REQ-UAV-RAMS-006: The UAV shall be able to withstand a drop of 2m on concrete without any mechanical damage
- REQ-UAV-RAMS-007: The UAV shall comply with IP-03² certification

2.2.2. Availability

Availability of the drone can be seen as the ratio of the operational period within a given time frame. On the other hand, it can also be defined as the degree, percent, or probability that a system will be ready or available when required for use [10].

¹<https://www.byhon.it/ramseengineering/> [Accessed: 16/05/2022]

²<https://www.pacergroup.net/pacer-news/understanding-ipcertification/> [Accessed: 16/06/2022]

When the latter definition of availability is considered, it can be seen as the result of reliability and maintainability. This shows how the RAMS characteristics are related to each other.

Within the availability characteristics of a drone, three types of availability are considered. These are; inherent availability, achieved availability and operational availability [10]

The drone has to conform to a certain requirement for availability. The requirement for the availability is:

- REQ-CUAS-OPER-016: The C-UAS shall be capable of deploying at least one UAV at all times.

2.2.3. Maintainability

The maintainability requirements are as follows:

- REQ-UAV-RAMS-002: The UAV's subsystems shall be able to be replaced completely between flights if damages occur
- REQ-UAV-RAMS-003: The UAV shall be able to be disassembled between flights for maintenance
- REQ-UAV-RAMS-006: The UAV shall be able to withstand a drop of 2m on concrete without any mechanical damage.

The above requirements impose a set of expectations on the design of the drone. These have, as an overlapping topic, that they discuss the maintenance of the drone. The ease with which this is done is called maintainability. This is something that is heavily influenced by the design of the drone, thus making it an inherent characteristic of system design.

As mentioned by requirements REQ-UAV-RAMS-002 and REQ-UAV-RAMS-003, maintenance shall be able to be performed in between flights. To ease the maintenance and as a result, reduce the effort of maintenance, the subsystems shall be able to be removed from the drone's structure independently.

To conclude, the maintainability of the drone has a large influence on the system design. When incorporated into the drone correctly, the cost of maintenance will be reduced, paired with the effort it takes to perform the maintenance.

2.2.4. Safety

As mentioned, safety refers to the prevention of hazards to humans and equipment. With the C-UAS operating at an airport, safety and security are extremely important for the success of the system.

Several requirements have been set to ensure adequate safety and security, which are as follows:

- REQ-UAV-RAMS-001: The UAV shall be able to be safely recovered with repairable mechanical damage (repairable means only the load-carrying structures may need to be replaced) at any point of the flight profile in the event of system failure
- REQ-CUAS-OPER-005: The C-UAS shall not interfere with airport ground operations.
- REQ-CUAS-OPER-008: The C-UAS communications shall not interfere with ATM communications.
- REQ-UAV-OPER-010: The UAV shall have a turnover time between flights of TBDs.
- REQ-GS-OPER-004: The ground station shall be able to provide an emergency cutoff.
- REQ-UAV-STAKE-003: The UAV shall adhere to the EASA drone regulations.

2.3. Technical Risk Assessment

The development of the technical aspects of the system results several risks that could compromise the design and functioning of the system. To prevent undesirable events which could result in damage to the vehicle, ground operations or even injuries to people in the covered area, a range of risks was analyzed. The risk areas were divided into three categories to make the analysis more structured and clear for future use: manufacturing risks, operational risks and system risks. The process of the technical risk analysis started with risk identification, followed by assessing the cause of the risk, then analyzing the effects of the risk and finally forming a mitigation plan for the risk. The risks identified will be ranked based on the likelihood of the risk and the overall impact of the risks as seen in [Table 2.1](#) and [Table 2.2](#) on a scale from 1 to 5. From this, the risk scores can be defined for each risk. Moreover, the final risk scores can be computed as the product of the impact and likelihood as be plotted in a risk map as done in for example [Table 2.8](#). For each type of risk (manufacturing risks, operational risks and system risks) a risk register and a risk map before and after mitigation are presented. This indicated how the mitigation plans aim to reduce the severity of the risk.

Table 2.1: Likelihood risk ratings and description

Score	Likelihood	Likelihood of occurrence
5	Frequent	Certain that it will occur at least once in the operation
4	High	Occurs often during operation (1 in 10)
3	Medium	Will sometimes occur (1 in 100)
2	Low	Has a rare chance of occurring (10 in 1000)
1	Minimum	Will almost never occur during operations (1 in 10,000)

Table 2.2: Impact risk ratings and description

Score	Impact	Likelihood of occurrence
5	Catastrophic	Causes unrepeatable damage causing termination of operation
4	Critical	Repairable damage causing termination of operation
3	Major	Operational abilities reduced
2	Significant	Small reduction in technical performance
1	Negligible	Minimal to no impact on operation

2.3. Technical Risk Assessment

Table 2.3: Manufacturing risk register

Risk ID	Risk Title	Cause	Effect	Likelihood rating	Impact rating	Risk rating	Type of action	Planned mitigation actions	Likelihood rating after response	Impact rating after response	Residual risk rating after response	Contingency action	Risk owner
RISK-TECH-MAN-1-1	Rise in material costs	Political events. Increase in scarcity. Environmental actions. Economical situation	Increase in production and maintenance costs	3	3	9	Mitigate	Use materials that are not probable to significant increase in price. Buy and store larger quantities of material when price is favourable.	2	3	6	Use stored materials	Structures and Materials lead (Alexander)
RISK-TECH-MAN-1-2	Cracks in structure	Wrong materials are used for given purpose. Wrong manufacturing methods are chosen.	Drone experiences structural failure	1	5	5	Mitigate	Formulate a quality control procedure during the manufacturing process to detect defects. Perform thorough analysis of manufacturing processes.	1	2	2		Quality officer (Baptiste)
RISK-TECH-MAN-1-3	Assembly delay due to wrong dimensions	Unclear communication between departments resulting in incompatible parts.	Delays in delivery and potential fees. Increase in production costs.	1	3	3	Mitigate	Systematic and clear communication between departments. Creating clear communication scheme.	1	3	3		CAD Lead (Baptiste)
RISK-TECH-MAN-1-4	Manufacturing delays	Workers being on a strikes	Delays in delivery and potential fees	1	3	3	Mitigate	Respect the workier conditions	1	2	2		Communications officer (Leon)
RISK-TECH-MAN-1-5	Injury at manufacturing workplace	Not enough care taken while manufacturing. Not adhering to safety rules. Insufficient safety rules	Worker injury	2	2	4	Mitigate	Detailed and effective safety system. Educating workers on correct safety measures. Periodic safety trainings	1	2	2		Market, Cost & Production Lead (Alex)
RISK-TECH-MAN-1-6	Using inexperienced manufacturers	Working on an innovative product meaning not many skills can be transferred	Delay in manufacturing process	2	2	4	Mitigate	Educating workers before letting them work on the drones	1	1	1		Project Manager (Koen)
RISK-TECH-MAN-1-7	Components from subcontractors not available in time	Change in regulations / partner being shut down. Manufacturing delays	Delays in production	5	3	15	Mitigate	Multiple subcontractors. Fees covering losses in case of delays. Storage of parts	4	2	8	Use stored parts	Market, Cost & Production Lead (Alex)
RISK-TECH-MAN-1-8	Damage of components from subcontractors	Wrong handling during transport.	New components need to be shipped causing a delay in the manufacturing process	3	3	9	Mitigate	Negotiate with subcontractors to issue detailed handling rules for the transport that the transport company will adhere to. Storage of parts	2	2	4		Market, Cost & Production Lead (Alex)
RISK-TECH-MAN-1-9	Insufficient quality of components from subcontractors	Wrong manufacturing methods used. Insufficient quality checks.	New components need to be shipped causing a delay in the manufacturing process	3	4	12	Mitigate	Clearly define quality control processes that the subcontractor has to perform. Issue fees to cover losses. Store parts	2	2	4		Market, Cost & Production Lead (Alex)

2.3. Technical Risk Assessment

Table 2.4: Operational risk register

Risk ID	Risk Title	Cause	Effect	Likelihood rating	Impact rating	Risk rating	Type of action	Planned mitigation actions	Likelihood rating after response	Impact rating after response	Residual risk rating after response	Contingency action	Risk owner
RISK-TECH-OP-1-1	Flight performance affected by weather	Extreme weather	Loss of control, mission failure	4	3	12	Avoid	Evaluate the environmental conditions ahead of the flight	3	3	9	Morph to configuration of maximum controllability and attempt return to base	Chief Engineer (Petr)
RISK-TECH-OP-1-2	Catching unintended objects	The payload sensors wrongly identify an object as an unlicensed drone	The unintended object is caught, the net is used wrongly	4	3	12	Mitigate	Design a scanning system that has a high reliability in terms of drone identification. Possible integration of operator approval of target	1	3	3		Payload (Daan)
RISK-TECH-OP-1-3	Battery overheating due to environmental conditions	Excessive external temperature	The batteries work in undesired ranges of temperature decreasing performance and increasing risk of fire	1	4	4	Mitigate	Evaluate the environmental conditions ahead of the flight	1	4	4		Structures and Materials lead (Alexander)
RISK-TECH-OP-1-4	Launching failure	The launching mechanism is wrongly set up or broken	The drone is unable to launch	2	4	8	Transfer	Educate the operators on the setup of the launching mechanism. Periodic maintenance checks of the mechanism. Positioning of launch mechanism into non-critical area.	2	4	8	Send an error message to operators and request maintenance	Project Manager (Koen)
RISK-TECH-OP-1-5	Wrong base station set-up	Inexperienced operators	Launch will be done improperly / charging stations not working as expected	1	2	2	Transfer	Educate the operators on the setup of the base stations	1	2	2		Project Manager (Koen)
RISK-TECH-OP-1-6	Unlicensed drone is too large to catch	The net is not large enough to catch the unlicensed drone	The unlicensed drone will not be caught by our drone.	2	2	4	Avoid	Determine the size of the unlicensed drone before trying to catch it	1	2	2		Payload (Daan)
RISK-TECH-OP-1-7	Operators unable to reach the basepoints	The terrain is too rough or it is prohibited to be there	The flight will start from an undesired location, causing a unoptimized flight path.	1	1	1	Transfer	Check before selecting the basepoints the accessibility of the location.	1	1	1		Communications officer (Leon)
RISK-TECH-OP-1-8	Object strike	The drone hits another flying object	Catastrophic loss of vehicle	2	5	10	Mitigate	Frequently scan the surrounding area for incoming objects	1	5	5		ATM lead (Jason)
RISK-TECH-OP-1-9	Being attacked by another drone	A hostile party plans on taking control of airspace	Potential loss of vehicle	1	5	5	Mitigate	Incorporate a fight-or-flight response as an action	1	2	2		Chief Engineer (Petr)
RISK-TECH-OP-1-10	Structural failure	Improper maintenance	Loss of vehicle	2	2	4	Transfer	Educate the operators on how to perform the maintenance and have a quality control manager	1	2	2		Project Manager (Koen)
RISK-TECH-OP-1-11	Charging station failure	Loss of power	Drone unable to operate	2	4	8	Mitigate	Multiple sources of power. Own source of power (solar panel for example)	1	3	3		Propulsion & Electronics lead (Leon)
RISK-TECH-OP-1-12	Obstruction on drone sensor	Environmental matters (dirt/mud/snow etc.)	Loss of precision in guidance system	3	3	9	Mitigate	Periodic cleaning/maintenance of the drone. Detection of sensor malfunction prior to flight (pre-flight checks)	1	2	2		Chief Engineer (Petr)
RISK-TECH-OP-1-13	Battery failure	End of operational life	Loss of power	2	2	4	Mitigate	Periodic replacement of batteries	1	2	2		Propulsion & Electronics lead (Leon)
RISK-TECH-OP-1-14	Net miss	Unpredicted enemy manoeuvre.	Mission failure	4	2	8	Mitigate	Incorporation of learning mechanism/database to improve predictability of enemy maneuvers. Use of larger net	2	2	4		Payload lead (Daan)

2.3. Technical Risk Assessment

Table 2.5: Technical systems risk register

Risk ID	Risk Title	Cause	Effect	Likelihood rating	Impact rating	Risk rating	Type of action	Planned mitigation actions	Likelihood rating after	Impact rating after	Residual risk rating after	Contingency action	Risk owner
RISK-TECH-SYS-1-1	The drone loses contact with the ground station	The antenna breaks or there is a failure in the communications system. Loss due to range	The drone does not know where to go, no information about the surroundings	2	5	10	Mitigate	Set up a back-up communication system to retrieve the drone safely	2	4	8	Activate backup communication systems. Automatically return to base and report an error	ATM lead (Jason)
RISK-TECH-SYS-1-2	Engine(s) failure	A fire in the engine, Power connection to the energy unavailable, rotor breaking due to impact load	Decrease in thrust, loss of altitude	2	5	10	Mitigate	Perform aerodynamic design for 'gliding' mode to retrieve the drone safely	2	4	8	Perform emergency landing at pre-determined area or attempt glide flight to the base	Propulsion & Electronics lead (Leon)
RISK-TECH-SYS-1-3	Drone is unable to morph	Structural failure of mechanical morphing system	The morphing surfaces do act as free-moving surfaces	1	5	5	Mitigate	Include fail safe design to ensure controllability even when morphing surfaces are not controllable. Quality checks	1	3	3		Structures and Materials lead (Alexander)
RISK-TECH-SYS-1-4	The morphing mechanism gets stuck.	Actuators stop working	The morphing surfaces will stay stuck in a configuration	2	4	8	Mitigate	Make sure the drone can safely land in either the loitering or attacking configuration (failsafe design)	2	2	4		Aerodynamics lead (Thymen)
RISK-TECH-SYS-1-5	Wing failure	Flying outside the design load envelope	Loss of lift, instability and loss of controllability	1	5	5	Mitigate	Program the control software to avoid maneuvers exceeding design speed	1	5	5		Structures and Materials lead (Alexander)
RISK-TECH-SYS-1-6	Failure of tracking system	Sensor malfunction	The drone will not be able to sense the unlicensed drones	2	2	4	Mitigate	Periodic maintenance and tests	2	1	2		Payload lead (Daan)
RISK-TECH-SYS-1-7	Failure of catching mechanism	Structural failure	The drone will not be able to catch the unlicensed drone	2	2	4	Mitigate	Periodic maintenance and tests	2	2	4		Payload lead (Daan)
RISK-TECH-SYS-1-8	Power system failure	Short circuit due to water/moisture	Loss of power	2	5	10	Mitigate	Encase the electronics in a water proof casing	1	5	5		Propulsion & Electronics lead (Leon)
RISK-TECH-SYS-1-9	Unpredictable behaviour	Sensor malfunction	Flight data such as the angle of attack or velocity unavailable	2	4	8	Mitigate	Use back-up sensor for the critical sensors and make them easy to replace to minimize maintenance time	1	4	4		Control lead (Shenil)
RISK-TECH-SYS-1-10	Software error	Bug in the software	The drone will be uncontrollable	2	5	10	Mitigate	Run through an extensive verification and validation plan	2	4	8		Control lead (Shenil)
RISK-TECH-SYS-1-11	Cyber attack	Software protection not up to standard	The drone can be controlled by an outside party	2	5	10	Mitigate	Incorporate a high-quality security system. Periodically update security system	1	5	5		Project Manager (Koen)
RISK-TECH-SYS-1-12	The deployed net entangles drone rotors	Unpredictable aerodynamics of the net	The drone is immobilized and cannot provide thrust to continue flight	3	5	15	Avoid	Launch the net using high pressure rather than letting it fall, this will ensure it is away from the drone	1	4	4		Payload lead (Daan)
RISK-TECH-SYS-1-13	Drone communication lost	Power loss, drone out of range, failure of comms	No more communication with drone, cannot uplink commands or downlink data	2	5	10	Avoid	Ensure drone operational boundaries with a margin to account for inconsistencies in wind	1	4	4	Create margin for operational boundaries	ATM lead (Jason)

Table 2.6: Technical system risk map before mitigation

Impact	5	RISK-TECH-SYS-1-3 RISK-TECH-SYS-1-5	RISK-TECH-SYS-1-1 RISK-TECH-SYS-1-2 RISK-TECH-SYS-1-8 RISK-TECH-SYS-1-10 RISK-TECH-SYS-1-11 RISK-TECH-SYS-1-13	RISK-TECH-SYS-1-12		
	4		RISK-TECH-SYS-1-4 RISK-TECH-SYS-1-9			
	3					
	2		RISK-TECH-SYS-1-6 RISK-TECH-SYS-1-7			
	1					
		1	2	3	4	5
		Likelihood				

Table 2.7: Technical system risk map after mitigation

Impact	5	RISK-TECH-SYS-1-5 RISK-TECH-SYS-1-8 RISK-TECH-SYS-1-11				
	4	RISK-TECH-SYS-1-9 RISK-TECH-SYS-1-12 RISK-TECH-SYS-1-13	RISK-TECH-SYS-1-1 RISK-TECH-SYS-1-2 RISK-TECH-SYS-1-10			
	3	RISK-TECH-SYS-1-3				
	2		RISK-TECH-SYS-1-4 RISK-TECH-SYS-1-7			
	1		RISK-TECH-SYS-1-6			
		1	2	3	4	5
		Likelihood				

Table 2.8: Manufacturing risk map before mitigation

Impact	5	RISK-TECH-MAN-1-2				
	4			RISK-TECH-MAN-1-9		
	3	RISK-TECH-MAN-1-3 RISK-TECH-MAN-1-4		RISK-TECH-MAN-1-1 RISK-TECH-MAN-1-8		RISK-TECH-MAN-1-7
	2		RISK-TECH-MAN-1-5 RISK-TECH-MAN-1-6			
	1					
		1	2	3	4	5
		Likelihood				

Table 2.9: Manufacturing risk map after mitigation

Impact	5					
	4					
	3	RISK-TECH-MAN-1-3	RISK-TECH-MAN-1-1			
	2	RISK-TECH-MAN-1-2 RISK-TECH-MAN-1-4 RISK-TECH-MAN-1-5	RISK-TECH-MAN-1-8 RISK-TECH-MAN-1-9		RISK-TECH-MAN-1-7	
	1	RISK-TECH-MAN-1-6				
		1	2	3	4	5
		Likelihood				

Table 2.10: Operational risk map before mitigation

Impact	5	RISK-TECH-OP-1-9	RISK-TECH-OP-1-8			
	4	RISK-TECH-OP-1-3	RISK-TECH-OP-1-4 RISK-TECH-OP-1-11			
	3			RISK-TECH-OP-1-12	RISK-TECH-OP-1-1 RISK-TECH-OP-1-2	
	2	RISK-TECH-OP-1-5	RISK-TECH-OP-1-6 RISK-TECH-OP-1-10 RISK-TECH-OP-1-13		RISK-TECH-OP-1-14	
	1	RISK-TECH-OP-1-7				
		1	2	3	4	5
		Likelihood				

Table 2.11: Operational risk map after mitigation

Impact	5	RISK-TECH-OP-1-8				
	4	RISK-TECH-OP-1-3	RISK-TECH-OP-1-4			
	3	RISK-TECH-OP-1-2 RISK-TECH-OP-1-11		RISK-TECH-OP-1-1		
	2	RISK-TECH-OP-1-5 RISK-TECH-OP-1-6 RISK-TECH-OP-1-9 RISK-TECH-OP-1-10 RISK-TECH-OP-1-12 RISK-TECH-OP-1-13	RISK-TECH-OP-1-14			
	1	RISK-TECH-OP-1-7				
		1	2	3	4	5
		Likelihood				

2.4. Contingency Management

While planning the project approach and allocating resources it may occur that the predicted budgets, time and manpower are grossly underestimated, thus causing delays in the project timeline and at times complete incoherence in subsystem designs. Therefore it is important to account for these compounding underestimations via contingency margins throughout the project workflow and product design. Technical performance management (TPM) is a technique that can be used to predict the future values of key performance parameters of the project and product under development based on current assessments of design maturity³. This method of contingency management means that future technical budgets, time and manpower can be estimated, leaving big enough margins to account for intermediate losses.

This chapter focuses on assessing the contingency measures for the mass budgets, power budgets, financial budget, and time budget of the project to ensure that the development of the Air-Guard system can be conducted smoothly and with enough margins of error.

2.4.1. System Mass Contingency

The mass of a system can fluctuate through the different stages of design maturity, therefore it is important to define contingency margins in the early stages of design to leave enough design space to develop the system. The system mass contingency margins are presented in this section of the report based on the design maturity of the Air-Guard system, the full details of the contingency plan are laid out in Table 2.12. It can be seen that the early stages of design account for larger margins as the details of the design and layout are still vague. Therefore larger margins were defined such that the design still has room to be optimized in the future.

Systems that involve larger amounts of research and design such as the drone payload and morphing mechanism are given even larger mass margins as compared to other systems, to account for the ambiguity of these systems and the need for further research. It is expected that these systems will be much more primitive in the early stages of design, therefore larger margins leave less room for error.

Table 2.12: Mass contingency margins based on design maturity

Mass Contingency %								
Design Phase/Maturity	Morphing Mechanism	Structures	Wiring/Cabling	Batteries	Sensors	Communications	Propulsion	Payload
Conceptual estimate (Based on experience, design options, sketches)	30	20	15	15	20	15	20	30
Preliminary design/Layout calculations (Preliminary H/W mock-up)	30	15	15	15	20	15	15	25
Final layout design (Final sketches and final H/W mock up engineering model)	25	15	10	10	15	10	10	15
Detailed design (Detailed hardware design)	15	10	5	5	10	5	5	10
Qualification design	10	5	3	3	5	3	3	5
Flight ready design	5	3	0	0	2	0	0	3

2.4.2. Mission Power Budget Contingency

Design of the electrical power system of the system and further defining the power budget of the system in the early stages of design are victim to large amounts of ambiguity. The contingency margins to account for the maturity of the design and further the different mission phases ensure that the power budget can be optimized

³Technical Performance Measurement (TPM): <https://acqnotes.com/acqnote/careerfields/technical-performance-measurement> <https://acqnotes.com/acqnote/careerfields/technical-performance-measurement> [Accessed: 06/05/2022]

2.4. Contingency Management

as the project advances without the need to backtrack to previous design phases. [Table 2.13](#) presents the primary power budget contingency plan based on design maturity, the margins decrease from the conceptual design down to the flight-ready design where a 5% margin is still defined to account for the reliability of the power system. Going further into the mission operations, [Table 2.14](#) defines the power budget contingencies on the mission phases throughout the design phases. The combination of the two power budget contingency plans ensures that the system has power at all times.

Table 2.13: Power budget contingency margins based on design maturity

Design Phase/Maturity	Power Budget Contingency %
Conceptual estimate (Based on experience, design options, sketches)	30
Preliminary design/layout calculations (Preliminary H/W mockup)	25
Final layout design (Final sketches and final H/W mock up engineering model)	15
Detailed design (Detailed hardware design)	10
Qualification design	5

Table 2.14: Power budget contingency margins based on mission phase

Mission Phase	Power Budget Contingency %
Drone start-up and setup	10
Drone launch + climb to operational altitude	10
Cruise phase + loitering mode operations	20
Attack mode and chasing unlicensed drone	25
Return to GS	10

2.4.3. Financial Budget Contingency

Placing contingency margins on financial budgets ensures that the chances of underestimating the expected cost at each design phase are kept as low as possible. [Table 2.15](#) displays the financial contingency margins for the project, taking into account the level of detail known by the project members at each project stage. The margins decrease as the maturity of the product increases as the team can more accurately predict the costs of components and manufacturing processes.

Table 2.15: Financial budget contingency margins based on design maturity

Design Phase/Maturity	Financial Budget Contingency %
Conceptual estimate (Based on experience, design options, sketches)	30
Preliminary design/Layout calculations (Preliminary H/W mock-up)	25
Final layout design (Final sketches and final H/W mock up engineering model)	15
Detailed design (Detailed hardware design)	10
Qualification design	5

2.4.4. Time Contingency Management

Through experience it is usually seen that the most volatile periods of product development occur during the preliminary conceptual design stages, with a decrease in uncertainty as the project progresses. The Air-Guard project is expected to be no different, with the largest periods of uncertainty in the required time coming from the conceptual and preliminary design phases. [Table 2.16](#) displays the contingency margins taken when planning the time required for each phase of the project, ensuring that there is enough time accounted for such that there can be safe planning of the project's progress.

Table 2.16: Time contingency margins based on design maturity

Design Phase/Maturity	Time Budget Contingency %
Conceptual estimate (Based on experience, design options, sketches)	30
Preliminary design/Layout calculations (Preliminary H/W mock-up)	30
Final layout design (Final sketches and final H/W mock up engineering model)	20
Detailed design (Detailed hardware design)	20
Qualification design	15
Flight ready design	5

2.5. Project Sustainable Development Strategy

While the core focus of the Air-Guard system is to neutralize the threat of unlicensed drones in restricted airspace, the mission should also employ long-term sustainability strategies such that the mission does not create more problems than it is trying to solve. Therefore, the Air Guard system must ensure that during the period the system is active, the environmental, technical, social, economic and operational sustainability is preserved. In this section of the report, the sustainable development strategy for the Air-Guard mission will be presented such that the long-term sustainability of the project is guaranteed.

The general approach will be described in [Subsection 2.5.1](#) followed by a discussion of individual components of the sustainability, environmental, social, economic and technical model in [Subsection 2.5.2](#), [Subsection 2.5.3](#), [Subsection 2.5.4](#) and [Subsection 2.5.5](#) respectively.

2.5.1. Sustainability Approach

For the Air-Guard system, the aspects of environmental, social, economic and technical/operational sustainability will be considered. A combination of all four sustainability efforts should result in the project achieving long-term sustainable deployment while solving the intended problem. The sustainable development approach will be based on the sustainability meta-model created by [B.Penzenstadler and H.Femmer](#).

Sustainability Philosophy

Given that the sustainability of a project can be traced down to the active actions performed by the system and its members, it should also be paired with an active mindset/philosophy to promote the employment of such actions. The lean manufacturing philosophy focused on the elimination of waste throughout the duration of the project. It is an important method when considering the efficient use of resources and time [12]. The use of a lean manufacturing mindset would allow the group as a whole, to work more efficiently and also waste fewer resources as a result. While not a direct contributor to sustainability, the aim to make the most efficient use of resources and minimize waste is an aspect that in the long term will contribute to the sustainable operation of the project.

The Sustainability Model

[B.Penzenstadler and H.Femmer](#) discuss the formulation of a generic sustainability model that would ensure that all aspects of project and product sustainability are considered over the project's lifetime. The principal idea is to evaluate the dimensions of sustainable development, incorporating the values that promote them along with their respective indicator and activities that support the development of sustainable ideas [11]. The creation of a conceptual model follows from this process that [B.Penzenstadler and H.Femmer](#) deem as the meta-model for sustainable development, allowing for products and companies to analyze and construct actions for sustainable development. The diagram of the meta-model for sustainable development can be seen in [Figure 2.2](#)

The goals, dimensions, regulations, values, indicators and activities can be defined as follows [11]:

- **Goals:** The goals can be defined as the main sustainability objective of the project as a whole.
- **Dimensions:** A dimension is defined as the viewpoint or aspect on sustainability for the goals.

- **Values:** Values are defined as a morale that is an expression of the dimensions mentioned previously. Values may apply to multiple dimensions.
- **Indicators:** The indicators are usually qualitative or quantitative metrics used to approximate or score a value.
- **Regulations:** The regulations can be defined as an optional element that supports or negates a value.
- **Activities:** For the model, activities are defined as an action that contributes to the enforcement of a value or set of values that contribute to the goal.

Understanding these aspects of the model will then allow for the elaboration of this model concerning the Air-Guard system. Figure 2.1 displays the top-level of the model and the legend that will be used in the following sections. This top-level will be expanded on in their respective subsection detailing the values, indicators, regulations and activities that lead to the sustainable development of the project.

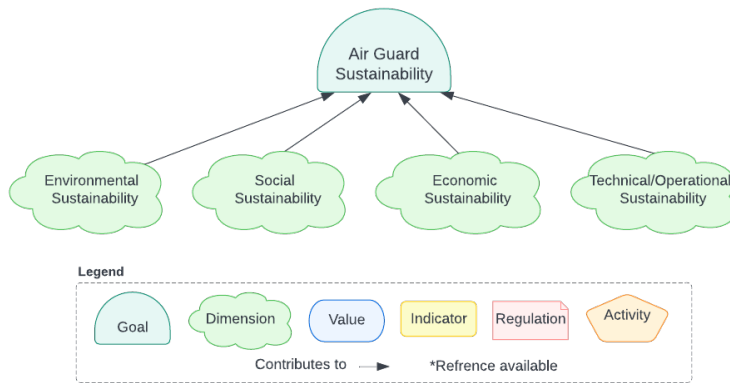


Figure 2.1: Top level of the Air Guard sustainability model

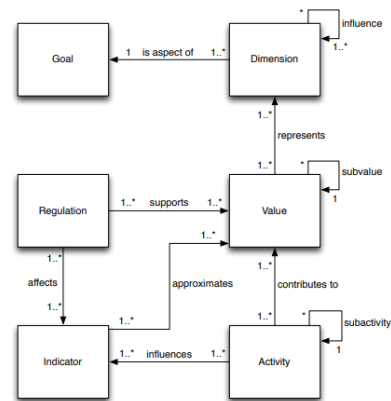


Figure 2.2: Meta Model for sustainability [11]

2.5.2. Environmental Sustainability

The environmental sustainability of a project revolves around the values of protecting natural resources, according to the United Nations⁴. The concept of environmental sustainability also involves the concern and active awareness of current consumption and production patterns leading to unsustainable use of natural resources in the long-term. The Air-Guard project will aim to acknowledge these aspects of environmental sustainability that will hopefully lead to lower emissions and a reduction in the use of critical natural resources.

Figure 2.3 displays the expansion of the sustainability model, starting with the values the project as a whole aim to hold, leading down to the actions the project needs to take to uphold these values. It also takes into account regulations such as the airport/drone noise regulations and drone size regulations.^{5 6} Breaking down the goal of environmental sustainability involves the project employing the following actions.

1. **Sustainable operations:** The consideration of long-term sustainable operations involve the reduction in energy consumption and waste throughout the entirety of the Air Guard project. In general, the 3 proposed ideas to uphold these values break down to the aspects of the propulsion source, charging methods and energy sources.
 - All-electric propulsion: Since the Air-Guard project involves drone operations, an obvious direction to moving forward is the use of all-electric propulsion to reduce emissions in the long term.
 - Renewable energy sources: Given that the project involves all-electric propulsion, the energy used in charging and production of electricity has to be considered. For the Air-Guard project it is an aim to make use of renewable energy sources for the acquisition of power such that there is minimal emis-

⁴World Economic and Social Survey 2014/2015: https://www.un.org/development/desa/dpad/wp-content/uploads/sites/45/publication/2015wess_ch5_en.pdf [Accessed: 04/05/2022]

⁵Noise zones around Amsterdam Schiphol Airport: <https://www.government.nl/topics/environment/noise-nuisance/aircraft-noise> <https://www.government.nl/topics/environment/noise-nuisance/aircraft-noise> [Accessed: 04/05/2022]

⁶Rules for the recreational use of drones: <https://www.government.nl/topics/drone/rules-pertaining-to-recreational-use-of-drones> <https://www.government.nl/topics/drone/rules-pertaining-to-recreational-use-of-drones> [Accessed: 04/05/2022]

sions. Proposed ideas involve solar panels to produce the required electricity for the ground operations (for example for charging the batteries, powering the communication systems and powering the detection systems).

- Replaceable and rechargeable batteries: While the drone runs on electric propulsion there is an aim to make use of rechargeable batteries to prolong the lifespan and use of one drone, these batteries shall also be able to be recycled, such that there is minimal wastage of used components.
2. **Optimize of material usage and manufacturing:** The use of different materials plays a large role in the management of natural resources and the recycling characteristics of materials after use. Therefore, a large emphasis will be put on the use of sustainable materials and manufacturing methods to achieve the highest efficiency with lowest waste
- Designing with 75% of the drone mass coming from recyclable materials: The requirements for the Air-Guard UAV resulted in the formulation of 75% of the drone mass being comprised of recyclable materials. In doing so, it enables the reuse of drone structures such that the residual waste is minimized. The material sustainability practices should ensure that the energy input to recycle the material should not exceed the energy input to manufacture the material. Additionally, using natural fibers and bio-replacements should ensure that the consumed natural resource is abundant, fast growing and does not cause compromises to the natural biodiversity of the area.
 - Additive, topology optimised manufacturing: Additive manufacturing methods results in a lower amount of waste from the manufacturing process. This, in combination with topology optimised manufacturing ensure that only a critical amount of material is used and that the product is manufactured in the most efficient way possible for the project.

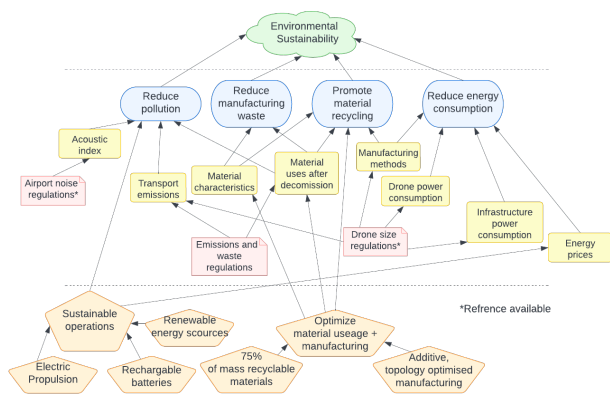


Figure 2.3: Environmental sustainability model for the Air Guard

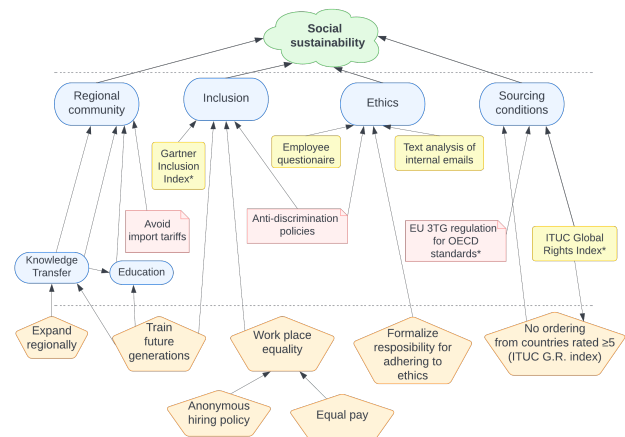


Figure 2.4: Social sustainability model for the Air Guard

2.5.3. Social Sustainability

The social sustainability dimension includes protecting existing social systems and enabling future desired social structures. The Air-Guard project will achieve social sustainability by implementing the following tasks to support the values shown in Figure 2.6.

1. **Expand regionally:** manufacturing and development plants should be expanded regionally to ease knowledge transfer.
2. **Train future generations:** future work force generations must be trained ahead of time to mitigate knowledge losses due to demographic change.
3. **Work place equality:** while qualification determines new employee acquisition, equality and anti-discrimination are important to consider potential hires from all backgrounds and maintain an inclusive working atmosphere. The latter leads to a more efficient work environment benefiting sustainability dimensions.
 - An anonymous application policy ensures that application documents can be assessed in an objective manner.

- Equal pay removes a tension driver between employees. Tensions contradict a sustainable work environment.

The affected value is inclusion. Its change can be measured with the Gartner Inclusion Index as an indicator [13].

4. **Formalize responsibility for adhering to ethics:** enforcement of values is not possible without distributing responsibilities. Assigning the responsibility formally through a job description will increase valuing ethics throughout the project.
5. **No ordering from countries rated ≥ 5 (ITUC G.R. index):** valuing decent working conditions in sourcing countries can be enforced through a policy referring to the ITUC global rights index [14]. Moreover, the import of some materials is regulated⁷.

2.5.4. Economic Sustainability

Economic sustainability entails the use of a broad set of decision making values and practices to achieve economic growth and minimizing the resulting adverse effects of harmful environmental trade-offs [15] Essentially economic sustainability aims to conserve the longevity of local and global economies through the elimination of unsustainable business practices that deplete natural and economic resources faster than can be accounted for.

For the Air-Guard project the economic sustainability shall focus on the core aspects of maintaining the longevity of the system and ensuring that economic trade-offs and practices only aid to promote the project's sustainable impact. Preservation of assets and the generalisation of the system for a number of applications is therefore critical. Therefore, through expansion of the economic sustainability goal as seen in Figure 2.5, the following actions to preserve the values of the project are as follows:

1. **Economic optimization of operations:** To maintain asset value and to promote the economic longevity of the system the optimization of the operation with respect to use of available economic resources is imperative, therefore the following activities are hoped to be employed to reach this goal.
 - Autonomous loiter + attack of UAV: Automation of the in-flight operations of the drone is hoped to promote the life of the system and also remove the added personnel costs that come with the incorporation of a drone system.
 - Easy drone accessibility + replace battery: To improve the maintenance of the drone and further the resources needed to maintain the operations of the drone, the aim of the project is to create an easy to maintain system containing parts that can be swapped out, fixed and incorporated in other drones.
2. **Optimization of manufacturing:** Preservation of local economic markets through the Air-Guard system is another aspect of high importance. The project aims to not only aid the strengthening of local markets but also streamline production processes to reduce waste as a result of these processes.
 - Manufacture locally: An important aspect of aiding the development of local economies is the creation of job opportunities that not only help the local economy, but also increase the available skills in the workforce. The Air-Guard project aims to incorporate local manufacturing methods and manpower to sustain the longevity of local economies.
 - Reliable raw material supply: It is imperative that the raw material supplied to the project is sourced fairly and is monetized such that no party in the sourcing of these raw materials is taken advantage of.
 - Use of universal production methods: Where not applicable, it is aimed to make use of universal production methods to reduce tooling and manufacturing costs while still achieving the same required material and part performance.

⁷<https://eur-lex.europa.eu/legalcontent/EN/LSU/?uri=celex:32017R0821> [Accessed: 04/05/2022]

2.6. Resource Allocation

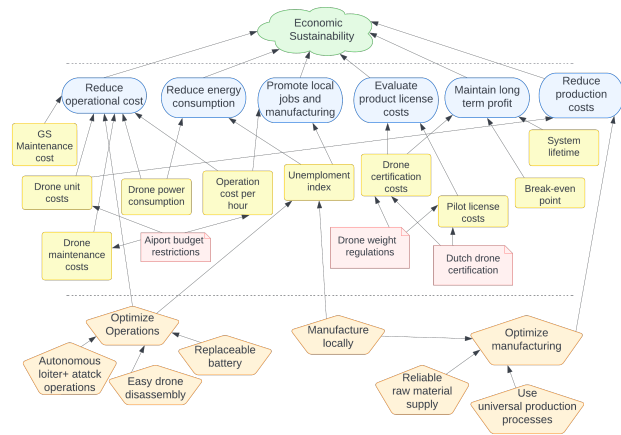


Figure 2.5: Economic sustainability model for the Air Guard

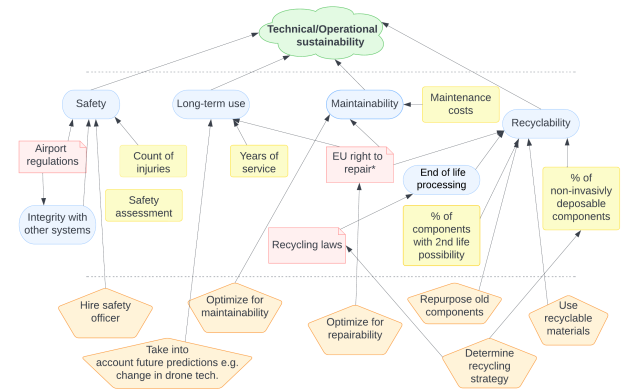


Figure 2.6: Technical/Operational sustainability model for the Air Guard

2.5.5. Technical/Operational Sustainability

The technical and operational sustainability dimensions spans a particular long period in time. Thus, implementing the following tasks can have a positive snowball effect on the project sustainability.

1. **Hire safety officer:** continuous safety during operations must be ensured. The complex task to anticipate risks and update safety protocols, taking into account developments in ATM and the Air-Guard system, is best tackled by hiring a dedicated safety officer.
2. **Use technology forecasts:** the Air-Guard project aims to solve an evolving problem. Thus, the chosen technology must be updatable and updated to be a sustainable solution. Predictions of developments in the market for commercially available drones can be used to adapt the Air-Guard system in advance.
3. **Optimize for maintainability:** during the period of operations, maintenance must be carried out. An optimized design can ease this, increasing the chances of the system staying usable. For example, placing mountings of wearing parts easily accessible.
4. **Optimize for repairability:** similar to a maintainable design, a repairable one consolidates the system's long-term use. For example, sufficient documentation allows generic technicians to repair small defects.
5. **Re-purpose old components:** the technical design can take into account that some system components at the product's end of life are re-purposed for other, lower-performing applications.
6. **Determine recycling strategy:** a strategy can explicitly highlight recyclable components. This allows for including sustainability as a category in trade-offs on a technical level.

2.6. Resource Allocation

To ensure a successful completion of the design it is essential to allocate the limited resources available during the project as optimally as possible to minimize time waste, and ultimately, complete it within the allocated time.

First, the different design activities are grouped in individual systems. This is done by identifying system functions, which add to the top-level functions in Figure B.3, in the appendix. Design activities follow system functions and thus provide a good indication of how the design process can be structured. These can be visualized in Figure B.4, which is also located in the appendix. It can be seen how the Command and Data handling aspect of the mission represents an important aspect of the design, as the flight model of the drone has to be developed. Furthermore, the structural design of the drone also adds to the complexity of the process, mainly due to the necessity to design the morphing mechanisms.

Following from this process, a rating is attributed to the different systems, to assess the complexity of the design activities, such that the proper human resources can be attributed to each one of them. This process is summarized in [Table 2.17](#). Additional resources such as wind tunnels, 3D printers and destructive, and non-destructive testing facilities will have to be used in the future stages of the design such that the performance of the UAV can be validated fully.

Table 2.17: Resources allocation

System	Description of design activity	Resource rating	Lead engineer	Support engineers
Propulsion	Selection of optimal propulsion system from commercially available options, according to mission specifications	4	Alexander	Thymen
Electronics	Sizing and selection of optimal electronics according to mission specifications	2	Leon	-
Flight management	Development of flight model for the whole mission profile, including navigation and data handling	10	Shenil, Daan	-
Tracking, Counter measures	Selection of readily available detection and tracking system, according to mission specifications	2	Koen	-
Communication	Selection of readily available communication system according to mission specifications	1	Leon	-
Payload	Complete design of net launching mechanism, and net shape.	5	Daan	Baptiste, Jason
Active structures	Complete design of all moving structures, including control actuators, and morphing mechanism	9	Alexander, Koen	Alex
Passive structures	Complete design of fixed structures, and analysis of stresses and deformations	8	Alex, Leon	Baptiste
Controllability and Stability	Study of controllability and stability in all morphing modes	4	Petr, Jason	-
Aerodynamics	Study of the aerodynamic design of the drone air frame, in all morphing modes	8	Thymen, Petr	Baptiste, Jason, Daan, Shenil
Ground segment	Operational study of ground station, including selection of hardware components	2	Jason, Koen	-

2.7. Market Analysis

In this section, a market analysis will be carried out to evaluate the demand and competition, optimize the design for the needs of a wide range of customers and make the final product attractive and financially sustainable. In [Subsection 2.7.1](#) and [Subsection 2.7.2](#) the launching and other potential customers will be identified and the reasons for their interest will be discussed. [Subsection 2.7.3](#) then focuses on identifying and evaluating existing drones already developed for anti-drone protection to identify where value can be added to attract customers. Similarly, [Subsection 2.7.4](#) presents substitutions for drone-based anti-drone systems. Finally, [Subsection 2.7.5](#) uses all gathered information to identify the market gap that the air-guard system could fill in.

2.7.1. Identification of Customers

As mentioned, [Park et al.](#), [Lykou et al.](#) show that sensitive air spaces deal with an increasing frequency of safety threats due to UAVs [16, 17]. The impact of this threat depends on the type of airspace. It was decided to focus on one airspace type, which can act as a launching customer of the counter-drone UAV, due to the large financial motivation for airport protection. Furthermore, the current legal requirements for the airspace should allow for autonomous counter-UAV systems.

The analysis yielded that a large airport, like Schiphol, has the most significant loss as a result of rogue drones flying in its airspace, as many flights have to be diverted or canceled. This translates into substantial financial losses, making it interesting for parties to invest in efficient counter-UAV technologies.

2.7.2. Other Potential Customers

Besides the launching customer, there are other possible applications for the counter-drone UAV:

- Military defense (defense of facilities or moving assets). As drones are used more and more in modern warfare, an efficient counter-drone system is more useful than ever.
- Border control. Drug smuggling is possible to be done by drones, which must be neutralized.
- Bird pest deterrents. The counter-drone can be modified to a counter-bird UAV, in order to catch the birds that do damage to the crops.
- Paparazzi countering. Drones are illegally used to spy on VIPs, thus invading their privacy.
- Wildlife protection. There are many nature reserves where operating drones is prohibited as not to disturb the fauna and flora.
- Government buildings guarding. Espionage and terrorism using drones is becoming more common, thus a new way of defending critical sites is needed.
- Entertainment. There might be a market for drone enthusiasts that would like to use counter-drones for entertainment purposes.

In [Table 2.18](#), all the secondary applications are considered, and the reason why it is not the launching application is stated:

Table 2.18: Possible applications for the Air-Guard

Application	Why not chosen as launching customer
Military defense	Harder to scale due to foreign military's preferring local solutions, Ethics of potential destructive use
Border control	Not a large market, no direct financial threat
Bird pest deterrents	Not a large market, lack of funding
Paparazzi countering	Lack of legality
Wildlife protection	Lack of funding
Sensitive space	Not large enough financial incentive
Entertainment	Lack of legality

In [Table 2.18](#) the statement 'Lack of legality' was made for the paparazzi countering the use case of the UAV. For this the following explanation can be given: when the drone is operated privately by a civilian the current legislation will limit the design space for the UAV severely. To be the owner/ operator of this system would have to have continuous permission from a governmental entity such as law enforcement to operate this drone within legal bounds. This makes it highly impractical and therefore less economically viable compared to other options.

2.7.3. Competitors

To ensure the economic viability of our product, an analysis of competitors, i.e. systems that perform a similar mission by similar methods, is essential. Firstly, Delft Dynamics ⁸ has developed a drone that aims to solve the same problem by attaching a net shooting mechanism to a quad-copter-style drone. They have an autonomous tracking system that tracks and catches the unlicensed drone. While they have proven their technology works and have made great advances in this field, they still lack range and endurance as quad-copter drones lack these aspects. The drone developed by LAMAT launches a net using the kinetic energy stored in the propellers. This system can be used to catch light UAVs ⁹. The main disadvantage of this system is its very limited range and endurance, reliance on the skill of the human operator, and therefore no autonomy/continued protection.

The MARSS extrasensory protection UAV is another competitor which uses a dual-function quad-copter, fixed-wing design and takes down drones by hitting them in a kamikaze style, destroying itself as well ¹⁰. This system's disadvantages are that it can only take down larger UAVs to be effective, due to smaller ones being easily missed. Another competitor is the Military Force Protection (MFP) drone from DARPA which uses a vertically stacked counter-rotating propeller design, which can be launched from a (military) vehicle to take down rogue drones which are e.g. threatening a military convoy. The MFP uses strings, which are launched from the drone at high speed, to take down the rogue drones by entangling the propellers [18]. The main disadvantage of this system is its limited maneuverability, which makes it very hard to intercept more maneuverable drones and its range which requires that the drone is deployed close to the threat, which makes it less versatile.

2.7.4. Substitutes

In addition to the competitors analysed in [Subsection 2.7.3](#), it is equally important to analyze systems that attain a similar goal by means of a different method. A list of substitutes is given in [Table 2.19](#), together with a list of their main advantages and disadvantages. Most of these substitutes are either illegal when used against civil operators or are not scalable. This means that the main substitute to the C-UAS are birds of prey.

⁸<https://www.delftdynamics.nl/> [Accessed: 13/06/22]

⁹<https://lamat.me/works/interceptor.html> [accessed: 16/05/2022]

¹⁰<https://www.marss.com/marss-interceptor> [Accessed: 2022/04/28]

Table 2.19: *Substitutes for defence against UAS [19]*

Method	Advantages	Disadvantages
RF Jamming	<ul style="list-style-type: none"> • Medium range (few km) • Directional jamming that minimizes interference 	<ul style="list-style-type: none"> • Could interrupt communication signals, autonomous drones are immune • Illegal in many countries • Could cause the rogue drone to crash due to uncontrolled flight
GPS Jamming	<ul style="list-style-type: none"> • Disrupts rogue drone GPS link, making it hard to control. • Medium to short range 	<ul style="list-style-type: none"> • Dangerous near airports as aircraft also use GPS • Could cause the rogue drone to crash due to uncontrolled flight • Illegal in many countries • Only holds for GPS enabled drones
Protocol Manipulation	<ul style="list-style-type: none"> • Takes control over communication link of rogue drone • Can safely land the rogue drone in a designated area • Low-cost technique 	<ul style="list-style-type: none"> • Illegal against civilian users • Success depends on the communication encryption • Complicated method • Autonomous UAVs not using GPS are immune
High Power Microwaves or Lasers	<ul style="list-style-type: none"> • Long-range countermeasure • Destroys rogue drone electronics • Disables drone flight 	<ul style="list-style-type: none"> • Might negatively affect other aircraft • Could cause the rogue drone to crash due to uncontrolled flight • Illegal for civil aviation
Birds of Prey	<ul style="list-style-type: none"> • Can safely land the rogue drone in a designated area 	<ul style="list-style-type: none"> • Birds are also dangerous for aircraft • Agility of rogue UAVs may prevent capture • Birds are difficult and expensive to train

2.7.5. Identifying the Market Gap

When combining the information found in [Subsection 2.7.3](#) and [Subsection 2.7.4](#), the market gap can be found, which is essential to realize where a new product will have the highest economic viability. The gap here is a legal solution that has a large range, is independent of a human operator, and can catch both slower and highly maneuverable drones of a wide range of sizes in a timely manner.

When looking at the future, one can see that the usage of drones will increase significantly, which will consequently increase the number of incidents similar to what happened at Gatwick airport in Jan 2019, resulting in losses of 1.8 million euros per hour if additional measures are not taken [1] [20]. The incident in Gatwick included a drone circling the airport, causing all the flights to be grounded for 33 hours. This shows that the market demand for these types of defense UAVs will increase significantly in the near future, backed up by a very large financial motivation due to the high costs associated with the incidents, as described earlier.

3. Design Overview

This chapter discusses the general design overview. Section 3.1 discuss how this design process differs from ordinary designs. To expand on this, a background study will be given in Section 3.2. To see which subsystems need to be designed. Section 3.3 studies all functions of the system and what are the consequences for the design. Then, Section 11.1 discusses all aspects related to air traffic management and how the system aims to fit in that environment. Lastly, Section 3.5 discusses the trade-offs that were made in the midterm review.

3.1. Design Approach

Discrete control surfaces of conventional fixed wing aircraft such as ailerons, rudder and elevators allow for total control of roll, yaw and pitch rotations respectively. However, the control surfaces on birds are continuous and consist of feather-tendon interactions that allow for a wide range of control sensitivities surpassing that of conventional aircraft. As a result, birds pose higher levels of maneuverability [21]. The comparison of control methods for conventional aircraft and birds can be seen in Figure 3.1, in which the higher fidelity of control is evident in bird morphology via the various degrees of freedom of tail and wing morphing.

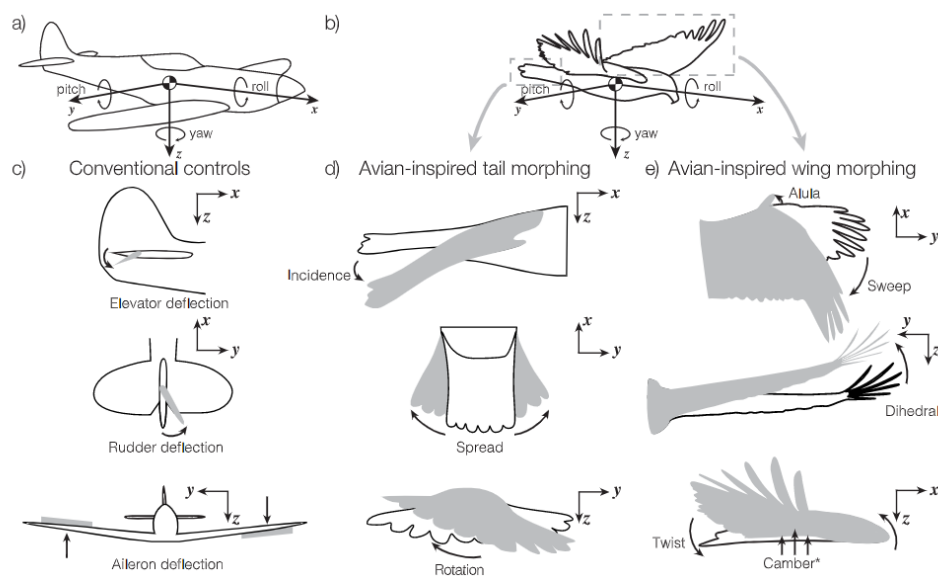


Figure 3.1: Active flight control methods for a) conventional aircraft and b) birds. c) Degrees of freedom of conventional controls as compared to d) avian tail morphing and e) avian wing morphing [21]

The combination of the bird neurological reflex-control and dynamic morphing capabilities means that high performance can be achieved over numerous flight conditions. Structural adaptation of dynamic control surface morphing and its implementation into drone technology would thus give rise to a new series of higher efficiency, higher maneuverability and more robust drones through which the envelope of drone applications can be further extended.

The design of the Air-Guard drone aims to incorporate the design of wing and tail morphing such that the flight characteristics and stability can be fine-tuned mid-flight. This would mean that the drone would be able to closely emulate the flight behavior of certain bird species and make use of the increased performance to better chase and neutralize unlicensed drones. Further discussions and evaluation of the extent of wing and tail morphing will be described Chapter 6 and Chapter 7. However, it is important to consider that the design must facilitate both the functions of more efficient and maneuverable flight, while also being capable of providing a reliable unlicensed drone capturing method.

3.2. Technology Background

The Air-Guard system is based on the concept of morphing control surfaces of a UAV to increase its agility. However, it is not the first time that this concept has been explored. A number of technological institutes such as Stanford University and The École Polytechnique fédérale de Lausanne (EPFL) have previously investigated and built flying prototypes making use of the morphing of control surfaces to increase the maneuverability of a drone. This section of the report aims to provide a background of the morphing drone concept and in turn provide a proposed application of the concept for the Air Guard project.

Investigation of the two approaches to the concept appears to yield two very different designs, focused on the same central mechanism of the morphing wing. In general, the development of both concepts revolves around the attempt to accurately replicate the bio mechanism of a pigeon wing as seen in Figure 6.3, by morphing the inner and outer surfaces of the wing to achieve coarse and fine control. The general differences in the designs of both institutes can be seen by comparing Figure 3.2 from Stanford University and Figure 3.3 from École Polytechnique fédérale de Lausanne. While Stanford University seems to completely embrace the use of real feathers and the formation of a complete morphing wing in their design, EPFL takes a different approach using polyester as a replacement for feathers and further only makes use of the active morphing mechanism at the ends of the wings, keeping the inner wing fixed and inducing a forward sweep in that area. Additionally, the EPFL design concept also uses a morphing tail that further aids in the agility of the concept. Apart from these differences, both designs utilize electric motors for propulsion and lightweight structures such as foam board and wood [5] [4].

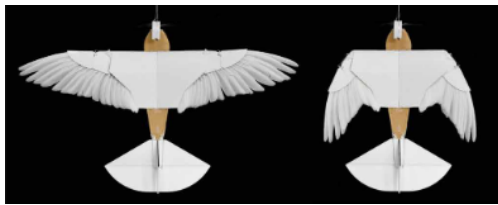


Figure 3.2: Design prototype from Stanford University [5]

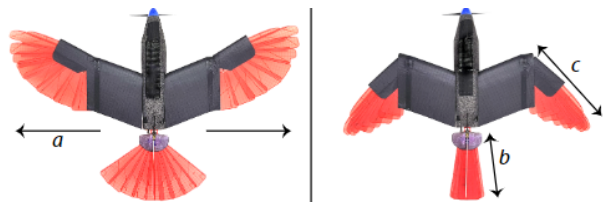


Figure 3.3: Design prototype from EPFL [4]



Figure 3.4: Maneuverability of the EPFL drone [4]

The extent to which morphing wings aid in increased maneuverability can be clearly seen in the flight demonstrations of both designs. Specifically, the EPFL design shows a greater degree of maneuverability due to the inclusion of a morphing tail surface. The drone is able to perform sharp pull up maneuvers and turns with ease as can be seen in Figure 3.4, therefore it is clear that the idea of active morphing wings does indeed increase the agility and is a promising concept for a number of applications. The further implementation of such concept will be discussed in the following chapters of the report.

3.3. Functional Diagrams

The functional diagrams display the essential functionalities of the system, such that the general workings of individual subsystems can be identified and designed for their specific tasks. This section of the report aims to display the functional flow diagram of the Air-Guard drone concept, as well as the functional breakdown of the system, such that further details can be identified.

3.3.1. Functional Flow Diagram

The goal of a functional flow diagrams is to present the functions of the system in a chronological way. The functions are generated to see how the system operates in its environment and which subsystems need to be designed in order to cover its complete operation. The top level functions are shown in Figure 3.5 and cover the mission in the broadest sense. The functional flow diagram is presented in Figure B.1 and consists of three levels of depth: the top level functions (blue), second level functions (orange) and third level functions (yellow).

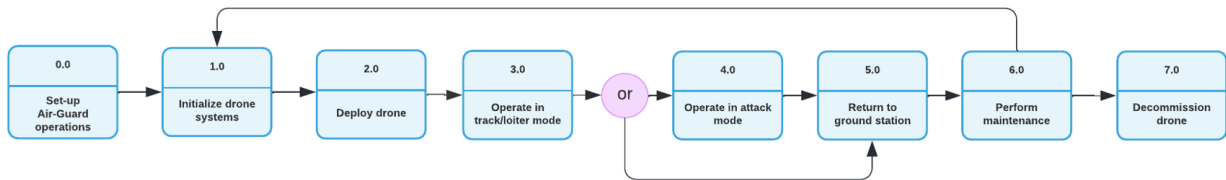


Figure 3.5: Top Level Functions of the Air-Guard system

3.3.2. Functional Breakdown Structure

A functional breakdown structure (FBS) adds to the functional flow diagram by adding a fourth layer of detail and by structuring the functions by mission phase instead of a chronological order. The functional breakdown structure aids in creating requirements for each subsystem and thus creating a more clear design space in which the subsystems need to be designed. The functional breakdown structure is presented in Figure B.3.

3.4. Requirements and Compliance Matrix

All requirements were identified and formulated in the baseline review [22]. They are presented in Appendix A. In addition, it is also given whether the design complies to the requirements.

3.5. Summary of Trade-Offs

In this section, a summary will be given of the trade-offs performed during earlier stages of design to give a better insight as to where the final design originates from. When performing a trade-off the most relevant criteria for each decision have to be found first, subsequently they can be assigned a weight and each option is given a score for each of the criteria. The quantitative or numerical trade-offs use a scale from 1 and 10, where 10 is the best performance for that specific criterion and 1 is the worst performance. This score is then multiplied by the criteria weight to obtain the weighted score, these are then summed such that the final decision can be made. As for the qualitative trade-off, a similar weighting system was used, as can be seen in Table 3.1. In Subsection 3.5.1 the trade-offs for the relevant subsystem are given, which had to be done before the larger configuration trade-offs were performed. These are given and described in Subsection 3.5.2.

Table 3.1: Qualitative trade-off criteria color code

Excellent, better performance than requirements	
Good, performance meets requirements	
Correctable deficiencies	
Unacceptable	

3.5.1. Subsystem Trade-Offs

In this section, an overview of minor subsystem trade-offs are given, with the winner of each highlighted by bright yellow.

Table 3.2: Take-off method trade-off

Criteria	Operator Safety	Footprint	Reliability	Weight perf.	Cost	Autonomy	
Weight	3	6	8	8	3	3	
Hand thrown	3	8	7	10	5	0	208
Take off with wheels	6	5	7	3	7	7	170
Sliding	6	3	3	8	7	5	160
Rail system	8	6	8	7	7	8	225
Winch	7	4	6	6	5	3	165

Table 3.3: Landing method trade-off

Criteria	Distance	Weight perf.	Durability	Complexity	Operator safety	
Weight	9	8	6	5	9	
Catching drone in hand	8	9	7	9	0	231
Land on belly	6	6	4	9	10	261
Land on wheels	5	3	7	7	10	236
Hook system	10	6	5	3	6	237

Table 3.4: Catching method trade-off

Criteria	Mass perf.	Min. allignment	Deployment device complexity	Operating range	Sustainability	Effect on drone performance	
Weight	8	10	8	6	2	4	
Single+Double drop	6	8	8	5	10	5	262
Shooting	5	7	7	9	9	7	266

Table 3.5: Battery integration and recharging method

Criteria	Mass perf	Downtime	System Complexity	Sustainability	
Weight	8	6	6	5	
Fixed battery / Wired charging	9	4	8	7	179
Fixed battery / Induction charging	9	2	7	6	156
Swapable battery /Wired charging	8	8	6	8	188
Swapable battery / induction charging	8	8	5	7	177

Table 3.6: Target detection method trade-off

Criteria	Mass	Complexity	Detection efficiency	
Weight	5	5	8	
Ground-based	10	8	8	154
Drone-based	2	4	4	62

Table 3.7: Tracking method trade-off

Criteria	Mass	Accuracy	Reliability	Complexity	
Weight	8	6	4	7	
Visual	8	8	5	10	202
Infrared	8	6	8	9	195
Lidar	0	7	8	7	123
Radar	0	9	9	7	139

Table 3.8: Trade-off of materials used for morphing

Criteria	Mass	Structural rigidity	Complexity	Sustainability	Flight performance	Scalability	Bio-inspired	
Weight	8	7	6	4	7	4	4	
Synthetic feathers	10	4	5	8	6	8	8	276
Real feathers	10	6	5	4	8	4	10	280
Compound platelets	6	8	6	8	6	9	8	282
Elastic membrane	8	7	4	6	6	3	4	231
Rigid skin	8	9	8	8	2	9	2	265

Table 3.9: Payload position trade-off

Criteria	Aerodynamics	Complexity	Weight	Activation time	
Weight	8	4	6	7	
Front comes off	6	3	6	9	177
Front opens	3	2	4	5	102
Bottom opens	8	5	6	5	175
Bottom comes off	7	3	6	9	186
Bottom exposed	1	8	8	9	168

Table 3.10: Types of tail morphing trade-off

Criteria	Structural Rigidity	Complexity	Integration Motor Shaft	Integration Servo	
Weight	8	4	7	6	
EPFL	7	5	7	8	173
Neural Network	4	4	7	6	133
Salmiak	5	8	3	9	147
Telescopic	8	7	8	1	154

Table 3.11: Wing morphing mechanism trade-off

Option	Criterion				
	Mass Performance (8/10)	Actuation (6/10)	Complexity	Morphing (9/10)	Maintenance (5/10)
True Bio-inspired	Only one actuator required for the single elbow joint	Simple movement of a single actuator, Combination of movement of platelets and hinge		High morphing of both surface area and sweep, but no independent control of sweep and surface area change	Single hinge and rod very reliable and need little maintenance, rubber bands in between the platelets need more "maintenance" but are easily accessible
Single-hinge w. Rod	Two actuators required, longer rods with more connections to the platelets	Actuator placement for platelets movement very close to trailing edge for effective movement, this actuator also has to move with the elbow joint further increasing complexity		Independent control of surface area change and sweep change, morphing is more limited due to actuation of the separate systems being contradictory	Harder to replace the rods within the wing and more connections on the platelets, but need less maintenance overall

3.5.2. Configuration Trade-Offs

After performing the smaller subsystem trade-offs, the four final design options were defined as shown in Figure 3.6. To make the decision on the optimal design choice, larger configuration sub-System trade-offs were performed, as described below. From these it was concluded that design concept 4 with a conventional tail was the optimal design for the given set of mission requirements. However after further investigation into the propulsion system design, as described in Chapter 8, and the disadvantages described in the engine configuration discussion, it was found that the dual engine option was superior.

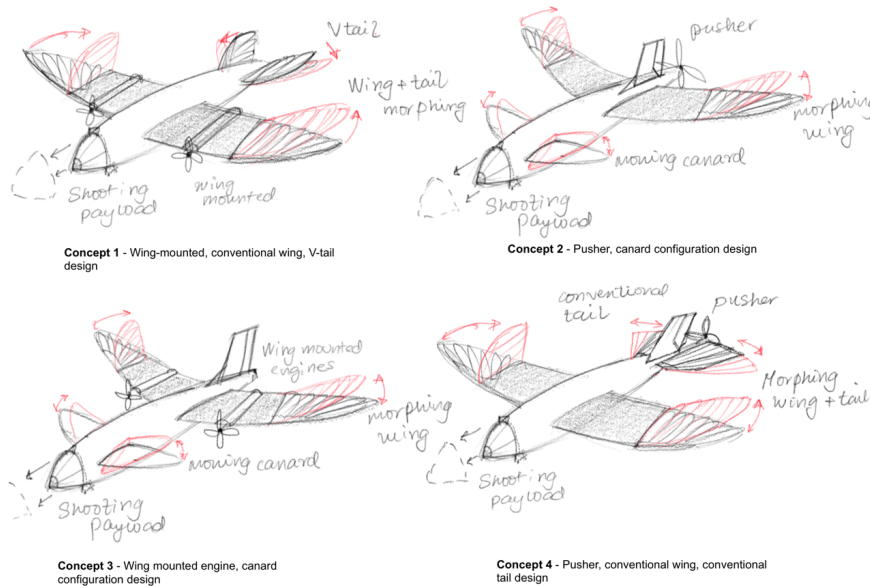


Figure 3.6: Design concepts entering final trade-off

Table 3.12: Design efficiency trade-off

Design option	Design efficiency trade-off scores				Total
	Propulsion system	Structures	Stability and control	Morphing integration	
Concept 1	5	7	8	4	24
Concept 4	7	6	7	7	27
Concept 3	5	5	5	4	19
Concept 2	7	5	5	6	23

Table 3.13: Configuration trade-off table for adaptability, risk and technology readiness level

Design option	Trade-off scores				Total
	Adaptability	Design risk	Manufacturing risk	TRL	
Weights	4	7	6	7	
Concept 1	7	7	7	9	182
Concept 4	7	8	7	9	189
Concept 3	6	5	6	4	123
Concept 2	6	4	5	3	103

Table 3.14: Configuration trade-off table for bio-inspiration and system complexity

Design option	Trade-off scores		Total
	Level of bio-inspiration	System complexity	
Weights	6	7	
Concept 1	8	9	111
Concept 4	7	8	98
Concept 3	5	4	58
Concept 2	3	5	53

Wing Morphing

Both the EPFL and Stanford concepts make use of different degrees of morphing, with the Stanford concept making use of a double hinge design and EPFL a single hinge design[4][5]. Both concepts also identify the use of primary feathers for coarse correction and secondary inner feathers for fine corrections. For the Air-Guard design, the alula is a key aspect in bringing the performance of a morphing wing to a new level, as will be discussed in more detail in Subsection 6.3.4. A total of 5 concepts were developed and are presented in Figure 3.7 in the form of rough sketches to depict the working principles of the concepts.

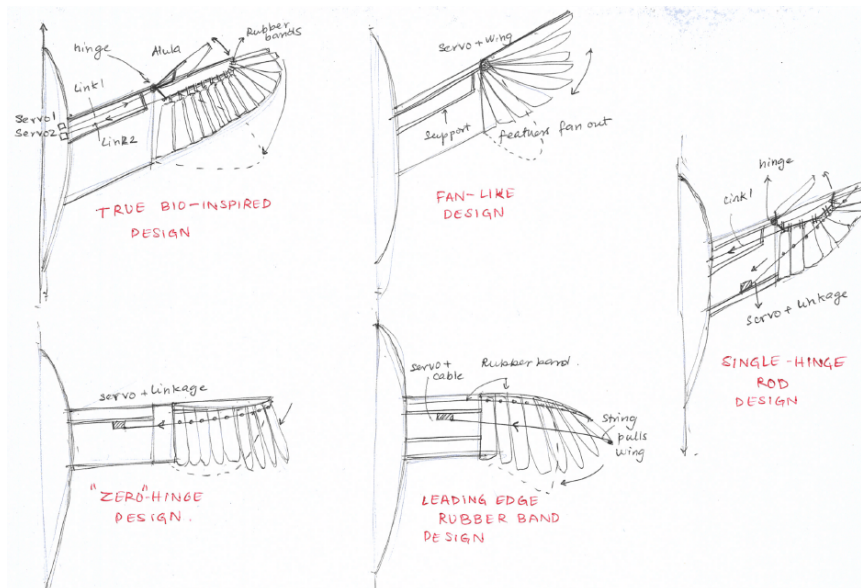


Figure 3.7: Design concepts for the morphing mechanism design

Further analysis provided several valuable takeaways; The "Zero-hinge" Rod Design was disregarded due to the limited morphing allowed by this mechanism. The Fan-like design was discarded due to the required thickness of the mechanism at the leading edge and the limit in achievable morphing. The leading edge rubber band design was also disregarded due to the placement of the rope having a high probability of interference with other structures and/or aerodynamics and limited stiffness due to the number of joints in the load carrying structure. The two remaining design options entered a more detailed qualitative trade-off as can be seen in Table 3.11. This resulted in the "True Bio-inspired" design emerging victorious.

Engine Configuration

Two main design paths were found, being a configuration with dual wing mounted engines with relatively small propellers, and the single engine configuration with a larger propeller in a pusher configuration mounted at the rear of the fuselage. It is important to note, that for the single engine design the motor would be mounted more centrally within the fuselage, so as not to cause interference with the tail morphing mechanism, and to keep the center of gravity of the UAV more centralized. This also means that the motor and the propeller would be connected via a shaft running through the fuselage, which could limit the degree to which the tail can deflect.

The method which explains how to estimate the performance of propeller based propulsion systems is explained in [Subsection 8.2.1](#). This and the previously mentioned disadvantages that go hand in hand with the single engine option made the winner the dual engine design.

Wing Configuration

The trade-off for the wing configuration was focused on a quantitative basis. Through setting up a class I and class II weight estimation, the center of gravity range and relative static stability and maneuverability were determined, taking into account the required positions of all other subsystems. When expelling the payload, the shift in the center of gravity is the highest for both canard configurations. In addition to this, the center of gravity for the conventional configuration is closer to the quarter-chord point of the wing than is the case for the canard configuration. This indicates that, with the used layout of the drone subsystems, the conventional configuration will lead to a more maneuverable drone. This resulted in the conventional configuration being chosen.

Tail Configuration

The shape of the tail of the drone has an effect on the stability and control performance. For this trade-off, four different tail designs have been considered. The trade-off has been performed qualitatively, and it is shown in [Table 3.15](#). The outcome of the trade-off is a conventional tail. The decision regarding the rudder is presented in [Subsection 7.3.2](#).

Table 3.15: Tail configuration trade-off

Option	Criterion						
	Mass performance (8/10)	System complexity (8/10)	Failure tolerance (7/10)	Drag Performance (6/10)	Required control forces (5/10)	Bio-inspired (6/10)	Ground clearance (5/10)
V-tail	Good mass performance, only 2 surfaces controlling yaw and roll	Poor - High complexity of coupled yaw and roll	Poor - coupling of controls reduces reliability	Good - best drag performance	Higher control forces to control aircraft	Best bio inspired design	Good ground clearance
Inverted V-tail	Good mass performance, only 2 surfaces controlling yaw and roll	Okay complexity of coupled yaw and roll - better than V-tail	Bad- Reliability marginally better than V-tail	Good - equal drag performance to V-tail	Higher control forces to control aircraft	Okay-Not too bio inspired	Bad ground clearance
Conventional	Okay mass performance, conventional configurations are most common	Good - low complexity due to uncoupled controls	Best reliability due to better designs	Okay - typical expected drag	Typical expected control forces	Least bio-inspired design	Good ground clearance
Y tail	Better mass performance than conventional	Better complexity than V-tail and inverted V-tail	Good - better reliability than V-tail	Better drag performance than conventional tail	Lower control forces than V-tails	Good - less bio inspired than V-tail	Worst ground clearance

4. Fuselage Design

The fuselage forms the body of the drone. Next to the payload, it houses the electronics (Section 4.1), acts as a frame for other mounting groups to attach (Section 4.2), and provides structural integrity (Section 4.2).

4.1. Electronics

The electronics subsystem contains several components. In this section, the communications (Subsection 4.1.1) and telemetry sensors (Subsection 4.1.2) are described. Their energy consumption yields the power budget in Subsection 4.1.4. The chosen battery to close the budget is presented in Subsection 4.1.5. Finally, the electrical interface layout is described in Subsection 4.1.6..

4.1.1. Communication

For receiving and transmitting data, the UAV is equipped with an antenna. To select and size this antenna, the data and link budgets are calculated. The UAV receives and transmits several messages: a message that a rogue drone was detected, GNSS data, and images for ground processing. The required maximum data rate R is the sum of the transmitting (TX) and receiving (RX) information packages tabulated in Table 4.1.

Table 4.1: Breakdown of required data rates

Item	Data Size [bits]	Data Rate [bits/s] (tranceiving frequency)
TX system health	800	800 (1Hz)
RX detection of rogue drone	8	8 (1Hz)
RX position of rogue drone	48 ¹	480 (0.1Hz)
TX own position to ATM	48	14.4 (0.33Hz)
TX end of mission and outcome	8	8 (1Hz)
TX end of mission position	48	48 (1Hz)
TX infrared image for processing	1080000	1080000 (1Hz)
TX image for processing	8640000	8640000 (1Hz)
RX position of rogue drone from processing	48	48 (1Hz)

This yields a required minimum data rate of 9,721,407 bits per second or rounding up $\approx 9.8\text{MB/s}$. This requires picking a communication frequency at least in the high-frequency band. However, this band and the next higher very-high-frequency band are occupied by other applications near an airport. Only in the ultra-high-frequency band at 900 MHz, a subband is available for remote control devices. Conventionally, the 900MHz band is used for UAVs which require low data rates [23]. The bandwidth B of the 900 MHz band is 26 MHz. Following this convention increases the number of available off-the-shelf components.

The quality of the communication link depends heavily on the signal-to-noise ratio. The received signal power P_{RX} can be calculated using Frii's Equation (Equation 4.1), which is graphically shown in the link schematic diagram in Figure 4.1. Where P is the power, G_{amp} is an amplifier gain, G_{ant} is an antenna gain, and L_{FS} is the free-space path loss. The extra subscript TX denotes units of the transmitter, RX of the receiver.

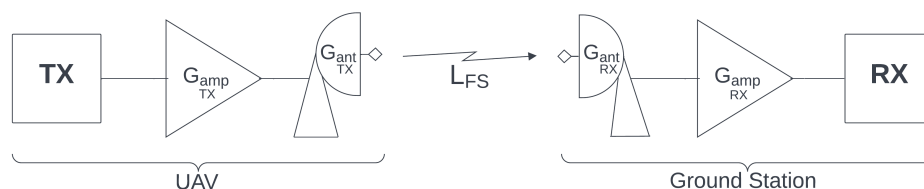


Figure 4.1: Link schematic diagram including gains and components

¹<https://www.thethingsnetwork.org/forum/t/bestpractices-when-sending-gps-location-data-howto/1242>

[Accessed: 16/05/2022]

$$P_{RX}^{[dB]} = P_{TX}^{[dB]} + G_{ampTX}^{[dB]} + G_{antTX}^{[dBi]} - L_{FS}^{[dB]} + G_{antRX}^{[dBi]} + G_{ampRX}^{[dB]} \quad (4.1)$$

The chosen flight controller has a communication interface delivering $P_{TX} = 1W = 0dBW$. The gain of the transmitting antenna G_{antTX} depends on the type of antenna. Furthermore, the type of antenna must function on-board the UAV, i.e., at a different orientation relative to the ground station. Therefore, an antenna with a high directivity cannot be used. Further, a bulky antenna would have to be placed inside the fuselage, but might then be electromagnetically shielded. The latter currently does not pose a problem, as the fuselage consists of balsa wood. Therefore, a flat ceramic patch antenna is chosen, which is small enough to fit space constraints inside the fuselage. The selected antenna has a gain of $2.5dB^2$.

Future design iterations will possibly demand better performance, e.g. more omnidirectionality and higher gain while keeping the same form factor, which can pose a problem. A solution to this is to use an electronically steered antenna, also known as a phased array antenna. This antenna can steer its main lobe and can be manufactured flat onto the fuselage, making the antenna independent of possible shielding by the fuselage without jeopardizing aerodynamics. Another method of closing the link-budget is to add amplifiers, as shown in [Equation 4.1](#).

The equation for the free-space path loss in dB is [Equation 4.2](#), where d is the distance, f the frequency, and c the speed of light.

$$L_{FS}^{[dB]} = 20 \cdot \log \frac{4\pi df}{c} \quad (4.2)$$

At a maximum distance of 30km and a frequency of 900MHz, $L_{FS} = 121.1dB$. The ground station too must be equipped with an antenna. A turnstile antenna, i.e. two orthogonal dipole antennas deliver $G_{antRX} = 1.54dBW$. Finally, [Equation 4.1](#) yields a signal power at the receiver of $-117dBW$.

The noise power can be calculated through [Equation 4.3](#).

$$P_{noise} = k \cdot T_{sys} \cdot B_{eqnoise} \quad (4.3)$$

Where k is the Boltzmann Constant, T_{sys} the equivalent noise temperature, which is assumed to be room temperature, and $B_{eqnoise}$ the equivalent noise bandwidth. Thus, $P_{noise} = -130dBW$, resulting in an S/N of $12.94dBW$.

The capacity C [bits/s], which is the theoretically achievable bit-error free rate without coding, is given by the Shannon–Hartley theorem in [Equation 4.4](#).

$$C = B \cdot \log_2 \left(1 + \frac{S}{N} \right) \quad (4.4)$$

Yielding that $C \gg R$, thus, coding is not required to transmit the required data rate.

This link functions reciprocally, i.e. when the ground station is transmitting and the UAV is receiving the same values allow for an error free link.

4.1.2. Sensors

In order for the drone to receive sufficient awareness, while minimizing weight and complexity, it is crucial to select sensors accordingly.

An overview of the selected components can be found in the following table:

Table 4.2: Sensor selection

Sensor	Selection	Specifications
Tracking camera	Foxeer Falkor 3 mini	1200TVL resolution, 16:9, 158 deg FOV
Infrared camera	Foxeer Night cat 3 mini	1200TVL resolution, 16:9, 115 deg FOV, 0.00001 LUX minimum illumination
Inertial Measurement Unit	Pixhawk-4 w orange cube	Vibration isolation on two of the IMU's, with a third fixed IMU as a reference / backup, also includes Compass and Barometric Pressure Sensor
GPS	TBS M8.2 GPS GLONASS	2m accuracy, 1-10Hz Refresh rate

²Taoglas 960-ISMP915356A02: <https://eu.mouser.com/ProductDetail/Taoglas/ISMP.915.35.6.A.02?qs=PqoDHHvF64%252BLG10QJvZ1%252Bg%3D%3D> [Accessed: 06/06/2022]

Providing the drone with a wide array of sensory inputs provides redundancy, and removes single points of failure. This is why the drone can choose between different ways of navigating and tracking during the flight profile. The latter can be achieved with its two cameras, which allow operation in both day and night conditions. This can be complemented with radar data transmitted from the ground station, such that the Air-Guard position relative to the rogue drone is known even if it is not in the view of the camera. Navigation and determining position and velocity for the autopilot on the other hand are achieved by using GPS or with ground station data. Since the former does not provide accurate altitude values, a barometric pressure sensor provides the necessary redundancy. Lastly, the attitude of the drone is determined with the use of the drone's three inertia measurement units (IMU), which include accelerometers, gyroscopes, and a compass.

4.1.3. Actuators

In conventional aircraft, the control surfaces and high-lift devices are actuated through hydraulic systems. Here, the actuation loads can be delivered by electrical servo-motors. Servo-motors are brushed DC-motors equipped with position feedback, and a gearbox.

The required actuation force was calculated in [Subsection 6.4.3](#). Accordingly, the Savox SC-1257TG³ and Savox SH-0256⁴ motors were chosen. Four units of the former are used to actuate the tail morphing, elevator, and two main wing morphing mechanisms. Two of the latter servos actuate the two alulas, resulting in 6 units in total.

4.1.4. Power Budget

Derivation of the power budget ensures that the battery is sized such that the required power is available at all times for all systems during a nominal mission. In order to create the power budget, however, it is important to gather the voltages and currents required from all electronic components such that the power they draw under nominal conditions can be calculated, this is displayed in [Table 4.4](#). It should be noted that the propulsion power is not constant and changes during each mission phase as various speeds are required, thus this power is sectioned into each mission phase. Moving forward in the definition of the power budget, the component power draw can be restructured such that the nominal mission phases are taken into account, looking at [Table 4.3](#) the contribution of each subsystem in terms of power consumption is detailed in a nominal 75 minute mission timeline. These power consumption values are summed such that the power draw per mission phase is derived - again, it should be noted that the power draw from the propulsion system was calculated using the thrust required during the mission phase multiplied by the velocity. Further multiplication of the power draw with the mission phase duration yields the consumption in *Wh* which can be lumped together with the 10% power contingency margin giving the final specification of the battery - 126Wh

Table 4.3: Total power budget per mission phase

Mission Phase	Time duration [s]	Subsystem power consumption [W]						Power consumption [Wh]
		Payload	Propulsion	Comms	CDHS	Sensors + Electronics	Morphing Mechanism	
Take-off	36	0	44.53	1.25	14	2.88	3.4	0.66
Loiter	3600	0	58.99	1.25	14	3.48	3.4	81.12
Attack + fire payload	120 + 1.9 payload firing	20.4	399.09	1.25	14	3.28	3.4	14.04
Return	600	0	88.48	1.25	14	2.88	3.4	18.33
Total power Consumption [Wh]								114.16
Total power Consumption with 10% contingency [Wh]								125.57

³Savox SC-1257TG: <https://www.savox-servo.com/Servos-c-1338/Coreless-Motor-c-1348/Savox-Servo-SC-1257TG-Digital-Coreless-Motor-Titanium-Gear/> [Accessed: 05/06/2022]

⁴Savox SH-0256: <https://www.savox-servo.com/Servos-c-1338/Brushed-Motor-c-1340/Savox-Servo-SH-0256-Digital-DC-Motor/> [Accessed: 05/06/2022]

Table 4.4: Overview of electrical component power consumption

Subsystem	Components	#	Operating voltage [V]	Operating current [A]	Power consumption [W]
Payload	Solenoid valve MHJ9	1	12	1.7	20.4
Propulsion	T-Motor F100 motors	2	Changes per mission phase		
	AIR 40A 6S motor controllers	2			
Communication	915MHz Ceramic Patch Antenna				1.25
CDHS	Pixhawk-4 w orange cube	1	5.6	2.5	14
Sensors + Electronics	Foxeer Falkor 3 mini visual light tracking camera	1	12	0.095	1.14
	Foxeer Night cat 3 mini infrared camera	1	12	0.095	1.14
	LED operational light	4	3	0.05	0.6
Morphing Mechanism	Main wing morphing servo (SC-1257TG servo)	2	6	0.1	1.2
	Alula servo (SH-0256)	2	5	0.1	1
	Elevator servo (SC-1257TG servo)	1	6	0.1	0.6
	Tail morphing servo (SC-1257TG servo)	1	6	0.1	0.6

4.1.5. Battery

From the power budget calculations the requirement for the battery size is 126 *Wh*. As a result it was decided that a commercial off-the shelf battery would be chosen. Searching for a battery of apt size led to choosing the Gens ace 6S 6000mAh 22.2V 45C Lipo Battery⁵ that satisfied all the relevant power requirements.

Not all components require the full voltage potential delivered by the battery. Thus, simple buck converters will be used to step down the voltage. If in future design iterations other electrical components are used which require a high power, but have a low duty cycle, the battery does not necessarily have to be changed. Instead, capacitors can be used to deliver the required higher voltage.

4.1.6. Hardware Diagram, Electrical Block Diagram and Data Handling Diagram

To define hardware interactions, it is required to understand where hardware is mounted onto the drone. [Figure 4.2](#) displays the power and data connections that are planned onboard the drone, additionally the location where systems are mounted, and further subsystem definitions are also displayed. The diagram aims to understand the flow of data and power for the drone subsystems, as seen in the diagram, the main power distribution is controlled by the battery management system (BMS) with the flight controller being routed to all avionic systems to control and actuate surfaces. Since [Figure 4.2](#) already contains the detailed electrical connections and the data flows, the electrical block diagram and data handling diagram are already implemented in this figure.

⁵Gens ace 6S 6000mAh 22.2V 45C Lipo Battery with EC5 Plug: <https://www.gensace.de/gens-ace-6s-6000mah-22-2v-45c-lipo-battery-with-ec5-plug-2154.html> [Accessed: 15/06/2022]

4.2. Fuselage Configuration

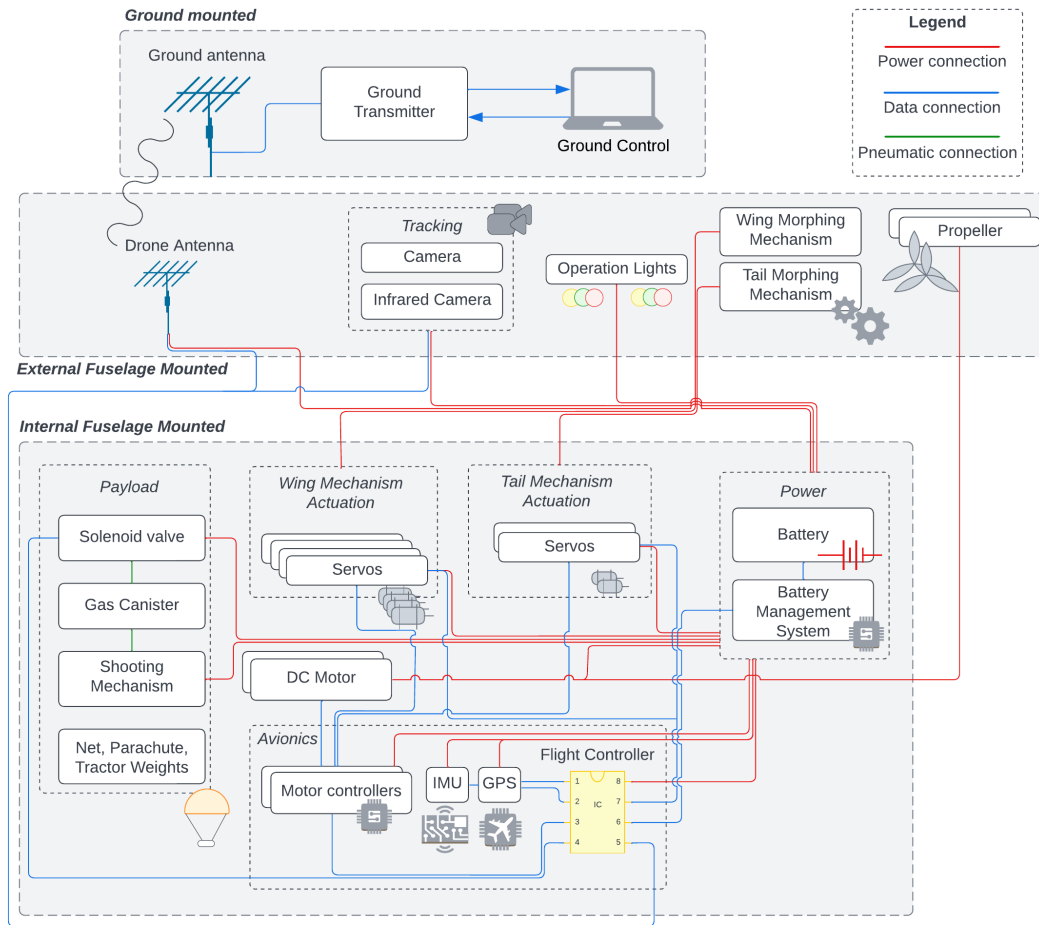


Figure 4.2: Overview of hardware power and data connection

4.2. Fuselage Configuration

Having an overview of the flight hardware gives a clear picture of how the fuselage should be designed. It is important to ensure that these components are fitted in a manner that is easily serviceable, and recyclable with minimum energy consumption. Furthermore, the contribution of the fuselage to the drag of the complete airframe is 10%, as resulted from CFD analysis. This amount is non-negligible, and it is so important to minimize the frontal cross-section and wetted surface. Figure 4.3 and Figure 4.4 provide an overview of the fuselage layout. Due to the need for mounting surfaces, which would allow for ease of assembly and recycling, a frame structure is used. This consists of four trusses running longitudinally along the fuselage.

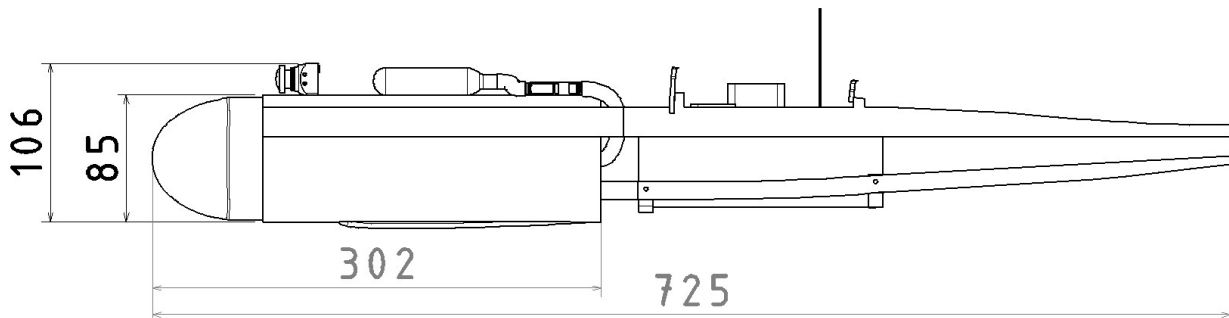


Figure 4.3: Fuselage internal dimensions (mm)

As can be seen, the fuselage consists of two main sections, namely the payload, and the flight hardware sections. The payload section is mounted around the payload tube, which is made to sustain the high pressure during payload deployment. Due to its large strength, it is subsequently used to mount several components. These include the skid block, which is used upon landing, to provide friction with the ground.

Furthermore, the cameras are mounted on top of the payload tube. Although ensuring a large field of view is an important aspect to consider, limiting parasite drag dictates that a smoother, sharper nose should also be factored into account. For this reason, a smooth transparent cover is placed in front of the cameras. According to [Raymer](#), a minimum over-nose angle of 10 deg is acceptable for fighter aircraft. Thus, the placement of the cameras and the shape of the nose are chosen such as to respect this lower limit.

Lastly, the gas canister and pneumatic system are also placed on top of the payload tube. This leaves sufficient space. Due to the need of accessing these components frequently, a hatch is a cut-out on the top fuselage skin.

The central structure of the fuselage houses the battery and the flight controller. This is because it is important to limit the shift in the center of gravity after payload ejection, by placing the empty mass as close to that of the net. A second hatch is placed at the bottom of the drone, to provide quick access to the battery, as well as the flight controller.

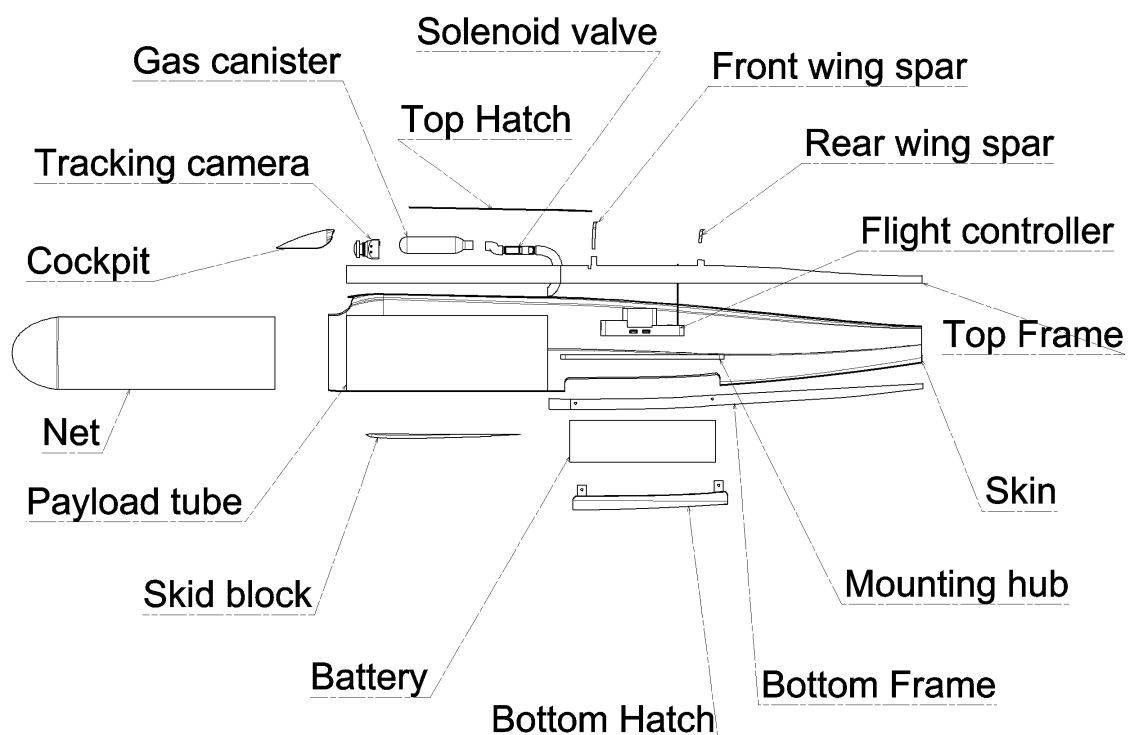


Figure 4.4: Fuselage exploded view

4.3. Structures

In this section, the steps and analysis used in the design of the fuselage structure are described. First, all the necessary components were sized and arranged in a way that resulted in a favorable c.g. location while also being in a streamlined shape. Then, a fuselage was constructed in CATIA to cover and connect all components.

The loads on the fuselage are caused by the weight of the components and the aerodynamic forces. The main forces are shown in [Figure 4.5](#), as a function of the distance from the nose in the longitudinal direction. The biggest two positive values correspond to the components with the highest weight, payload and battery, while the negative load is due to the lift force.

From [Figure 4.5](#), the shear force diagram and moment diagram can be constructed, shown in [Figure 4.7](#) and

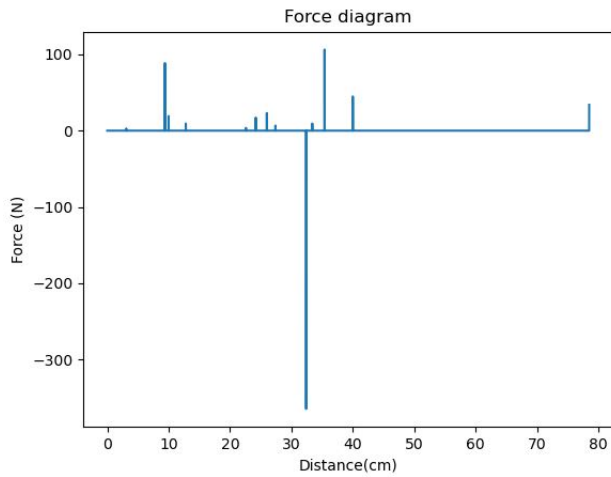


Figure 4.5: Forces acting on the fuselage as a function of the longitudinal position

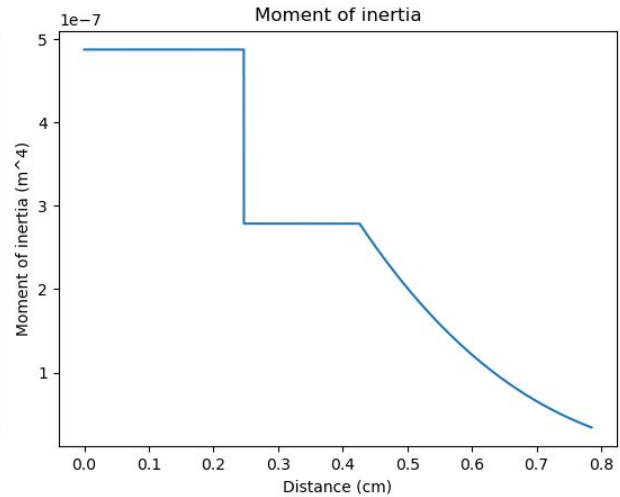


Figure 4.6: Moment of inertia of the cross section of the fuselage as a function of longitudinal distance from the nose

Figure 4.8. As expected, the highest shear force and moment are located at the location of the wing. For the moment diagram, there should be a jumps at the location of the wing and horizontal stabiliser, as these introduce point moments in the structure, but they were not taken into account as preliminary calculations showed that those moments were considerably lower than the moment caused by the shear force. This is also the reason why the graph does not end with a moment value of 0.

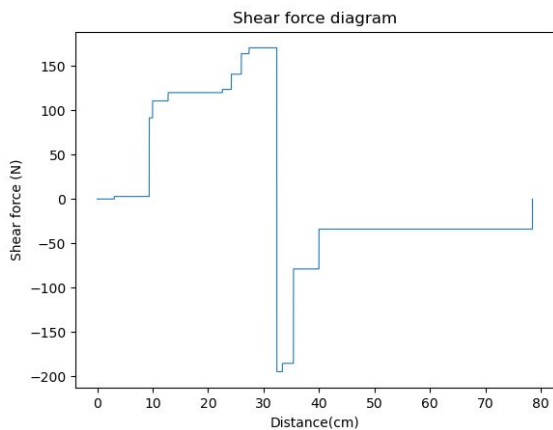


Figure 4.7: Shear force in the fuselage as a function of longitudinal position

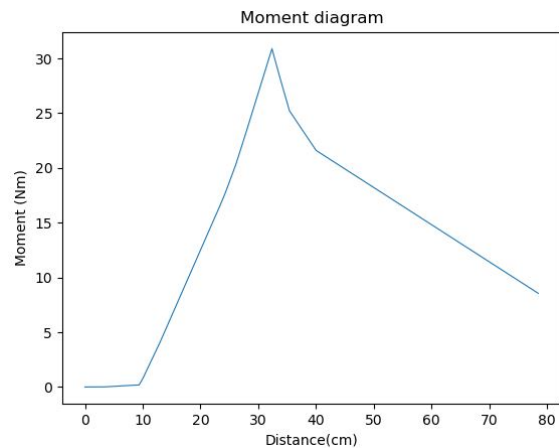


Figure 4.8: Moment in the fuselage as a function of longitudinal position

The load-bearing structure of the fuselage is considered to be comprised of 3 different parts, as shown in Figure 4.9. The sketch of the cross-section of the fuselage is shown for each part. For simplification, the fuselage is considered to be circular. Thus, for the first section, up to $x_1 = 24.7$ cm, the tube that carries the payload is also considered to be load-bearing, hence the two concentric circles. Next, from x_1 up to $x_2 = 42.6$ cm, the second section has 4 stringers at about equal distances on the fuselage arc. The last section, from x_2 onward, has the same shape as the previous one but is considered to be tapering linearly.

Before analyzing the loads in the structure, the boom idealization is used, as described in Subsection 6.5.1. This results in a structure with 4 booms that carry normal loads, while the skin carries shear loads.

Then, the moment of inertia as a function of longitudinal position from the nose can be calculated and it is shown in Figure 4.9. This is based on a fuselage thickness of $t = 1$ mm and a boom area of 22 mm^2 , which is a conservative value, being less than the area of the booms used. The first section has the highest moment of inertia because of the cylinder carrying the payload, then there is a sudden drop. For the last section, because of the tapering, the

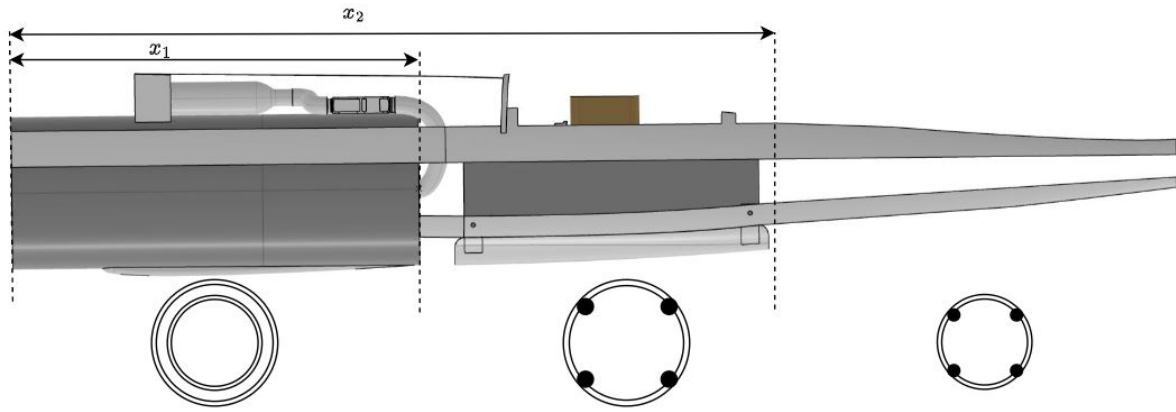


Figure 4.9: Cross-section for different sections of the fuselage

moment of inertia is steadily decreasing.

Applying the loads using Equation 6.4 and Equation 6.3, the maximum shear and normal stress can be calculated for each section, at each position. Figure 4.10 and Equation 6.3 illustrate the maximum shear and normal stress at each longitudinal location of the fuselage. Consequently, the maximum shear stress is about 1.6 MPa while the maximum normal stress is a bit over 3.5 MPa.

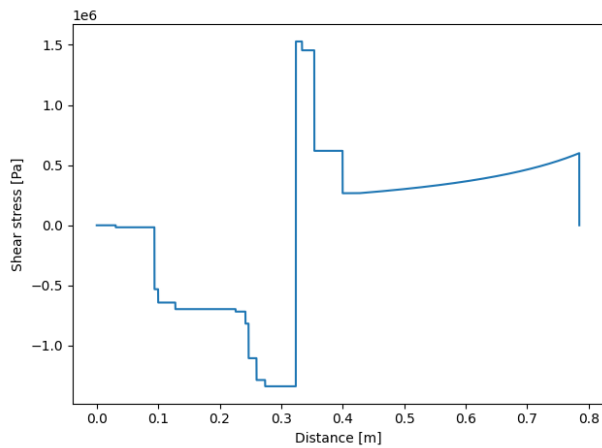


Figure 4.10: Maximum shear stress in the cross section as a function of longitudinal distance

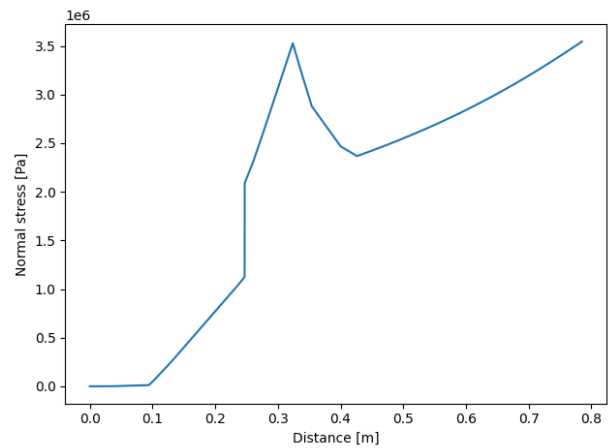


Figure 4.11: Maximum normal stress in the cross section as a function of longitudinal distance

Considering the relatively low stresses in the structure, the material that was decided upon is balsa wood. Balsa wood has $\sigma_y = 16$ MPa and $\tau_{max} = 4.5$ Mpa, considerably higher than the expected stresses. Balsa wood also results in a low weight structure, due to the low density and it is a renewable material with a relatively low carbon footprint

5. Payload Design

The payload is one of the most important subsystems of the Air-Guard drone, as it is the system responsible for the capture of unlicensed drones. The payload is of great influence on the size of the morphing UAV, as the UAV needs to be built around the payload system.

This chapter will describe the design process of the payload subsystem. First, the requirements for the payload will be discussed in Section 5.1. Then, a description of the payload design process and characteristics will be given in Section 5.2.

5.1. Requirements

The purpose of the payload is to immobilize the unlicensed drone and bring it to the ground in a controlled manner, without harming ground personnel or damaging ground infrastructure. Additionally, there are system-level requirements that drive the payload design, which regard the mass of the drone that need to be caught. Based on REQ-UAV-PERF-002 (see Table 5.1), it was decided early on that the unlicensed drone would not be returned by the morphing UAV, but instead would float down to the ground using a parachute, as a 10 kg additional mass would drive the design of the UAV too much. Because of this, a payload consisting of at least a net and a parachute needed to be designed.

From these constraints, the payload requirements were generated. Table 5.1 shows the system-level and payload requirements. It is also indicated with a check mark whether the final design complies with this requirement.

Table 5.1: Payload system requirements

Identifier	Requirement	Verification Method	Compliance
<i>System-level</i>			
REQ-UAV-PERF-001	The minimum mass of drones that the UAV shall be able to immobilize shall be 0.5 kg	Test	✓
REQ-UAV-PERF-002	The maximum mass of drones that the UAV shall be able to immobilize shall be 10 kg	Test	✓
<i>Subsystem-level</i>			
REQ-UAV-PAYL-002	The parachute shall slow down the rogue drone to a maximum vertical speed of 4 m/s	Test	
REQ-UAV-PAYL-003	The parachute shall deploy within 5 seconds of net deployment	Demonstration	✓
REQ-UAV-PAYL-005	The net shall expand to a size of 4 m ² after shooting	Test	✓
REQ-UAV-PAYL-007	The net shall have a size of 2 m by 2 m	Inspection	✓
REQ-UAV-PAYL-008	The nose profile after payload ejection shall not induce static instability	Test	✓
REQ-UAV-PAYL-009	The nose shape after payload ejection shall not induce separation along any point on the fuselage and wing surfaces	Test	✓

5.2. Component Description

The payload system consists of two parts: a launched part that is ejected from the drone after the payload deployment, and a fixed part. First, the drone catching method will be discussed, then the design of the launched part will be discussed. Then, a quantification of the aerodynamic effects of payload deployment will be given and lastly, the design of the fixed part will be described.

5.2.1. Drone Catching Method

The drone catching method is inspired by OpenWorks' SkyWall system¹. When the morphing UAV approaches an unlicensed drone, a capsule is ejected from the nose using pressurized gas, as shown in the first part of Figure 5.1. This capsule contains the net and parachute. When the capsule is airborne, pyrotechnics will release weights, as seen in part two of the figure. These weights are attached to the net and will deploy it. After the net entangles and

¹<https://openworksengineering.com/skywall-patrol/> [Accessed: 23/05/2022]

immobilizes the drone, the parachute will deploy, ensuring a safe descent, which is shown in the last two parts of Figure 5.1. The parachute will emit an acoustic warning signal, while the weights on the net contain warning lights and a tracker. After landing, a ground team can locate the GPS tracker and recover the unlicensed drone. A visualization of the drone and payload in action during the drone attack phase is depicted in Figure 5.3.

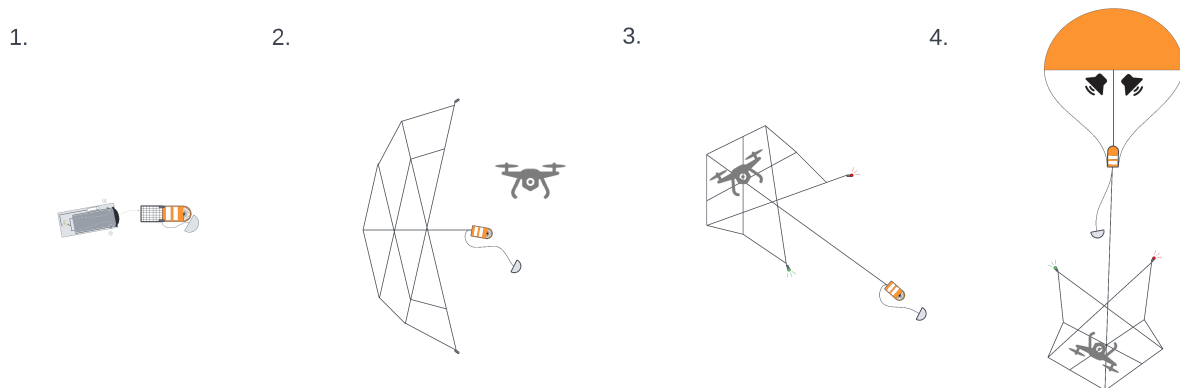


Figure 5.1: Deployment of the payload system

5.2.2. Launched Part

The launched part of the payload consists of a canister housing a parachute and a net with weights. It is located in the nose of the UAV and ejects forward in the direction of flight. This was decided upon to facilitate aiming and to reduce the moment created by ejecting the payload. In total, the launched part of the payload weighs 690 grams. Its position inside the nose of the drone can be seen in Figure 5.2.

Parachute

The parachute used is the DRS-10 parachute which is manufactured by Drone Rescue Systems². It can slow down a 10 kg drone to 5 m/s, after which it would have about half of the kinetic energy of an adult jumping as high as possible, guaranteeing the safety of buildings and ground personnel. The descending speed does not comply with REQ-UAV-PAYL-002, which set a descent speed of 4 m/s. The reason this parachute was chosen, is because the 4 m/s requirement is relatively strict and results in a much higher parachute mass than the current solution. However, to justify this decision the parachute will emit a noise warning during descent, which allows ground personnel to detect the parachute earlier on so they can move out of the way. Additionally, the parachute can autonomously decide when to deploy. This can be based on a timer (to comply with REQ-UAV-PAYL-003) or motion-based. The parachute fully deploys within 8 to 13 meters, depending on the weight of the drone caught.

Net

A net made of high-density polypropylene will be used to catch the drone. This material is also used in current drone net systems that are in place in drone testing areas³. The net is square and measures 2x2 m, leaving some margin to catch drones of up to 1 m in diameter and complying with REQ-UAV-PAYL-005 and REQ-UAV-PAYL-007. The spacing between the net wires is 15 cm, to make sure drones of 30 cm and larger can be captured.

Weights

Attached to the net are four weights, which are deployed after the capsule is deployed. The weights ensure the net expands and covers as much area as possible. Two weights contain warning lights to ensure visibility of the descending drone during nighttime. One of the weights also includes a GPS tracker manufactured by Orbit to aid in recovering the unlicensed drone and parachute⁴.

²<https://dronerescue.com/drs-10/> [Accessed: 22/05/2022]

³<https://www.networldsports.ng/drone-netting-standard-size> [Accessed: 22/05/2022]

⁴<https://findorbit.com/products/orbit-glasses> [Accessed 22/05/2022]

Capsule

All the above components will be housed inside a capsule made of acrylonitrile butadiene styrene, a relatively strong and lightweight plastic. The capsule will be ejected in one piece when the UAV approaches an unlicensed drone. The capsule also contains pyrotechnics that propel the net weights outward.

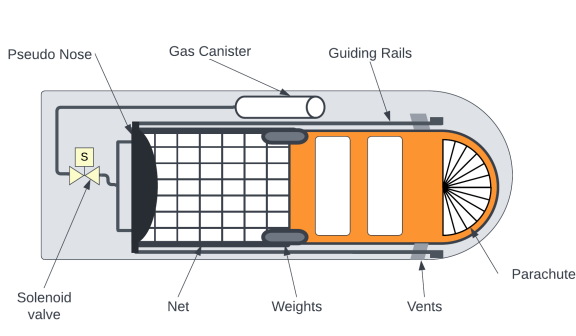


Figure 5.2: Location of the ejected payload part inside the fuselage

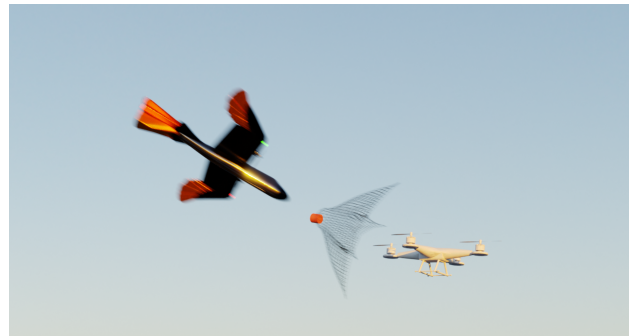


Figure 5.3: Depiction of payload deployment during attack

5.2.3. Aerodynamics of the Fuselage After Deployment

The current payload configuration brings a number of uncertainties due to the presence of a large cavity at the front of the nose, during the return phase of the mission. Potential effects include a large increase in drag, a decrease in longitudinal and lateral stability, as well as the onset of harmful vibrations due to vortex instability.

In order to quantify these effects, two fuselage configurations were analyzed using STAR-CCM+, using the SST k-omega turbulence model⁵. The later allows for an accurate prediction of stall, separation, and turbulent flows.

The fuselage was simulated at a dive velocity of 40 m/s, and at landing conditions. This is because these are the most extreme flight conditions the drone experiences after ejecting the payload. An overview of simulation conditions can be found in Table 5.2:

Table 5.2: Simulation parameters

	Flight conditions		Physics model	
	V	α	ρ	μ
Unit	m/s	deg	kg/m ³	kg/m/s
Dive	40	0	1.225	1.86E-5
Landing	12	10		

Simulation results do not indicate any onset of separation of the airflow around the payload opening during these conditions. This proves that an open payload tube will not have a large impact on the aerodynamic performance of the wing, or the tail. Furthermore, the geometry of the simulations, which consist of only the fuselage shape, indicate that this statement is conservative, as the proximity of the propeller to the fuselage can theoretically negate the effect of turbulent air around the fuselage. Other simulation outputs are summarized in the following table:

Table 5.3: Simulation outputs

	Dive			Landing		
	Closed nose	Open nose	Multiplication factor	Closed nose	Open nose	Multiplication factor
C_L	-0.0004	0.0008	-2	0.0006	0.0003	0.6
C_D	0.0030	0.0180	5.8	0.004	0.0190	5
C_m	-0.0002	0.0004	-1.6	0.0026	0.0017	0.7

⁵https://www.cfd-online.com/Wiki/SST_k-omega_model [Accessed: 10/06/2022]

Table 5.3 shows that the lift generated by the fuselage remains relatively low in both cases, compared to the contribution of the wing. Furthermore, the simulations indicate a very large increase in C_D . The hole caused by launching the payload results in an increase of 45% in the drone's profile drag. Lastly, the change in moment around the drone's center of gravity due to the fuselage is also minimal, relative to the full configuration, for which moment coefficients can be found in Section 7.3.

All in all, the only measurable negative effect of an open nose is an increase in drag. Yet, this only occurs during the return phase of the mission, during which maneuverability and efficiency are not of primary importance.

However, STAR-CCM+ does not simulate flow instability. The nature of the fuselage geometry in open conditions can be prone to produce such an effect, as can be seen in Figure 5.4. For this reason, it was decided to implement a solution, that ensures the hole the payload leaves after deployment will be closed off.

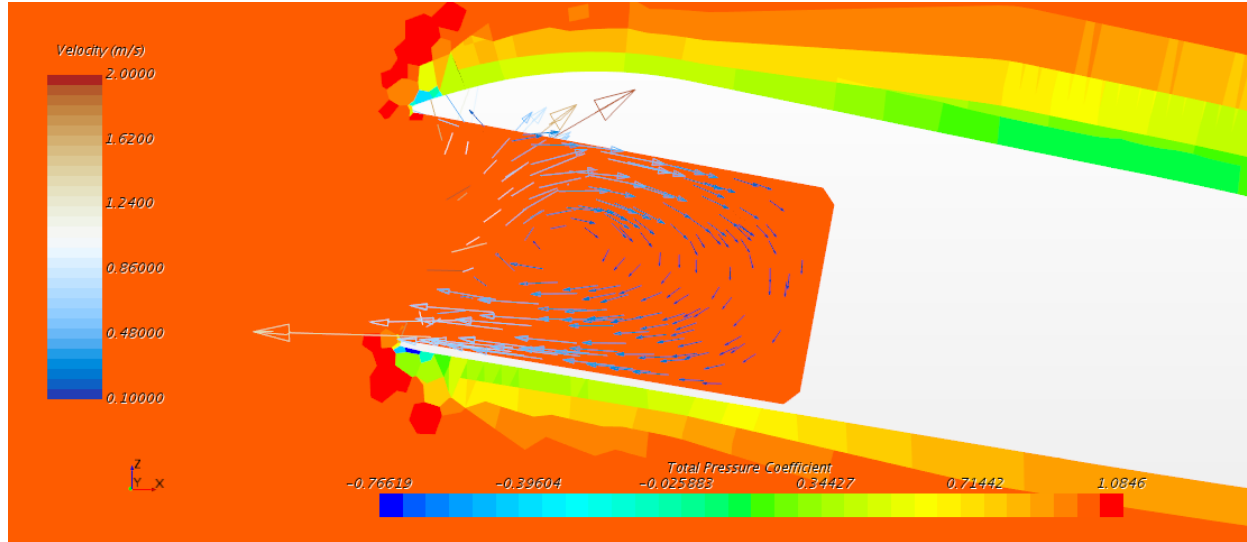


Figure 5.4: Flow behavior inside the nose during landing conditions

5.2.4. Fixed Payload

The fixed part of the payload remains attached to the UAV and contains a gas canister and valves to propel the payload canister forwards. As described in the previous section, an open nose after payload deployment is undesirable. To ensure the hole is closed after the payload is deployed, a pseudo-nose is in place that slides forward on guard rails after deployment.

Pneumatics

A canister containing high-pressure CO_2 will be used to propel the payload. As can be seen in Figure 5.2, it is located above the ejected payload part. A solenoid valve is used to control the flow of the gas ⁶.

The muzzle velocity of the ejected payload is calculated assuming adiabatic expansion of the CO_2 , which leads to Equation 5.1 [25]. The definition of the variables can be found in the list of symbols.

$$V_m = \sqrt{\frac{2}{m_{pl}} \left(\frac{P_0 V_0}{\gamma_{\text{CO}_2} - 1} \left(1 - \left(\frac{V_0}{A_b L_b + V_0} \right)^{\gamma_{\text{CO}_2}} \right) - A_b L_b P_{atm} - L_b c_f \right)} \quad (5.1)$$

To ensure the deployment speed of the payload is sufficient to reach its target, a numerical simulation was done, based on a simplified drag model. Assuming horizontal deployment, the dynamic motion of the payload capsule in the x-direction of the drone body frame can be expressed as follows:

⁶[https://nl.rs-online.com/web/p/pneumaticsolenoid-valves/1752145?cm_mmc=NL-PLA-DS3A-_-google-_-CSS_NL_NL_Pneumatics_26_Hydraulics_Whoop-_- \(NL:Whoop!\)+Pneumatic+Solenoid+Valves-_-1752145&matchtype=&pla-341889919132&gclid=CjwKCAjwkYGVbHArEiwA4sZLuLfmYJh50UPVxIs1JqfC36mA64_Vj91UgEQBG9XIytsYKw4GLaw.ds](https://nl.rs-online.com/web/p/pneumaticsolenoid-valves/1752145?cm_mmc=NL-PLA-DS3A-_-google-_-CSS_NL_NL_Pneumatics_26_Hydraulics_Whoop-_- (NL:Whoop!)+Pneumatic+Solenoid+Valves-_-1752145&matchtype=&pla-341889919132&gclid=CjwKCAjwkYGVbHArEiwA4sZLuLfmYJh50UPVxIs1JqfC36mA64_Vj91UgEQBG9XIytsYKw4GLaw.ds) [Accessed: 15/06/2022]

$$F_D = ku^2 = m_{pl}\dot{u} \tag{5.2}$$

In this equation, k is the drag parameter defined as $k = C_D \frac{1}{2} \rho A_b$. Solving this differential equation for the distance traveled by the payload capsule leads to Equation 5.3, and from this the horizontal distance relative to the UAV can be obtained as seen in Equation 5.4, where u_0 is the muzzle velocity of the payload capsule.

$$x = \frac{m_{pl}}{k} \ln\left(\frac{m_{pl} + u_0 kt}{m_{pl}}\right) \tag{5.3} \quad x_{rel} = \frac{m_{pl}}{k} \ln\left(\frac{m_{pl} + (u_0 + u_d)kt}{m_{pl}}\right) - u_d t \tag{5.4}$$

Using a 12 g CO₂ canister, a muzzle speed of 24 m/s can be obtained. The velocity relative to the UAV as a function of time can be seen in Figure 5.5. It should be noted that in this model, the drag is assumed to stay constant, while in reality, the deployment of the net and catching the drone will likely increase the drag. This is compensated for by increasing the drag parameter k by 50%. Figure 5.6 shows that after deployment, the UAV has around 11 s of maneuver time to not hit the net. During this time, the UAV will move 1 m vertically, to avoid the 2x2 m net.

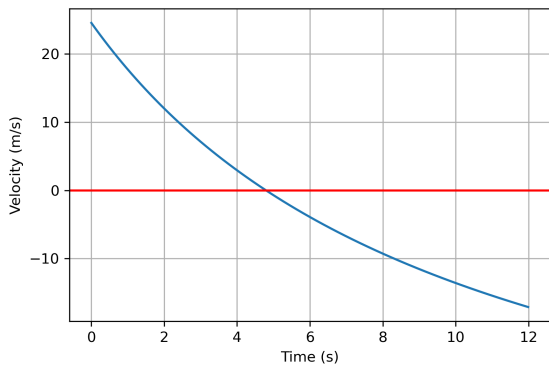


Figure 5.5: Horizontal payload velocity relative to UAV

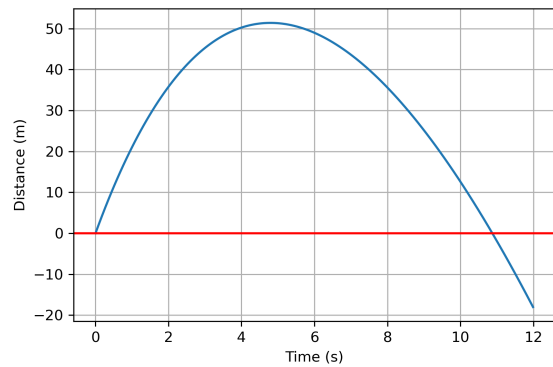


Figure 5.6: Horizontal payload distance relative to UAV

Pseudo-nose

As discussed in Subsection 5.2.3, to avoid additional drag generated after deployment of the payload, a pseudo-nose is positioned behind the payload canister. When the payload is deployed, the pseudo-nose is designed to slide along guard rails to the front of the UAV, where it locks in place as can be seen in Figure 5.2. The additional pressurized gas behind it is released through a set of vents in the side of the barrel. It has to be ensured that there is a tight seal around the guiding rails on the pseudo-nose in order to eliminate the possibility of gas leaking when the payload is pressurized. The vents are also to be placed in the front of the fuselage such that the capsule is given the relevant impulse via the pressurized gas such that it can still be launched.

6. Main Wing Design

The wings are the main lifting surfaces of the UAV. In conventional fixed-wing drones, the wings are stationary, with roll control employed via independent control surfaces making up small sections of the wing. However, the design of morphing wings requires an unconventional design approach taking into account the changes in aspect ratio, wetted surface area, and wing loading that arise as a result of the morphing process. Studying bird wing design and the actuation processes applied by avian morphing wings are thus crucial to understanding the fundamentals of attitude control of the drone as a whole. This chapter of the report details the iteration of the design process of the wing derived from the preliminary sizing, including an aerodynamic analysis, a study of the structures, and a study of the morphing mechanics.

6.1. A Study into Avian Wing Morphology

Avian morphing mechanisms operate both passively and actively to alter aerodynamic moments and forces in flight. The active morphing mechanism is realized via the movement of the bone structure, actuating the movement of the inboard and outboard feathers of the wing [21]. The dominant skeletal joints that influence the feather actuation are the shoulder, elbow and wrist joints that coarsely control the feathers with fine control coming from the finger joints as seen in Figure 6.1. The formation of these joints forms a conventional four-bar linkage that is under-actuated via an elastic tendon running along the feather endings, controlling their extension [5]. Although the majority of wing morphing is accomplished via the extension-retraction mechanism of the four-bar linkage, there also exist two other degrees of freedom that come from two additional linkages controlling out of plane deformations such as dihedral angle and wing twist, these additional morphing capabilities were not aimed to be implemented into the design as the rigid link implementation of these aspects increased constraints in actuation of the wing feathers while adding more weight into the design.

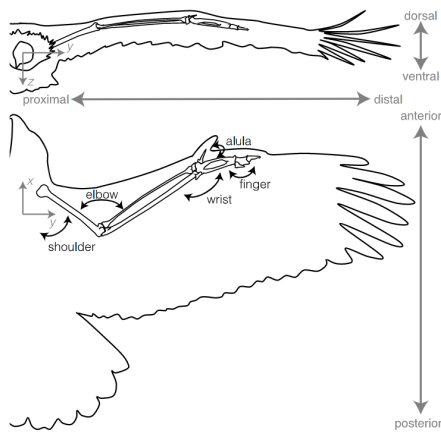


Figure 6.1: The skeleton structure of a bird's wing [21]

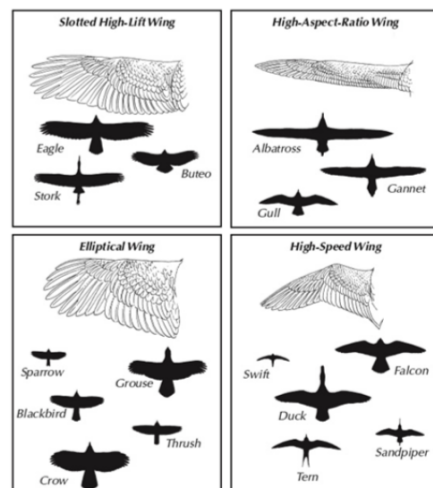


Figure 6.2: Wing planforms for different species of bird [26]

The genetic variance across various species of birds naturally results in a wide variation in the wing geometry, as seen in Figure 6.2. There are multiple combinations of aspect ratio, span and taper ratios that are each specifically adapted to multiple flight regimes. Therefore, when understanding the inner mechanisms of wing morphing and planform design, it is important to observe the relation between technological, so research based design, and evolutionary design such that the most efficient design strategies are implemented.

Further research on bird wings has also shown that the movement of feathers is not uniform and is determined by their position on the wing. Studies into the movement of feathers show, that there exist multiple regions of feather actuation that correspond to coarse and fine control. Observation of part D of Figure 6.3 shows tracking data on the deflection of pigeon wing feathers versus the wrist angle deflection. It is seen that the innermost feathers of the wing have much smaller deflections as compared to the outer feathers of the wing, meaning that the control and maneuvering characteristics are most affected by the deflection of the outer feathers of the wing [5]. As a result, it was decided that the drone would incorporate wing morphing of only the outboard feathers, reserving the inner wing for the majority of the lift production along with housing the structures and electronics of the wing.

6.2. Requirements

Another aerodynamic advantage achieved via the evolution of bird wings is the presence of slots, as observed in Figure 6.4. These slots, formed by the lack of feather overlap, are thought to reduce drag over wings and optimize the lift over drag ratio [27]. The presence of these slots means that each feather acts as its own aerodynamic surface as in Figure 6.5, breaking up wing tip vortexes as seen in Figure 6.4 and as a result, it greatly improves aerodynamic performance. It has been studied that the presence of slotted wing tips caused a reduction in drag coefficient by 25-30% as compared to complete wings [27]. These effects are aimed to be incorporated into the design such that the effects of the reduction in drag can be achieved.

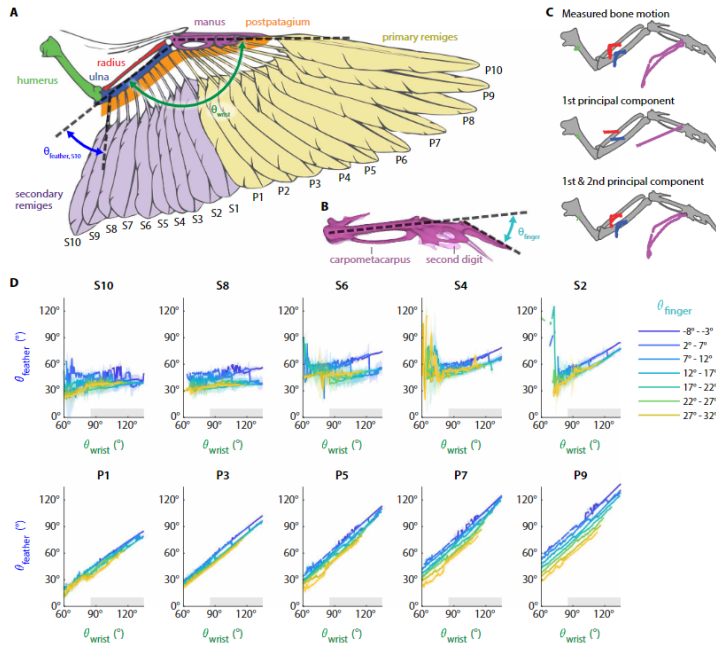


Figure 6.3: Bio mechanism of a pigeon wing [5]



Figure 6.4: Effects of slotted wing tips on wing tip vortexes [27]



Figure 6.5: Wind tunnel effects of slotted wings [27]

The results of prior studies and evolutionary aerodynamic advantages are large factors that have played roles in the incorporation of the high-performance design of the UAV's wing planform. The goal was to create an efficient design inspired by avian morphology such that the advantages of avian flight can be adapted to traditional drones via incorporation of bio-inspired mechanisms and design of artificial feathers. Further discussion into the incorporation of previously under-utilized aspects of bird wing design is also discussed in Subsection 6.3.4 where the bionic leading edge slat, the alula is discussed.

6.2. Requirements

Table 6.1: Wing system requirements

Identifier	Requirement	Verification Method	Compliance
REQ-UAV-RAMS-004	The morphing mechanism of the UAV shall be able to operate with 90% reliability	Analysis	✓

6.3. Wing Aerodynamics

The size and shape of the wing are most crucially guided by aerodynamics. Since the wing is the main lifting body, it needs to produce substantial amounts of lift while keeping the drag to a minimum. This section explains how the wing was designed and what its aerodynamic properties are. Subsection 6.3.1 explains what software was used to do the computations. Next, Subsection 6.3.2 shows the airfoils used and Subsection 6.3.3 shows the wing planform. To increase the maximum lift of the drone, an alula is added, which is explained in Subsection 6.3.4. The results are presented in Subsection 6.3.5.

6.3.1. Software Used

For the aerodynamic analysis, several programs were used. For the preliminary airfoil and planform design, XFLR5 has been used to get a rough estimate of the aerodynamic performance¹. XFLR5 has been run in the lifting line theory setup (as recommended in [28]). However, it should be noted that this method underestimates the viscous drag. XFLR5 also has trouble implementing the fuselage effects [28] so OpenVSP was used to model the drone in more detail.

OpenVSP is a NASA-based open-source aerodynamic simulation tool². OpenVSP uses VSPAero to run two simulation methods: VLM and panel method. As explained by Shahid et al., the VLM method is preferred when using thin airfoils and when computation time is important. For this reason, all simulations with OpenVSP are run on the VLM setting [29]. VLM was also used to have a better comparison with the data from EPFL and Stanford as a way to validate the results. However, one of the downsides is that VLM lacks a detailed viscous drag analysis [28], which might cause uncertainties in the drag estimations.

6.3.2. Airfoil Analysis

The main wing is divided into two sections, with the inner section using a thick airfoil to generate a notable portion of the lift and to house the internal structures and components. On the other hand, the outer section will morph and to ensure reliable morphing they will therefore use a thin airfoil. For the inner part, the Selig S4233 airfoil was used. For the outer part of the wing it was initially decided to use a thin cambered feather-like airfoil, but to improve the morphing reliability this was changed to a thin plate.

To house the morphing mechanism, the beginning of the outer part contains a section where a fairing is located at the leading edge. When comparing the airfoils to that of a bird, a similar pattern can be seen where the inner part consists of a thicker airfoil, then the thin airfoil continues with a transition area where a fairing is located at the front. The cross-sections of the airfoils can be seen in Figure 6.6 and the aerodynamic coefficients in Figure 6.7. It should be noted that the wing does not achieve the intended $C_{L_{max}}$ of 1.8 but by adding the propeller effects (Section 8.3) and alula (Subsection 6.3.4) this can be achieved, as will be shown later.

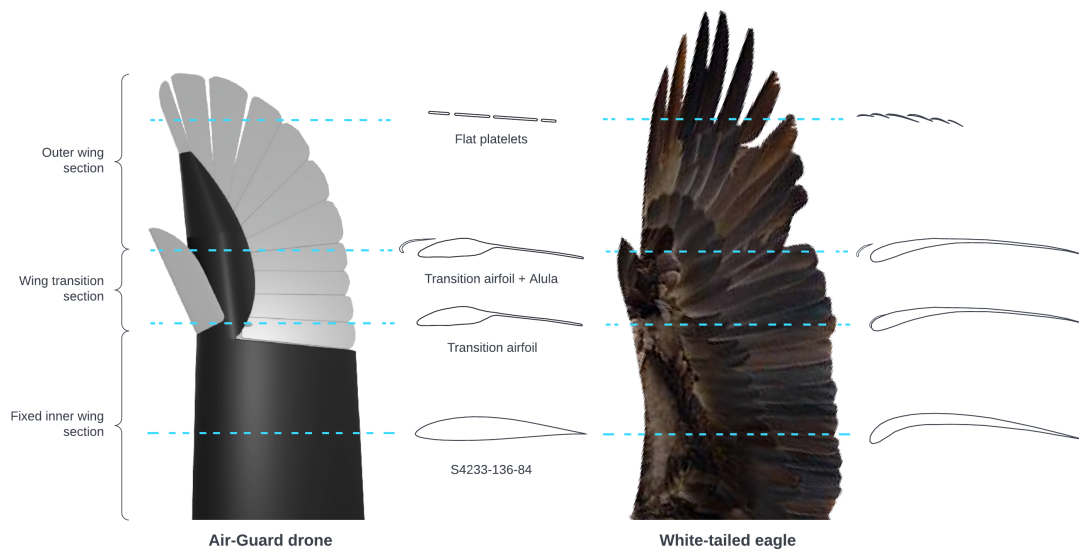


Figure 6.6: Cross section of the inner, transition and outer airfoils as compared to that of a White-tailed eagle

¹<http://www.xflr5.tech/xflr5.htm> [Accessed: 2022-05-8]

²<http://openvsp.org/> [Accessed: 16/05/2022]

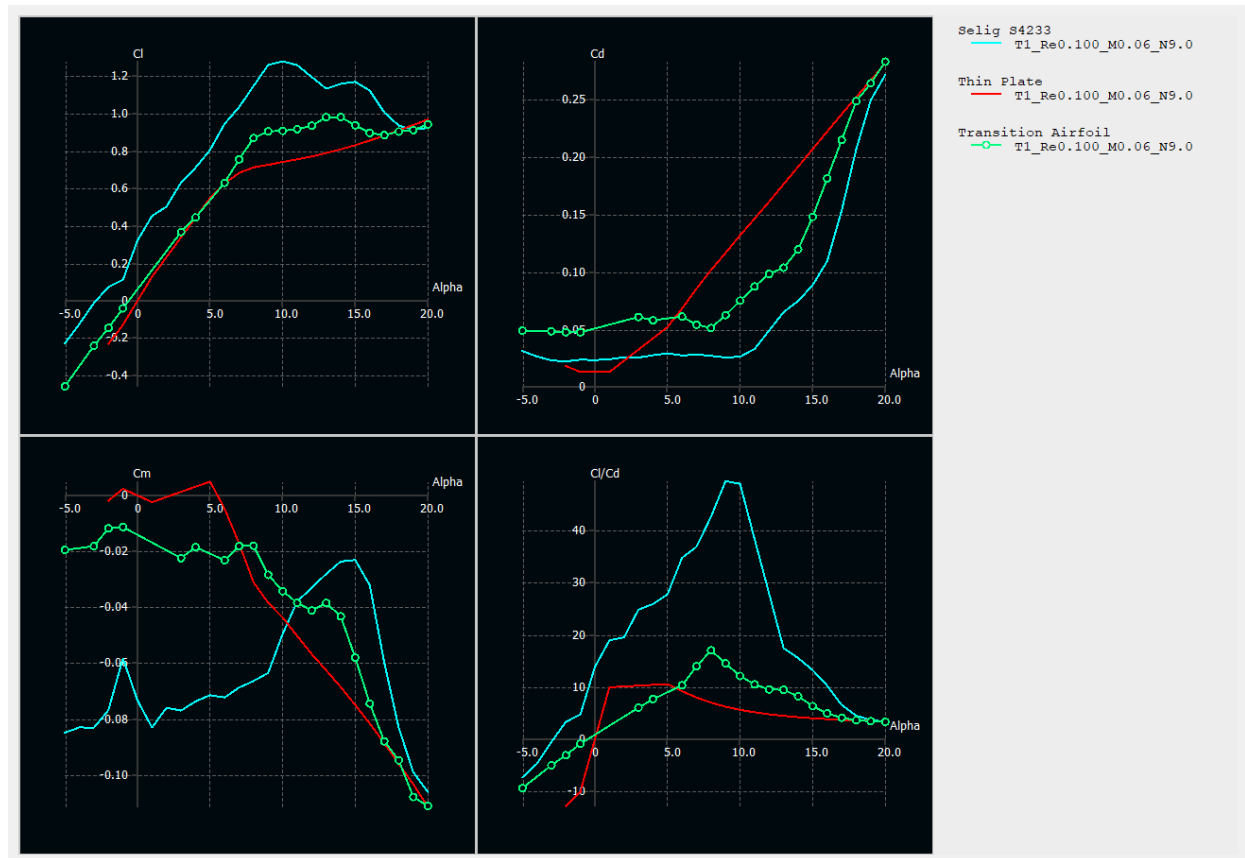


Figure 6.7: Aerodynamic properties of the inner, transition and outer airfoil for $Re = 100000$, $M = 0.060$.

6.3.3. Wing Planform

Changes made to the wing planform

Compared to the wing planform made during the midterm report several changes were made to meet the requirements. The original wing design was designed to optimize lift over drag but did not meet the optimal velocity and maximum velocity requirements and the roll performance was not adequate. Therefore, the taper of the inner section was decreased such that area of the inner wing increased and thus a smaller aspect ratio was needed. This meant that a larger part of the wing could morph and improve the roll authority. This also has the advantage that it decreases the moment of inertia around the x-axis, thus making the vehicle roll more easily.

Morphing sections

The span-wise starting point of the morphing section was found using the wing loading diagrams for attack and loiter. Here, it was discovered that the area needed to decrease by $0.1m^2$ between the unmorphed and morphed state. Using OpenVSP, the morphed sections were modeled using flat plate sections and the influence was analyzed. Four different configurations were created and are shown in Figure 6.8. When moving the platelets backward, the aerodynamic center moves backward and thus makes the drone more stable. The morphing sections are also used to roll the drone. This is possible since the extended part will produce more lift than the retracted part, thus creating a moment around the x-axis. Figure 6.9 presents the spanwise lift distribution, where this difference in lift can be seen.

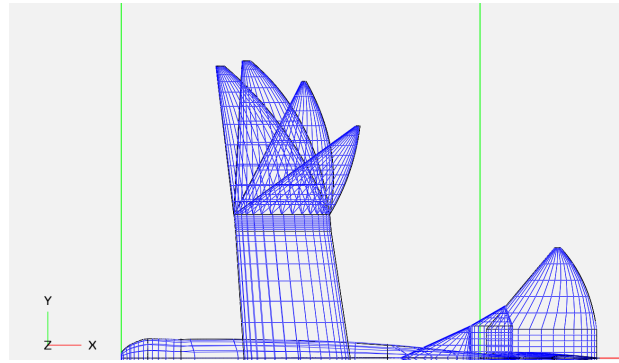


Figure 6.8: Morphing section used for aerodynamic analysis on OpenVSP

Analysis on lift distribution

Figure 6.9 shows the lift distribution for a fully extended and fully retracted wing. Note that the graph shows two dips; this is where the airfoils transition into each other which causes an irregularity in the simulation. This irregularity could not be removed from the simulations but since they were deemed similar for all of them it was ignored.

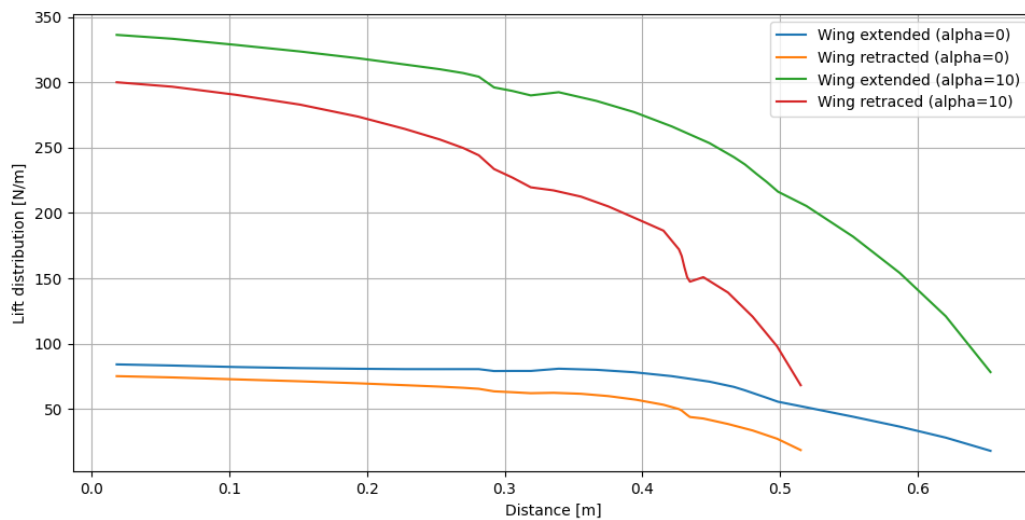


Figure 6.9: Lift distribution comparison between fully extended and fully retracted wings for $Re=250000$, $\alpha = 0^\circ$ and $\alpha = 10^\circ$

6.3.4. Alula

Following the discussion on avian morphology in Section 6.1, a deeper dive into biological bird wing design yielded interesting results which seem to have not been utilized in any current morphing drone concept. A set of feathers formally known as the alula was observed, the alula feathers are positioned close to the leading edge of the wing as seen in Figure 6.10 and Figure 6.11 and are thought to be homologous in its biology to the human thumb. Alulae have been discovered to act as a leading edge slat delaying stall and energizing the flow over the top of the wing such that larger dive angles can be achieved as well as lower and more comfortable landing speeds [21]. It is further researched that alulae are passively deployed at high angles of attack playing large roles in the deep-stall or post-stall regimes thus it has been observed that these feathers are usually involved during take-off and landing maneuvers [26].

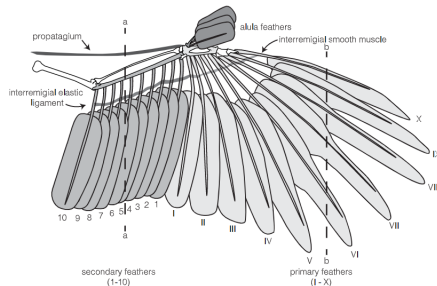


Figure 6.10: The position of the alula feathers on bird wings [21]



Figure 6.11: The alula feathers in use during the flight of a peregrine falcon

Further performance studies on the effectiveness of the alula have also displayed that the vortex generator effect of the alula in energizing the flow over the wing delays flow separation as seen in Figure 6.12, where digital particle image velocimetry was used to track fine particles and understand the flow behavior over the alula [30]. Furthermore, wind tunnel investigations on the lift-area versus drag area polar on bird wing sections show that at high angles of attack, the alula is beneficial in increasing the maximum lift coefficient. At speeds close to the intended loiter speeds of the Air-Guard drone of around 20m/s and intended stall speed of 12m/s, the effect of the alula on the lift area coefficient of the wing can be seen in the bold lines of Figure 6.13 where the alula is observed to increase the lift area coefficient of the wing. Studies have also shown that alulae increase the achievable dive angle of birds, which may be an advantageous trait for the Air-Guard drone during the attack dive maneuvers, the results of the study of the diving angles of four Eurasian magpies with alula (blue) and without alula (red) are displayed in Figure 6.14 where the net advantage in descent angle with the alula is clearly seen.

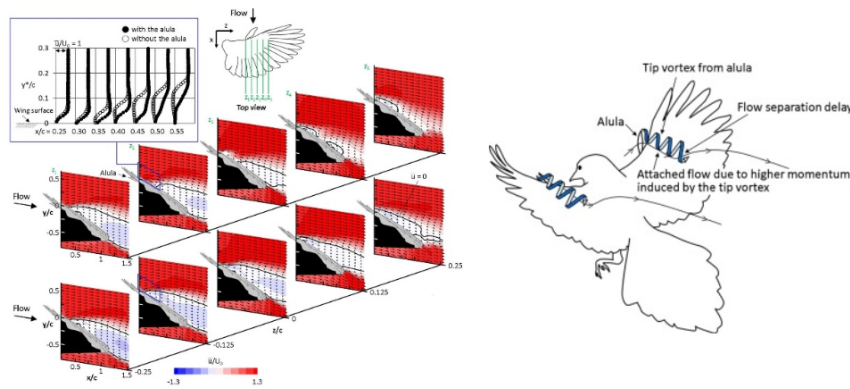


Figure 6.12: Digital particle image velocimetry to display the role of the alula in delaying flow separation over the wing [30]

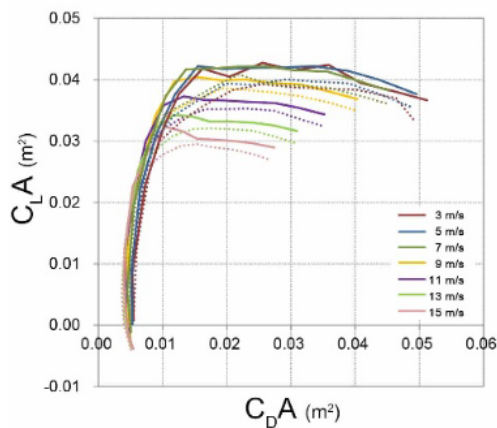


Figure 6.13: Lift-area versus drag-area polar for with alula (bold lines) and without alula (dotted lines) [30]

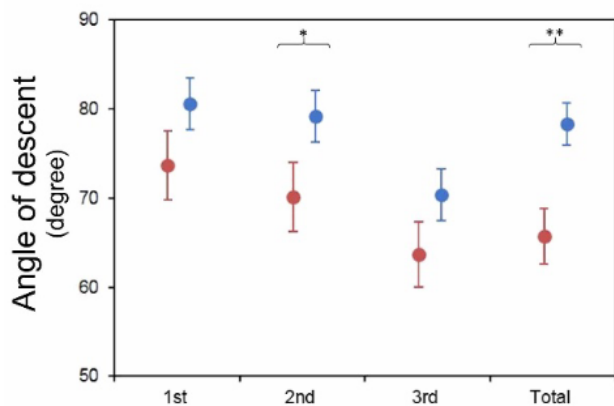


Figure 6.14: Angles of descent of four Eurasian magpies with alula (red) and without alula (blue)

Alula Sizing

Statistics on alula properties have shown that the alula positions usually vary between 50 to 60% of the half span of the wing and make up close to 17.5% of the half span. These statistical measurements were taken into consideration during the sizing of the alula surface. The requirements on $C_{L_{max}}$ were already defined based on the stall speed requirements and in turn meant that a maximum lift coefficient of 1.8 was to be reached. The studied increase in lift coefficient via wind tunnel testing due to the alula was seen to be close to 22% thus the sizing of the alula was partly derived via the statistical biological estimations to achieve a change in C_L of 0.3[26]. The results of the sizing are presented in Table 6.2 with Figure 6.15 as reference to the parameters.

Table 6.2: Alula parameters as a result of statistical biological sizing

Parameter	Value	Unit
S	0.026	m^2
b	0.14	m
c	0.04	m
Overhang	25	% of local chord

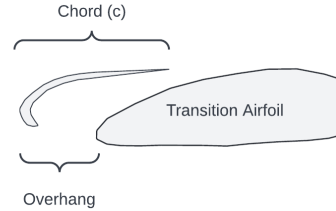


Figure 6.15: Alula sizing parameters

Given that the alula has been preliminary sized for the required change in lift coefficient, it is difficult to quantify exactly the effects of this mechanism on the drone due to the limitations of the aerodynamic analysis software. Modeling the alula on traditional aero-analysis software yields inconsistent results and the modeling of such a unique leading edge slat accurately requires more complex fluid dynamics simulations or traditional wind tunnel testing. However, looking at current studies performed with similar alula sizing methods have shown promising results leading to the increase in the overall $C_{L_{max}}$ as displayed in Figure 6.16 in which the overall max lift coefficient increase is around 0.4, close to what is required by the alula designed for the Air-Guard drone [8]. As result, it needs to be noted that a more rigorous analysis of the alula must be conducted under formal wind tunnel testing or more complex CFD to understand the extent of its effects on the drone, however, it is estimated to allow the drone to achieve its target $C_{L_{max}}$ with the sizing methods developed via statistical measurements and literature [26][30][8].

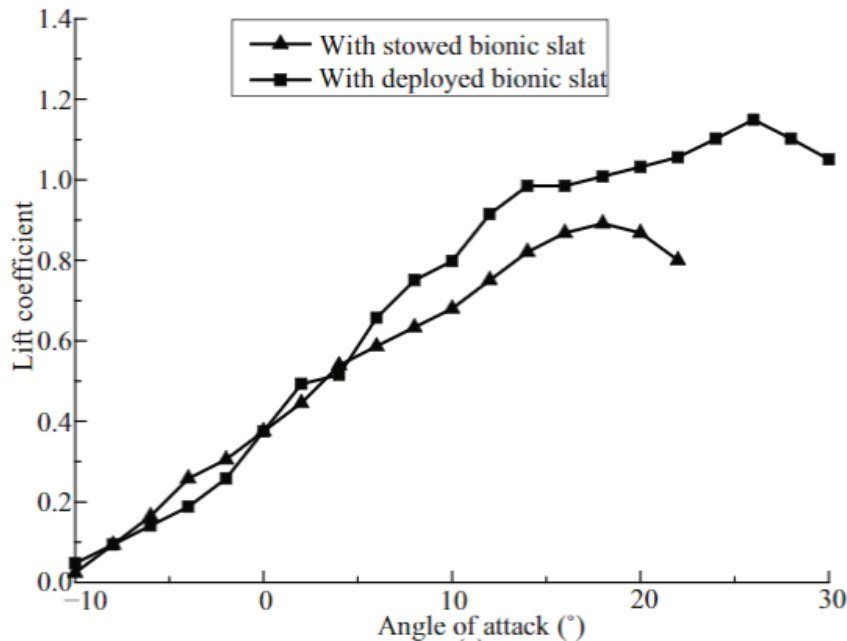


Figure 6.16: The effect of alula on $C_{L_{max}}$ analyzed at $Re = 4 \cdot 10^4$ [8]

6.3.5. Results

Flowing from the aerodynamic calculations and the most optimum planform layout, the design of the wings converged to the following final parameters seen in Table 6.4.

Table 6.3: Wing parameters and aerodynamic coefficients part 1

Parameter	Value	Unit
S_{inner}	0.148	m^2
$S_{extended}$	0.248	m^2
$S_{retracted}$	0.148	m^2
b_{inner}	0.65	m
$b_{extended}$	1.34	m
$b_{retracted}$	1.096	m
$AR_{extended}$	7.24	-
$AR_{retracted}$	6.12	-

Table 6.4: Wing parameters and aerodynamic coefficients part 2

Parameter	Value	Unit
$C_{L_{max}}$	1.3	-
C_{D_0}	0.021	-
Taper Ratio	0.9	-
Leading Edge Sweep	-5	deg
X_{LEMAC}	0.208	m
MAC	0.217	m

Aerodynamic characteristics

The analysis was run in openVSP for two different configurations, one with the wings extended and one with the wings retracted, Figure 6.17. Figure 6.18 shows the drag coefficient against the angle of attack. Here it can be seen that when retracting the wings, the drag decreases, especially at higher angles of attack. Figure 6.19 presents the lift curve for the wing and fuselage for the two different states. OpenVSP does not accurately predict stall so at higher angles of attack the accuracy of the C_L estimations should be carefully considered. However, the lift slope and lift at lower angles of attack are still useful to get an indication of what the behavior of the drone looks like around cruise conditions. Figure 6.20 shows the lift coefficient over the drag coefficient for different angles of attack. After morphing the wings 50 degrees backwards, the efficiency of the wings decreases by 15% as compared to fully extended wings.

Another important aspect of the wing is the pitching moment, but since the tail plays a large part in the stability, this will be discussed in Section 7.3.

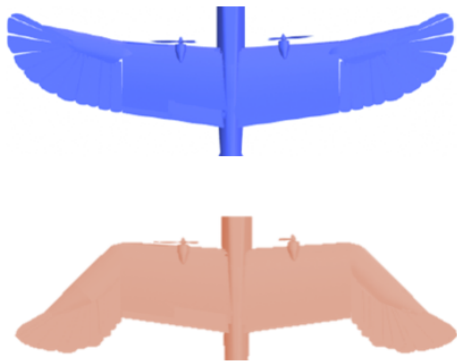


Figure 6.17: The extended (blue) and retracted (orange) positions of the wings

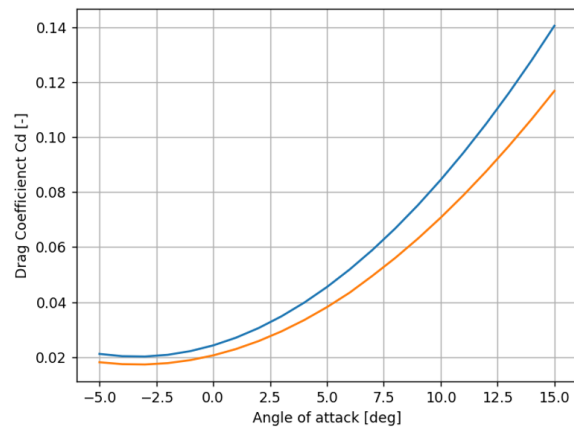


Figure 6.18: Drag coefficient vs angle of attack for fully extended wings and fully retracted wings ($Re=250000$)

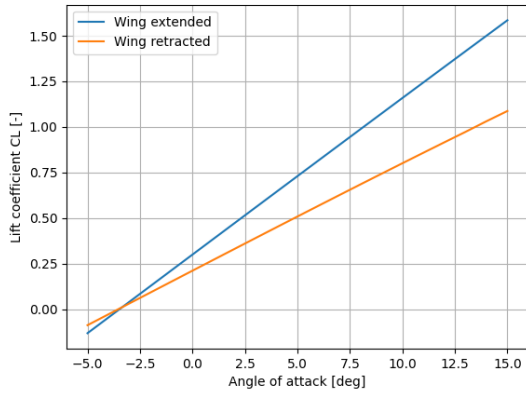


Figure 6.19: Lift coefficients vs angle of attack for fully extended wings and fully retracted wings ($Re=250000$)

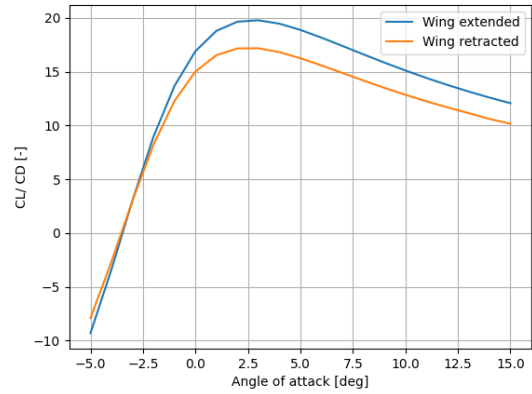


Figure 6.20: Lift over drag coefficient vs angle of attack for fully extended wings and fully retracted wings ($Re=250000$)

Rolling characteristics

Rolling the drone will be done by asymmetrically morphing the wings. As can be seen in Figure 6.21, the extended wing will produce more lift and will create a moment around the x-axis. This moment will cause the drone to rotate around that axis.

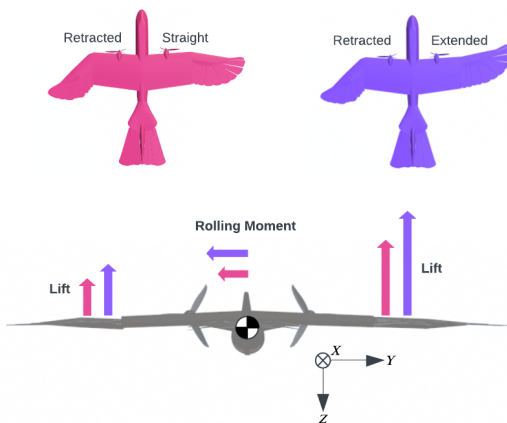


Figure 6.21: Types of morphing configurations for asymmetric rolling

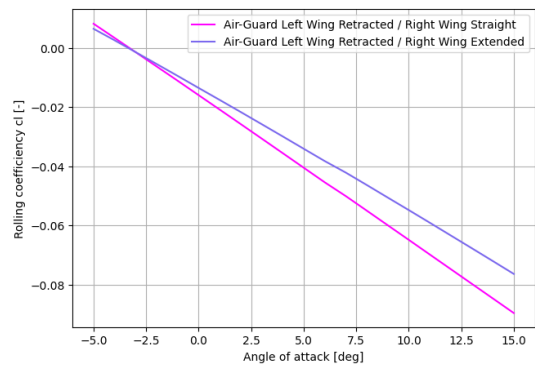


Figure 6.22: Rolling coefficient vs angle of attack for asymmetrically morphed wings ($Re=250000$)

The rolling characteristics are often represented by the rolling coefficient C_l , which is plotted against the angle of attack in Figure 6.21. Interestingly, the roll rate increases when flying at a higher angle of attack. This is because the platelets produce more lift at higher angles of attack, and therefore the difference between the left and right wing will increase as well at higher angles of attack.

Furthermore, Chang et al. discovered that there is asymmetric coupling present between the roll and yaw control due to wing morphing described as adverse roll-yaw coupling. Looking at the results from the flight dynamics model developed in Chapter 9 it was evident that the Air-Guard drone showed similar asymmetric coupling, where morphing of the wings cause a rolling moment and an adverse yawing moment. It was observed that the magnitude of the rolling moment coefficient is 25 times larger than the yawing moment coefficient causing a roll toward the side of the wing that has been retracted.

Stall prediction

Using Star-CCM+, the airflow around the drone was modelled to predict at which angle the wings would stall. Using this software no separation was found for a significant part of the wing below an angle of attack of 20°. The platelets near the wingtips did stall. However, it was considered that the alula and the fairing will delay stall for the platelets. A detailed analysis on stall of the wingtip should be done using wind tunnel tests. As seen in Figure 6.19, the intended $C_{L_{max}}$ was already achieved at 15° angle of attack, so it will be assumed that it does not stall before. However, using different models to simulate and analyze the same model is not advised since the computations rely on different assumptions, even though the aerodynamic coefficients are deemed to be similar as can be found in Table 13.1. Due to this, it is heavily advised to use wind tunnel testing to get a more accurate prediction of the stall angle of attack.

6.4. Morphing Wing

In this section the design of the wing morphing mechanisms including the kinematic movement and the actuation are discussed in Subsection 6.4.2, Subsection 6.4.1 and Subsection 6.4.3 respectively.

From the aerodynamic analysis, as discussed in Subsection 6.3.3, it was found that an area change for the wing of 0.1 m² is required. This yielded the requirement that the mechanism needs to deflect 10 degrees forward and 50 degrees backward with respect to the leading edge spar, which is located at 25% of the chord of the fixed part of the wing. By deflecting the hinged spar, the mechanism changes the sweep and area of the wing, altering the aerodynamic characteristics of the wing. These are used to control the movement of the drone during flight, as discussed in Chapter 9. The same holds for the alula, which is required to have an area of 0.026 m² and needs to create around 25 % of the local chord in overhang, as discussed in Subsection 6.3.4.

6.4.1. Wing Morphing Kinematics

To determine the position of the actuator, hinges, and actuation point on the hinged spar, a 2D kinematic model of the morphing mechanism was made, as can be seen in Figure 6.23. Using this 2D model an equation is constructed to relate the deflection of the hinged spar, θ , and the horizontal deflection of the actuator arm, u , as can be seen in Equation 6.1. The variables p , d , s and k represent the geometrical positions of all elements used to form the aforementioned equation, as can be seen in Figure 6.23.

$$u = \frac{1}{2}(\pm\sqrt{2}\sqrt{4dpcos\theta - 4dp + 4dssin\theta + 2k^2 + 4ks - p^2 cos(2\theta) + p^2 - 2pssin2\theta + s^2 cos2\theta + s^2} - 2k + 2psin\theta - 2scos\theta) \quad (6.1)$$

To keep the moment of inertia around the roll-axis as low as possible, and to have enough room within the wing, the actuator was placed as inboard as possible. The exact position is $s = 13$ mm, $p = 10$ mm, $k = 255$ mm and $d = 42$ mm. Using these position parameters and Equation 6.1 the position of the actuation point and required actuation range were found. This is visualized in Figure 6.24.

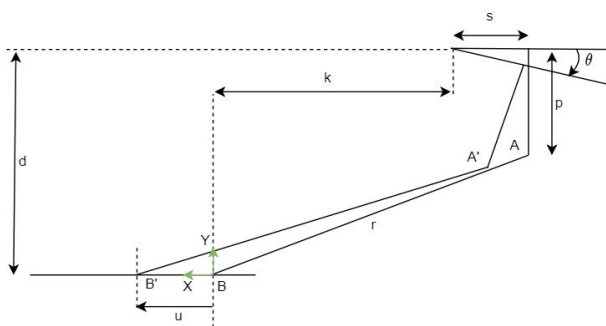


Figure 6.23: Kinematics diagram in variable form for wing morphing

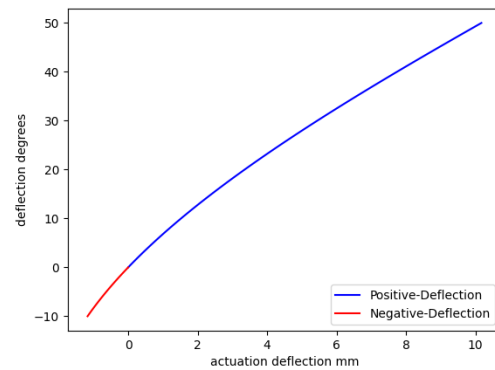


Figure 6.24: Wing-Morphing : actuation vs. deflection

As for the Alula, a more simplified approach was taken due to more limited positioning options for the actuator within the fairing of the hinged spar, giving fewer variables and loads to consider when designing for a certain actuation range. Therefore, the position of the actuator was chosen via a more trial and error approach within the 3D modeling software CATIA, taking into account the available space and the deflection range of the alula.

6.4.2. Mechanism Design

Using the information and conclusions drawn from [Section 6.1](#), [Subsection 6.3.2](#), the structural requirements in [Subsection 6.5.2](#) and the aforementioned requirements on how substantial the morphing needs to be for both the wing itself and the alula, the final design can be constructed based on the initial concept selected during preliminary design. The final design in both its fully extended state and retracted state can be seen in [Figure 6.25](#) and [Figure 6.26](#) respectively. It is important to note that even though the images suggest that the alula and wing are morphed simultaneously, they can be controlled independently as they each have their separate actuators.

To ensure that the platelets' movement is dictated by the movement of the spar, the outermost feather is rigidly connected to the spar itself. Each subsequent platelet is attached to the elastic tendon running from the fixed outer platelet to the inner platelet, as can be seen in [Figure 6.27](#). This ensures the platelets' movement are constrained to the relative movement of its neighbors. The innermost platelet is constrained to the trailing edge spar via a pin and channel connection, as can be seen in [Figure 6.28](#). The elastic tendon running along the pins where the platelets are attached was estimated to have a pre-stretch of 0.63N in the fully collapsed position and a spring force of around 4N, this was based on the EPFL morphing UAV [4].

The platelets' mounting point and size were designed such that there is no interference between feathers when overlapping, this was done using a height and length offset of the platelet mounting pins. The first three platelets, when counting from the inboard part of the wing, are mounted in a staircase-like height progression. This is also the case for the outer two platelets. The inner platelets were stacked in an alternating fashion, as they don't need to overlap as much as the inner and outermost feathers.

The size and distribution of the platelets were made such that a continuous planform is accomplished for all but the 3 outermost platelets, inspired by the feather distribution as discussed in [Section 6.1](#). According to [Wissa et al.](#), the separated tip feathers will help to reduce induced drag while soaring and delay stall during high angle of attack maneuvers, also described in [Section 6.1](#). This can also be seen in [Figure 6.27](#).

After the platelets were positioned and the spar's dimensions were found, the fairing and alula could be designed. The fairing was constructed according to the airfoil specified in [Subsection 6.3.2](#). In addition to these airfoil shapes, an "elbow"-like fairing was added to the inboard section of the morphing wing. This was done to ensure a no-gap transition from the fixed part of the wing to the morphing part in all morphed configurations. This addition to the fairing was made such that it does not interfere with the movement of the spar, and is housed within the leading edge of the fixed-wing when "not needed", which can also be seen in [Figure 6.25](#) and [Figure 6.26](#). Using the fairing's shape and the required dimensions of the alula dictated by [Section 6.3](#), it was made such that it is a part of the fairing, therefore it will sit completely flush with the rest of the fairing when not in use, as can be seen in [Figure 6.26](#). The thickness of the alula is only a part of the total fairing thickness such that when in use the surface behind the alula can still act as a fairing for the flow. The shape of the alula, as shown in [Subsection 6.3.2](#) is modeled after a leading edge slat as used in regular aircraft and the alula feather used by birds as described in [Section 6.1](#).

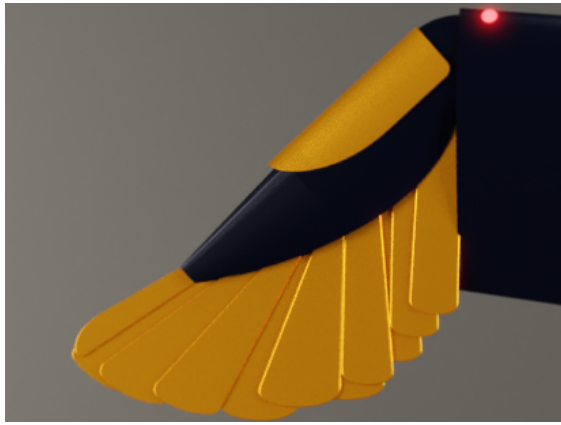


Figure 6.25: The morphing wing in fully retracted position

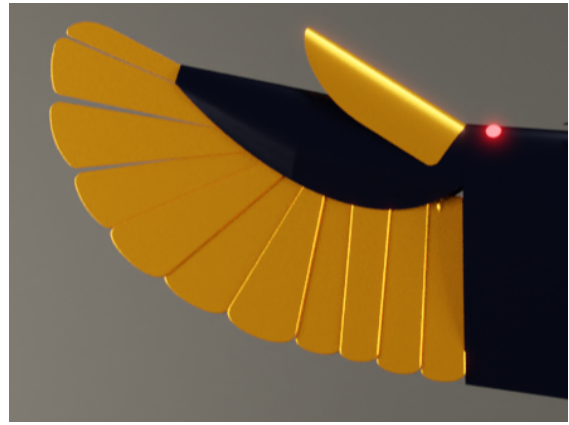


Figure 6.26: The morphing wing in fully extended position

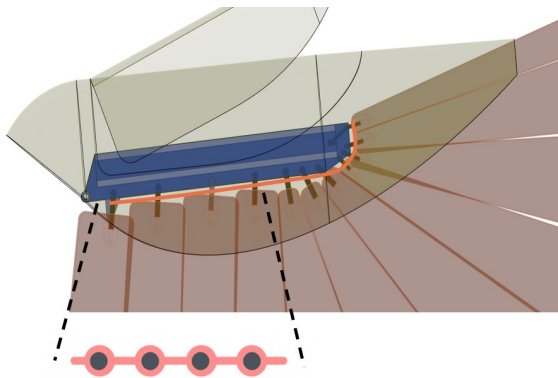


Figure 6.27: Detailed view of morphing mechanism and platelet



Figure 6.28: View of the inner platelet pin-channel connection to the trailing edge spar

6.4.3. Actuation

To ensure the proper functioning of the mechanism the loads on the actuator were estimated using the required elastic tendon stiffness, as mentioned in Subsection 6.4.2 and the aerodynamic drag along the morphing part of the wing, found using the methods described in Section 6.3. The flight condition where the UAV pulls out of its 67.5 m/s dive, where it has to be able to morph its wings from fully retracted to fully extended position was identified as the most critical condition for the actuator loads. These calculations were therefore performed in both the fully extended and fully collapsed morphing conditions, using the actuator position found in Subsection 6.4.1. The results for both the elastic tendon force offset and aerodynamic drag offset can be found in Table 6.5.

Table 6.5: The force for the wing actuation

	Extended	Retracted
Drag offset [N]	5.5	4
Tendon offset [N]	4	0.63
Total Force [N]	9.5	4.63

From Table 6.5 and the additional arguments for actuation speed, longevity and a safety factor, the actuator was chosen to be the Savox SC-1257TG servo with a 1.5 cm actuator arm, since this meets the requirements for both the actuation force, as described before, and the required longevity of this actuator as it uses very wear-resistant titanium gears. It provides an actuation speed of around 3.33 rad/s, based on the datasheet provided by the manufacturer, under the loading condition as described in Table 6.5, and the kinematic relation from Subsection 6.4.1.

6.5. Structures

Due to the morphing mechanism, the design of the load bearing structure is more extensive than usual. Different design approaches are taken for the fixed and morphing part because of the different requirements. Thus, the main role of the inboard part is to provide lift and structural support, whereas the outboard part must be able to morph over an extensive range. Two separate subsections are dedicated to the explanation of the design process of these parts, [Subsection 6.5.1](#) and [Subsection 6.5.2](#).

6.5.1. Wing Box Fixed Wing

The structure of the fixed wing is constructed from a load carrying skin and two spars. The shear and bending stresses are analyzed using beam idealization theory in a Python script. The resulting stresses are used to select a material and determine the necessary thicknesses.

The cross-section of the fixed wing is shown in [Figure 6.29](#).

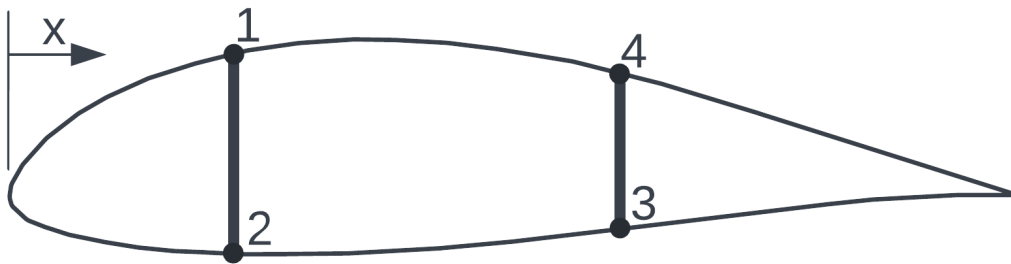


Figure 6.29: The cross section of the wing box

The python script takes as an input the *.dat* file of the airfoil, chord length, number of spars, and spar positions. Then, the following steps are taken:

1. A cubic spline is constructed through the coordinate points of the airfoil *.dat* file.
2. The spline is sectioned at the spar locations, yielding six elements, which are cast into objects.
3. For each element the arc length, area, and centroid are calculated. From this the global centroid and moments of inertia can be calculated.

To facilitate the analysis of the structure, the boom idealization is used [32, p. 559], which simplifies the structure into 4 booms which carry all normal loads, whereas the skin and spar elements carry only shear loads. The booms are set up at points one to 4, as seen in [Figure 6.29](#), thus each element is connected to two booms. The load carrying capability of an element is transferred to the adjacent booms by increasing the boom area according to the boom idealization formula shown in [Equation 6.2](#).

$$B_1 = \frac{t \cdot l}{6} \left(2 + \frac{\sigma_2}{\sigma_1} \right) \quad (6.2)$$

Where t and l are the element thickness and arc length between two booms, respectively and $\frac{\sigma_2}{\sigma_1}$ is the ratio of the normal stresses experienced by the booms, calculated in [Equation 6.3](#).

$$\sigma_z = \frac{(M_x I_{yy} - M_y I_{xy}) y + (M_y I_{xx} - M_x I_{xy}) x}{I_{xx} I_{yy} - I_{xy}^2} \quad (6.3)$$

Once the boom objects are initiated, the idealized moments of inertia and system centroid can be calculated.

After the structure was idealized, the next step was to construct the loading diagrams. These are based on the lift distribution for the critical flight condition where the loading factor is the highest, and were found by integrating along the span of the wing. [Figure 6.30](#), [Figure 6.31](#) and [Figure 6.32](#) show the shear force, moment and torsion diagrams for the half of the main wing as a function of spanwise location.

The shear force diagram shown in [Figure 6.30](#) is typical for a wing, the only difference is the kink in the middle, which is due to the limitations of the simulating software to properly treat the change from the fixed part of the wing to the morphing one.

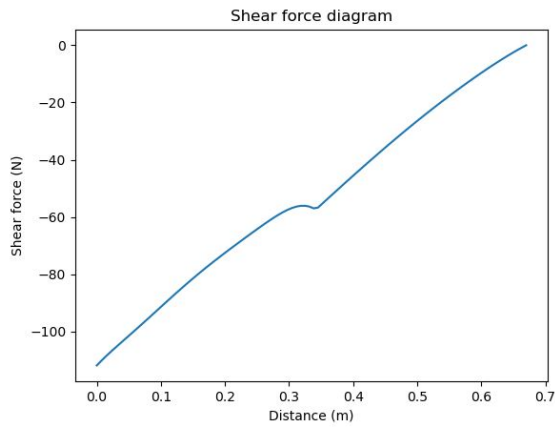


Figure 6.30: Shear force diagram for the main wing as a function of spanwise location

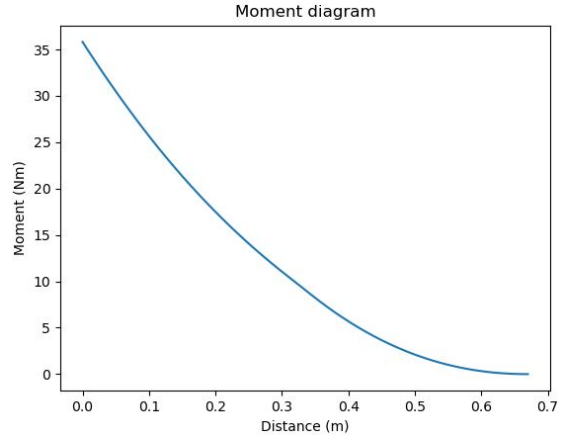


Figure 6.31: Moment diagram for the main wing as a function of spanwise location

[Figure 6.31](#) shows the moment diagram, where the moment increases from 0 at the wing tip, to ≈ 35 Nm at the root. The shape of the diagram is according to the expectations for this kind of loading.

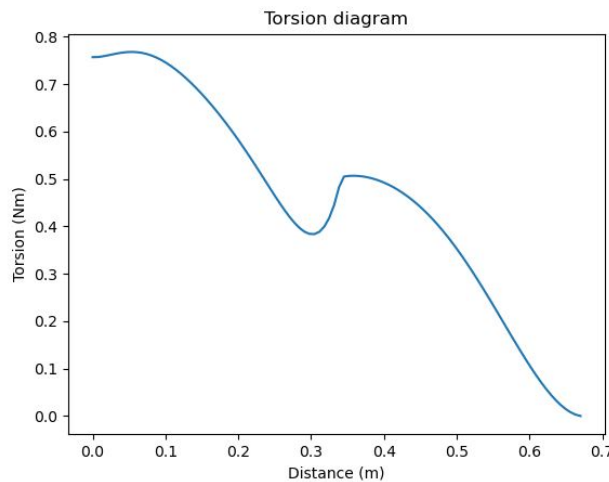


Figure 6.32: Torsion diagram for the main wing as a function of spanwise location

Lastly, in [Figure 6.32](#), the torsion as a function of the spanwise location is shown. Again, the unusual shape in the middle has the same cause as in [Figure 6.30](#), namely the limitations of the simulating software. All the loads in these diagrams were multiplied by a safety factor of 1.5 for the structural analysis.

The shear loads due to a shear force were calculated using the procedure described in [32, p. 569]. First, 'cuts' were made in one section from each cell and the open section shear flows in the other sections were calculated using [Equation 6.4](#).

$$q_s = q_b + q_{s0} = -\frac{V_y I_{yy} - V_x I_{xy}}{I_{xx} I_{yy} - I_{xy}^2} \left[\sum_{r=1}^n B_r y \right] - \frac{V_x I_{xx} - V_y I_{xy}}{I_{xx} I_{yy} - I_{xy}^2} \left[\sum_{r=1}^n B_r x \right] + q_{s0} \quad (6.4)$$

in which V' s are the shear forces, I' s the moments of inertia, B_r is the boom area and x and y the distance of the boom from the centroid in x and y direction. Then, to find the constant shear flow, which is different for each of the 3 cells and the twist rate, 4 equations are written. Equation 6.5 is written for each of the 3 cells, resulting in 3 equations. Also, the twist must be equal as the airfoil rotates, but does not suffer distortion.

$$\frac{d\theta}{dz} = \frac{1}{2A} \oint \frac{q_s ds}{tG} \quad (6.5)$$

Where A is the enclosed area of a cell, t , the thickness of the cell's walls, G the shear modulus and q_s the shear flow.

The 4th equation is a moment equivalence between the applied force and the resultant forces from the shear flows. Now, with 4 equations and 4 unknowns, the system can be solved for the constant shear flows in each cell and the twist rate of the airfoil. Finally, in order to find the total shear flows due to shear loading, the basic shear flow must be added with the constant shear flow for each section.

Next, the shear flows due to torsion must be taken into account. In each of the three cells, a different shear flow is considered. The deformation for all of the cells must be equal for the same reason as listed above, and it is given again by Equation 6.5:

This results in 3 equations, with 4 unknowns: the shear flows in the three cells and the twist rate. The last equation represents the torque equivalence given by Equation 6.6:

$$T = 2A_I q_I + 2A_{II} q_{II} + 2A_{III} q_{III} \quad (6.6)$$

Where T is the torque on the section, A_I , A_{II} and A_{III} are the area of each cell and q_I , q_{II} and q_{III} are the shear flow in each cell. With these shear flows known, the shear flows in each section can be calculated by simple addition and simplification.

The final shear flows due to both shear force and torsion are found by addition. Then, for the sizing of the structure, the shear stress is needed in each section, which is found by dividing the shear flow by the thickness, $\tau = \frac{q}{t}$.

As the highest loads are at the wing root, the highest stresses were also found to be there, thus that is the section that drives the design.

Lastly, an iteration program starts by allocating a thickness to each skin element and spar. Then, the stress is calculated by dividing the previously obtained forces by the geometrical area. This stress is compared to a list of materials. Of all materials that are sufficient, i.e. those that deform elastically only, the lightest one is picked and stored. These nested loops, one for different skin thicknesses and one for different spar thicknesses, produce a table with the different geometries, the best material, and resulting mass. Sorting this list by ascending mass and picking the first entry returns the best performing geometry-material combination by mass. The materials considered are four aerospace grade aluminum alloys (Al6013-T6, Al6262-T6, Al7010-T75451, Al7150-T6151), balsa wood, and quasi-isotropically laid CFRP. The material properties are sourced from the *CES EduPack* materials database [33]. Now, a remaining question is how to pick the range of thicknesses over which the program iterates. The specific strength (strength divided by density) for both tensile and shear stress is significantly higher for the aluminum alloys than for the balsa wood. However, the required thickness of an alloy spar would be < 0.3 mm, which is too thin to manufacture. Therefore, a lower bound of 2 mm for the spars and 1 mm for the skin was picked. Starting the iteration at this lower bound returned that the lightest wing-box consists of purely balsa wood with a spar thickness of 3 mm and a skin thickness of 1.5 mm. This results in a structural mass for the fixed wing section of 127 g. An alloy design with the same dimensions would be more than ten times heavier.

Spar Buckling

Next to the manufacturability, there might be minimum thickness requirement due to buckling. For thin plates loaded normally, Equation 6.7 calculates the critical buckling load σ_{cr} [32].

$$\sigma_{cr} = C \frac{\pi^2 E}{12(1-\nu^2)} \frac{t^2}{b} \quad (6.7)$$

Where C is the clamping coefficient, ν the Poisson ratio, and b the spar height. The spar is clamped by the skin on all sides, thus, $C = 6.98$. For the above-mentioned result of the iteration, the critical buckling stress is 3.9 GPa, which is much larger than the maximum experienced normal stress of 5 MPa. Thus, the spar thickness is also sufficiently strong for buckling.

6.5.2. Morphing Part

The main component of the morphing part of the wing is the morphing spar, illustrated in Figure 6.33. It consists of a closed section, such that it can sustain torsional loads, but also two flanges with perforations to allow for platelets mounting.

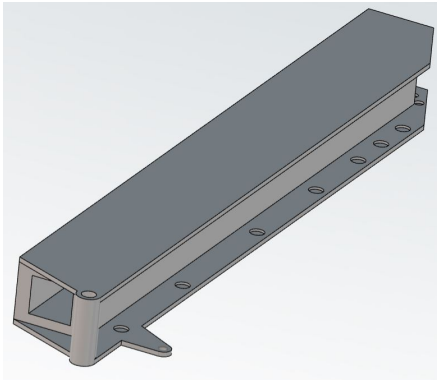


Figure 6.33: A model of the morphing spar

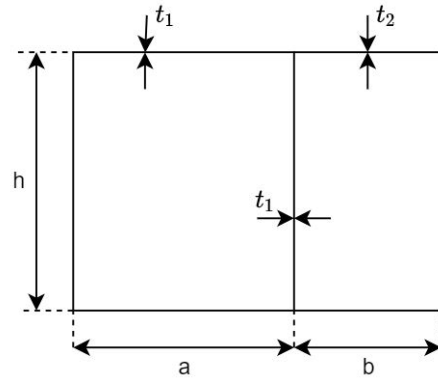


Figure 6.34: The cross section of the wing morphing spar

The loads that this part has to withstand are shown in Figure 6.30, Figure 6.31 and Figure 6.32, but only considering spanwise location from 0.325 m to 0.67 m, as that interval corresponds to the morphing part of the wing. The maximum loads were found, then multiplied with a safety factor of 1.5.

Figure 6.34 shows the sketch of the cross-section, but for the analysis, just the closed section was considered, which is a rectangle with sides with length h and a . This was decided as the primary purpose of the flanges of length b is to enable platelets mounting, thus they are not good load carrying parts: b and t_2 are considerably smaller than a and t_1 , respectively. Also, for torsion, which is considered a big factor as the spar is all the way at the front, the open section does not make a notable difference. Moreover, the forces in the horizontal plane are not considered because they are much lower than in the vertical direction, same with the M_y as it is much lower than M_x . Also, the moment of inertia of the structure is higher. All values seen in the figure were kept as variables during the design process, to enable optimization according to the loads.

The code written takes as an input the spar's geometry and applied loads, and gives as an output the shear stresses and normal loads. A material is then chosen and the total mass calculated. By changing the values of h , a , t_1 considering the constraints enforced by the space available, the optimum design was reached.

First, the moment of inertia, I_{xx} , was calculated. Then, for calculation of the shear stresses due to shear loads, a 'cut' was made in the structure in the top left corner. From there, for each of the sides, the open section shear stresses were calculated with Equation 6.8, where V_x and I_{xy} are 0:

$$q_s = -\frac{V_y I_{yy} - V_x I_{xy}}{I_{xx} I_{yy} - I_{xy}^2} \int_0^s t y ds - \frac{V_x I_{xx} - V_y I_{xy}}{I_{xx} I_{yy} - I_{xy}^2} \int_0^s t x ds \quad (6.8)$$

Next, the section was 'closed' and an equation for moment equivalency was written, which takes into account the moment caused by the external force, open shear flows in each side and the constant shear flow, so that the value of the latter can be found. Lastly, the open shear flows for each section are added with the closed shear flow, so

that the shear flows due to shear force in each section are found. In order to get the shear stresses, the flows are divided by the thickness of each section.

The shear stresses caused by torsional loads can be straightforwardly computed using Equation 6.9:

$$\tau = \frac{q}{t} = \frac{T}{2tA_m} \quad (6.9)$$

Where A_m is simply $h \cdot a$. The shear stresses due to torsion must then be added to the ones found due to shear, thus the total shear stresses in the structure are found.

The last load that needed to be applied was the bending moment. Equation 6.10 shows the formula for normal stress due to bending, where M_y and I_{xy} are 0.

$$\sigma_z = \frac{(M_x I_{yy} - M_y I_{xy})y + (M_y I_{xx} - M_x I_{xy})x}{I_{xx} I_{yy} - I_{xy}^2} \quad (6.10)$$

The highest loads are experienced by the top and bottom flange, as the distance from neutral axis is highest there. The highest shear stress experienced by the structure, considering the safety factors, was $\tau = 200$ MPa, while the maximum bending stress was $\sigma = 17$ MPa.

Analyzing the initial structure, it was found that the loads greatly exceeded the material capabilities of aluminum. Some corrective actions needed to be made, h was increased by 50% and a and t_1 tripled. Aluminum 6013-T6 was chosen as a suitable material, as all aluminum alloys considered in Subsection 6.5.1 can sustain the loads, but this has the lowest density, of 2700 kg/m^3 . Also, it is commonly used in aerospace industry and is recyclable. Given the final dimensions and the material used, the total mass of the morphing spar is 69 grams.

The final values of the parameters are shown in Table 6.6:

Table 6.6: Values of the parameters of the morphing spar

Parameter	h	a	b	t_1	t_2
Value (mm)	14	15	6	3	1

6.5.3. Platelets and Connector Pins

To size the thickness of the platelets, the highest loaded platelet was selected for analysis. Once the required thickness was found for this one, it was applied to all other platelets to facilitate easier manufacturing. To find the platelet in the position with the highest loading, the lift distribution along the chord of a flat plate was analyzed at the angle of attack corresponding to the critical loading condition of the drone. As can be seen from Figure 6.37 and Figure 6.8 the platelet with the most critical loading is the third platelet when counting from the tip, as it has the highest exposed span and chord wise lift fraction combination. Subsequently, a correction factor was applied to the lift distribution along the platelets length to accommodate for the chord wise lift fraction this platelet carries. The bending moment diagram and shear force diagram for the critical platelet can be seen in Figure 6.35 and in Figure 6.36. Using Equation 12.2 with a width of 13 mm and a thickness of 1 mm, a bending stress of 360 MPa was found. The shear and bending found at the root of the platelet were then also applied to the connector pin where it was found that the loads at the root using the same equation as mentioned before, but now with a circular cross-section of diameter 3 mm and the root of the pin being offset 5 mm from the root of the platelet, yielded a bending stress of 295 MPa.

6.5.4. Material Selection

Taking the aforementioned loads into account, it was preferred to make use of carbon fiber, however, the processing of the material and the overall production process was deemed too wasteful and energy inefficient, thus it was required that a substitute should be found to conserve the weight and structural performance. Through further research, it was found that a company called NematX have developed a method in which the material Celanese LCP Vectra A950-VF3001 can be 3D printed in such a way that the structural and physical properties are similar to that of carbon fiber composites, making use of such material would ensure that the structural integrity of the wing structure would be maintained and the weight of the system can be minimized [34].

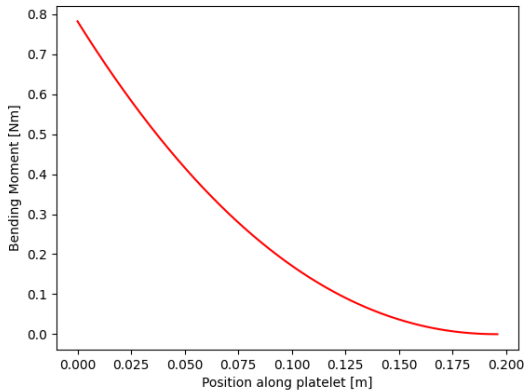


Figure 6.35: Bending moment per length for the 'critical' platelet

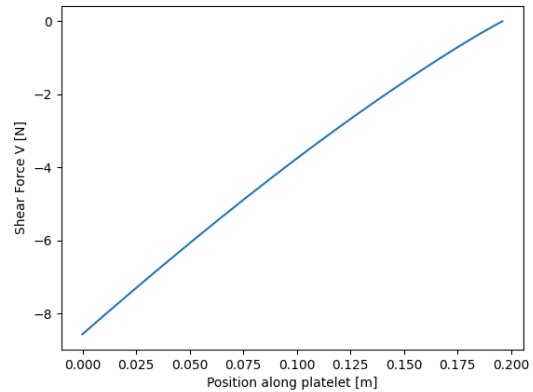


Figure 6.36: Shear force per length for the 'critical' platelet

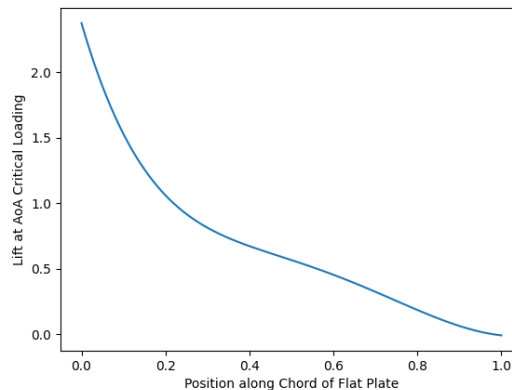


Figure 6.37: The chord-wise lift distribution at the angle of attack of the critical loading condition

6.5.5. Joints

Joints represent weak spots in the structure because they are subject to possible stress concentrations. In this section, multiple joints for the wing are considered, in multiple failure modes. Due to time constraints, it is not possible to analyze all failure modes for all the joints. It was decided to analyze the main joints in the failure modes that seem to be critical.

Connection between morphing spar and fixed wing

One of the most difficult parts of a morphing design is to transfer the loads from the morphing to the fixed part. This is because instead of a distributed load over a greater surface, there is a point force and moment introduced through a single joint.

For the hinge connecting the morphing and fixed part of the wing, three failure modes were considered. First, looking at the highlighted blue rectangle in Figure 6.38, there is a shear force of 86 N and a moment of 14.46 Nm acting on that surface. These magnitudes result from looking at Figure 6.30 and Figure 6.31 for a distance of 0.325 (end of fixed section) and multiplying with a safety factor of 1.5. This surface has sides of 3 respectively 12 mm. Calculating maximum shear and bending stress using Equation 6.10 and the fact that the shear stress is shear force divided by area, leads to 2.38 MPa in shear and 200 MPa in bending.

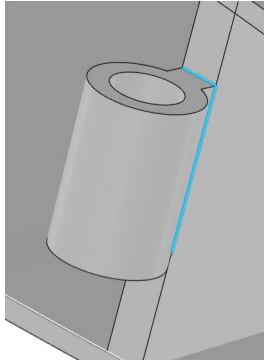


Figure 6.38: The hinge point of the morphing spar

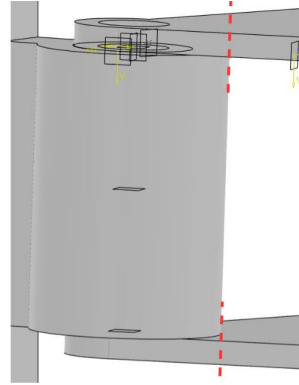


Figure 6.39: Shear planes of the morphing spar at the hinge location

As the spar is made from balsa wood, the normal stress caused by bending greatly exceeds the ultimate stress. To solve this issue, it was decided to reinforce the end of the spar, at the location of the hinge, with an aluminum plate that would ensure a carry the high stress and transfer the loads smoothly over a larger area into the wooden spar.

The third failure mode is the shear of the flanges of the morphing spar, as shown in Figure 6.39. The red dotted lines correspond to the weakest link. The approximate cross-sectional area of the two flanges is 18 mm^2 , and using the same shear force value of 86 N leads to a shear stress of 5 MPa, which aluminum can easily withstand.

Connection between platelets and morphing spar

Each platelet is connected to the morphing spar via a T-shaped rod as seen in Figure 6.40. Due to the aerodynamic forces, the platelet introduces a bending moment in the morphing spar through the rod. This is considered to be a critical joint as the bending moment can be relatively high, while the indentations for the rod placement are quite small.

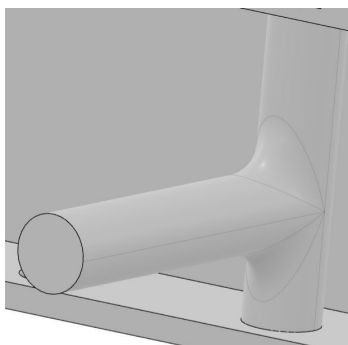


Figure 6.40: A model of the platelet hinge

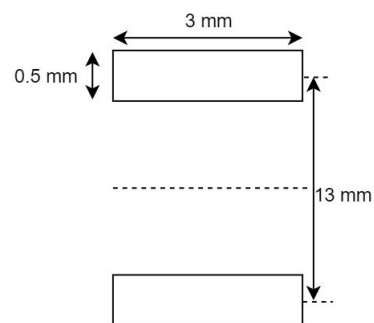


Figure 6.41: The geometry of the surface subject to stresses due to platelet bending moment

Figure 6.41 shows the surfaces that take the bending moment. They are the indentations where the rod enters the spar. The moment of inertia can be calculated, then after applying a moment of 1.17 Nm (considering safety factor of 1.5), which is for the highest loaded platelet, it is found that the maximum normal stress in 60 MPa, which is considerably less than the yield stress of aluminum.

Connection between wing and fuselage

The wing is connected to the fuselage through the spars. Based on the shear flows in the spars calculated using the code described in [Subsection 6.5.1](#), at the root, the forces in the spars considering a safety factor of 1.5 are 185 N and 34 N. Bolting is used for joining as it allows for the wing to be demounted. Moreover, aluminum plates of 0.5 mm thickness are mounted on each side of each spar in the location of the connection to reinforce the structure. It is considered that the front spar is connected with 3 bolts, while the aft one has 2 bolts. For preliminary estimations, the bolt diameter is chosen as 2.5mm. For the following calculations, both the yield stress and maximum shear stress are considered to be 150 MPa, which is much lower than the real values, but this simplifies the calculations and emphasizes that the exact type of aluminum alloy is not important. The rivet fracture force is given by [Equation 6.11](#):

$$F_{ult} = \frac{\pi}{4} D^2 \tau_{fracture}^{rivet} \quad (6.11)$$

This leads to a rivet fracture of 736 N, much higher than the 185 N in the front spar. Next, for bearing fracture, [Equation 6.12](#) is used:

$$F_{ult} = p_{b-fracture} D^{hole} t^{sheet} \quad (6.12)$$

A conservative value for the bearing stress for aluminum alloys is around 800 MPa [12], resulting in a bearing fracture force of 2060 N, again much more than the encountered forces.

A maximum deformation of the holes of 2% is considered acceptable, and the force for this deformation is given by [Equation 6.13](#).

$$F_{ult} = 1.5 p_{2\%} D^{hole} t^{sheet} \quad (6.13)$$

Considering the above-mentioned values, and $1.5 p_{2\%} = 790$ MPa [12], leads to a limit force of 1975 N.

Lastly, there is the possibility that the two thin aluminum plates shear out. At the root, the spars are 3 cm and 1.4 cm in height. Bolting in the middle would mean 1.5 and 0.7 cm to the end of the spar for the bolt to shear through. Considering [Equation 6.14](#):

$$F_{max} = \tau t d \quad (6.14)$$

This leads to, for aft spar, to a shear out force of 525 N, considerably higher than the total lift force.

7. Tail Design

In this chapter, the tail design will be presented. Reasoning for the design choices made will also be given. First, some background information is given on how birds move their tail in Section 7.1. Then the design process is explained in Section 7.2. Afterwards, the aerodynamics of the tail are discussed in Section 7.3. Lastly, a description of the morphing mechanism and the tail structure is given in Section 7.4 and Section 7.5 respectively.

7.1. A Study into Avian Tail Morphology

Tails are a prevalent feature in both aircraft and birds. However, the methods in which the tail is utilized for the stability and control in both instances may differ. While conventional aircraft have vertical and horizontal tails mounted perpendicular to each other, birds only include a horizontal tail surface. The lack of discrete control surfaces on a bird's tail and its wings, means that there is a much more continuous surface. This surface is augmented continuously by changing incidence angle, tail spread, and tail rotation, the latter of which replaces the rudder in ensuring continuous directional stability [21]. These degrees of freedom aid the birds in increasing efficiency, performance, and/or stability. Therefore, the principle of tail morphing could also be beneficial for conventional fixed-wing drones. Observing Figure 7.1 and Figure 7.2 the tail spread and elevator mechanism are displayed. These two mechanisms are the ones that are chosen for the incorporation into the Air-Guard UAV. The rotational degree of freedom was omitted and instead, a vertical tail was added to maintain the directional stability of the drone.

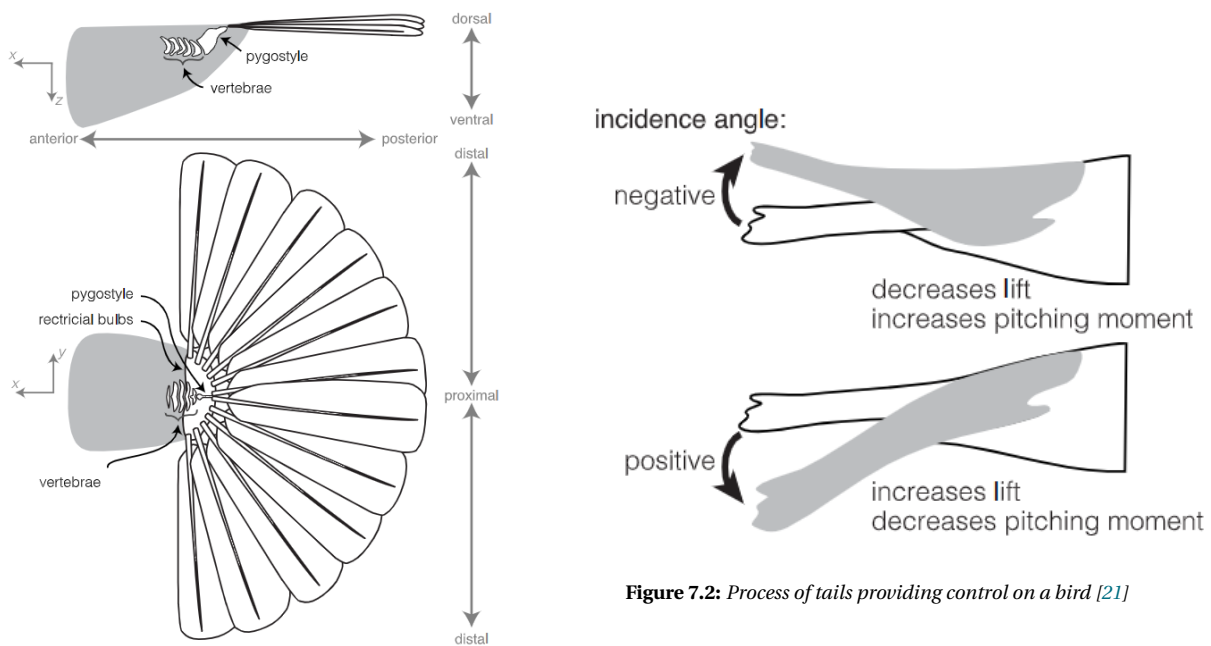


Figure 7.1: Avian tail biology [21]

The process of tail morphing to decrease tail area and control elevator deflection is used by birds to fundamentally alter the stability characteristics such that the most effective optimization of tail lift versus wing lift is achieved [21]. Tail spread in birds allows for the alteration of the tail volume coefficient and at the same time increases the lift distribution such that the tail forces can be attenuated to provide the most efficient, least drag-inducing surface [21]. Such aspects were considered in the design of the tail, mainly focusing on altering the longitudinal stability of the drone giving rise to multiple stable and unstable flight regimes.

7.2. Design Process

This section will discuss the design process for the tail. First, the control surfaces that need to be actuated are discussed. Then, a description of the sizing and process of the tail is given.

7.2.1. Actuated Control Surfaces

In a conventional aircraft, control about the three-axis is provided by deflection of three types of control surfaces: ailerons for roll, elevator for pitch, and rudder for yaw. This is, however, not the case for the designed UAV. In this case, roll will be provided by the morphing of the main wing. To roll to the left, for example, the left-wing would morph and so reduce its surface area, producing less lift than the right-wing, resulting in a moment around the longitudinal axis (together with other phenomena which will be discussed in the flight dynamics chapter) and so rolling motion.

The remaining control surfaces, rudder, and elevator were kept conventional and their sizing design will be discussed later in this chapter.

7.2.2. Sizing and Positioning of Horizontal Tail

The number one priority considering stability was to ensure that the aircraft is stable and trimmable in pitch. This would be achieved by a horizontal tail positioned behind the main wing, as it was decided in the preliminary design phase that the drone would use a conventional configuration.

Two major design choices then have to be made: the area and longitudinal position of the tail. The method used for this purpose consists of the following steps:

1. All components of the aircraft are split into fuselage and wing groups, depending on their general position.
2. The longitudinal positions of centers of gravity of both groups are determined w.r.t. their own reference systems.
3. A c.g. excursion plot is created by considering the extreme c.g. positions for different longitudinal positions of the wing w.r.t. fuselage.
4. A scissor plot is created by constructing stability and control curves as functions of longitudinal c.g. position.
5. C.g. excursion and scissor plots are combined.
6. Optimal longitudinal wing position is selected to ensure both stability and control with minimum tail area.

These steps will be now covered in detail in individual subsections

Definition of wing and fuselage groups

As the first step, all major components of the UAV had to be allocated to either wing or fuselage group. As a general rule, a component should be allocated to the wing group if its position is dependent on the position of the main wing.

Determination of c.g. positions

For the two groups of components, the longitudinal position of their centers of gravity had to be calculated. For the fuselage group, this position is given as a fraction of total fuselage length, while for the wing group, the percentage of MAC was used.

For a given group, the c.g. position would be calculated by considering the position and weight of each individual component and then applying :

$$X_{c.g.} = \frac{\sum X_i \cdot W_i}{W_{tot}} \quad (7.1)$$

Where, X_i and W_i are c.g. position (in the appropriate reference system) and weight of the individual component and W_{tot} is the total weight of the group. The positions of the components were obtained from a CAD drawing which was created for this purpose following the preliminary design and which showed the layout of the components inside the wing and fuselage.

It is important to point out that while the c.g. position of the wing group is constant regardless of flight phase, the center of gravity of the fuselage is significantly affected by ejection of the payload. For that reason, the c.g. position

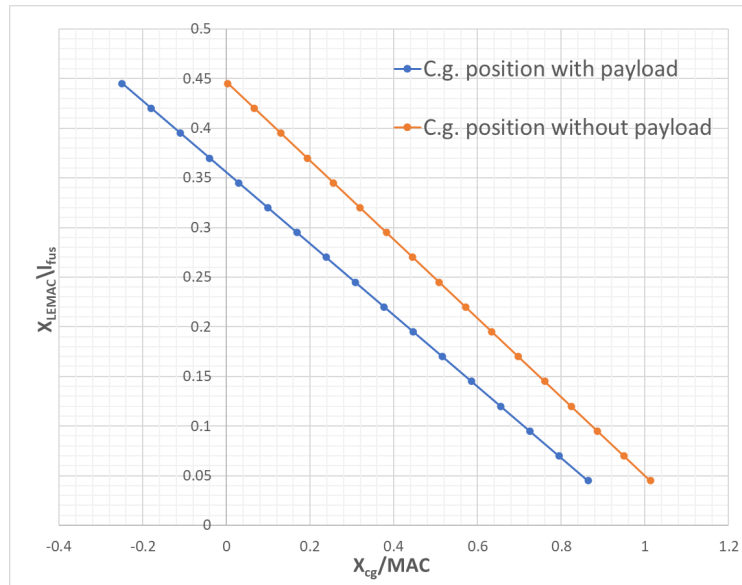


Figure 7.3: C.g. Excursion of the UAV

of the fuselage group was calculated with and without payload. As this is the only change in mass distribution throughout the flight, these two conditions determine the most aft and forward position of c.g.

7.2.3. Constructing Center of Gravity Excursion Plot

Knowing the c.g. positions for individual groups as well as the most extreme c.g. positions that can be experienced during flight, a c.g. excursion plot was obtained. This plot is constructed by placing the wing at various positions with respect to the fuselage and recording the c.g. range (following from ejection of payload) of the complete operational empty weight. These values are then presented in the plot, which shows c.g. position w.r.t. fuselage at the x-axis and longitudinal position of the wing w.r.t. to the fuselage at the y-axis as shown below:

7.2.4. Scissor Plot

A scissor plot is a tool that shows the minimum required horizontal tail area (as ratio w.r.t. to the area of the main wing) as a function of c.g. range. This minimum area is constrained by two factors; stability and controllability. In this case, controllability refers to the ability to trim the aircraft for a given airspeed. These constraints are shown in the plot by two lines. The left one represents the controllability constraint, while the right one represents the stability. Furthermore, for a conventional aircraft a stability margin of +5 % is included, to take into account other stability factors such as stick-free stability or minimum control force, since the stability curve is constructed solely for stick-fixed scenario [35]. For the UAV however, which will feature an active control system and is designed to perform maneuvers comparable to dogfights, high stability is not desirable for this case. For that reason, a stability margin of -5% was used instead, to ensure that the drone meets the maneuverability requirements. This number was selected as this amount of instability can be observed in the design of jet fighters equipped with active control systems [24].

In the following paragraphs, the process of constructing both stability and control curves will be described.

Stability curve

The stability curve is described by the following relation:

$$\frac{S_h}{S} = \frac{1}{\frac{C_{L\alpha_h}}{C_{L\alpha_{1-k}}} \left(1 - \frac{d\epsilon}{d\alpha}\right) \frac{l_h}{\bar{c}} \left(\frac{V_h}{V}\right)^2} \bar{x}_{cg} - \frac{\bar{x}_{ac} - 0.05}{\frac{C_{L\alpha_h}}{C_{L\alpha_{1-k}}} \left(1 - \frac{d\epsilon}{d\alpha}\right) \frac{l_h}{\bar{c}} \left(\frac{V_h}{V}\right)^2} \quad (7.2)$$

First, the position of the aerodynamic center w.r.t MAC had to be estimated. This was done by simply adding individual contributions from the main wing and fuselage. The aerodynamic center of the main wing was assumed to be at quarter chord of the main wing as the drone will fly only at fully subsonic regimes where no shift in the aerodynamic center due to compressibility should be observed [24]. The contribution of the fuselage was then calculated by considering its two effects. The fuselage shifts the aerodynamic center forward (increasing stability) by producing lift by the nose, while at the same time shifting the aerodynamic center aft (decreasing stability) due to loss of lift at the wing-fuselage intersection. Both of these effects are captured in Equation 7.3 :

$$\left(\frac{x_{ac}}{\bar{c}}\right)_{wf} = \left(\frac{x_{ac}}{\bar{c}}\right)_w - \frac{1.8}{C_{L_{\alpha_4-h}}} \frac{b_f h_f l_{fn}}{S \bar{c}} + \frac{0.273}{1 + \lambda} \frac{b_f c_g (b - b_f)}{\bar{c}^2 (b + 2.15 b_f)} \tan \Lambda_{1/4} \quad (7.3)$$

The dimensions used in Equation 7.3 related to fuselage geometry are shown in Equation 7.4.

To get the lift rate coefficient for the tail alone ($C_{L_{\alpha,h}}$), DATCOM method was used [36]:

$$C_{L_{\alpha_h}} = \frac{2\pi A_h}{2 + \sqrt{4 + \left(\frac{A_h \beta}{\eta}\right)^2 \left(1 + \frac{\tan^2 \Lambda_{0.5 C_h}}{\beta^2}\right)}} \quad (7.4)$$

In Equation 7.4 the coefficient beta is 1 as the Mach number for all flight conditions is negligible. For the geometry coefficient, reference values for jet fighters were considered initially. After sizing, the actual values were adjusted to match the morphing geometry following from morphing mechanism. The DATCOM method was further used to calculate the lift rate of the whole aircraft without a tail:

$$C_{L_{\alpha_{1+h}}} = C_{L_{\alpha_{e0}}} \left(1 + 2.15 \frac{b_f}{b}\right) \frac{S_{net}}{S} + \frac{\pi}{2} \frac{b_f^2}{S} \quad (7.5)$$

Where, b_f is fuselage diameter (following from CAD drawings and resulting from payload size). In Equation 7.5 the wing lift rate coefficient was readily available since preliminary design as a result of XFLR5 simulations. The S_{net} is the wing area when the section inside the fuselage is not considered.

The next value needed for Equation 7.2 was the V_h/V ratio, which was taken as 0.85 since a fuselage-mounted horizontal tail was selected in preliminary design [35]. Similarly, the downwash gradient was taken as 0 initially, since no empirical model was available for aircraft of such small scale. Finally, the tail's moment arm was initially estimated by looking at the CAD drawings and selecting a reasonable first estimation. After the first estimation, this value was treated as a design variable and was iterated multiple times to achieve the requested elevator tail effectiveness while keeping unused fuselage space minimal. Note that cruise conditions were considered for the stability curve as that is the most limiting flight phase [35].

Controlability curve

Similar to stability, the control curve is described by a linear equation [37]:

$$\frac{S_h}{S} = \frac{1}{\frac{C_{L_h}}{C_{L_{A-h}}} \frac{l_h}{\bar{c}} \left(\frac{V_h}{V}\right)^2} \bar{x}_{cg} + \frac{\frac{C_{mac}}{C_{L_{A-h}}} - \bar{x}_{ac}}{\frac{C_{L_h}}{C_{L_{A-h}}} \frac{l_h}{\bar{c}} \left(\frac{V_h}{V}\right)^2} \quad (7.6)$$

The maximum tail lift coefficient was then considered as -1 since the selected morphing design of the tail didn't allow for integration of separate lifting surface [37]. Furthermore, the fully movable tail is desirable regardless, as it provides the maximum maneuverability since it is able to provide the most lift.

The moment coefficient needed next composes of the wing contribution and fuselage contribution for the given configuration. The wing contribution was obtained from the XFLR5 analysis mentioned earlier while the following relation was used to enumerate the effect of the fuselage since XFLR5 can not reliably simulate the effects of the fuselage:

$$\Delta_{fus} C_{mac} = -1.8 \left(1 - \frac{2.5b_f}{l_f} \right) \frac{\pi b_f h_f l_f}{4S\bar{c}} \frac{C_{L_0}}{C_{L_{\alpha_{A-h}}}} \quad (7.7)$$

All the lift coefficients in Equation 7.6 were also obtained from the preliminary analysis for landing conditions, as this scenario is the most limiting for control [37]. The remaining factors have already been discussed in the stability curve section.

7.2.5. Scissor Plot Analysis

With both curves constructed and c.g. excursion known, the scissor diagram was assembled. However, not only one unique plot was created. The plot is affected by design choices such as tail arm, wing planform design, tail design, or respective vertical positions of the main wing and tail. That means that the plot was changed with every design iteration.

Traditionally, the goal of such iterations is to select the longitudinal position of the wing such that the tail area is minimal while providing sufficient controllability and stability. In this case, however, the design is made more complex by three factors. Firstly, the drone is required to operate in two general modes of flight; a cruise mode for patrolling, with an emphasis on efficiency, and an attack mode where the top priority is maneuverability in order to be able to catch the unlicensed drone in a dogfight like scenario. These two modes then put directly opposite requirements on stability, as in cruise mode the drone should be fully stable to minimize the energy needed to maintain leveled flight and to minimize trim drag, while in attack mode the drone should have about 5% negative stability margin to maximize agility [24]. The second factor is the fact that the horizontal tail will be able to morph. That means that the surface area of the tail will not be constant as for conventional aircraft, but will vary based on commands from the control system. The final factor is the c.g. position. When the payload is on board, it shifts the c.g. forward (since the payload has to be positioned in the nose as decided upon in preliminary design), increasing stability and reducing maneuverability, while its ejection leads to rapid aft c.g. shift, resulting in decreased stability. These effects are directly opposite to what would be desired in both phases. Based on these considerations, the following design constraints were established based on the most limiting cases:

- The minimal tail surface area should be able to provide a 5% negative stability margin with payload onboard
- The maximal tail surface area should be able to provide at least 5% negative stability margin (but zero neutral or even positive margin) after the payload is ejected.

These constraints should ensure that the drone is sufficiently agile when pursuing the unlicensed drone, while stable enough to be able to return to base once the payload is ejected. Furthermore, the analysis was performed considering only the fully extended wing, as it was reasoned that the tail should allow meeting all control and stability requirements on its own, without depending on the main wing morphing.

The iterations considered during the design process were the tail arm, the position of batteries to alter c.g. excursion, and the position of the main wing. The final scissor plot for the selected configuration can be seen below:

In this plot, the lower dashed line shows the selected Sh/S for the minimum tail area, while the top dashed line shows the same for the maximal tail area. The main wing position stays the same for both cases at the value for minimum Sh/S .

The following table then summarizes the values and dimensions for the final configuration:

Table 7.1: Outcome of horizontal tail sizing

Dimension	Value	Unit
l_h	0.4875	[m]
Most forward $X_{c.g.}$	0.307	[% of MAC]
Most aft $X_{c.g.}$	0.508	[% of MAC]
$X_{LEMAC} / l_{fuselage}$	0.245	[-]
Maximum Sh/S	0.32	[-]
Minimum Sh/S	0.105	[-]
Maximum tail volume V_h	0.6812	[-]
Minimum tail volume V_h	0.2235	[-]

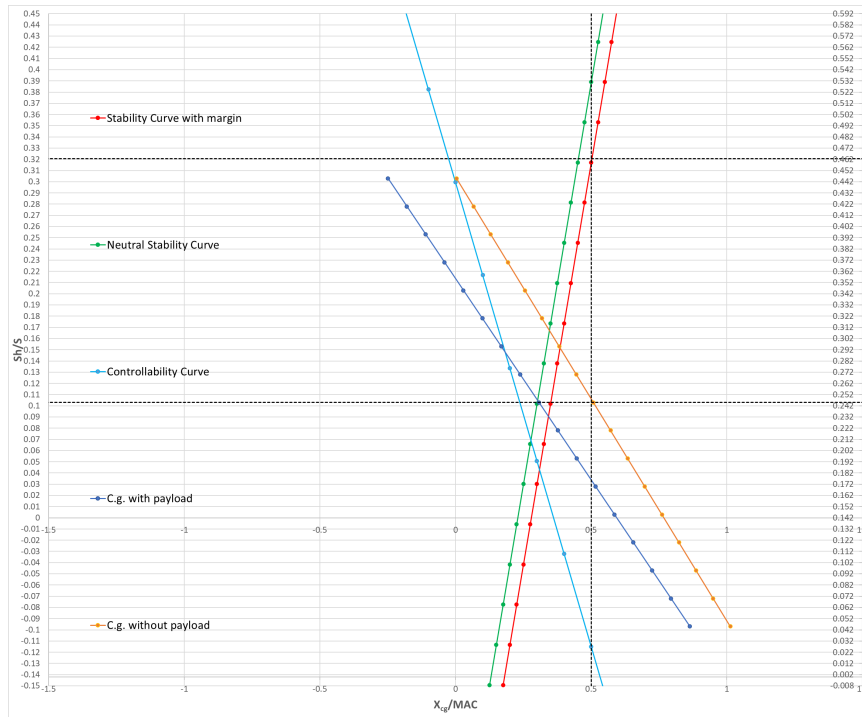


Figure 7.4: Scissor plot for final configuration

7.3. Tail Aerodynamics

Now that the rough dimensions of the tail have been found they can be modeled in OpenVSP and analyzed to verify if they behave as expected.

7.3.1. Airfoils and Fairing

For the tail, a thin plate airfoil will be used. While this would not be aerodynamically superior to a symmetric NACA airfoil for example, the thin plate does make the morphing mechanism easier to implement. To house the morphing mechanism a fairing will be used to improve the airflow over this part. Including this fairing in the OpenVSP simulation suggests that it improves the lift produced by the tail by 20%.

7.3.2. Vertical Tail & Rudder

The vertical tail was made using a NACA0010 airfoil and was modeled and positioned such that the $C_{n\beta}$ was positive. The vertical tail was positioned on the elevating and morphing surface of the horizontal tail such that the directional stability was maintained during deflections. When changing the elevator deflection the effectiveness of the vertical tail saw a large decrease since the leading edge sweep changed drastically and the tail would be positioned in the wake of the horizontal tail under some elevator states. For this reason, the area of the tail was divided between the upper and lower side of the horizontal, creating a cross tail. There was a choice to omit the rudder and allow for the combination of the differential thrust of the dual engine configuration along with the adverse roll/yaw coupling of morphing wings to actively control the yaw of the aircraft [5]. The adverse roll/yaw coupling seen in the morphing wings designed by Stanford University displayed the ability for the morphing of wings to control the roll and yaw in the situation that the drone rudder was locked such that steady-state turns were achievable [5]. Figure 7.5 demonstrates the ability of the pigeonbot to perform these steady-state turns purely through the deflection of one or both wings [5]. There have also been studies documenting the ability to achieve yaw control via differential thrust in airliners and drones. Thus it was decided that a controller would be implemented to provide the appropriate yaw authority in combination with wing morphing.

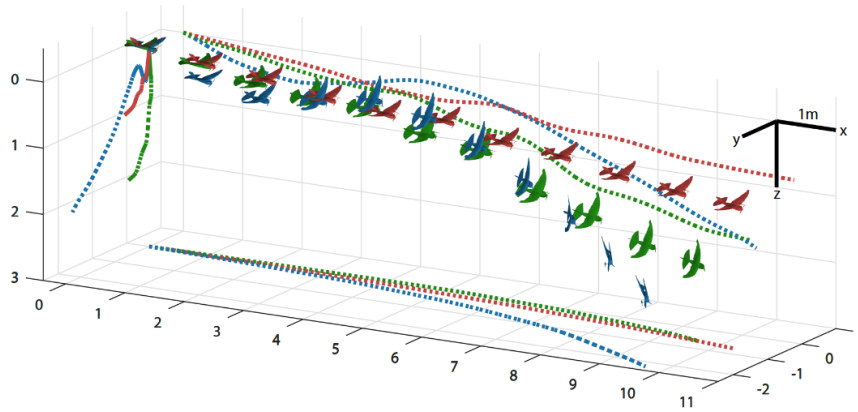


Figure 7.5: Stanford pigeon bot performing turns via wing morphing [5]

7.3.3. Lift Distribution on Tail

When morphing the tail outwards, the surface area increases, which consequently increases the lift produced by the tail. Figure 7.6 shows the lift distribution of the tail against the spanwise location for a fully extended tail and a fully retracted tail.

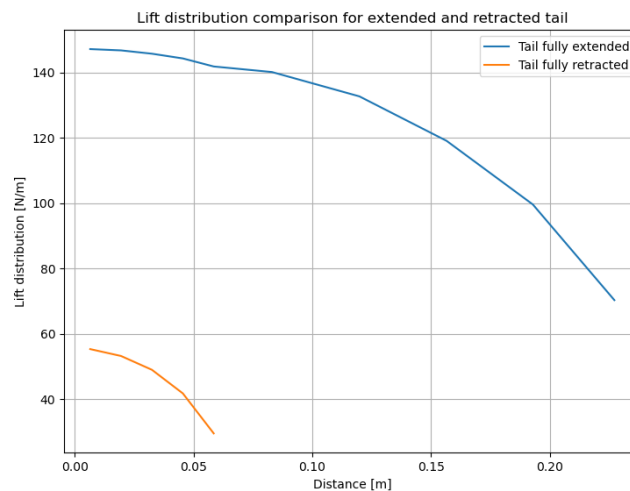


Figure 7.6: Lift distribution comparison between fully extended and fully retracted tail at $\alpha=15^\circ$

7.3.4. Effectiveness of Tail Morphing on Aerodynamics, Stability and Controllability

Morphing the tail should allow the drone to control its stability. Figure 7.7 shows the pitching moment coefficient against the angle of attack around the center of gravity for four different morphing states both with and without the payload. When carrying a payload, the drone can become unstable, and thus highly maneuverable, when morphing the wings out and the tail in. To become stable again, either the wings need to be retracted or the tail needs to be extended. The former moves the aerodynamic center of the wing back and the latter increases the lift at the tail; both increasing the negative pitching moment around the center of gravity. After ejecting the payload the center of gravity moves aft, thus making the drone unstable. During this phase, the only objective of the drone is to land for which the drone needs to be as stable as possible. Figure 7.7 shows that without payload the drone is stable when morphing the wings backward and the tail outwards. While this state is less efficient it does make the drone statically stable, unlike the other morphing states.

This analysis only considers static longitudinal stability. A detailed look at the dynamic stability can be found in Section 9.3.

7.4. Tail Morphing

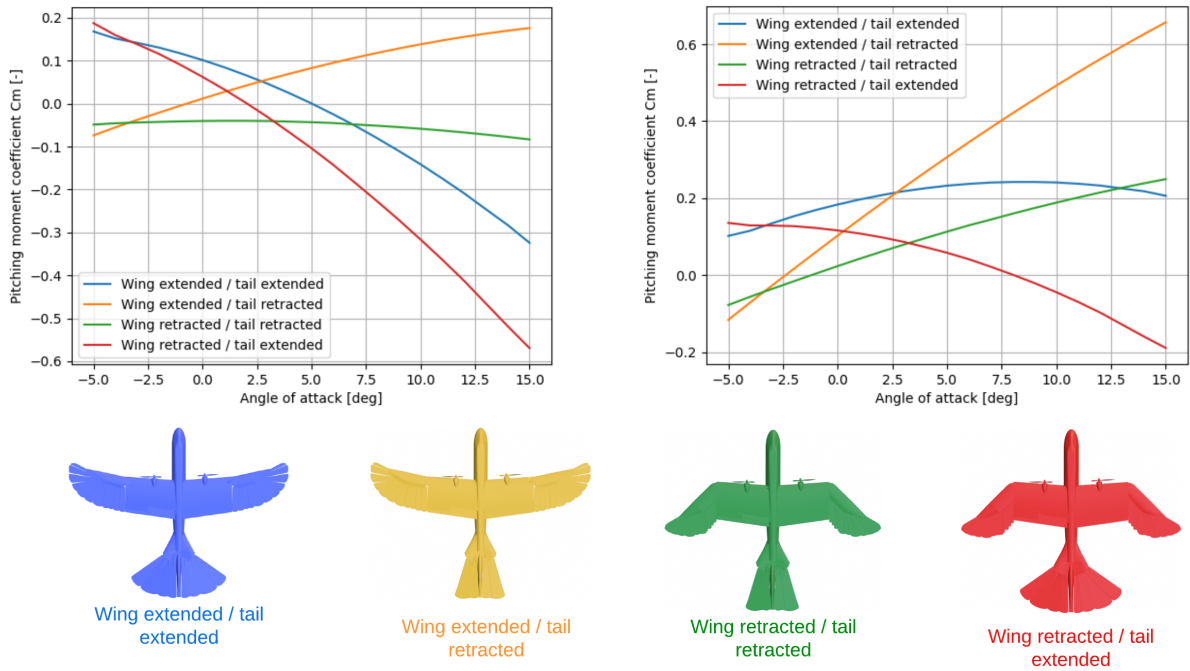


Figure 7.7: Pitching moment vs angle of attack for different morphing states with payload (left) without payload (right)

7.4. Tail Morphing

As described in Section 7.1, bio-inspired tail morphing can take on three different forms. The types of tail morphing that is implemented for the drone is surface area morphing and deflecting the tail up and down with respect to the body. These mechanisms corresponding to these morphing behaviors are described in Subsection 7.4.1 and Subsection 7.4.2 respectively. Additionally, the vertical tail is mentioned in Subsection 7.4.3, whereas the integration of the tail mechanisms with the fuselage is described in Subsection 7.4.4.

7.4.1. Surface Area Morphing

The mechanism that will allow surface area tail morphing for the drone is split up into three main parts. These are the bracket, the connection rods and the tail platelets. The connection rods can be retracted or extended. The positions are shown in Figure 7.8 and Figure 7.9 respectively.

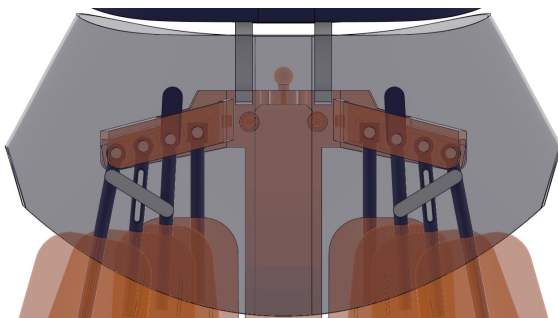


Figure 7.8: Retracted position of the tail morphing mechanism

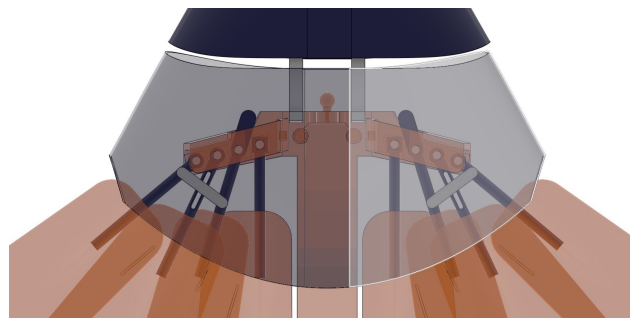


Figure 7.9: Extended position of the tail morphing mechanism

Bracket

Firstly, the bracket is the main structural component of the mechanism. It is where all the parts of the tail are combined. As can be seen in Figure 7.10,

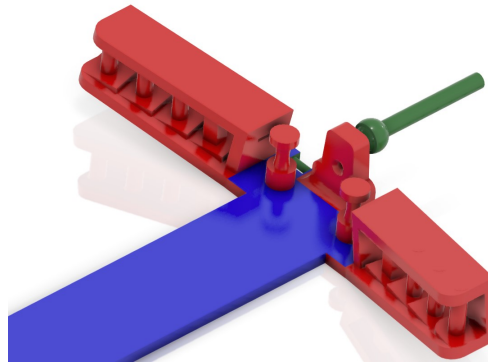


Figure 7.10: Internal structure of the tail

it is symmetrical around the nose-tail axis. The bracket is split up into 3 component groups; the surface area morphing group (red), the elevator control group (green) and the vertical tail group (blue).

The pins belonging to the surface area morphing group allow the rods and platelets to rotate along the y-axis. On the other hand, the pads below, and above the pins prevent the rods to deflect upwards or downwards.

In addition to the above, the pins are positioned above each other to prevent jamming. Due to the height difference between the rods, the platelets will be able to be retracted further without colliding. This increases the amount of morphing. Furthermore, the pins are positioned above each other instead of below, due to the tail producing negative lift the majority of the time. Due to this, the primary deflection of a platelet will be downwards, which will result in the platelets coming closer together and forming a more continuous area. For this reason, the pins are positioned vertically, thus with an angle to the pads, to allow the platelets to morph outwards horizontally.

Moreover, the distance between the pins in the x and y position, the outer platelet will be able to deflect outwards up to 60 degrees and inwards to 11.5 degrees. This results in an increase in area of at least 200%.

Connection Rods

The connection rods function as the bridge between the bracket and the lift-producing platelets. As can be seen in [Figure 7.11](#) and [Figure 7.12](#), the connection rod has a place for the pin to be inserted into.

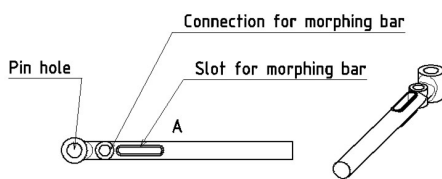


Figure 7.11: Normal connection rod

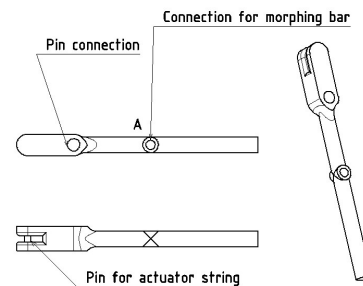


Figure 7.12: Rod that drives the morphing

In addition to this, there is room for the morphing bar to guide the connection rods during surface area morphing.

Tail Platelets

Due to the difference in the maximum morphing angle between the platelets, the platelets have to be sized differently. If this were not the case, manufacturability would increase, but the performance of the tail would decrease due to the non-continuous nature of the tail area. Therefore, the platelets are sized to minimize the area between the platelets when morphed outwards completely. The platelets in [Figure 7.13](#) are shown in order, from the most inboard platelet on the left, to the most outboard platelet on the right.

Morphing Bar

The movement of the platelets is facilitated by an actuator positioned in the fuselage. As the actuator is positioned close to the center of gravity, a connection is necessary. This is provided by a string running from the servo horn to the small hole, wrapping around the guiding rollers, and connecting to the second connection rod. By pulling the string, the connection rod is rotated outwards. The second connection rod is the only rod that is directly connected to the movement of the servo horn.

In order to morph the third and fourth platelet, a morphing bar is set up that connects these connection rods. The morphing bar is positioned in a skewed manner, to allow the platelets to morph out at different rates. This decreases the difference in platelet area. The morphing bar and its position with respect to the connection rods are shown in [Figure 7.14](#).



Figure 7.13: The 4 types of tail platelets

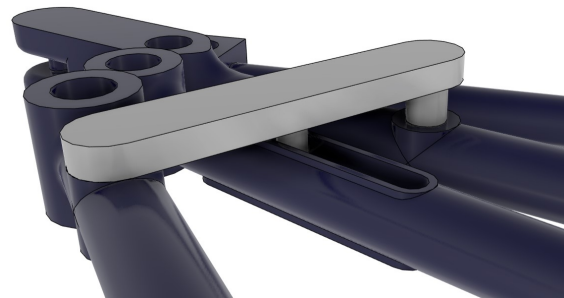


Figure 7.14: Connection of the morphing bar to the outer three tail connection rods

As can be deduced from [Figure 7.14](#), the pins connected to the morphing bar differ in height to accompany the vertical distance between the connection rods.

7.4.2. Elevator Deflection

To add to the longitudinal stability and controllability of the drone, the tail will perform elevator movement. This is done by rotating the entire tail, including all the platelets 15 degrees up or down. This is done through a system connecting the actuator to the tail bracket. The system is composed of two rods. One connects to the tail bracket and one connects to the actuator. [Figure 7.15](#) shows the rod connection to the tail bracket.



Figure 7.15: Ball and socket joint on the tail bracket for elevator deflection

The two rods are positioned to decrease the moment the actuator has to produce to be able to rotate the tail. The first rod is connected to the tail bracket via a ball-and-socket joint, to allow movement within the joint. In addition, it is connected to an axis further forward in the fuselage. The rod coming from the actuator is also connected to this axis but at 3 times the distance from the rotating axis than the rod coming from the tail bracket. As the distance is 3 times as large, the moment the actuator needs to produce is three times as small.

7.4.3. Vertical Tail

The vertical tail that is implemented on the drone is shown in [Figure 7.16](#).

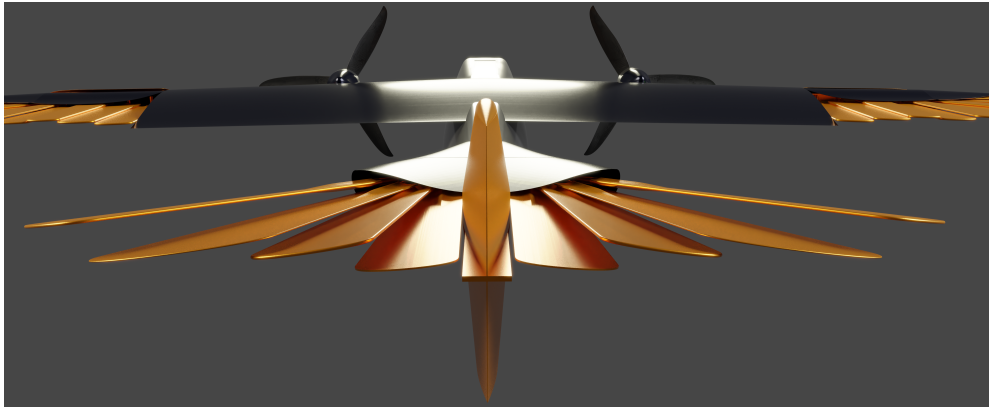


Figure 7.16: Vertical tail attachment to morphing structure

As can be seen, the vertical tail is split by the horizontal tail. The reason for this is elaborated in [7.3.2](#). The vertical tail is connected to the rest of the tail structure through the bracket. The bracket includes a beam that extends from the base pad to which the vertical tail can be mounted. However, due to the fact that the beam is rigidly connected to the bracket, the vertical tail will move with the horizontal tail.

7.4.4. Integration with the Fuselage

The tail structure interacts with the fuselage in two ways. It is rigidly connected to the internal fuselage structure and the tail fairing is connected to the fuselage skin.

Through bars rigidly connected to the fuselage frames whilst allowing the bracket to rotate when showing elevator movement. The bars transfer the loads generated by the tail platelets to the fuselage frames.

The fairing of the tail has two main functions. It shields the bracket and connection rods from the incoming flow. As these structures do not provide any positive aerodynamic contribution, the structures should be covered up. In addition, the fairing is shaped as a symmetrical airfoil. This delays the onset of stall over the platelets and directs the flow over the fuselage smoothly to the tail. Furthermore, the fairing is shaped such that it performs similarly to a dorsal fin. This, together with the symmetrical nature of the fairing delays stall even more.

7.4.5. Actuation of the Tail

To ensure proper functioning of the tail mechanism, the loads on the actuator have been estimated using the aerodynamic drag along the chord of the wing for surface area morphing and perpendicular to the chord for the elevator deflection. The flight condition where the UAV pulls out of its 67.5 m/s dive is where it has to be able to morph its tail and deflect the elevator. This was identified as the most critical condition for the actuator loads. The aerodynamic forces acting on tail platelets were used to determine the force necessary to hold the mechanism in the most critical position. The required force for the surface area morphing is 84.48 N and 769.04 N. As described in [7.4.2](#), the force on the actuator will be downsized 3 times, resulting in an actuator force of 256.35 N.

From the above-mentioned forces and the additional arguments for actuation speed, longevity and a safety factor, the actuator was chosen to be the Savox SC-1257TG servo with a 1 cm actuator arm, since this meets the requirements for both the actuation force, as described before, and the required longevity of this actuator as it uses very wear-resistant titanium gears. It provides an actuation speed of around 3.33 rad/s, based on the datasheet provided by the manufacturer, under the critical loading condition.

7.5. Structures

As for the morphing of the wing, the platelets of the horizontal stabilizer are mounted on a spar, in this case called the tail morphing spar. As the loads for the tail are lower than for the wing, this spar is simply a C-spar with indentations in the horizontal flanges to mount the platelets. The idealization used for this component is shown in Figure 7.17:

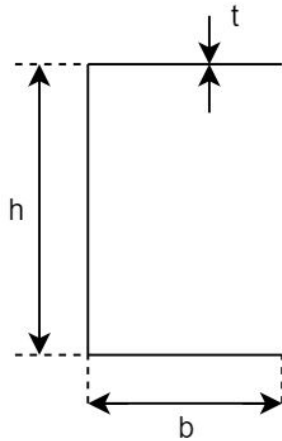


Figure 7.17: Sketch of the cross section of the tail morphing spar

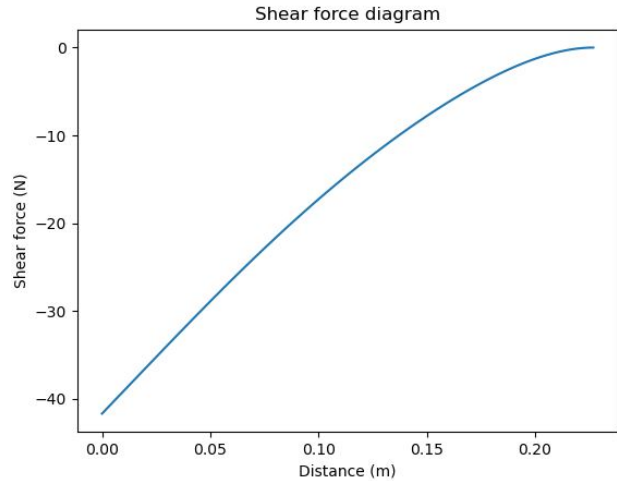


Figure 7.18: Shear force diagram for the horizontal tail as a function of spanwise location

The shear force, moment and torsion diagrams shown in Figure 7.18, Figure 7.19 and Figure 7.20 respectively, correspond to the lift distribution shown in Figure 7.6, for the fully extended tail. This lift distribution is for the critical flight condition, which is when the loads are highest, the tail platelets being extended. All three diagrams are typical results from the lift distribution over a lifting surface.

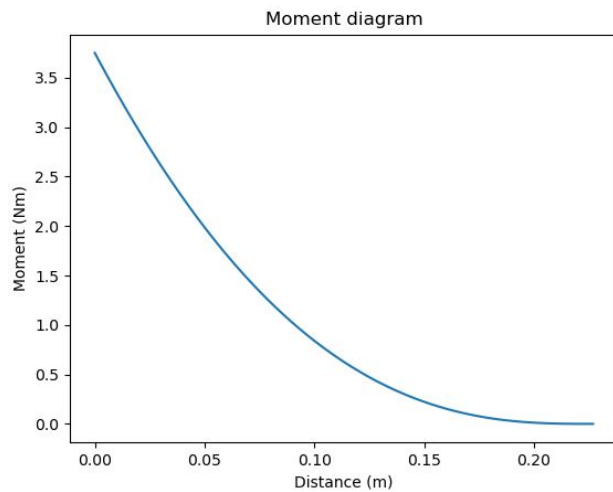


Figure 7.19: Moment diagram for the horizontal tail as a function of spanwise location

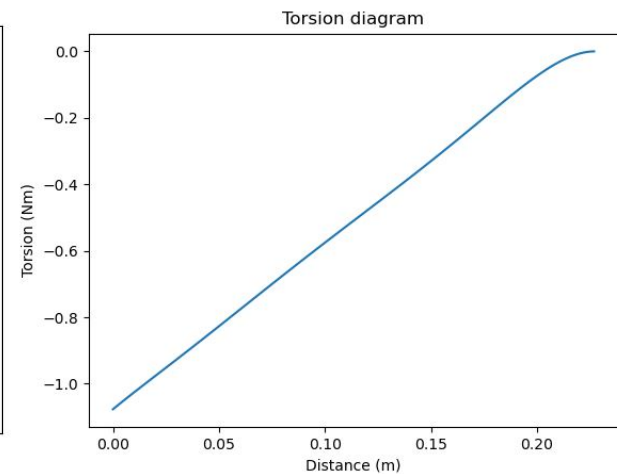


Figure 7.20: Torsion diagram for the horizontal tail as a function of spanwise location

For the structural analysis of the tail morphing spar, the section at the root was considered critical as there the loads are highest. The magnitude of the highest loads was identified, then multiplied by a safety factor of 1.5.

Again, the code constructed took as input the geometry and the loads and gave as an output the highest stresses present. As for the morphing spar for the wing, loads in the horizontal plane and M_y moments were not taken into account as they were considered negligible in relation to the other ones.

First, the shear center and moment of inertia of the section were calculated. As this is an open section structure,

Equation 6.8 could be straightforwardly used to find the shear stress at each point in the section. Due to the fact that the platelets of the horizontal tail are relatively long, the extra torque due to the shear force not being applied in the shear center must be taken into account. Thus, considering the lift acting at 25% of the chord, the term $V_y \cdot (0.25c + \zeta)$ must be added to the torque, where c is the chord length and ζ is the location of the shear center. ζ is added to the distance as the shear center is located to the left of the cross-section as seen in Figure 7.17.

Then, to compute the maximum shear stress due to torsion, Equation 7.8 is used:

$$\tau_{\max} = \frac{3T}{st^2} \quad (7.8)$$

Where s is the 'length' of the cross section, $2b + h$. Then, as done previously, the shear stresses are added up, then divided by thickness to find the maximum shear stress.

Considering the bending, Equation 6.10 is used to find the maximum normal stress, which is at the top and bottom flange, as the distance from the neutral axis is highest there.

A tail morphing spar geometry already existed as it was used to construct the morphing mechanism. After applying the loads to this structure, the maximum shear stress was 22 MPa and the maximum normal stress was 4 MPa. Considering these values of stress, Aluminum Al6013t6 was chosen as a suitable material because of its good mechanical properties, combined with low density and the fact that it is a mature technology in the aerospace industry.

7.5.1. Joints

The joints in the morphing mechanism of the tail need in detail analysis as they represent concentration points for the loads.

Connection between rods and platelets

The loads generated by the platelets are transferred through the connection rods to the tail bracket. This means that the connection rods and platelets will be subjected to a shear force and bending moment. To size the platelets, the bending moment has been determined for the outermost platelet, as this has been found to be under the highest loading. As a result, the root of the platelet is 575 MPa when the platelet is 1 mm thick and 40 mm wide. Due to this loading, the platelets will be constructed out of the Nematx material.

For the loading in the connection rods, the shear stress and bending stress created by the critical platelet are used. This came down to 312 MPa bending stress and 1.5 MPa shear stress. This means that also for the connection rods, the Nematx material paired with a diameter of 5 mm and 2.5 mm long rod is sufficient.

Connection between platelets and morphing spar for the tail

The connection rod between the platelets and spar is subject to a bending moment. The same approach as in Figure 6.5.5 is taken. Considering the moment at the platelet root (multiplied with a safety factor of 1.5) equal to 3 Nm, which is for the highest loading platelet, results in a maximum normal stress of 26 MPa, well below aluminum's capabilities.

8. Propulsion Design

In this chapter, the design for the propulsion system is discussed. Firstly, the requirements and the compliance of the design with respect to those are shown in [Section 8.1](#), secondly the propulsion system design process including the influence of forward flight velocity on the performance of the system and the interaction with the wing are given in [Subsection 8.2.1](#) and [Section 8.3](#).

8.1. Requirements

In this section, the relevant requirements for the propulsion system are given in [Table 8.1](#), with the compliance of our design added.

Table 8.1: Requirements on the UAV propulsion system

Identifier	Requirement	Verification Method	Compliance
REQ-UAV-PERF-012	The UAV shall have a maximum climb rate of at least 12 m/s	Demonstration	✓
REQ-UAV-PERF-013	The UAV shall have a maximum operating speed of 45 m/s	Demonstration	✓
REQ-UAV-SUS-003	The UAV shall be 100% electrically powered	Inspection	✓

8.2. Propulsion System Design Process

In addition to the requirements mentioned in [Table 8.1](#), the following considerations also had to be taken into account whilst designing the propulsion system :

- The efficiency of the propulsive system for the flight conditions encountered during the UAV's mission
- How and where the propulsion system will be integrated within the UAV
- The effect of the propulsion system on the UAV's overall maneuverability during flight

Two main design options were found as described in [Section 3.5](#).

It is important to note that for the single engine design the motor would be mounted more centrally within the fuselage to prevent interference with the tail morphing mechanism and to keep the center of gravity of the UAV more centralized, which also limits the cg shift. This also means that the motor and the propeller would be connected via a shaft running through the fuselage, which could limit the degree in which the tail is able to move. To choose the optimal design, their performance is analyzed as discussed in the following sections.

8.2.1. Influence of Forward Flight on Propeller Efficiency

When examining the performance of a propeller-based propulsion system, the thrust and power efficiency need to be analyzed not only for static conditions, but also for the full range of flow velocity encountered during the mission. As explained by [Garnaer](#), the thrust coefficient is directly related to the advance ratio (J), which is dependent on the revolutions per second (n), diameter (D), and velocity (V), as shown by [Equation 8.1](#), with the inputs being in imperial units [38]. The graph showing the relation between C_t and J , with the pitch of the blade over the diameter (p/D) as a parameter, is given in [Figure 8.1](#). In this graph, it can be seen that the maximum C_t is achieved when $J = 0$. However, as J approaches 0, the portion of the blade affected by stall will increase, and the amount of the blade that is affected by this increases with a higher p/D ratio, making the graph in that region inaccurate [38]. The thrust is then given by [Equation 8.2](#) with inputs being C_t , the density (ρ), given in slugs per feet cubed, revolutions per second (n), and D , given in feet. The power coefficient C_p and the effective power are given in [Figure 8.2](#) and [Equation 8.3](#). Using the advance ratio and the thrust and power coefficients, the power efficiency of the propeller can be calculated from [Equation 8.4](#) as described by [Garnaer](#) [38]. With this efficiency, one can calculate the shaft power needed by simply dividing the power from [Equation 8.3](#) with the aforementioned efficiency.

$$J = \frac{V}{n \cdot D} \quad (8.1)$$

$$T = C_t \cdot \rho \cdot n^2 \cdot D^4 \quad (8.2)$$

$$P_s = \frac{C_p \cdot \rho \cdot n^3 \cdot D^5}{550} \quad (8.3)$$

$$\text{Eff} = \frac{J \cdot C_t}{C_p} \quad (8.4)$$

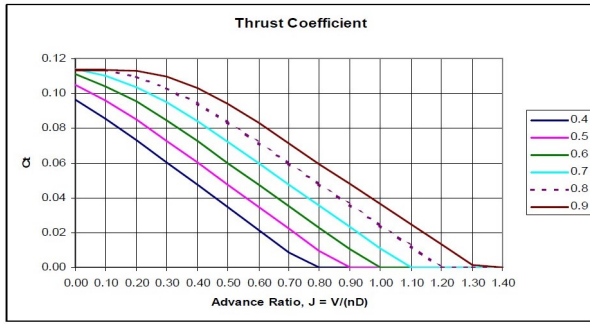


Figure 8.1: Thrust coefficient versus advance ratio, p/D a parameter [38]

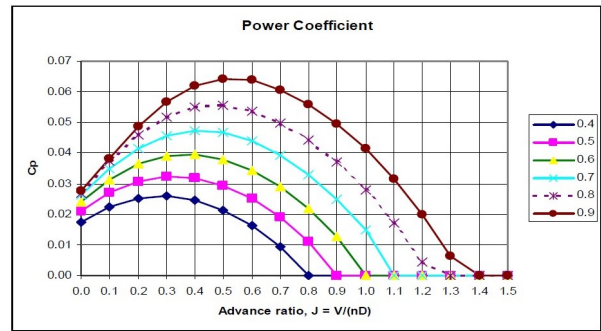


Figure 8.2: Power coefficient versus advance ratio, p/D a parameter [38]

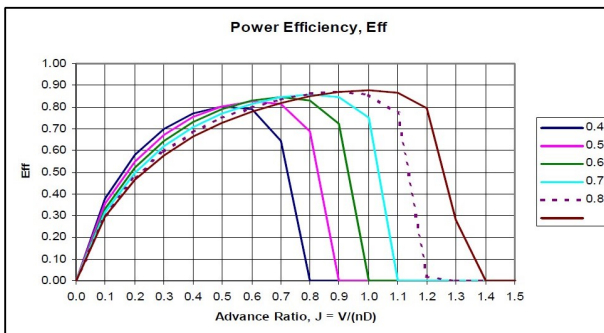


Figure 8.3: Power efficiency coefficient as a function of J and p/D a parameter [38]

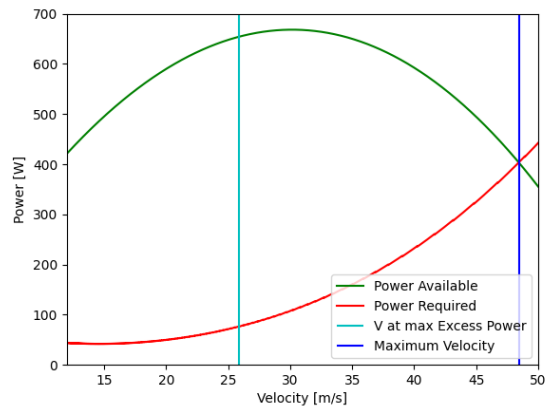


Figure 8.4: Power available and power required during horizontal flight

When comparing the single large diameter propeller with two smaller propellers such that they achieve the same maximum total static thrust, it can be seen that the single-engine and propeller combination would require an unrealistic rpm for the engine since this type of engine is not able to be fit within the fuselage. This, in combination with the interference the shaft causes with the morphing tail, led to the single-engine option being ruled out. Therefore, the dual-engine design was pursued instead and sized to meet the requirements, as described in Subsection 8.2.2 and Chapter 10.

8.2.2. Engine and Propeller Selection

Using the methods described in Chapter 10 and the parameters such as thrust, power and efficiency calculated using the methods described in Subsection 8.2.1, the engines were selected to be the T-motor F100¹ with the Gemfan GF7040 propeller². The efficiency was calculated for the operational flight velocities such that the thrust equals the drag and is visualized in Figure 8.6. Here, it can be seen that the propeller efficiency during steady straight flight is almost constant, with a value of around 0.85. The efficiency of the propellers when operating at maximum thrust is not constant, as can be seen in Figure 8.5. It does however increase with increasing flight velocity with an upper limit when the angle of attack of the blades becomes close to or equal to zero. Combining the information found on the drag with respect to velocity from aerodynamic analysis as described in Section 6.3 with the power calculated from Subsection 8.2.1, Figure 8.4 can be generated. The velocity for which the power available minus the power required is maximum is indicated by the line drawn in cyan, which is 25.89 m/s, this velocity can be used to get the maximum rate of climb which is calculated in Chapter 10, the dark blue vertical line indicates the point where the excess power becomes zero indicating the maximum flight velocity possible,

¹<https://store.tmotor.com/goods.php?id=1177&from=rss> [Accessed: June 21, 2022]

²<https://www.team-blacksheep.com/products/product:3786> [accessed: June 21, 2022]

which is 48.43m/s. It is important to note that in this case the power available, as seen in Figure 8.4 cannot be assumed to be constant, which can probably be attributed to the combination of an electrical engine without a gearbox, and a fixed-pitch propeller being used. This assumption is normally used for propeller aircraft, to find the speed at which the maximum climb rate can be achieved, resulting in the speed for maximum lift over drag for a propeller aircraft [24]. As the power available is not constant, this results in a different velocity for the maximum rate of climb.

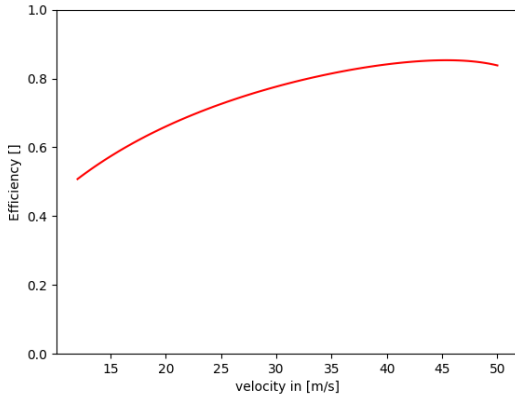


Figure 8.5: Propeller efficiency at maximum RPM

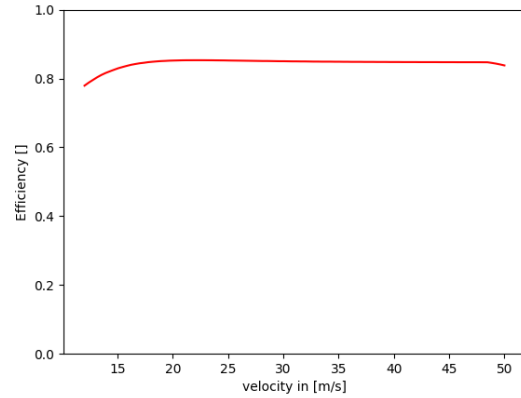


Figure 8.6: Propeller efficiency at thrust equals drag

8.3. Propeller Influence on Lift

When propellers are attached in front of the wing, they cause a change in the airflow going over a section of the wing. The two most notable effects are the swirl created by the rotation of the flow, and the increased airflow velocity also known as the jet effect. The swirl effect is caused by the rotation of the propellers, which cause upwash on one side of the wing and a downwash on the other. Since the propellers rotate in the direction such that the upwash is on the inboard side, the lift locally increases inboard of the propellers and decreases outboard of the propellers. The jet effect is caused by the fact that propellers function by having a larger exit velocity than inlet velocity and thus the wing sees an increase in velocity, which locally increases the lift. In addition, this will also keep the air attached to the wing at higher angles of attack, potentially delaying stall [R. T. Johnson and Sullivan](#).

As described by [R. T. Johnson and Sullivan](#), the combination of the jet and swirl effect can increase the effective lift by up to 30%. Preliminary experiments performed in OpenVSP ([Figure 8.7](#)) show a similar trend as can be seen in [Table 8.2](#) where an increase of 20% was found at low angles of attack. At higher angles of attack, the increase in lift is also followed by an increase in drag, so the effective L/D decreases.

Since the results from these simulations are heavily dependent on the flight conditions, model accuracy and meshing, the increase in lift and drag will not be accounted for in the performance analysis. Instead, a more qualitative approach is taken, and it is assumed that the propellers will have an advantageous effect on the performance.

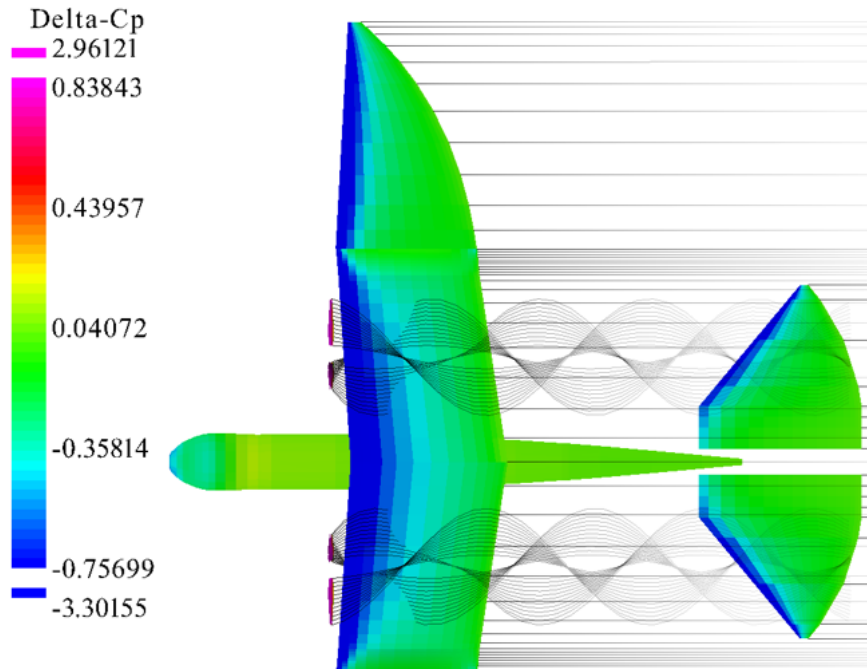


Figure 8.7: Pressures due to propeller influence for an angle of attack of 10 degrees computed by openVSP.

Table 8.2: Changes in C_L and C_D due to propeller effects

Condition	α	C_L	C_D
No Propeller	0	0.14	0.04
No Propeller	10	1.36	0.11
With Propeller	0	0.17	0.04
With Propeller	10	1.64	0.15

9. Flight Dynamics

This chapter describes the development and implementation of a flight dynamics model for the Air-Guard UAV. Such a model is required for performing multiple design actions: verifying maneuverability requirements, verifying stability requirements and designing a flight controller. The model was designed iteratively, starting with a simple model and increasing the accuracy as time passed. First, a linear model was created, then a more precise non-linear model was required, as the wing and tail morphing introduce non-linear behaviour.

First, the development of the linear model is discussed in [Section 9.1](#). The development of the non-linear model will then be discussed in [Section 9.2](#) and the results of the dynamic analysis is given in [Section 9.3](#). The controller design is discussed in [Section 9.4](#) and finally, recommendations for the model are presented in [Section 9.5](#).

9.1. Linear Flight Dynamics Model

First, a linear model was developed using Python to assess preliminary stability characteristics. This model assumed the conventional linearized equations of motion as described by [Mulder et al.](#). This model was then verified using the data and results for the Cessna Citation I. [\[40\]](#)

When applying the model to the morphing UAV, aerodynamic data from OpenVSP could be used for the stability derivatives in a certain flight condition. For the control derivatives however, an estimate needed to be made. This is where the linear model has its boundaries: the stability derivatives of the UAV change when the wings are morphed. Additionally, the control derivatives of the morphing parts are also influenced by the degree of morphing and can also not be assumed constant. The coupling of stability derivatives and morphing makes the linear model an inaccurate representation of the UAV.

9.2. Non-linear Flight Dynamics Model

This section describes the development of the non-linear flight dynamics model, which will simulate the UAV dynamics with greater accuracy. First the reference frames used throughout the model are discussed in [Subsection 9.2.1](#). Then, the equations governing the dynamics and kinematics of the model are introduced in [Subsection 9.2.2](#). Next, in [Subsection 9.2.3](#), the main assumptions are covered and their implications are discussed. Then, it is explained how the forces and moments on the UAV are obtained ([Subsection 9.2.4](#)) and implemented ([Subsection 9.2.5](#)). Finally, the structure of the final model is shown in [Subsection 9.2.6](#).

9.2.1. Reference Frames

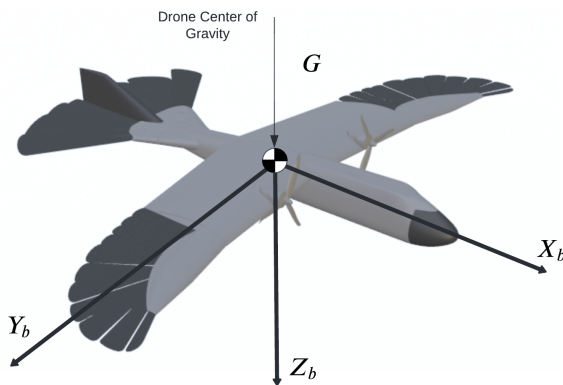


Figure 9.1: Definition of the UAV's body frame

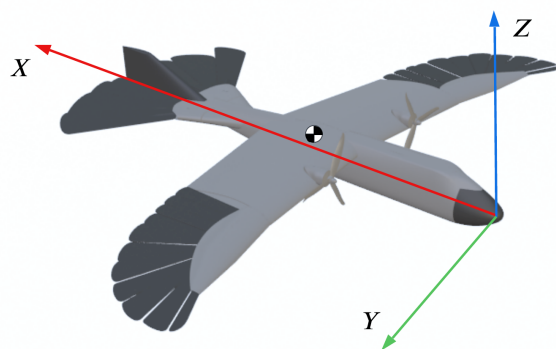


Figure 9.2: Definition of OpenVSP's body frame

The equations of motion ([9.4](#) to [9.6](#)) are expressed in the UAV's body frame, which can be seen in [Figure 9.1](#). However, to find the external forces and moments it is often easier to derive them in different reference frames and later express them in the UAV's body frame. This holds for the external aerodynamic forces and moments and the gravity force.

To retrieve the aerodynamics forces and moments the aerodynamic software *OpenVSP* is used. In contrast to more

conventional reference frames as used in [40], OpenVSP has its own definitions for its stability and body frame which can be seen in Figure 9.2. To express these forces and moments, they are transformed from the OpenVSP stability frame to their body frame and lastly to the UAV's body frame. This is done using the transformation matrix in Equation 9.1, where the first matrix has been derived from openVSP¹.

$$\mathbb{T}_{bVA} = \begin{bmatrix} \cos(\pi) & 0 & -\sin(\pi) \\ 0 & 1 & 0 \\ \sin(\pi) & 0 & \cos(\pi) \end{bmatrix} \cdot \begin{bmatrix} -\sin(\alpha) & 0 & \cos(\alpha) \\ \cos(\alpha)\cos(\beta) & -\sin(\beta) & \sin(\alpha)\cos(\beta) \\ \cos(\alpha)\sin(\beta) & \cos(\beta) & \sin(\alpha)\sin(\beta) \end{bmatrix}^{-1} \quad (9.1)$$

Here, the subscript b indicates the UAV's body frame, while VA indicates OpenVSP's stability frame. The aerodynamic moments on the other hand are defined differently² and are readily available in the UAV's body frame, requiring no further transformation. The gravity force is defined in the inertial, vehicle-carried frame and then expressed in the UAV's body frame. This re-expression is performed using Equation 9.2.

$$\mathbb{T}_{bE} = \begin{bmatrix} -\sin\theta \\ \sin\varphi\cos\theta \\ \cos\varphi\cos\theta \end{bmatrix} \quad (9.2)$$

Lastly, a transformation from the vehicle body reference frame to the earth reference frame is needed to determine the UAV's north position, east position and height. This transformation can be seen in Equation 9.3:

$$\mathbb{T}_{Eb} = \begin{bmatrix} \cos(\psi) & \sin(\psi) & 0 \\ -\sin(\psi) & \cos(\psi) & 0 \\ 0 & 0 & 1 \end{bmatrix} \begin{bmatrix} \cos(\theta) & 0 & -\sin(\theta) \\ 0 & 1 & 0 \\ \sin(\theta) & 0 & \cos(\theta) \end{bmatrix} \begin{bmatrix} 1 & 0 & 0 \\ 0 & \cos(\phi) & \sin(\phi) \\ 0 & -\sin(\phi) & \cos(\phi) \end{bmatrix} \quad (9.3)$$

9.2.2. Equations of Motion

The governing equations of the flight dynamics model assume a simplified form and are taken from [40]. The dynamic vector equations can be seen in Equation 9.4 and Equation 9.5, while the kinematic vector equation is given in Equation 9.6. The navigation equation which expresses the motion of the UAV in the earth-fixed reference frame is given in Equation 9.7.

$$\left. \frac{d\mathbf{V}}{dt} \right|_b = \frac{1}{m} (\mathbf{F}_{ext}^b) - \boldsymbol{\Omega}_{bE}^b \times \mathbf{V}_E^b \quad (9.4)$$

$$\left. \frac{d\boldsymbol{\Omega}_{bE}^b}{dt} \right|_b = \mathbf{I}^{-1} \left(\mathbf{M}_{ext}^b - \boldsymbol{\Omega}_{bE}^b \times (\mathbf{I} \cdot \boldsymbol{\Omega}_{bE}^b) \right) \quad (9.5)$$

$$\begin{bmatrix} \dot{\phi} & \dot{\theta} & \dot{\psi} \end{bmatrix}^T = \begin{bmatrix} 1 & \sin(\theta)\tan(\theta) & \cos(\phi)\tan(\theta) \\ 0 & \cos(\phi) & -\sin(\phi) \\ 0 & \frac{\sin(\phi)}{\cos(\theta)} & \frac{\cos(\phi)}{\cos(\theta)} \end{bmatrix} \begin{bmatrix} \phi & \theta & \psi \end{bmatrix}^T \quad (9.6)$$

$$\left. \frac{d\mathbf{X}}{dt} \right|_E = \mathbb{T}_{Eb} \cdot \mathbf{V}_b \quad (9.7)$$

Here, \mathbf{V}_E^b and $\boldsymbol{\Omega}_{bE}^b$ are the aircraft's translational and rotational velocity vectors in the vehicle carried frame expressed in the body frame. Similarly, \mathbf{V}_b^b and $\boldsymbol{\Omega}_b^b$ are the aircraft's translational and rotational velocity vectors in the body frame expressed in the body frame. Next, \mathbf{F}_{ext}^b and \mathbf{M}_{ext}^b are the external force and vectors, respectively, expressed in the body frame. Then, ϕ , θ and ψ are the aircraft's roll, pitch and heading angles respectively. Lastly, m and I are the aircraft's mass and moment of inertia tensor, respectively.

¹<https://groups.google.com/g/openvsp/c/Pb93zCFufJA/m/f5587bROBAAJ> [Accessed: 15/06/2022]

²<https://groups.google.com/g/openvsp/c/Pb93zCFufJA/m/f5587bROBAAJ> [Accessed: 15/06/2022]

Equations 9.4 to 9.7 describe the motion of the UAV over time, once the external forces, moments, mass and inertia tensor of the UAV are provided. With these equations, the dynamics of the UAV can be described as in Equation 9.8, where \mathbf{x} are the states and \mathbf{u} the control inputs, as defined in Equation 9.9.

$$\dot{\mathbf{x}} = f(\mathbf{x}, \mathbf{u}) \quad (9.8)$$

$$\mathbf{x} = [u \ v \ w \ p \ q \ r \ \phi \ \theta \ \psi \ x_N \ x_E \ h]^T, \quad \mathbf{u} = [\delta_{m_\ell} \ \delta_{m_r} \ \delta_{m_t} \ \delta_t \ \delta_{e_\ell} \ \delta_{e_r}]^T \quad (9.9)$$

9.2.3. Assumptions of Equations of Motion

Equations 9.4 to 9.7 have been simplified due to the following assumptions:

1. The vehicle mass does not change
2. The Earth is flat and non-rotating
3. The effect of rotating masses may be neglected
4. The vehicle is a rigid body
5. The moment of inertia of the vehicle does not change
6. I_{XY} and I_{YZ} as computed in the body frame are zero

The first assumption is a valid assumption as the flight simulation is performed either before or after ejecting the payload. Hence the vehicle mass does not change during the simulation and stays at a constant value of 3.75 kg when the payload is not ejected, as mentioned in Section 10.1. However, if the payload ejection would be simulated, either the equations of motion (EOM) have to be altered or a sensitivity analysis has to be performed to assess the error.

Similarly, the second assumption is deemed to be valid because of the short simulation time, short distances travelled during the simulation and by the vehicle having a higher rotational rate than the Earth. As a consequence of this assumption the vehicle carried frame is assumed to be an inertial reference frame [40] and the EOM are expressed in the vehicle's body frame.

In terms of the third assumption, the main rotating masses are propellers which might cause gyroscopic effects and thus alter the UAV dynamics. Given the low mass of the propellers (15.8 grams for both) this effect is neglected. However, because of their high maximum rotational velocity of 20433 RPM it is worth investigating these effects in the next design phase.

Only the validity of the last three assumptions are questionable for the simulator's application, because the UAV (asymmetrically) morphs itself for control during the simulation. The morphing may induce several aero-elastic effects, negating the fourth assumption. Modeling these effects would significantly increase the complexity of the model, hence to create a preliminary flight dynamic model within the given time span these effects were assumed to be negligible. Still, it is believed that this assumption could have a non-negligible impact and its effects ought to be investigated and modelled in the next design phase.

The last two assumptions may cause errors in the simulations and lead to more conservative performance estimates. The inertia tensors for three different morphing states were computed in CATIA. These configurations include the payload, a neutral tail deflection and a fully morphed tail (40°), but are calculated for 3 different wing morphing states. The 3 wing morphing states were both wings fully deflected (0°), left wing fully deflected but right wing fully retracted (50°) and both wings fully retracted. Compared to the fully deflected state, the single tucked wing had a 14.5% smaller I_{XX} and a 8.2% smaller I_{ZZ} , while I_{YY} increased with a negligible amount. In terms of the fully retracted state, I_{XX} reduced with 28.9%, I_{ZZ} with 16.7% and I_{YY} again increased negligibly compared to the fully extended state. These changes in moment of inertia are non-negligible and starkly contrast the assumptions of the EOM, leading to reduced accuracy in the model's prediction. The main effect is likely to be witnessed in terms of the roll and turn performance, as only the largest value of I_{XX} will be used in the program.

9.2.4. Obtaining Forces and Moments Acting on the Body

With the mass and inertia tensor discussed in [Subsection 9.2.3](#), the remaining unknowns in the equations of motion are the external forces and moments expressed in the body frame. Three sources of external forces and moments are assumed to act on the vehicle: propulsive, gravitational and aerodynamic. To quantify these forces and implement them in the simulation, independent models have been created which will be further discussed.

Engine Model

Using the methods described in [Chapter 8](#), a thrust calculator was made such that the thrust could be calculated with the air density, the engine RPM setting and the flight velocity as inputs. The engine RPM setting is the input the flight controller gives to control the engine thrust, and the density and airspeed are inputs from onboard sensors. Using this model, the engine RPM can be controlled by the flight controller to achieve the desired thrust. This propulsive force is assumed to act at the tip of the propellers.

Next, the moments created by the engine thrust are found by taking the cross product between the distance vector from the UAV center of gravity to the propeller tips and the thrust force. Since both the forces and moments are computed in the UAV's body reference frame, no further transformation is necessary.

Gravity Model

A flat earth gravity model has been assumed with a constant gravitational acceleration g of 9.81 m/s. The gravity force expressed in the UAV's body frame is calculated using [Equation 9.10](#), where \mathbb{T}_{bE} denotes a vector instead of a transformation matrix as can be seen in [Equation 9.2](#).

$$\mathbf{F}_g^b = m \cdot g \cdot \mathbb{T}_{bE} \cdot [1 \ 1 \ 1]^T \quad (9.10)$$

Aerodynamic Model

The aerodynamic coefficient vectors are expressed in OpenVSP's stability frame and are obtained through steady aerodynamic analysis. To prevent additional calculations within the simulator S and c have been set equal to 1 within OpenVSP, as they would otherwise depend on the morphing configuration. Each aerodynamic coefficient is assumed to be the sum of a base value and its partial derivatives multiplied with its respective state.

To dimensionalize the aerodynamic coefficients, the conventions mentioned in [\[40\]](#) have been adopted. As an example, the dimensionalization of the lift force is shown. First the coefficients relevant to the lift are partly dimensionalized as can be seen in [Equation 9.11](#):

$$\frac{dL}{d\beta} = C_{L\beta} \cdot \frac{1}{2} \cdot \rho \cdot V \cdot S \quad (9.11)$$

Then the lift force can be obtained using [Equation 9.12](#):

$$L = \frac{dL}{d\beta} \cdot |\beta| + \frac{dL}{dq} \cdot q + L_0 \quad (9.12)$$

Lastly, the force is transformed to the UAV's body frame by vector-matrix multiplication with \mathbb{T}_{bVA} .

Some stability derivatives, such as $C_{L\beta}$, do not show linear behaviour. This is caused by coupling of symmetric and asymmetric motions and the positive definition of side-slip. The lift coefficient here is assumed to change with the absolute value of the side-slip angle, as positive and negative side-lip angles have the same effect on lift.

A qualitative analysis was done to determine which stability derivatives were of influence on the force and moment coefficients. This analysis also takes into account the effects of morphing. The calculations for the force and moment coefficients can be seen in [Equation 9.13](#) and [Equation 9.14](#).

$$\begin{bmatrix} D \\ S \\ L \end{bmatrix} = \begin{bmatrix} D_0 \\ S_0 \\ L_0 \end{bmatrix} + \begin{bmatrix} \frac{dD}{d\beta} & 0 & 0 & 0 \\ \frac{dS}{d\beta} & 0 & 0 & \frac{dS}{dr} \\ \frac{dL}{d\beta} & 0 & \frac{dL}{dq} & 0 \end{bmatrix} \begin{bmatrix} \beta \\ p \\ q \\ r \end{bmatrix} \quad (9.13)$$

$$\begin{bmatrix} \ell \\ m \\ n \end{bmatrix} = \begin{bmatrix} \ell_0 \\ m_0 \\ n_0 \end{bmatrix} + \begin{bmatrix} \frac{d\ell}{d\beta} & \frac{d\ell}{dp} & 0 & \frac{d\ell}{dr} \\ 0 & 0 & \frac{dm}{dq} & 0 \\ \frac{dn}{d\beta} & \frac{dn}{dp} & 0 & \frac{dn}{dr} \end{bmatrix} \begin{bmatrix} \beta \\ p \\ q \\ r \end{bmatrix} \quad (9.14)$$

One might notice that there are no dependencies on angle of attack included in the aerodynamic coefficients. This is because the effects of angle of attack is already included in the base value of the coefficients, as the coefficients are obtained from CFD analysis for multiple angles of attack. The aerodynamic model also includes four control inputs: left and right wing morph, tail morph and tail deflection. When these surfaces actuate, the base values of the aerodynamic coefficients change. For example, morphing the right wing inwards will result in a positive C_{ℓ_0} coefficient. The effect of morphing on these coefficients can be seen in [Subsection 9.3.1](#). The other two control inputs, left and right engine throttle, are included in the engine model.

9.2.5. Implementation of Forces and Moments in the Simulator

The aerodynamic derivatives that are needed to calculate the forces and moments in the flight dynamics are computed using OpenVSP (more detail on OpenVSP can be found in [Section 6.3](#)). However, since morphing changes the values of the aerodynamic derivatives, one simulation was not sufficient. For this reason, a Python script was created that uses the OpenVSP API to automate the simulations. This script imports the drone model made in OpenVSP, adds the geometries from OpenVSP to a dictionary and simulates all of the possible combinations.

The UAV could be morphed in four different ways: left wing morphing, right wing morphing, tail morphing and tail rotation. The wings could morph between a minimum sweep of -10° and 50° , while the tail could do so between 0° and 40° . Tail rotation is similar to an elevator deflection, except that the entire tail now rotates between -15° and 15° .

For the initial runs, only the most extreme states were used (2 left wing, 2 right wing, 2 tail size, 3 elevator positions, 3 angles of attack) and the resolution was then increased once the model was finalized (4 left wing, 4 right wing, 3 tail size, 3 elevator position, 5 angles of attack). The wing deflections were: -10° , 0° , 25° and 50° , while the tail morphed between 0° , 20° and 40° . Lastly, the tail rotated between -15° , 0° , 15° .

After unpacking the aerodynamic data in Matlab, several N-D lookup tables were created for the coefficients. These lookup tables inherently perform a curve fitting between the data points for all dimensions. For simplicity, the fitting method was selected to be cubic splines as this still allowed for binary search trees, which reduces computation time.

With all the forces and moments now known, the resultant aerodynamic force \mathbf{F}_{ext}^b and moment \mathbf{M}_{ext}^b can be computed by simply summing the gravity, aerodynamic and propulsive contributions expressed in the body frame.

Finally, all unknowns are defined and the non-linear model can be set up and solved for using initial conditions for the states and the controls.

9.2.6. Resulting Model

Using Simulink, a model was created that takes the initial states and controls as input and outputs the derivatives and new states as a function of time. The block diagram of the model can be seen in [Figure 9.3](#).

The equations of motion block in the diagram have as inputs the state, control actuation and aerodynamic coefficients. The outputs are the derivatives of the states, as obtained using [Equations 9.4](#) to [9.7](#). The derivatives will pass through an integrator block to obtain the states of the next time-step, which feed back into the lookup table and equations of motion blocks.

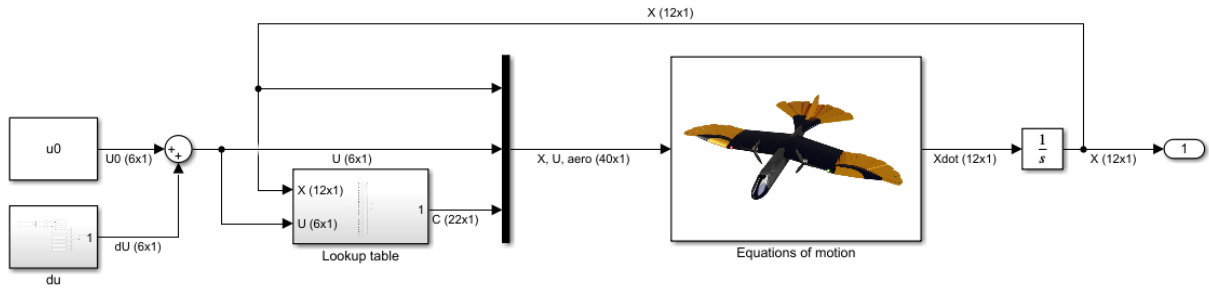


Figure 9.3: Non-linear Simulink model of the UAV

Flight Visualisation

The results of the flight simulation are visualized using a simple, readily available Simulink VR sink block. The visualization shows the attitude, rotational- and translational motion of the simulator. The inputs for this block are the earth-frame rotation angles from Equation 9.6 and the positions in the earth frame from Equation 9.7.

9.3. Analysis of UAV Flight Dynamics

In this section, the outcomes of the flight dynamics model will be discussed. First, an analysis of the characteristic motions will be done, then verification of the performance requirements will be executed.

9.3.1. Morphing and Aerodynamic Derivatives

Morphing induces unconventional interactions between the UAV and the air, leading to cross-coupled, non-linear aerodynamic derivatives as can be seen in Figure 9.4. This subsection displays observations on the aerodynamic coefficients due to only wing morphing and due to only tail morphing and tail deflections. Please note that these coefficients were non-dimensionalized for S and c set to 1, and an angle of attack of 0° .

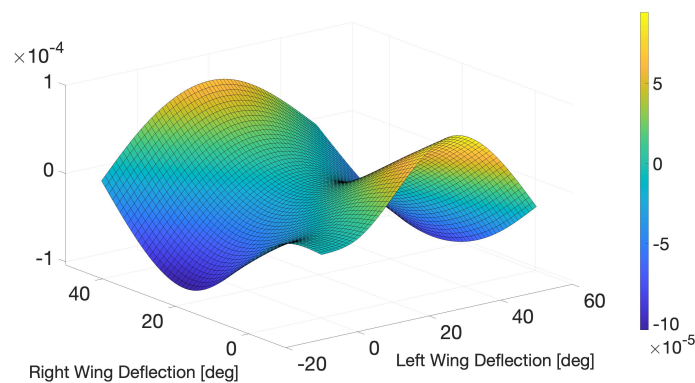


Figure 9.4: Display of aerodynamic non-linearities due to morphing

Coefficients and Wing Morphing

Most aerodynamic coefficients are affected by wing asymmetric wing morphing, especially those related to lateral motion. Figure 9.5 and Figure 9.6 display how the drag and side force change depending on the morph configuration. As expected, the drag is seen to be the largest near the fully extended configuration. The side force is the largest with one of the wings forwardly swept and the other around 25° .

The lateral dynamic behaviour and stability of aircraft are typically dependent on the interplay between the following aerodynamic coefficients: $C_{l\beta}$, C_{lr} , C_{nr} , $C_{n\beta}$, C_{lp} . Figures 9.7 till Figure 9.11 clearly display how these coefficients change as a function of asymmetric wing morphing. This leads to interesting conclusions on the dynamic stability of the UAV as a function of morphing and will be further discussed in Subsection 9.3.2.

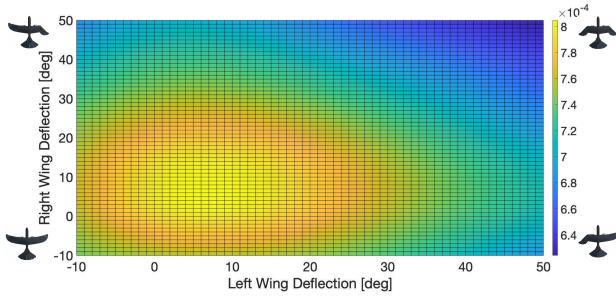


Figure 9.5: Drag coefficient C_D as a function of the wing morphing

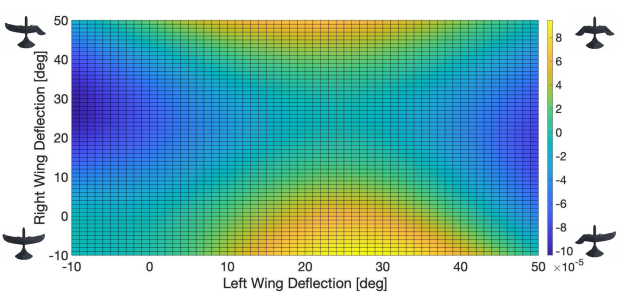


Figure 9.6: C_S as a function of the wing morphing

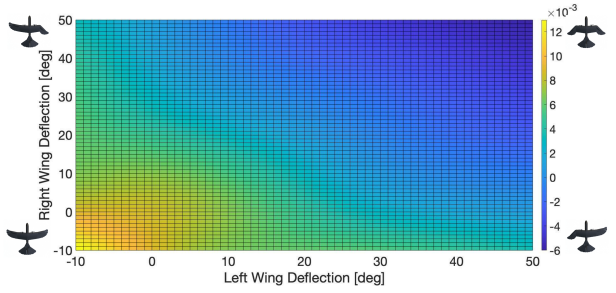


Figure 9.7: C_{l_β} as a function of the wing morphing

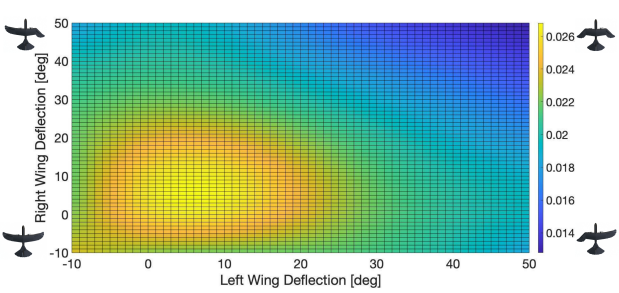


Figure 9.8: C_{l_r} as a function of the wing morphing

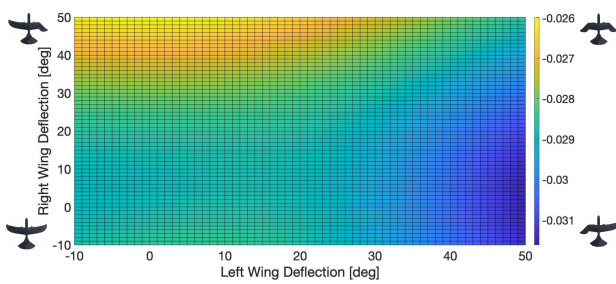


Figure 9.9: C_{n_r} as a function of the wing morphing

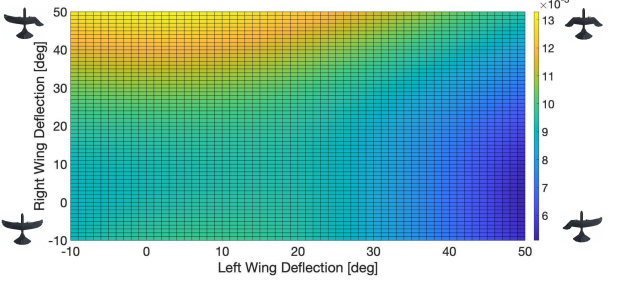


Figure 9.10: C_{n_β} as a function of the wing morphing

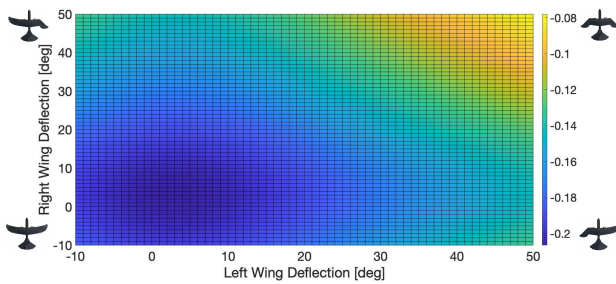


Figure 9.11: C_{l_p} as a function of the wing morphing

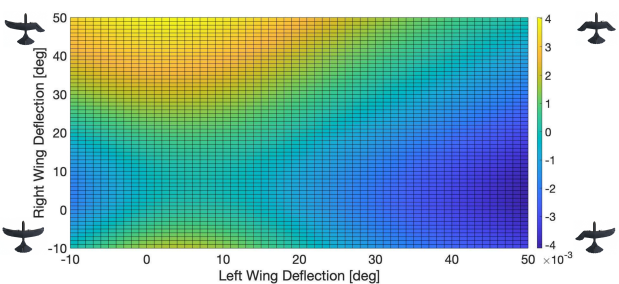


Figure 9.12: C_l as a function of the wing morphing

Furthermore, as was mentioned in Section 6.3 asymmetric morphing indeed proves to be effective for rolling, which can be seen in Figure 9.12.

Lastly, asymmetric wing morphing also slightly alters the longitudinal stability of the UAV, where the main effect can be witnessed on C_{m_α} .

Coefficients and Tail Actuation

Morphing the tail allows for great pitch authority and the generated moments can be seen in Figure 9.13.

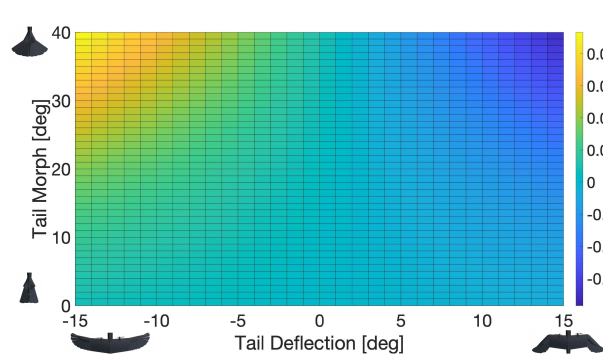


Figure 9.13: C_m as a function of the tail morphing

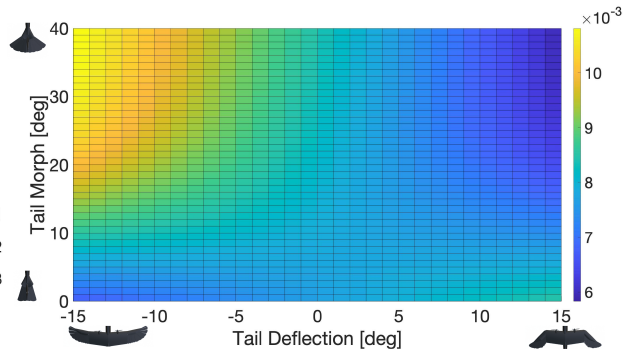


Figure 9.14: C_{l_β} as a function of the tail morphing

In addition, tail morphing and deflection were seen to largely influence the lateral aerodynamic coefficients, as can be seen in figures 9.16 until 9.14. This is likely because a tail rotation increases or decreases the effective sweep of the vertical tail, hence decreasing or increasing its effectiveness, respectively. This introduced interesting behavior of the tail on the lateral dynamic stability of the UAV and will be further discussed in Subsection 9.3.2.

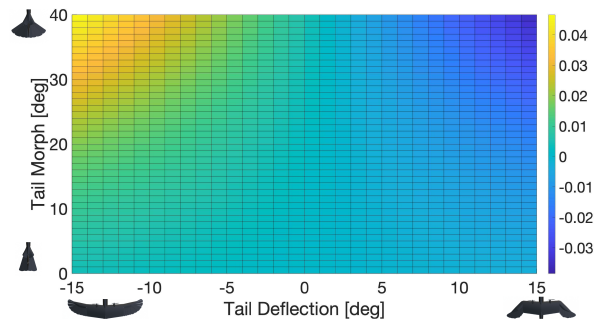


Figure 9.15: C_{l_r} as a function of the tail morphing

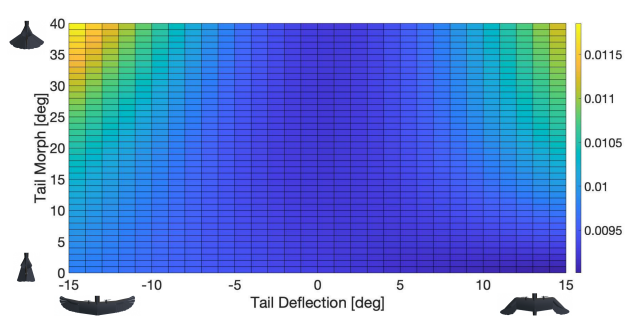


Figure 9.16: C_{n_β} as a function of the tail morphing

9.3.2. Dynamic Stability of the UAV

This subsection will discuss the dynamic stability of the UAV. First, the pole-zero plots for the UAV will be given for its extended and retracted wing-morphing positions. Then plots of some characteristic motions will be shown. Afterward, a small discussion will be provided on how morphing affects the dynamic spiral stability.

To properly assess the dynamic behavior of the UAV, the model had to be trimmed. Therefore a Matlab script was created that automatically finds the states and control inputs that trim the UAV for a given flight velocity. Afterward, a script has been written that linearized the model at the trim point.

From Figure 9.17 and Figure 9.18 it can be seen that there is dynamic instability for the UAV for both tucked and extended wing morphing positions, as there are positive poles. Furthermore, with tucked wings the dynamic instability increases as there are more positive poles. This can also be seen in Figure 9.19 and Figure 9.20.

Additional simulations were done to investigate the effect of tail morphing and asymmetric wing morphing. Figure 9.21 shows the same dynamic behavior mentioned before when the tail is slightly morphed. Figure 9.22 shows the rolling response to a step input when retracting the left wing. This shows that the roll of the UAV is undamped and active control inputs are needed to stop the roll.

As was mentioned in Subsection 9.3.1, the aerodynamic coefficients that concern the UAV’s lateral motion vary significantly due to morphing. This leads to interesting behavior on the lateral dynamic stability. Figure 9.24 shows how the spiral stability gets altered due to morphing, becoming increasingly unstable as the wings extend. In addition, due to the vertical being mounted on the horizontal tail, elevator deflections alter the lateral dynamic

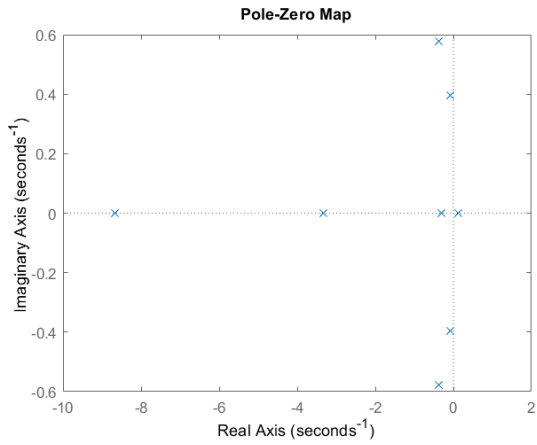


Figure 9.17: Poles and zeroes with wings extended

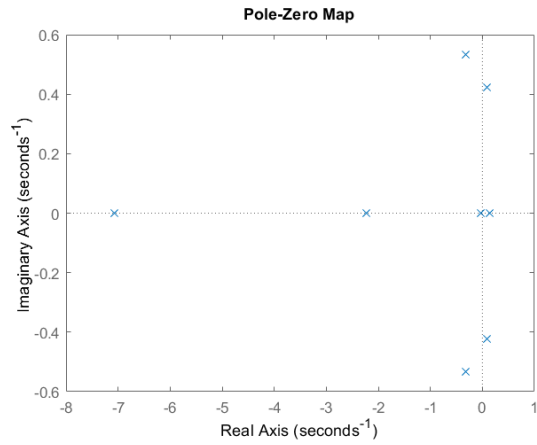


Figure 9.18: Poles and zeroes with wings retracted

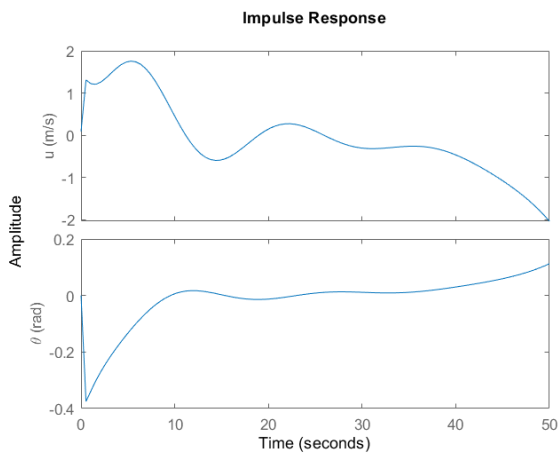


Figure 9.19: System response to tail input with wings extended

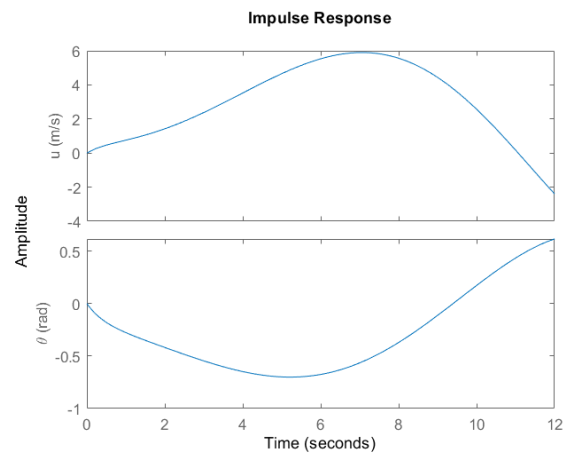


Figure 9.20: System response to tail input with wings retracted

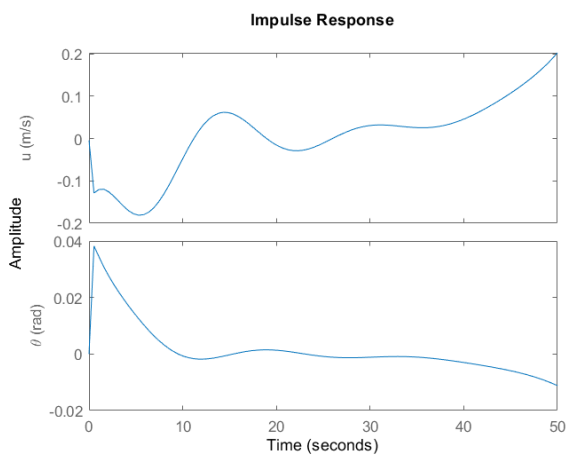


Figure 9.21: System response to tail morph input with wings extended

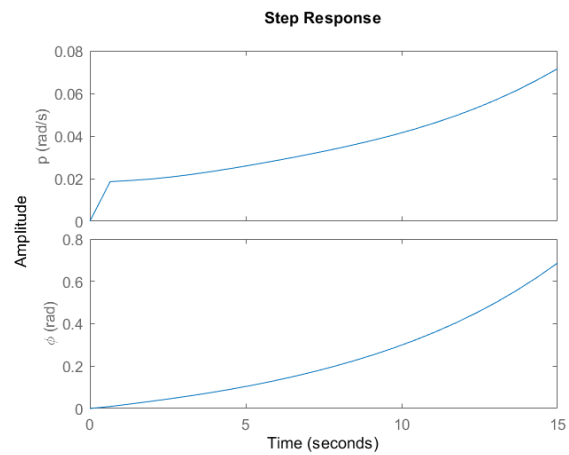


Figure 9.22: System response to positive left wing morph input with wings retracted

behaviour. This can be seen in Figure 9.24, where the spiral stability is affected by tail actuation.

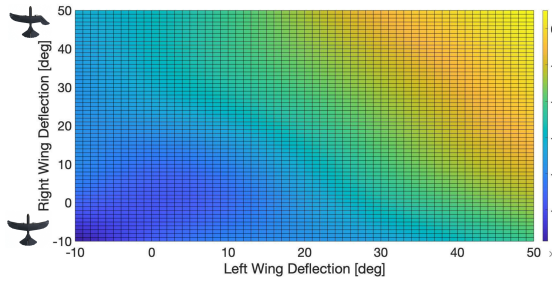


Figure 9.23: Spiral stability as a function of the wing morphing

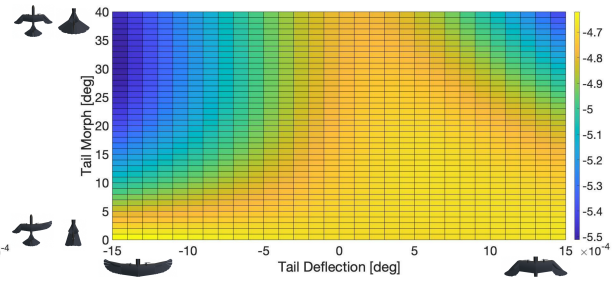


Figure 9.24: Spiral stability as a function of the tail morphing

9.4. Controller Design

The dynamic instabilities shown in Section 9.3 highlight the need for a flight controller. This section will describe the process of creating a control system for the morphing UAV. Several approaches were identified, but only one proved to be both successful and verifiable. Subsection 9.4.1 briefly explains the structure of the controller. Next, the design of the inner loop is presented in Subsection 9.4.2. Then, an ideal controller is presented, whose workings were unfortunately not verifiable in Subsection 9.4.3. Lastly, an alternative set of control loops based on PID control is presented in Subsection 9.4.4.

9.4.1. Structure of the Controller

The flight controller contains three loops. The inner loop controls the attitude dynamics of the UAV, the middle loop controls the attitude kinematics and the outer loop controls the translational dynamics of the UAV. The attitude dynamics essentially describe how the angular rates change due to the external moments acting on the UAV. Similarly, the translational dynamics dictate how the translational accelerations change due to external forces. Lastly, the attitude kinematics describe how the attitude angles change due to the angular rates.

Separate control loops are needed because each of them has different response rates and they also reduce the complexity of the flight controller. The dynamic loops are controlled using an incremental nonlinear dynamic inversion (INDI) approach, while the kinematic loop is controlled using regular nonlinear dynamic inversion (NDI) using the approach described in [41].

Certain controllers contain yet another control loop that controls the translational kinematics, such as the positions in the x , y and z -direction. However, this is typically not directly controlled in aircraft. Therefore the controller stops at the translational dynamic loop for now. In the future, this could be implemented to input a loiter path for the UAV.

9.4.2. Inner Loop Design

The inner loop forms the core of the flight controller and controls the roll rate p , pitch rate q , yaw rate r . It does so using the INDI approach mentioned in [41]. The INDI approach has been chosen since both the translational and rotational dynamics contain model uncertainties in the external forces and moments. The changes in control inputs are determined by Equation 9.15. [41]

$$\Delta \mathbf{u} = \mathbf{G}^{-1} \left(\begin{bmatrix} v_p \\ v_q \\ v_r \end{bmatrix} - \begin{bmatrix} \dot{p}_{-1} \\ \dot{q}_{-1} \\ \dot{r}_{-1} \end{bmatrix} \right) \quad (9.15)$$

Here, v_p , v_q and v_r are the virtual control inputs, and \dot{p}_{-1} , \dot{q}_{-1} and \dot{r}_{-1} are the roll acceleration, pitch acceleration and yaw acceleration from the previous time step. The virtual control inputs are defined as follows: $K \cdot (x - x_{ref})$, where K is a gain, x is the true value of the controlled variable and x_{ref} is the desired value of the controlled variable. Lastly, \mathbf{G} is the control effectiveness matrix and can be computed by taking the Jacobian between the controlled variables and the control inputs as seen in Equation 9.16.

$$\mathbf{G} = \begin{bmatrix} \frac{\partial V}{\partial u_1} & \dots & \frac{\partial V}{\partial u_6} \\ \frac{\partial p}{\partial u_1} & \dots & \frac{\partial p}{\partial u_6} \\ \frac{\partial q}{\partial u_1} & \dots & \frac{\partial q}{\partial u_6} \\ \frac{\partial r}{\partial u_1} & \dots & \frac{\partial r}{\partial u_6} \end{bmatrix} \quad (9.16)$$

Another set of inner loop control variables had been investigated, which were p , q , r and V , where V is the airspeed of the UAV. It was believed that because of the UAV’s electric engines the velocity would have similarly fast responses as the attitude dynamics and could therefore also be put in the inner loop. This proved to be the case initially as the acceleration indeed had fast dynamics. However, the deceleration seemed to rely on slower aerodynamic effects, leading to constant overshoots and divergence within this control loop, thus proving to be unsuccessful.

Control Effectiveness Matrix

The inner loop is over-actuated, meaning that there are more control inputs than control variables, leading to \mathbf{G} having a non-square form. This leads to the problem of control allocation, where different control inputs can lead to the same change in the controlled variable. For example for the UAV both a tail deflection and a change in the tail surface morphing can lead to a pitch rate. To solve this, [Matamoros and de Visser](#) propose to use a redistributed weighted pseudo-inverse of \mathbf{G} , however a regular pseudo-inverse was implemented to reduce the controller’s complexity [42].

The control effectiveness matrix had been computed for a only a single instance. This had been done by trimming the model at a tail morph setting of 30°. The control effectiveness for p , q and r were then estimated using [Equation 9.17](#)

$$\frac{\partial Y}{\partial u_i} = \frac{\partial Y}{\partial t} \cdot \frac{\partial t}{\partial u_i}, \quad (9.17)$$

where Y represents either p , q or r and u_i is control input i . For simplicity ramp inputs with a slope of 1 were given as control inputs as this lead to $\frac{\partial u_i}{\partial t}$ being equal to 1.

Results

The final inner control loop can be seen in [Figure 9.25](#).

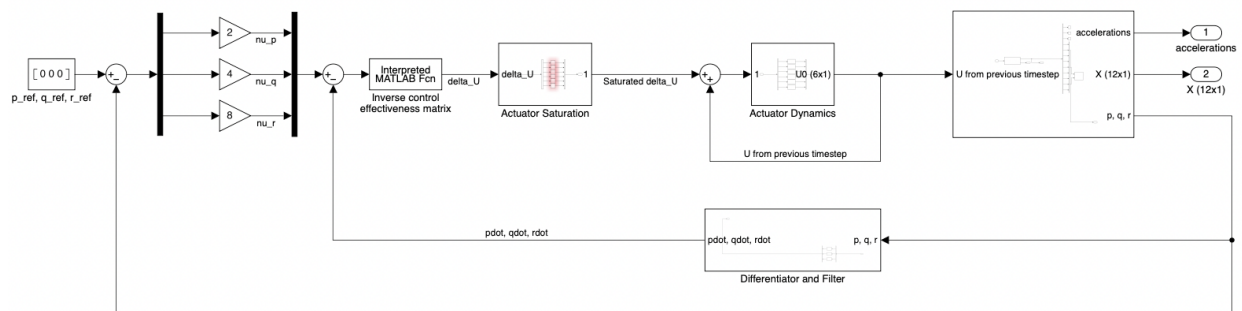


Figure 9.25: Inner loop of the controller controlling p , q and r

The responses of the inner loop to a step input in the reference roll rate, pitch rate and yaw rate can be seen [Figures 9.26](#) until [9.28](#). Convergence in the pitch and yaw rate can clearly be seen after a slight overshoot. The same hold for the roll rate initially, except for the slight divergence seen at the end. In the flight visualisation it was seen that at this point the roll became unsustainable due to the aerodynamic forces and moments introduced by the large roll angle. This shows that the inner loop can indeed follow references for the attitude rates.

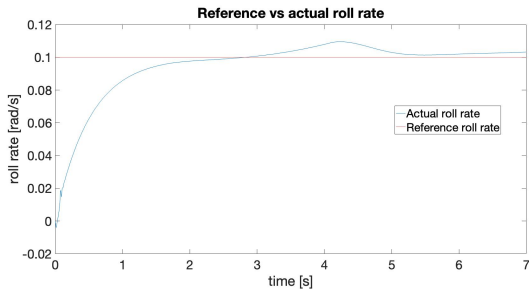


Figure 9.26: Reference and actual roll rate as a function of time

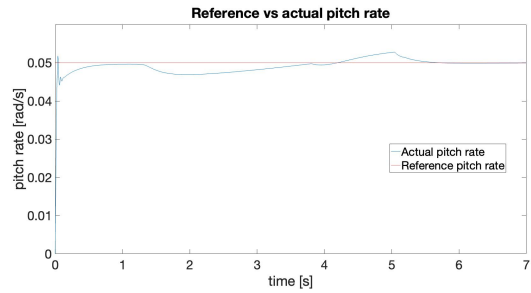


Figure 9.27: Reference and actual pitch rate as a function of time

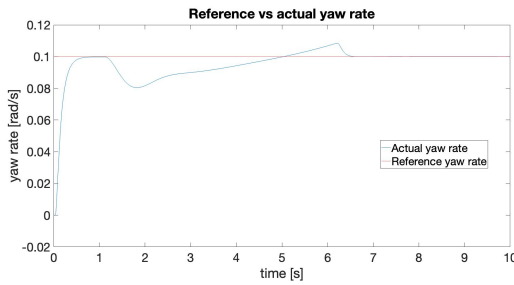


Figure 9.28: Reference and actual yaw rate as a function of time

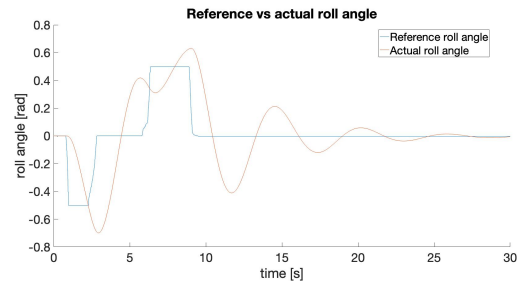


Figure 9.29: Controlled roll angle over time

9.4.3. Three Loop Design

An attempt had been made to create an ideal three-loop flight controller that directly controls the trajectory of the UAV. The middle loop, governing the attitude kinematics, would be described by the angle of attack α , angle of sideslip β and the aerodynamic bank angle μ .

Next, the outer loop would control the translational dynamics by controlling the aerodynamic heading angle χ and flight path angle γ . Both the middle and the outer loop were based on the model and equations described by [41]. However, the model was slightly adapted to accommodate for the differential thrust present within our inner loop. Furthermore, all of the gains were tuned using a PID controller in Matlab. However, the simulation was found to be extremely slow making it very difficult to verify whether the controller converges or diverges.

Therefore, it was decided to manually tune the 9 gains in the loop, which unfortunately turned out to be unfruitful, likely because of the following three reasons. Firstly, it could be the case that the gains were not properly optimized. Secondly, the control effectiveness matrix in the outer loop could have been improperly estimated, as it was done through inspection, similar to the inner loop. Lastly, the adaptation to account for differential thrust might have caused the controller to diverge. Even so, the controller was still able to control the UAV for some time before it diverges in a strong pitching maneuver, which is likely caused by the strong control inputs to reach the desired flight path angle.

9.4.4. PID Loop Design

Although the previous controller did not work, the inner loop still converges. This meant that a simple PID controller could be designed to control the attitude kinematics. For simplicity, this was done in terms of ϕ , θ and ψ . The results in terms of the attitude angles can be seen in Figures 9.29 and 9.30, while the rate convergence, in this case the roll rate, is displayed in Figure 9.31.

In addition, a small outer loop had been created that controls the velocity using a simple PID. However, even though it converges, its effectiveness remains limited as the attitude kinematic angles typically vary with the velocity and vice versa. Since this dependency has not been modeled, the range to which the velocity control responds is rather limited. Still, the controller remains very effective in controlling both the middle and inner loops.

9.4. Controller Design

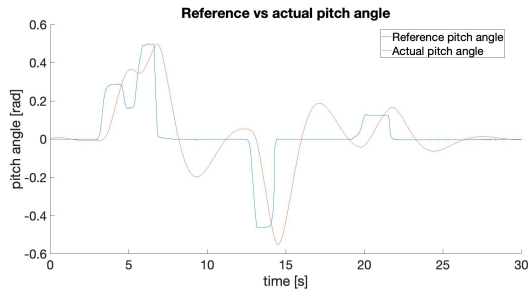


Figure 9.30: Controlled pitch angle versus time

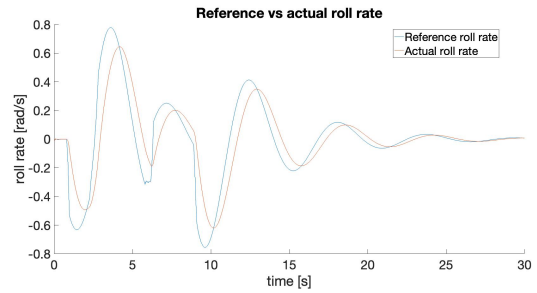


Figure 9.31: Controlled roll rate versus time

9.4.5. Performance Verification

Table 10.1 shows the performance requirements the UAV has to comply with. These maneuvers will be simulated using the model described before. As can be seen, two requirements were not met. A discussion on that can be read below.

Table 9.1: Performance Requirements for the UAV

Identifier	Requirement	Verification Method	Compliance
REQ-UAV-PERF-012	The UAV shall have a maximum climb rate of at least 12 m/s	Demonstration	✓
REQ-UAV-PERF-013	The UAV shall have a maximum operating speed of 45 m/s	Demonstration	✓
REQ-UAV-PERF-015	The UAV shall have pull over radius of less than 1m	Demonstration	
REQ-UAV-PERF-016	The UAV shall have sharp turn radius of less than 1.5m	Demonstration	
REQ-UAV-PERF-020	The UAV payload shall have a pointing accuracy of +/- 5 degrees	Test	✓

Climb Performance

Figure 9.32 shows the altitude of the UAV during a pull-up maneuver at maximum thrust and extended morph configuration. From the graph, it can be deduced that the UAV has a climb rate of 37.5 m/s, which is well over the requirement of 12 m/s.

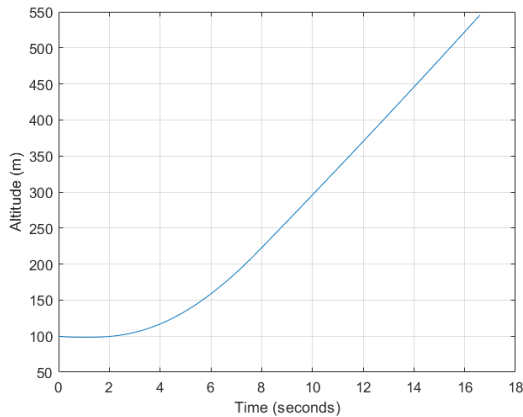


Figure 9.32: Altitude as function of time

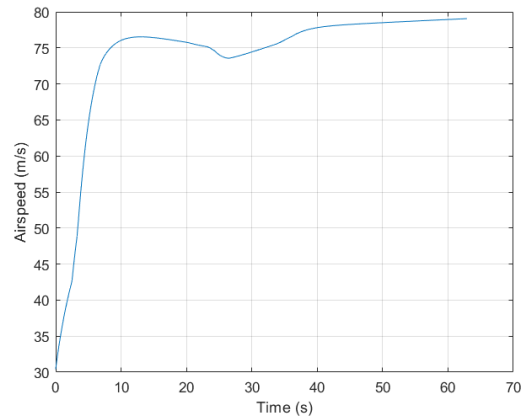


Figure 9.33: Airspeed as function of time

Operating Speed

The operating speed of the UAV is dependent on the maximum thrust that can be generated by the engine and the drag coefficient. Figure 9.33 shows the airspeed of the UAV in extended configuration at sea level using maximum thrust.

Pull-over and Sharp-turn Radius

The turn radius can be calculated using the force in the z-direction of the body axis and velocity in the x-direction using Equation 9.18:

$$r_{turn} = \frac{mu^2}{F_z} \tag{9.18}$$

u and F_z are variables that can be obtained from the model. Using maximum deflection of the controls, a minimum turn radius of 13.3 m could be obtained as seen in Figure 9.34. This however, does not comply with the requirements in Table 10.1. A reason for this could be that the model is only accurate for angles of attack between -12 and 12 degrees, as mentioned in Subsection 9.2.5. For such a high angle of attack maneuver, results may not be representative.

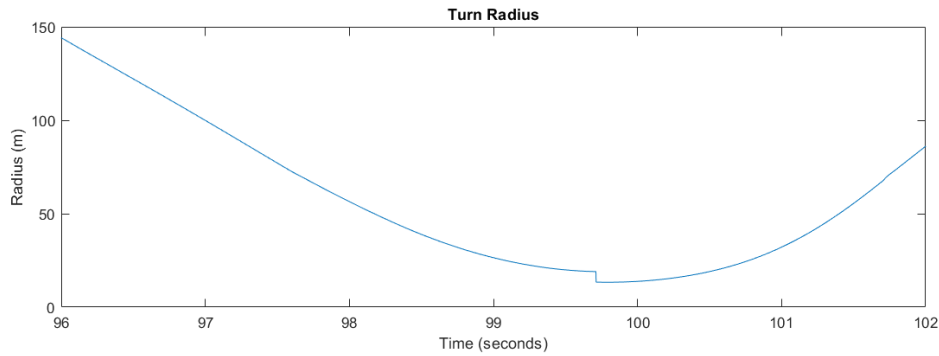


Figure 9.34: Turn radius during a pull-up maneuver

Pointing Accuracy

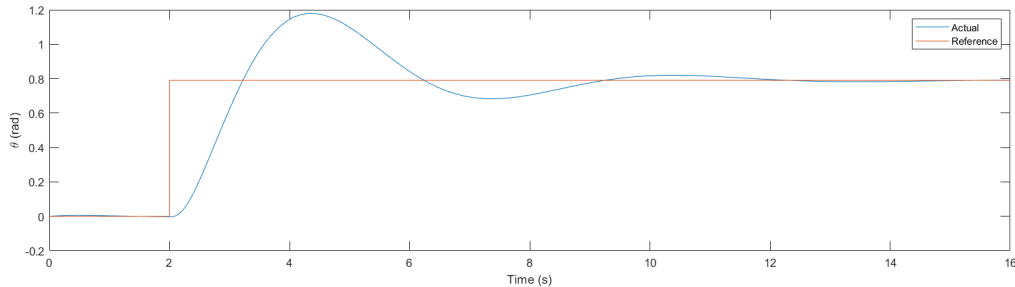


Figure 9.35: Response to a 45 degree reference pitch

Figure 9.35 shows the response of the UAV to a reference pitch input of 0.8 rad. It can be seen that the UAV converges to that pitch with great accuracy, although it takes around 12 seconds to do so. To reduce this time, the middle loop of the controller will have to be tuned more efficiently, as Figure 9.27 shows that the UAV can easily follow a reference pitch rate, proving its maneuverability.

9.5. Recommendations

The model described in this chapter is a better approximation to the UAV dynamics than a conventional linear model. However, it has its limitations, which is why this section will cover some recommendations for future iterations.

Right now, the model is limited by the resolution of aerodynamic data. For an angle of attack range of -12 to 12 degrees, the coefficients are retrieved directly from the aerodynamic analysis. However, beyond this range, the values are linearly extrapolated which can lead to inaccuracies for high angles of attack. More aerodynamic data

would be needed for more detail. Additionally, stall effects are not simulated by the OpenVSP data, so the model does not show the stall characteristics of the UAV. This can be solved by using a different CFD tool that takes stall into account. For very high pitch angles, inaccuracies are introduced as there is a singularity for the Euler angles at 90 degrees pitch. Using quaternions would solve this problem.

For a more accurate representation of the real world, wind shear and density changes can be added to the model. This would also allow simulation of the UAV's response to wind gusts. Additionally, aero-elastic effects could be modeled as the UAV is assumed to be a rigid body (with the exception of the morphing parts).

When morphing, the model does not take into account the moment of inertia change of the UAV or the effect of morphing on the internal moments of the craft. Using multibody dynamics (Kane's equations) could solve this problem. The rotational inertia of the propellers is also neglected in this model. The effect of this assumption would need to be investigated more before deciding whether to implement propeller effects into the model.

In addition, the control effectiveness matrices have only been evaluated for single operating points. However, since the control effectiveness varies as a function of the flight conditions and the morphing, it is recommended to dynamically update them during the simulation.

Furthermore, some trouble was experienced with proper gain tuning as the Matlab PID tuner often gave disproportionately large gains. Therefore, it is also recommended to perform more literature research on efficient and convergent PID gain tuning.

Finally, the inertial effect of shooting payload is not incorporated into the simulation. As the payload deploys, the UAV will experience a temporary moment and force. In future iterations, these moments and forces can be investigated and added to the model.

10. Performance

In order to evaluate the ability of the final UAV design to meet all requirements related to mass material and flight performance, a series of analytical calculations were carried out to estimate the achieved performance parameters as well as parameters that are important for the operation of the UAV. In this section, first, the mass performance is stated in the form of a mass budget, after which the material composition of the structures of the drone is stated. Next, the flight performance is detailed followed lastly by the evaluation of the flight performance.

10.1. Mass Performance

The design of subsystems of the drone involved many considerations on the material and mass of individual system components, given that these systems have been designed in detail the resulting mass of each subsystem and the total drone mass can be computed such that the performance can be defined in later sections. Table 10.3 displays all of the designed subsystems and their components, along with the number and mass of each component. Going further, the materials used in the structure of these components are also defined in order to evaluate the total sustainable material mass. The various subsystem contingencies as specified in Section 2.4 for the qualification design have also been implemented leading to a final drone mass of 3.754 kg.

10.1.1. Sustainable Material Evaluation

The requirement set on the materials and structures of the drone as seen below emphasized that 75% of the mass of structural elements of the drone must be sustainable or recyclable. Table 10.2 displays all the structural elements of the drone. Furthermore, the materials used in manufacturing are also displayed followed by their recycling methodology. It can be seen that close to 99% of the drone's structural mass can in some way be recycled such that the materials can be reused, reshaped, remelted or overall transformed for a different use.

Table 10.1: Performance Requirements for the UAV

Identifier	Requirement	Verification Method	Compliance
REQ-UAV-SUS-001	75% of the structural mass of the UAV shall be made of recyclable materials	Analysis	✓

Table 10.2: Structural mass composition with material recycling method

Drone group	Component	Mass of components [g]	Numer of components	Contingency Per drone group [%]	Manufacturing material	Recycling Method	Mass of components with contingency [g]																																																																			
Fuselage	Fuselage structure	85.506	1	5	Balsa wood	Composting/ wood chips	89.7813																																																																			
	Skid blocks		1		PLA	Remelting		Wing Group	Fixed wing structure	63.5	2	10	Balsa wood	Composting/ wood chips	139.7	Morphing wing spar	69	2	Aluminium 2024	Remelting	151.8	Morphing wing fairing	8.8746	2	Celanese VECTRA A950 LCP - NematX	Reshaping, Remelting	19.52412	Wing platelets + connectors	12.3	22	Celanese VECTRA A950 LCP - NematX	Reshaping, Remelting	297.66	Elastic Tendons	5	2	Thermoplastic elastomere	-	11	Alula	1.77792	2	Balsa wood	Composting/ wood chips	3.911424	Morphing tail structure	55.419	1	Celanese VECTRA A950 LCP - NematX	Reshaping, Remelting	60.9609	Tail Group	Tail fairing structure	6.6612	1	Celanese VECTRA A950 LCP - NematX	Reshaping, Remelting	7.32732	Tail platelets + connectors	34.1	8	Celanese VECTRA A950 LCP - NematX	Reshaping, Remelting	300.08	Vertical tail	37.44	1	Balsa wood 2 mm thick	Composting/ wood chips	41.184	Percentage of structural mass that can be recycled [%]			
Wing Group	Fixed wing structure	63.5	2	10	Balsa wood	Composting/ wood chips	139.7																																																																			
	Morphing wing spar	69	2		Aluminium 2024	Remelting	151.8																																																																			
	Morphing wing fairing	8.8746	2		Celanese VECTRA A950 LCP - NematX	Reshaping, Remelting	19.52412																																																																			
	Wing platelets + connectors	12.3	22		Celanese VECTRA A950 LCP - NematX	Reshaping, Remelting	297.66																																																																			
	Elastic Tendons	5	2		Thermoplastic elastomere	-	11																																																																			
	Alula	1.77792	2		Balsa wood	Composting/ wood chips	3.911424																																																																			
	Morphing tail structure	55.419	1		Celanese VECTRA A950 LCP - NematX	Reshaping, Remelting	60.9609																																																																			
Tail Group	Tail fairing structure	6.6612	1	Celanese VECTRA A950 LCP - NematX	Reshaping, Remelting	7.32732																																																																				
	Tail platelets + connectors	34.1	8	Celanese VECTRA A950 LCP - NematX	Reshaping, Remelting	300.08																																																																				
	Vertical tail	37.44	1	Balsa wood 2 mm thick	Composting/ wood chips	41.184																																																																				
	Percentage of structural mass that can be recycled [%]							99.02041898																																																																		

10.2. Analytical Performance Calculations

Table 10.3: Mass budget and material choice of the entire Air-Guard drone

Drone group	Component	Mass of components [g]	Numer of components	Contingency [%]	Mass of components with contingency [g]	Material of component
Payload	Parachute	315	1	5	330.75	-
	Net	179	1		187.95	HDPP (high-density polypropylene)
	Weights	25	4		105	Steel
	pyrotechnic charges	6.25	4		26.25	-
	GPS	10	1		10.5	-
	Lights	30	2		63	-
	Payload casing + psuedo nose	89.89182345	1		94.38641462	ABS
	gas canister	47	1		49.35	-
	pneumatic tubing	175	1		183.75	-
	Solenoid valve	30	1		31.5	-
Communication	Antenna	34.3	1	3	35.329	-
CDHS	Flight controller	73	1	3	75.19	-
Sensors and electronics	Tracking camera	10.2	1	5	10.71	-
	Infrared camera	12.2	1		12.81	-
	Battery	830	1		871.5	-
	Operational lights	10	4		42	-
Fuselage group	Fuselage structure	85.506	1	5	89.7813	Balsa wood
	Skid blocks		1			PLA
Wing group	Electric engines	67	2	10	147.4	-
	Propellers	14	2		30.8	-
	Motor controllers	26	2		57.2	-
	Fixed wing structure	63.5	2		139.7	Balsa wood
	Morphing wing spar	69	2		151.8	Aluminium 2024
	Morphing wing fairing	8.8746	2		19.52412	Celanese VECTRA A950 LCP - NematX
	Wing platelets + connectors	12.3	22		297.66	Celanese VECTRA A950 LCP - NematX
	Elastic Tendons	5	2		11	Thermoplastic elastomere
	Alula	1.77792	2		3.911424	Balsa wood
	Wing morphing actuators	52.4	2		115.28	-
	Alula actuators	15.8	2		34.76	-
Tail group	Morphing tail structure	55.419	1	10	60.9609	Celanese VECTRA A950 LCP - NematX
	Tail fairing structure	6.6612	1		7.32732	Celanese VECTRA A950 LCP - NematX
	Tail platelets + connectors	34.1	8		300.08	Celanese VECTRA A950 LCP - NematX
	Vertical tail	37.44	1		41.184	Balsa wood 2 mm thick
	Morphing tail actuators	52.4	1		57.64	-
	Elevator acuator	52.4	1		57.64	-
	Total mass with sub system contingencies [g]					3753.624479

10.2. Analytical Performance Calculations

This section considers only basic maneuvers for which analytical solution is readily available. More complex scenarios, such as super maneuvers (maneuvers that do not rely on aerodynamics, but on the thrust provided by the engines since $T/W > 1$) or maneuvers achieved by complex combinations of control inputs, will be analyzed using the flight dynamics model discussed in [Chapter 9](#).

The analytical calculations will be discussed in the following subsections. Each of these calculations was calculated for two situations that follow from requirements; for flight in at optimum cruise velocity (to be discussed below) at 450 m above sea level and for flight at attack velocity at 45 m/s at sea level. For parameters where it is relevant, optimum flight conditions were calculated as well (such as for minimum turn radius).

10.2.1. Optimal Cruise Speed

The optimal cruise speed is determined by considering the lift coefficient for which L/D is maximum. By rearranging the lift equation, one can calculate the speed at which the UAV should fly at a given altitude and weight as:

$$V_{opt} = \sqrt{\frac{2W}{\rho S C_{L,opt}}} \quad (10.1)$$

10.2.2. Thrust and Power Required

The thrust and power required for cruise are essential for estimating the power budget and so for sizing of the batteries. Furthermore, engines have to be able to deliver this power.

The minimum thrust required is calculated by considering steady, level flight at optimum cruise velocity. Under such conditions, the thrust equals drag and so:

$$T_{req} = C_{D,opt} \frac{1}{2} \rho V^2 S \quad (10.2)$$

The power required is then obtained by multiplying the thrust by the cruise velocity:

$$P_{req} = T_{req} \cdot V \quad (10.3)$$

This is however not the power to be drawn from the batteries. To obtain this value, the required power needs to be divided by the propeller efficiency. This efficiency was calculated for different flight conditions as part of propulsion system design (found in [Chapter 8](#)).

10.2.3. Maximum Rate of Climb

The maximum rate of climb is calculated by considering the difference between power required and power available at considered conditions. The formula is then:

$$ROC = \frac{P_a - P_{req}}{W} = \frac{P_{engines} \eta_{prop} - DV}{W} \quad (10.4)$$

It can then be shown that the maximum rate of climb for propeller aircraft is reached at maximum L/D flight conditions [24]. Furthermore, this relation is also used to determine the flight ceiling as that is defined as the altitude at which the maximum rate of climb is zero.

10.2.4. Stall Speed

The stall speed is obtained by rearranging the lift equation and considering the maximum lift coefficient achievable:

$$V_{stall} = \sqrt{\frac{2W}{\rho S C_{L,max}}} \quad (10.5)$$

10.2.5. Maximum Sustained Turn Rate

The turn rate in level turning flight is obtained by manipulation of equilibrium equations to get the following relationship[24]:

$$\dot{\psi} = \frac{g \sqrt{n^2 - 1}}{V} \quad (10.6)$$

Where for sustained level turn (for which the velocity is conserved and so thrust equals drag), the load factor is obtained as [24]:

$$n = (T/W)(L/D) \quad (10.7)$$

That means that the maximum achievable turn rate for leveled sustained turn occurs at cruise conditions (since the drone is designed to fly at L/D maximum) when the thrust is set to maximum setting, the maximizing the T/W ratio.

10.2.6. Instantaneous Turn Rate

A similar approach can be taken for cases where velocity is allowed to decrease, or the drone is allowed to lose altitude. In such a case, the thrust no longer has to equal drag and so the maximum load factor is limited only by the maximum lift coefficient achievable and by structural limits. The velocity at which the stall and structural limits intersect is defined as "corner speed" and provides the maximum achievable instantaneous turn rate. [24] To calculate this turn rate, Equation 10.6 is used again, for which velocity is increased until the corresponding load factor, obtained for maximum lift coefficient, reaches the structural limit of 8.7g.

10.2.7. Minimum Level Turn Radius

It can be shown that the turn radius of level flight is given by Equation 10.8:

$$R = \frac{V^2}{g\sqrt{n^2 - 1}} \quad (10.8)$$

If no specific velocity is considered, the minimum of this relation is not necessarily at the maximum load factor. To reach the minimum, an unsustained turn has to be considered again. The minimum radius is then reached at the same conditions as the maximum turn rate, that is at the corner speed. Furthermore, the same relationships for minimum radius and instantaneous turn rate hold for both turning flight as well as for pull-up maneuvers.

10.2.8. Maximum Range

For propeller aircraft, the maximum range is achieved at maximum L/D conditions [24]. The range itself is then calculated by obtaining the required power (as it was done in one of the previous subsections), also considering the efficiency of propellers. Next, the battery capacity is divided by this power to get the time for which the aircraft can fly. By multiplying this time by the optimum velocity, the maximum range is obtained. To make this estimation more precise, only the fraction of total energy stored, that is allocated for cruise should be considered. The flight time obtained as intermediate step is the also compared to the required endurance to evaluate if then UAV meets this requirement as well.

10.3. Results and Discussion

Table 10.4 provides the results of the above-discussed calculations compared to the values required by the customer. Note that while no specific requirement was given for optimal cruise velocity, the required value follows from dividing the required range by the required endurance. Similarly, no specific value was required for stall speed but the required value follows from the calculation of minimum landing distance, performed as part of the preliminary design.

The table shows that the designed UAV should be able to meet most of the requirements posted by the customer. The only parameters which would seem not to be met based on Table 10.4 are the minimum turn and pull-up radii. However, this is due to the fact that these requirements are so constraining, that they cannot be met in conventional flight regimes. A complex combination of thrust vectoring, morphing (of both the main wing and of the horizontal tail), sideslip and tail deflection would have to be performed to achieve a composed turn maneuver that would meet the minimum turn and pull-up radius requirements. While the feasibility of such maneuvers was demonstrated in other projects, such maneuvers would be very difficult to analyze analytically or even simulate, so a conclusion about the ability of the drone to meet this requirement would be truly tested only by means of test flight [4]. The calculated turn rate envelope is then provided in Chapter 9.

Secondly, it should be noted that while it was calculated that the drone would still be able to climb at 5000m above sea level, meeting the maximum ceiling requirement, this would have to be validated by flight test as well as the analysis was based on an aerodynamic model generated using OpenVSP software. This software uses the vortex lattice method and is not suitable for the analysis of viscous effects. Therefore, it is possible that the change in Reynolds number, associated with a large change in altitude, is not properly reflected in the change in drag and lift. Since no software was found, which would allow to efficiently model many complex configurations associated with the morphing capabilities of the drone, while also considering viscous effects, the meeting of the ceiling requirement would have to be further validated by either more detailed CFD simulations or real-world flight test. Finally, equations for both the maximum rate of climb and the maximum achievable velocity, consider the power required and power available to get the excess power. Discussion on how the available power is calculated and how the maximum excess power is found, is provided in [Subsection 8.2.2](#).

Table 10.4: Overview of Air-Guard drone performance parameters

Parameter	Required value	Achieved value	Conditions	Requirement i.d.
Min. cruise velocity	16.6 m/s	20.12 m/s	At 450m a.s.l.	-
Cruise Thrust	-	2.49 N	At 450m a.s.l.	-
Cruise Power	-	50.14 W	At 450m a.s.l.	-
max ROC	12 m/s	15.7 m/s	At sea level	REQ-UAV-PERF-012
Minimum turn radius	1.5 m	13.67m	At sea level	REQ-UAV-PERF-016
Minimum pull-up radius	1.5 m	13.67m	At sea level	REQ-UAV-PERF-015
Maximum turn rate	-	143 deg/s	At sea level	-
Stall speed	12 m/s	11.56 m/s	At sea level	-
Range	60 km	74.63 km	At 450m a.s.l.	REQ-UAV-PERF-023
Cruise endurance	1 h	1.03 h	At 450m a.s.l.	REQ-UAV-PERF-011
Max. velocity	45 m/s	48.43m/s	At sea level	REQ-UAV-PERF-013
Max. Ceiling	5000 m	>5000m	-	REQ-UAV-PERF-009

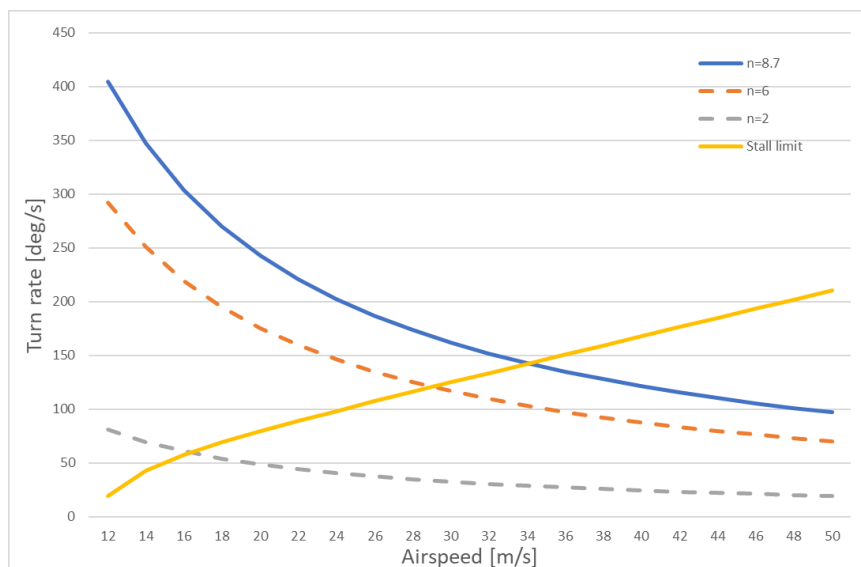


Figure 10.1: Analytical turn envelope of the Air-Guard drone

11. Operations

This chapter describes the activities that follow once the design is complete. First, the concept of operations and air traffic management will be discussed in [Section 11.1](#) after which the manufacturing plan will be described in [Section 11.2](#). Then, a cost analysis will be performed in [Section 11.3](#). [Section 11.4](#) describes the flow of activities once the DSE is finished, while in [Section 11.5](#) these activities are ordered in a Gantt chart. The return on investment will be described in [Section 11.6](#) and finally the software diagram is given in [Section 11.7](#).

11.1. Air Traffic Management

Air traffic management is "dynamic, integrated management of air traffic and airspace including air traffic services, airspace management, and air traffic flow management — safely, economically and efficiently — through the provision of facilities and seamless services in collaboration with all parties and involving airborne and ground-based functions" [43]. Therefore, this section is split up into five parts. Firstly, [Subsection 11.1.1](#) refers to the description of the two systems and the outline of the mission. Secondly, [Subsection 11.1.2](#) discusses the air and ground operations of the Air-Guard. Then, [Subsection 11.1.3](#) describes the air traffic services whereas [Subsection 11.1.4](#) describes the air traffic flow management. Lastly, [Subsection 11.1.5](#) describes the airspace management around the airport.

11.1.1. System Description and Mission Outline

The Air-Guard system encapsulates the process of using a morphing drone to neutralize an unlicensed drone. A more in-depth description of the system can be found in [Figure 11.1](#). It can be seen that the Air-Guard system or, more formally, referred to as the counter unmanned aerial system (CUAS), consists of the ground segment and the aerial segment. The ground segment consists of the ground operations and communications taking place while the system is active, this would in turn include the maintenance, charging, communication to air traffic management, and communication to the drone. The air segment includes the drone and its payload that will be used to immobilize unlicensed drones. These two systems work together to accomplish the mission objective and thus form the counter unmanned aerial system. As mentioned previously, there are stakeholders that are involved or interested in the project. Their relationships to the system are displayed in [Figure 11.1](#). Further, individual subsystem relations can also be seen in the system description diagram to understand what elements the mission consists of.

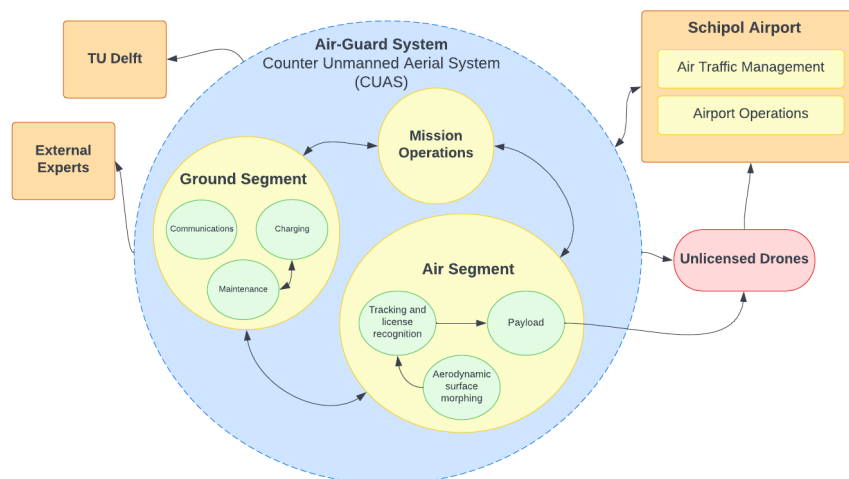


Figure 11.1: System description diagram for the Air-Guard system

Once it is understood what forms the basis of the Air-Guard system and identification of how external systems interact with Air-Guard, a basic idea of the operation concept can be defined. [Figure 11.2](#) displays the proposed operation concept that the Air-Guard system aims to perform. The drone should be able to be deployed on command, loiter, engage a detected target, neutralize it and then return to the ground where maintenance and charging of batteries can be carried out, defining the relation of the ground and air segment of the mission.



Figure 11.2: Proposed system operation sequence

11.1.2. Concept of Operations

The concept of operations of the drone is divided into two different sectors, air operations, and ground operations. The air operations describe the way the drone operates whilst flying above the designated airspace, whereas the ground operations describe the actions performed on and around the drone when it is not flying.

Air Operations

Schiphol airport in Amsterdam was chosen as the area of deployment of the system, this was chosen due to the fact that the project is being developed in the Netherlands, and as a result, the expertise in integration and operation is more readily available upon consultation. Amsterdam Schiphol airport is also the third busiest airport in Europe therefore it is also a good launching customer due to the high flow of air traffic that could be compromised ¹. Figure 11.3 represents the covered area of Schiphol airport that the Air-Guard system shall function within, in total the area covers approximately $28km^2$. The red area describes the monitoring zone of the airport, covering the entire $28km^2$. This area depicts the region, in which is any unauthorized drone detected and tracked. However, the mission also requires that the drone loiters around the area before even detecting an enemy drone. The loitering allows the drone to continuously be in the air and thus, lowers the response time. Therefore, loitering areas are also defined in Figure 11.3 with the proposed loitering path represented in Figure 11.4. This loitering path is approximately $30 km$ and this path should be covered 2 times in 1 hour. The loiter phase of the mission concept is important in order to achieve a quick response time, while loitering above the airport surface, the drone is able to remain in the air constantly and dive to neutralize an unlicensed drone threat as quickly as possible. The first iteration of the UAV will be designed to cover this area on its own. However, if the customer prefers a quicker reaction time, then multiple drones can be used to cover this area.

¹<https://gettocenter.com/airports/continent/europeDate> [Accessed: 19/06/2022]

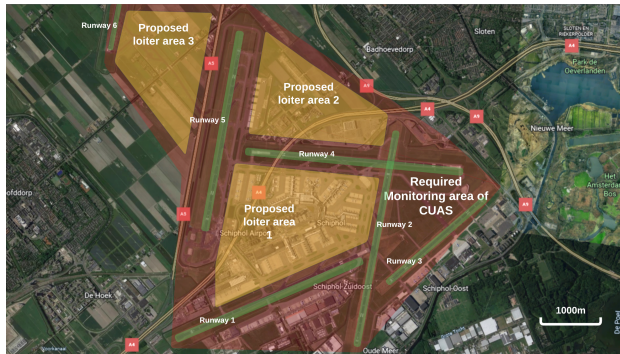


Figure 11.3: Planned C-UAS coverage area

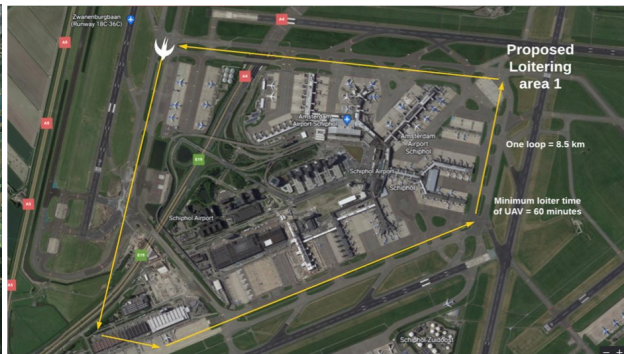


Figure 11.4: Planned loitering path of the UAV

Given that the loitering path and critical protection areas have been defined, the flight profile of the mission can be elaborated to give a better idea of how a hypothetical mission of the UAV could pan out during operations at Schiphol airport. Figure 11.5 describes the entire flight profile of the UAV during a nominal mission of loitering and neutralizing one unlicensed drone.

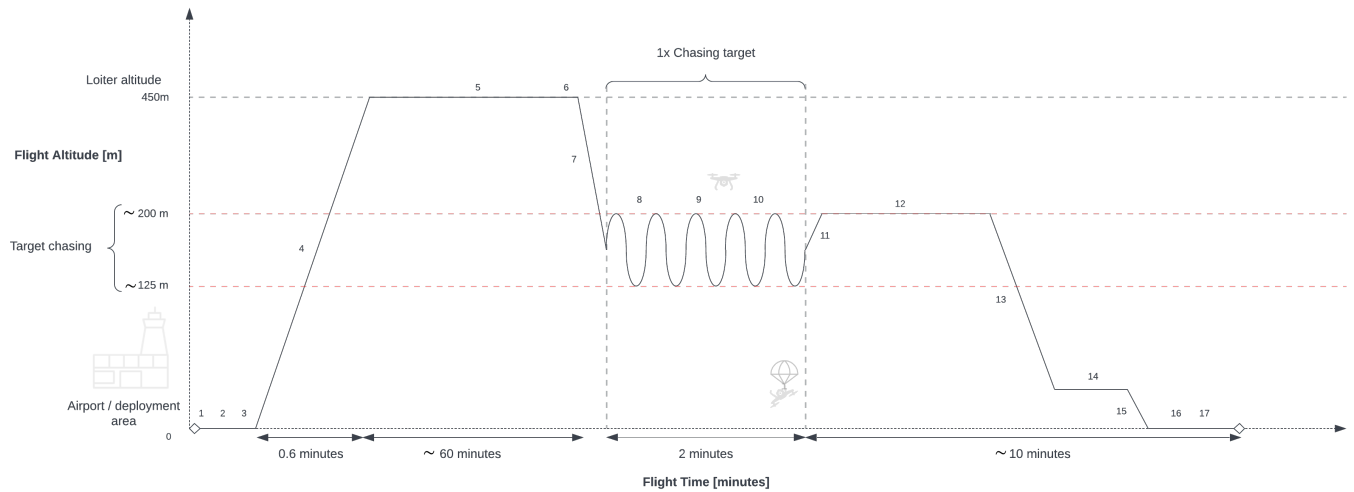


Figure 11.5: Possible flight profile diagram of the Air-Guard drone

Table 11.1 describes the various phases depicted as numbers in Figure 11.5 such that each part of the flight profile could be better understood. It should be noted that this is the optimum flight profile defined such that the drone loiters for 60 minutes before a target has been detected, triggering the dive and chase. The altitudes at which the UAV chases the unlicensed drone is again only illustrative, as it cannot be reliably predicted at what altitudes the unlicensed drones enter the action area.

Table 11.1: Flight profile description

#	Description of phase in flight profile
1	Start up systems
2	Pre-flight checks + load into launcher
3	Launch drone
4	Climb to loiter altitude
5	Loiter in specified path
6	Target detection
7	Dive to target
8	Arm payload + Chase target
9	Point payload to target
10	Fire payload
11	Climb to intermediate altitude
12	Cruise to landing zone
13	Descend to landing zone
14	Approach landing zone
15	Perform landing maneuver
16	Belly landing
17	Retrieve drone

However, the catching strategy is known. The drone will be loitering at relatively high altitude (450m above the airport surface) whilst waiting for an unlicensed drone. The ceiling of most commercially available drones is higher than 450m, but due to the wanted reaction time and the fact that most danger occurs with low-flying drones, this altitude was chosen. This ensures a quick reaction time while not interfering with the airport operations. Once a drone is detected via the ground segment and ATM (Air traffic management) in the action area, and further identified as an unlicensed drone, the Air-Guard drone will dive to intercept it. By positioning itself in the vicinity of the unlicensed drone, the net can be fired to catch it. If the unlicensed drone performs avoiding maneuvers, the drone will chase and predict the flight path for intercept.

However, the drone cannot go on flying for an unlimited time. According to the requirement REQ-UAV-OPER-001, listed in A, the drone will have to return to the designated landing spot when the drone battery has 20% of power remaining. The margin ensures that even if the drone has unfavorable flying conditions that require inefficient flying, the drone will still be able to reach the ground station. To prevent any harm to the airport operations, the drone shall avoid the areas described further in this section.

When the drone approaches the landing location and is prepared to land, it will slow down. The landing procedure for the drone is belly landing performed on a soft surface such as grass between the runways. To minimize the chance of damage during landing, the drone will have to slow down as much as possible. It will fly at minimum stall speed and pitch up heavily. Following this, the drone will pitch the tail up and land on the skid blocks to cushion the drone in belly landing.

Ground Operations

The ground operations consist of multiple stages including the launch operation, the landing operation with and without payload, and maintenance. These operations are described in this section.

Firstly, the launching operation will be performed with the aid of a human operator. For launching, the Eli UAV pneumatic catapult PL-8 will be used. This device is a pneumatic launcher that is capable of launching an 8 kg drone at 25 m/s at a 30 degree angle². To launch the drone, the responsible person will need to position the drone on the launcher and then release the pneumatic pressure.

Secondly, when the drone has completed the return to the landing spot, the drone shall be retrieved by the human operator. In addition to this, depending on if the drone has launched the payload canister, this shall be retrieved as well. The payload canister can be found through the GPS signal emitted by a locator that is incorporated in the trajectory weights (further discussed in Chapter 5). Special care shall be taken as the payload could include the unlicensed drone that could have landed in a potentially critical zones such as the runway and aircraft taxi paths. Once on the ground, the battery of the drone can be replaced with one of full charge and following the re-packaging of the payload the drone can be redeployed within 10 minutes of recovery if the payload is ejected and 3 minutes if the payload has not been ejected.

Lastly, to prolong the lifetime of the drone, maintenance to the drone shall be conducted once every fifty flights. This includes removing the components described in Section 11.2 in the opposite order to check for quality and inspection of the structures. In addition, after every flight, the battery shall be replaced by a fully charged battery, and visual inspections shall be performed.

²<https://eli.ee/products/7/uav-pneumatic-catapult-koopia-> [Accessed: 13/06/2022]

11.1.3. Air Traffic Services

Air traffic services give information to the incoming and outgoing aircraft and alert them of any potential threats. In short, the main purpose of the air traffic services is to prevent dangerous situations [43].

According to the evaluation report of the Dutch Drone Delta experiment at Rotterdam Airport, integration of manned and unmanned drones can be safe as long as a stable line of communication is established ³.

However, technical systems can be prone to failure. Therefore, in the case of a loss of communication with the control tower, the drone shall have backup procedures in place to prevent dangerous situations. Such failures include loss of communication with the control tower and loss of GPS signal.

When the drone has lost contact, it will determine its altitude. If the drone is below an altitude of 200 meters above the runway, the drone will initiate a steep climb. Once it has reached an altitude of 300 meters above the runway, it will level the pitch. Whilst doing so, the drone will perform a sustained turn at a constant turn radius. The drone shall remain in this maneuver and wait for the line of communication to be restored. In the case the drone runs out of battery, it will determine if it needs to cross routes used by air traffic to return to the landing spot. If not, the drone will maneuver to the designated landing location. However, when it needs to cross a runway, the drone will rise up to 450 meters, then cross the runway and fly towards the landing spot to land.

On the other hand, if the drone loses GPS signal, it will send a message through the available radio frequency link with the ground station. Then, an air traffic controller can overwrite the autopilot by using a remote control, i.e. the widely used control method for non-autonomous drones.

11.1.4. Air Traffic Flow Management

The focus of air traffic flow management is to avoid the congestion of certain control sectors ⁴. This is achieved through careful planning for arriving and departing aircraft. The planning takes into account a minimal delay in operations and assumes that airport operations are not influenced by drone operations. Therefore, the drone shall be operating without restricting the air traffic of the respective airport.

Three separate scenarios should be dealt with. These are when the drone needs to cross a runway and when an unlicensed drone needs to be caught above a highly populated area or above an aircraft.

If the drone needs to cross the runway, this can be done in two ways for the safety of the aircraft and the UAV. Due to the wake created by heavy and medium weight aircraft when taking off or landing, the drone needs to wait 3 minutes before crossing the path the corresponding aircraft has taken [43]. However, if waiting is not possible, due to the landing and take-off frequency of airplanes, the drone can also cross the runway independent of an aircraft landing or taking off if the vertical separation is at least 300 meters [43].

On the other hand, if the system detects an unlicensed drone, the airport operations will be halted. In that scenario, the drone shall be informed of the last departure time of the runway it needs to cross. If that is less than 2 minutes, the drone needs to stay above 300 meters from the runway before diving and chasing the unlicensed drone. Otherwise, if the departure time is longer than 2 minutes ago, the drone has the freedom to fly over the runway directly.

When an unlicensed drone has managed to infiltrate the airport area, special care has to be taken to minimize the chances of causing any damage to surrounding structures and technology. Therefore, the drone will prioritize interceptions in lower risk areas. To mitigate the risk of damage, an air traffic controller is summoned to follow the interception upon rogue drone detection. The controller can authorize the arming of the payload whilst the UAV flies to the rogue drone. This would likely happen simultaneously with ATM pausing airplane operation for the duration of the interception mission. At a later time, he can decide to disarm it, if necessary.

³<https://www.dutchdronedelta.nl/uitkomsten-use-case-3-3-drones-op-luchthavens/> [Accessed: 02/06/2022]

⁴<https://skybrary.aero/articles/air-traffic-management-atm> [Accessed: 15/06/2022]

11.1.5. Airspace Management

Drones are not allowed to fly anywhere without a special permit. The certification differs per area and country. In the Netherlands, extensive websites map restricted areas where no one is allowed to operate a drone ⁵. The area surrounding airport Schiphol is one of these examples.

To fly in these areas without being flagged as an unlicensed drone, one needs to receive permission. This can be done by unlocking the geo-fence for each drone. A special permit for the area surrounding Schiphol can be requested from the company that installs the geo-fences.

11.2. Manufacturing, Assembly & Integration Plan

Producing, integrating, and assembling the given design represents a large portion of the project's timeline. This section highlights how components are manufactured, and put together efficiently, to deliver a product that complies with design specifications. The top-level process is expanded in Figure 11.6.

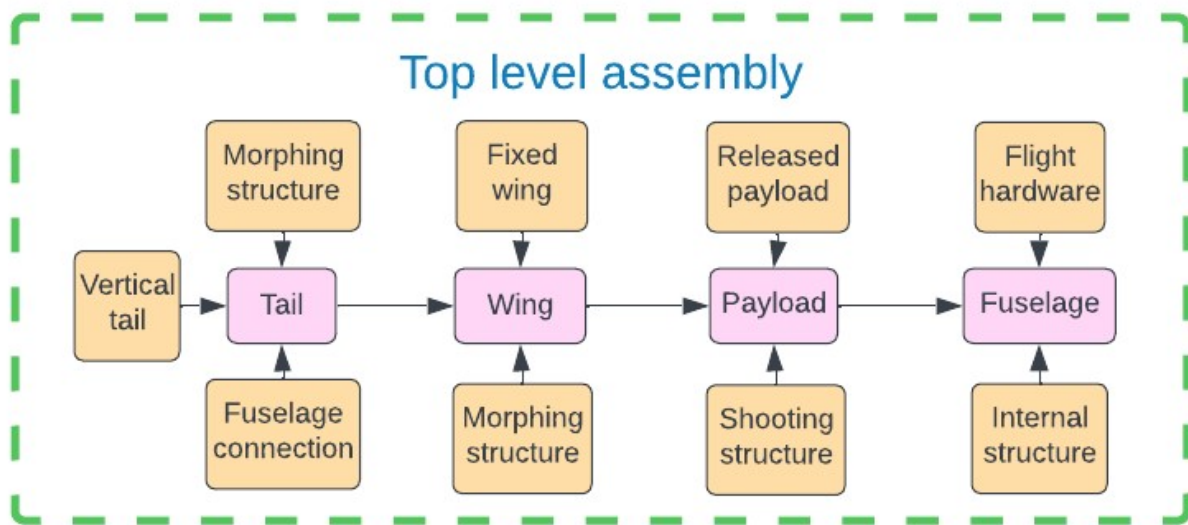


Figure 11.6: Top Level Assembly

As can be seen, the Air-Guard drone consists of four distinct main assemblies, which require very different manufacturing and integration steps. Materials and manufacturing processes were selected to minimize costs and produce a sustainable drone. These are summarized in Table 11.2. Moreover, details for manufacturing, assembling, and integrating flow are provided for each major drone assembly in Table 11.2, as well as Figure 11.7 - Figure 11.9.

⁵<https://map.godrone.nl/> [Accessed: 10/06/2022]

Table 11.2: Overview of parts material and manufacturing methods

Assembly	Component	N	Material	Manufacturing process
Payload	Payload casing+pseudo-nose	1	ABS	3d printing
	Net	1	HDPP	Weaving
	Weights	4	Steel	
	Payload tube	1	Al6013-T6	Thin sheet welding
Fuselage	Fuselage frame	1	Balsa Wood	Punching, then steam forming
	Fuselage skin	1	Balsa wood	Punching, then steam forming
	Skid Block	1	PLA	3d printing
Wing	Front + Rear spar	1	Balsa wood	Punching, then steam forming
	Skin	2	Balsa wood	Punching, then steam forming
	Morphing wing fairing	2	Celanese VECTRA A950LCP - NematX	3d printing
	Morphing wing spar	2	Al6013-T6	rubber forming with adhesive bonding of middle part
	Wing platelets + connectors	22	Celanese VECTRA A950LCP - NematX	3d printing
	Alula	2	Balsa wood	Punching, then steam forming
Tail	Morphing tail structure	1	Celanese VECTRA A950LCP - NematX	3d printing
	Tail fairing structure	1	Celanese VECTRA A950LCP - NematX	3d printing
	Tail platelets + connectors	8	Celanese VECTRA A950LCP - NematX	3d printing
	Vertical tail	1	Balsa wood	Punching, then steam forming

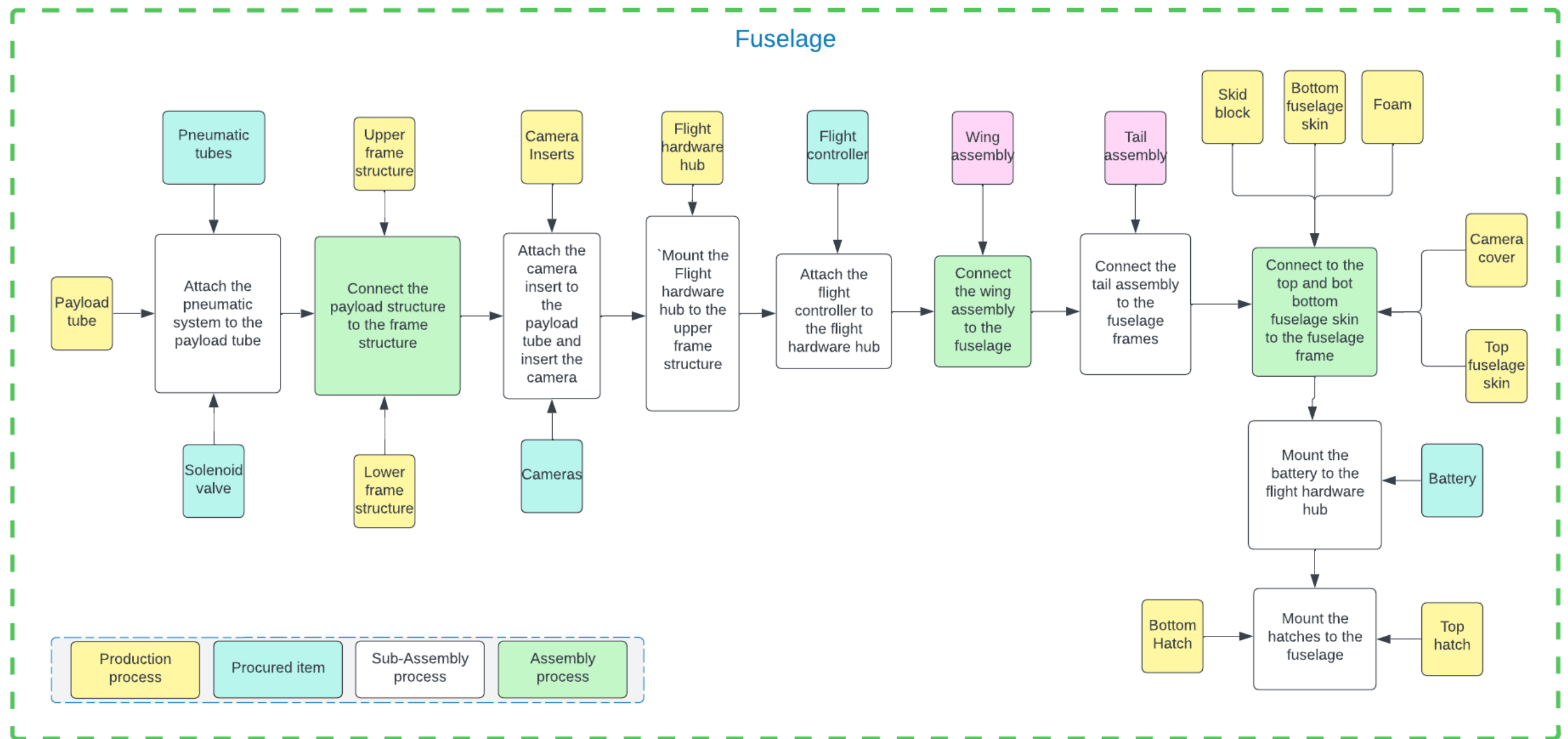


Figure 11.7: Fuselage Assembly

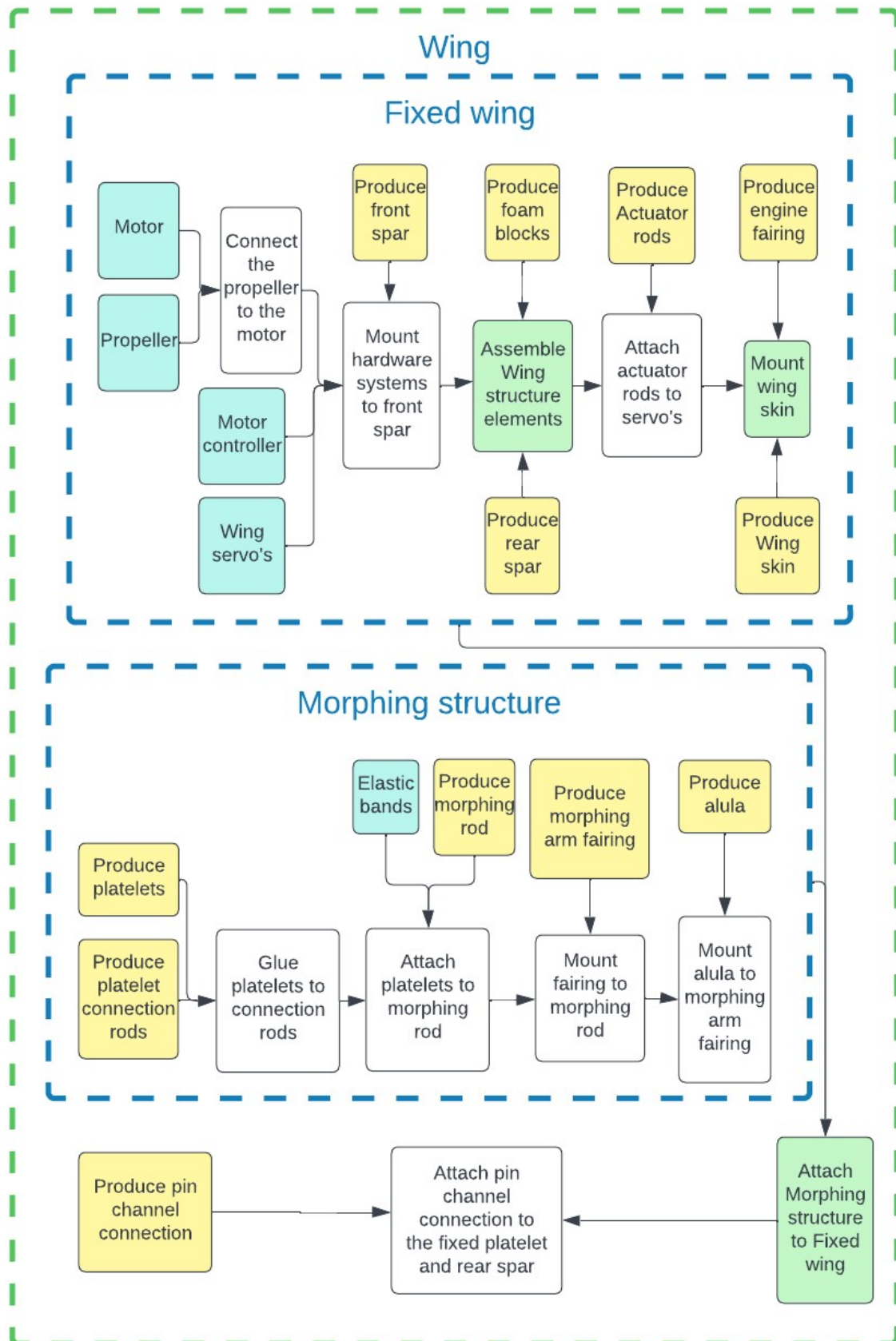


Figure 11.8: Wing Assembly

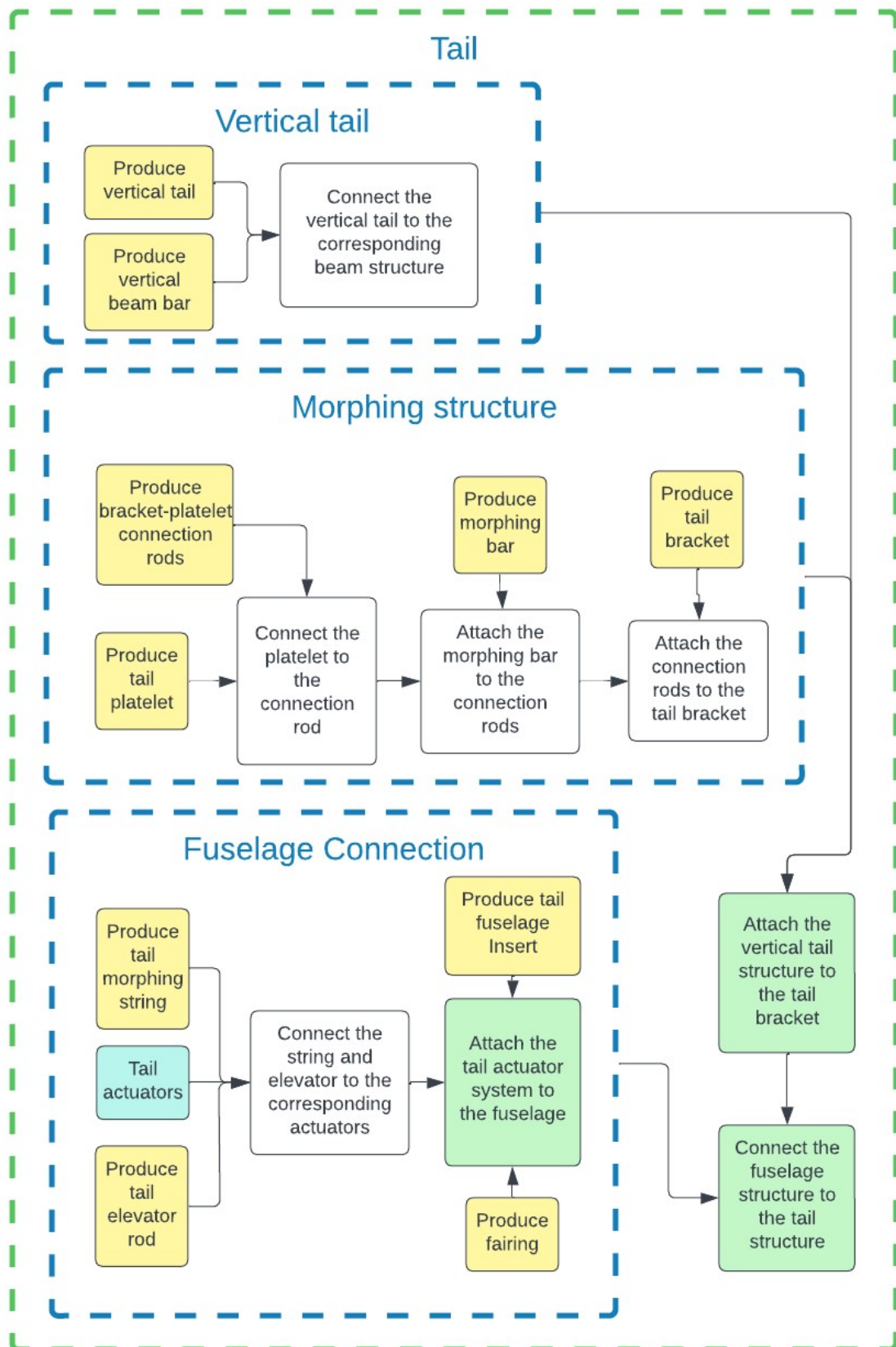


Figure 11.9: Tail Assembly

11.3. Cost Analysis

The cost of the Air-Guard system is split up into 5 different sectors: development, production, operation, maintenance and end-of-life. The addition of these sectors form the total budget.

The breakdown of the origin of the costs per sector can be seen in figure Figure 11.10 below.

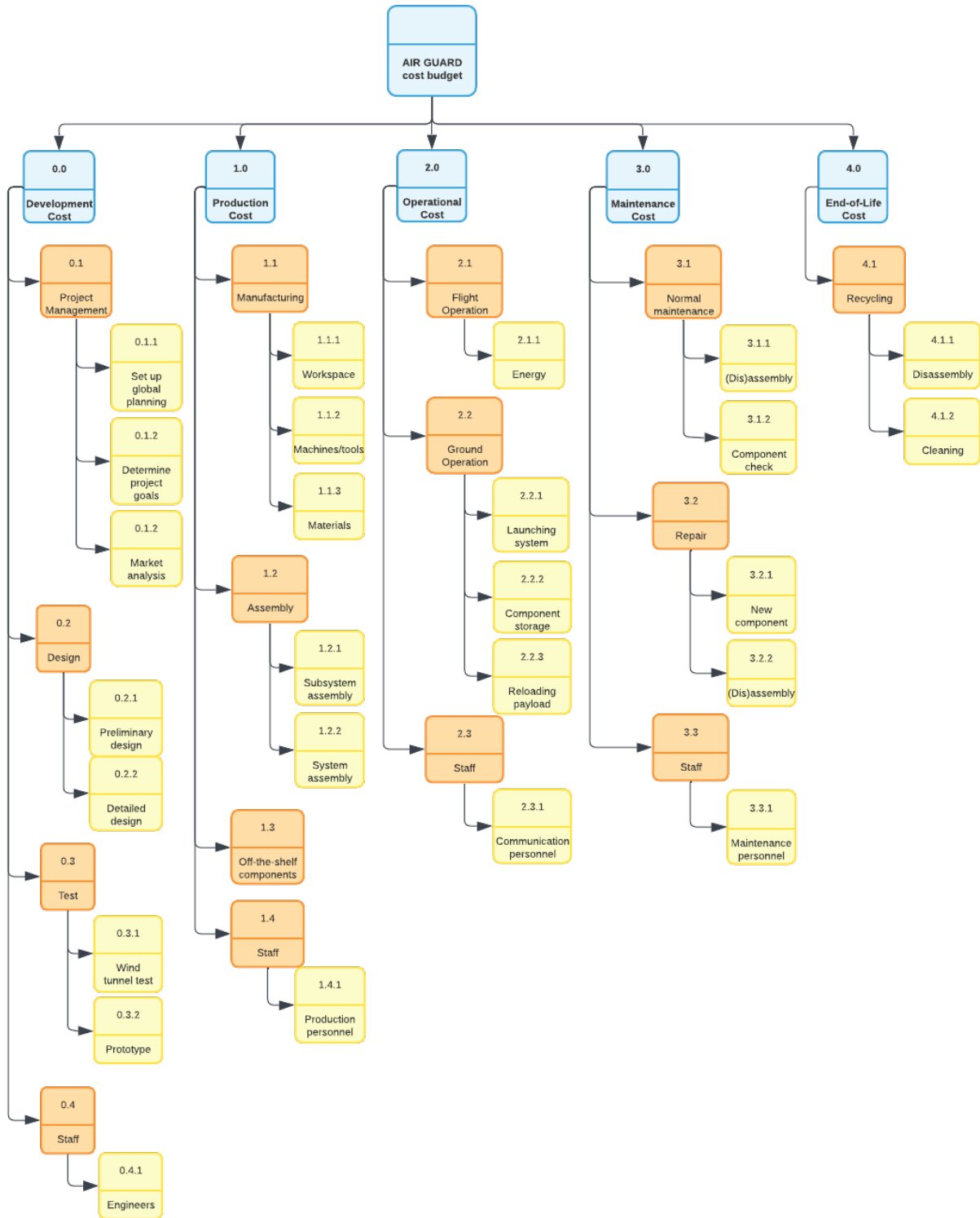


Figure 11.10: Cost breakdown structure

11.3. Cost Analysis

The costs of the development phase are worked out further in [Table 11.3](#), where workdays is the through-put time it takes for a task to be finished, workforce the number of engineers working on the task, and completion time is the product of the former two.

Table 11.3: Development costs for the Air-Guard project

Work Package based Costs					
Task	Id	Workdays	Workforce	Completion time (Engineering) Days	Labor Cost in €
Perform project planning	1	4	10	40	8796
Assign project roles	1.1	0.2	10	2	439
Define project development logic	1.2	2.4	10	24	5277
Define project rules	1.3	0.2	10	2	439
Define project need and goal	1.4	0.3	10	3	659
Conduct organizational risk analysis	1.5	0.5	2	1	219
Develop project plan report	1.6	0.8	10	8	1759
Perform functional analysis and requirement discovery	2	4	10	40	8796
Perform literature study	2.1	0.3	10	3	659
Perform market analysis	2.2	0.8	2	1.6	351
Perform functional analysis	2.3	2	5	10	2199
Allocate resource and budgets	2.4	1	1	1	219
Perform requirements discovery	2.5	2	3	6	1319
Perform technical risk analysis and contingency management	2.6	1.7	2	3.4	747
Create preliminary design concept	2.7	1	5	5	1099
Form baseline report	2.8	1	10	10	2199
Perform preliminary concept development	3	10	10	106	23309
analyse design option	3.1	3	5	15	3298
Analyse system interfaces	3.2	0.4	3	1.2	263
Perform design concept trade-offs	3.3	1	10	10	2199
Update project deliverables	3.4	0.6	10	6	1319
perform preliminary sizing	3.5	5	5	25	5497
Plan verification and validation	3.6	0.7	4	2.8	615
Conduct performance analysis	3.7	2	4	8	1759
Size subsystems	3.8	2	4	8	1759
Form midterm report	3.9	1	10	10	2199
Conduct mid term review	3.1	2	10	20	4398
Perform detailed design	4	19	10	190	41781
Perform detailed subsystem design	4.1	11	8	88	19351
Develop flight dynamics model	4.2	11	2	22	4837
Submit jury review	4.3	1	2	2	439
Update technical budgets	4.4	1	2	2	439
Create production plan	4.5	3	2	6	1319
Form final report	4.6	5	10	50	10995
Conduct final review	4.7	2	10	20	4398
Close out R&D	5	6	10	70	15393
Perform final presentations	5.1	6	10	60	13194
Meet tutor and coaches	5.2	0.5	10	5	1099
Final briefing and close out	5.3	0.5	10	5	1099

As can be seen in this table, the tasks are split up into the amount of time it takes to complete. Based on this time and the responsible person, the cost of labor can be determined.

In addition to this, the detailed cost breakdown of the production sector for the self-manufactured components

and off-the-shelf components can be seen in Table 11.5 and Table 11.4 respectively.

Table 11.5: Parts that need to be manufactured

Table 11.4: Price of the off-the-shelf components

Component	Price [€]
Parachute	2500.00
Pyrotechnic charges	30.00
GPS	10.00
Lights	5.00
Gas canister	2.00
Pneumatic tubing	20.00
Solenoid valve	72.60
Antenna	19.25
Flight controller	350
Tracking camera	36.90
Infrared camera	44.90
Battery	147.70
Operational lights	10.00
Electric engines	71.80
Propellers	8.00
Motor controllers	39.99
Wing morphing actuators	120.00
Alula actuators	120.00
Morphing tail actuators	60.00
Elevator actuators	60.00

Component	Time allocation [hr]	Manufacturing costs [€]
Net	5	15
Weights	2	10
Payload casing + pseudo nose	2	6
Fuselage frame	6	20
Skid blocks	0.16	2
Fixed wing Spars	1	5
Morphing wing spar	0.5	1
Morphing wing fairing	0.16	5
Wing platelets + connectors	0.16	10
Elastic Tendons	2	10
Alula	0.16	1
Morphing tail structure	2	2
Tail fairing structure	0.16	2
Tail platelets + connectors	0.16	5
Vertical tail	1	5

One component in the production costs stands out, in particular. The selected off-the-shelf parachute provides all the required performance and eliminates the need to produce the parachute, but on the other hand presents an unbearable increase in price. The reason for this high price is because the selected parachute provides additional functionalities that are not required for this design. Among these are: full autonomy (the parachute doesn't require connection to external systems or batteries), auto-deployment based on flight data or automatic flight termination computer. On top of that, ultralight design and high performance composite materials further increase the price⁶. If this parachute was used in production, it would make more than half of the total price. For that reason, it was decided to produce the parachute in-house, with a price target of 500 euros, reducing the complexity as well as the total production cost to 2,391 euros.

Finally, the direct operational costs are developed in Table 11.6

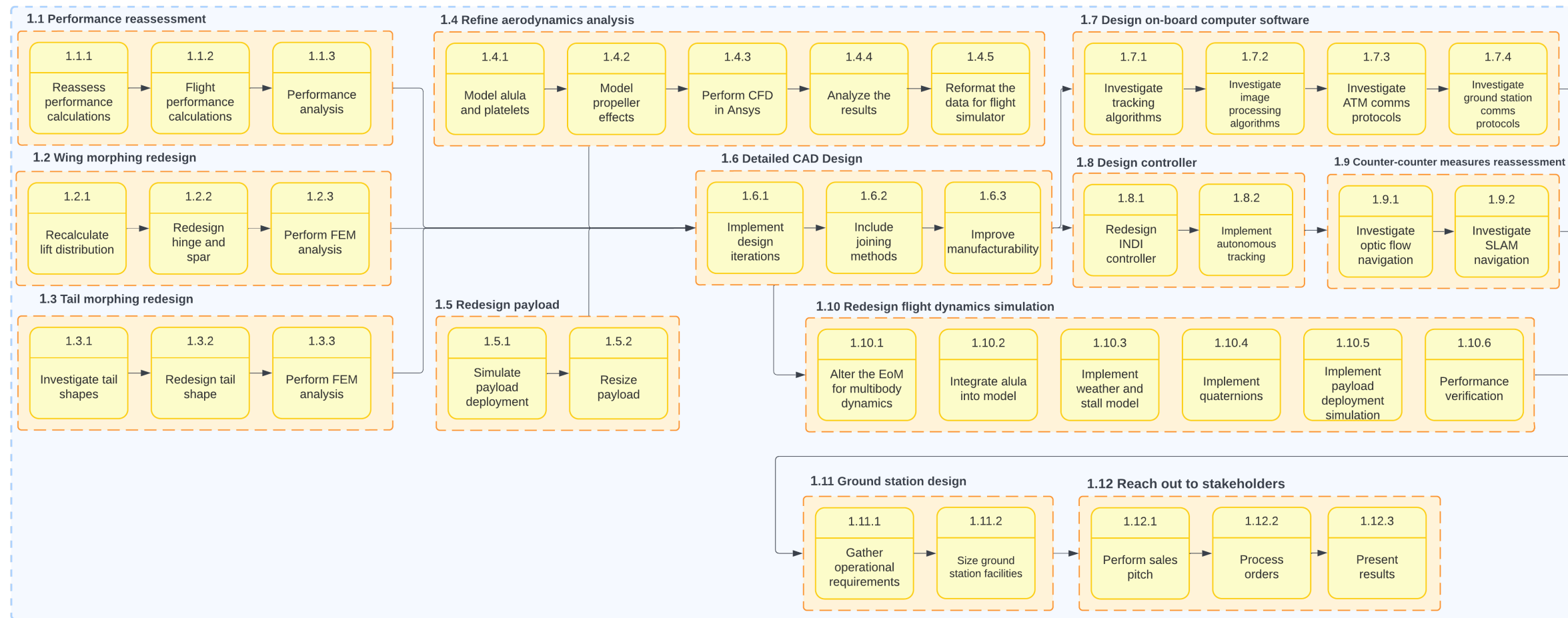
Table 11.6: Direct costs breakdown

Item	Cost per week [€]
Facilities rent	425
Office supplies	71
Cleaning	120
Travel expenses	175
Bank charges	2.5
Accounting and legal expenses	106.5
Computers	54
Parking spaces	210
Sales and marketing	1375
N. Weeks	10
Total Direct operating costs	25,390

⁶<https://dronerescue.com/drs-10/> [Accessed: 10/06/2022]

11.4. Project Design & Development Logic

1.0 Second detailed design iteration



2.0 Prototyping

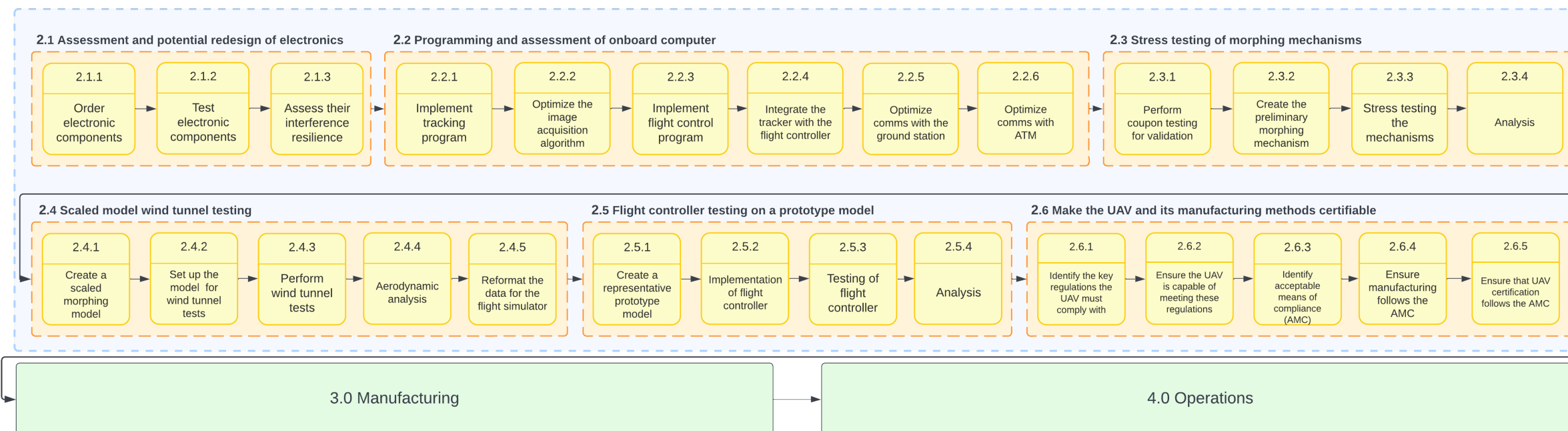


Figure 11.11: Project design and development logic

11.6. Return on Investment

Return on investment (ROI) is traditionally defined as the ratio between return and total costs of investments⁷. Or in mathematical terms:

$$ROI = \frac{\text{Net income}}{\text{Total cost of investment}} \cdot 100\% \quad (11.1)$$

Furthermore, the net income is defined as the difference between generated revenue and the total cost of investment. Both of these can then be further deconstructed. The total revenue is the number of products sold times the price of a single unit. The number of sold units can be estimated by multiplying the market volume of the product by the achievable market share. Similarly, the total costs can be subdivided into development costs, manufacturing costs, and direct operational costs. The Equation 11.1 thus becomes:

$$ROI = \frac{P_{unit} \cdot V_{market} \cdot AMS - (C_{dev} + C_{manf} + C_{dir.op.})}{C_{dev} + C_{manf} + C_{dir.op.}} \cdot 100\% \quad (11.2)$$

Where P stands for price (unit price in this case), C for cost (development, manufacturing or direct operational), V_{market} is the market volume and AMS is achievable market share. These values will be estimated in the following subsections.

11.6.1. Unit Price

As one of the requirements, the maximum unit price is required to be below 5000 euros (REQ-CUAS-STK-007). This price will be taken to calculate the ROI. Even though the unit price is 2,391 euros, the 5000 euro price will ensure that unforeseen expenses can be covered. Furthermore, additional investments would be required to produce detailed design and manufacturing processes for the ground station, which has to be present at every airport for the system to be operational. This cost was not estimated, as detailed development of the station was not considered in the project.

11.6.2. Market Volume

Sales data of competitor C-UAS is not public. Therefore, the market volume has to be estimated by considering the number of potential customers multiplied by the number of units that each customer would purchase on average. Airports are the primary target customer, the number of potential customers equals the number of airports that are facing the threat of breach of their airspace by rogue drones. Since the initial target market will be Europe, the number of affected airports is the number of European international airports, which is 347⁸.

Next, the current design of the drone is optimized to cover an airport size of Schiphol for one hour, after which the drone will be recovered and the battery has to be changed. Considering the time that will be used to recover the drone, reload the payload, replace the battery and attach the drone to the launch pad, it is safe to assume that 2 drones are required to maintain continuous patrol over the airport. Adding one more drone to account for unforeseen events, e.g. maintenance, results in a total number of 3 drones per airport. Furthermore, one ground station is required per airport. The total potential market volume is 1,041 drones to be sold (together with 347 ground stations).

11.6.3. Achievable Market Share

The achievable market share is the proportion of market volume that can be covered by the product, given various constraints and trends in the market. In this case, multiple factors come into play. The first one is the fact that UAVs are not the only way to prevent breaches by rogue drones. Other alternatives exist that are often preferred by customers. These include GPS spoofing devices, RF jamming devices, ground-based net shooting devices, or ground-based lasers. Not all of these options are suitable for airport protection. Radiofrequency or GPS jamming are examples of such systems since essential ground systems such as ILS, surveillance approach radars, radio communications as well as onboard approach, landing, and navigational systems would be affected, posing an unacceptable safety threat.

⁷<https://www.investopedia.com/terms/r/returnoninvestment.asp> [Accessed: 15/06/2022]

⁸<https://www.airportarrivals-departures.com/airports-in-europe.htm> [Accessed: 15/06/2022]

Secondly, it must be considered that not all systems provide the same service. While some systems (about 27% of all) combine both detection and mitigation functions, others specialize only in one of these categories. About 33% of the systems provide only detection and 40% are designed only for interdiction. The system designed in this project would fall into the last category. While the ground station would provide detection data to the UAV, the data itself would be provided by airport systems. That means that the airport must be equipped with sufficient detection equipment to allow for the full functionality of the system. Furthermore, out of the suitable solutions, 37.5% of systems use spoofing while 62.5% uses kinetic attack. The kinetic attack systems can be further divided into laser devices (20.8% of suitable systems), net shooting devices (33%), and drone-based systems (8.3%) [44]. The designed UAV combines the last two categories and thus, would serve as a substitute for such devices.

In conclusion, considering all the discussed factors and trends, the estimated achievable market share is 42%.

11.6.4. Net Income

As mentioned earlier, the net income is calculated by multiplying the unit price by the total market volume and by the achievable market share.

First, multiplying the number of airports to be served (347) by the achievable market share (42%) gives a potential reach of 146 airports. Considering 3 drones and 1 station per airport, then results in 438 drones and 146 stations. With 5000 being the price of a single drone, the net income is estimated to be 2,190,000, not considering the revenue that would be generated selling the ground stations.

11.6.5. Costs

Individual components of the total costs have been calculated in Section 11.3. Note that the period for which the initial costs were calculated was taken to be 10 weeks, while the manufacturing costs were obtained by multiplying the costs per unit by the number of drones to be sold as estimated previously.

11.6.6. Results

The following table shows all the values considered in the calculation of return on investment:

Table 11.8: Overview of ROI parameters

Item	Value	Item	Value
Market volume	1,041	Development costs	€98,076
Achievable market share	42%	Manufacturing costs	€1,047,258
Unit Price	€5000	Direct operational costs	€25,390
Net revenue	€2,190,000	Total costs	€1,170,724

By using Equation 11.2, a return on investment of **87%** is obtained. There is no objective metric that would allow evaluating if such ROI is good or not, as that depends on the risk tolerance and long-term investment strategy of a particular investor. Furthermore, this estimated ROI would be valid only for the very initial phase of the project, and so would have to be recalculated as soon as the product is released to the market, and its popularity can be quantified with more reliable data ⁹.

⁹<https://www.investopedia.com/terms/r/returnoninvestment.asp> [Accessed: 15/06/2022]

11.7. Software Diagram

From requirements, it was required that the drone would be able to autonomously loiter and avoid obstacles such that a high degree of hands-free operations would be possible. To satisfy the requirement, it is important to define a primary software control loop for an autonomous navigation system that actuates the morphing surface and controls the drone's attitude and altitude.

A simplified overview of the basic states of the drone is shown in [Figure 11.12](#) briefly depicting the various states of the systems and the loops in which they occur, further going into the software functionality of the drone if an unlicensed drone is detected [Figure 11.12 B](#) displays in interrupt sequence ending in the firing of the payload.

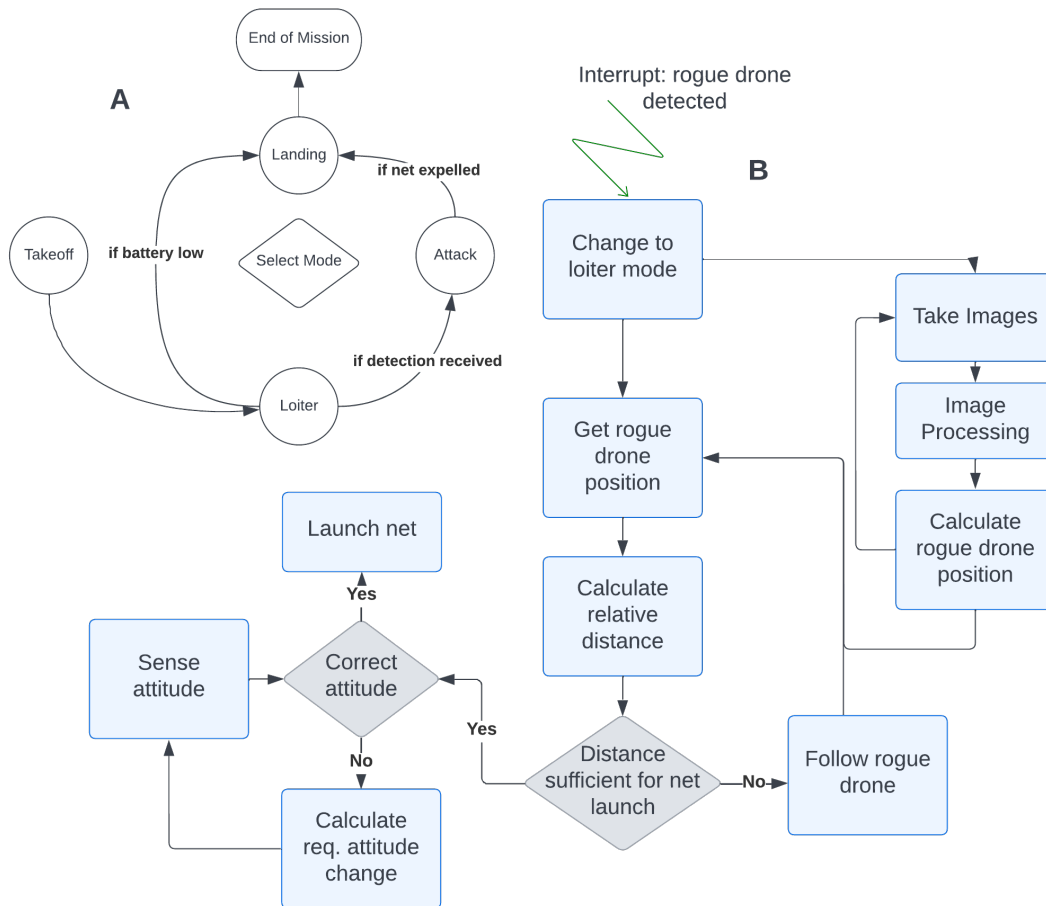


Figure 11.12: A: Air-Guard drone system state diagram B: Drone detection interrupt logic

12. Sensitivity Analysis

Performing sensitivity analyses on the drone systems can lead to more optimized design parameters. Ultimately, this process can converge to a more ideal design. This procedure is documented for structures, payload design, aerodynamics, and flight dynamics, in [Section 12.1](#), [Section 12.2](#), [Section 12.3](#), and [Section 12.4](#) respectively.

12.1. Structures

Sensitivity analysis is an important step in the design process of the structures as it provides insight into how the dimensions and mass would change for a change in the magnitude of the loads.

12.1.1. Wing Box

The wing box parameters depend on the stresses resulting from the loadings received from aerodynamics. Thus, the sensitivity analysis focuses on the sensitivity of the stress due to the applied loads. For this, the stress is plotted against different moment loads around x and y, shown in [Figure 12.1](#), the color darkness is proportional to the stress magnitude.

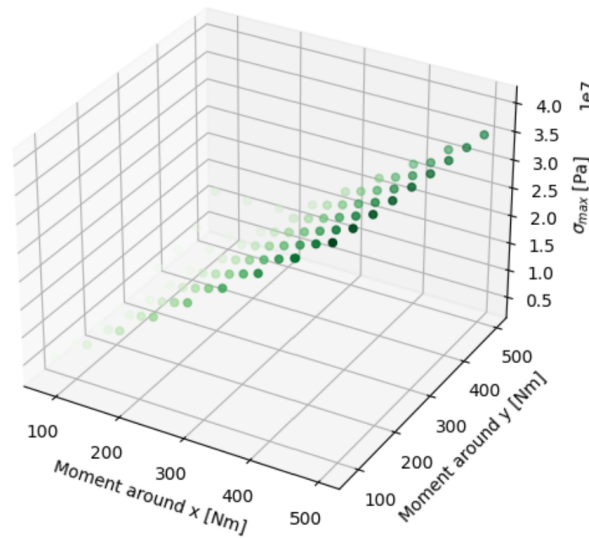


Figure 12.1: Maximum stress against moment loading in x and y

[Equation 6.3](#) suggests that the relation is linear, the plane shape shown in [Figure 12.1](#) confirms this expectation.

12.1.2. Morphing Spar

The morphing spar represents a key component in the morphing mechanism, thus a deep understanding of how it is affected by other parameters is important. As explained in [Subsection 6.5.2](#), V_x and M_y are disregarded because they are significantly lower than V_y and M_x , respectively. This, together with the fact that the analysed structure is symmetric ($I_{xy} = 0$), simplifies [Equation 6.8](#) and [Equation 6.10](#) to [Equation 12.1](#) and [Equation 12.2](#) respectively:

$$q_s = -\frac{V_y}{I_{xx}} \int_0^s t y ds \quad (12.1)$$

$$\sigma_z = \frac{M_x}{I_{xx}} y \quad (12.2)$$

It is clear from these equations that they are linear in V_y and M_x , respectively. Consequently, the sensitivity analysis performed by changing the loads does not lead to divergent results.

Considering the moment of inertia, the variation with the dimensions is not linear anymore. As an example, for a rectangle, the formula is given by [Equation 12.3](#):

$$I_x = \frac{bh^3}{12} \quad (12.3)$$

Thus, for bending around the x-axis, the stress decreases linearly with increasing b , but quadratically with h (not with h^3 as the distance to the neutral axis also increases linearly with h). To decrease the bending stress, it is more efficient to increase h rather than b , if not constrained by other factors. Looking at the shear caused by torsion, given by [Equation 6.9](#), it also varies linearly with the applied torque.

12.1.3. Other structures

The sensitivity analysis for the fuselage structure and tail were not carried out separately, because, for their structural analysis, the same formulas were used as in [Subsection 12.1.1](#) and [Subsection 12.1.2](#). This leads to the same results, making the section redundant.

12.2. Payload

A sensitivity study was performed to see how much the design of the payload would depend on other design changes.

The main driver of the payload subsystem is the parachute. With 315 g, its mass is half of the ejected payload mass. The parachute size is driven by the mass of the drones the UAV needs to be able to catch (REQ-UAV-PERF-002), as heavier drones need bigger parachutes to float down at a safe rate.

If the required drone mass would increase beyond 10 kg, a heavier parachute would be needed. As most drone parachutes beyond this class are rated for 20 kg or more, the mass of the parachute would increase to 500 - 1500 g^{1 2 3}. This would cause a snowball effect, further increasing barrel size, mass, and center of gravity shift, which decreases stability.

This is why a thorough market analysis was performed at the beginning of the design process, to investigate the range of drones that the UAV would encounter during operations. From this, it was concluded that consumer drones rarely weigh more than 4 kg, making the chance of needing a bigger parachute very small.

12.3. Aerodynamics

A sensitivity analysis was performed on the aerodynamic analysis of the wings. The main part of the aerodynamic analysis was done in OpenVSP and to verify that the results are valid, a few input changes have been done to see if the results are consistent. Changes in parameters were modelled in openVSP by hand and simulated.

OpenVSP also displays the convergence rate. Only the results that show expected behavior in the convergence rate were used while designing. For the process of modeling the drone, this meant that sometimes the model or meshing had to be changed due to the results not being consistent or converged.

¹<https://www.ebay.com/itm/143696891140> [Accessed: 13/06/2022]

²<https://www.foxtechfpv.com/foxtech-parachute-with-ejector-capsule-for-20kg-uav-airplanes.html> [accessed: 15/06/2022]

³https://www.austars-model.com/recovery-parachute-for-20kg-class-uavuasmultirotor_g16491. [Accessed: 15/06/2022]

12.4. Flight Dynamics Model

The flight dynamics model is highly sensitive to the models of the external forces and moments. It is least sensitive to the gravity model, as the UAV loiters at relatively low speeds and altitudes, allowing a flat earth model to be assumed. The sensitivity on the engine model is moderate as a small change in the values of the thrust output only causes a small change in the simulator's behavior. This may also be attributed to the aerodynamic model as it causes a 'damping' effect for small fluctuations in the other external forces and moments.

Lastly, the simulator proves to be most sensitive to the aerodynamic model. This is because the aerodynamic forces and moments are derived from the coefficients output by OpenVSP. In combination with the UAV's small inertia yet high velocity, a tiny change in the aerodynamic coefficients can induce a non-negligible force or moment acting on the vehicle. This was noticed when OpenVSP's aerodynamic solver output small floating-point errors in the lateral aerodynamic coefficients in their 5th decimal digit. After being dimensionalized at a flight velocity of 35 m/s this led to a moment of at least 0.075 Nm , which is non-negligible. Hence the reliability of the flight dynamic model is most dependent on the aerodynamic model used and its accuracy.

In addition, the n-D lookup tables tend to propagate errors if faulty aerodynamic data is provided such as outliers. For example one of the configurations in OpenVSP contained a small twist difference between the two wings, leading to a disproportionately large increase in the drag, as can be seen in Figures 12.2 and 12.3. Even with a linear interpolation scheme, the error propagation is quite noticeable and it is even worse for the cubic spline scheme.

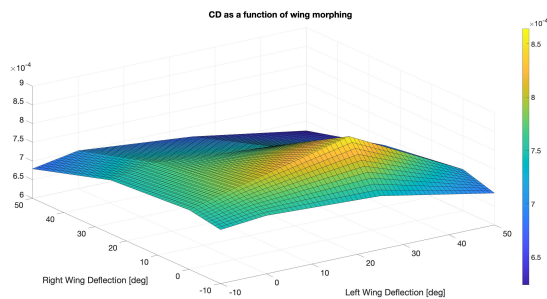


Figure 12.2: C_D as a function of wing morphing with a single outlier

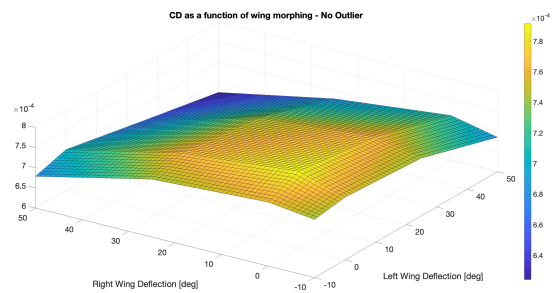


Figure 12.3: C_D as a function of wing morphing without an outlier

13. Verification & Validation

This chapter documents the Verification and Validation steps that were taken, to prove that the various design methods actually result in requirement compliance, and ultimately mission success. Payload, structures, flight dynamics, and aerodynamics can be found in [Section 13.2](#), [Section 13.1](#), [Section 13.5](#), and [Section 13.4](#) respectively

13.1. Structures

The first step in the structural analysis of different components was to construct the loading diagrams. To verify them, different 'sanity checks' were performed such as:

- Check the magnitude of output values.
- Check if at the tip of the structure the magnitude of forces and moments is 0.
- Check if the curvature of the graph is correct (higher values for shear translate into a steeper graph for moments).
- Check if the values of shear force at the root equal the total lift force.

Then, for idealizations, it was checked if the centroid and moments of inertia were around the same value as for the real structure. To check the stresses in the wing box, similar parameters as in an example problem from [Megson](#) book, were loaded in the code. The results of the stresses proved to be similar, although there existed significant differences between the inputs due to the lack of data. Moreover, it was checked if the resultant force from the internal shear flows adds up to the external shear force applied to the structure.

Considering both wing and tail morphing spars, the shear stresses were plotted for loads on the x and y-axis separately for verification. The typical load distribution for the cross-sections was known, as shown in [Figure 13.1](#). Thus, under a vertical load, the structure (in black) would have the shear stress distribution shown in red. The shear stress increases linearly in horizontal flanges but varies cubically in vertical flanges. The stress distribution calculated by the code is then compared with the expected results.

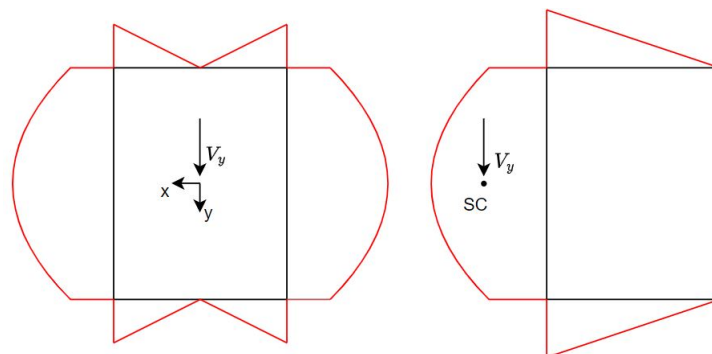


Figure 13.1: Shear distribution under a load acting in the shear center of the section

For the fuselage, the moment of inertia as a function of longitudinal position can be checked for its 'jumps' and variations. Thus, the 3 sections of the fuselage can be seen in [Figure 4.9](#). Because the second section does not contain the aluminum cylinder, there is a sudden drop, while for the third section, there is an expected decrease in moment of inertia due to the tapering.

For all the calculations, parameters were varied and the results were checked. Examples of tests performed are:

- higher force/ moment leads to higher stresses
- higher moment of inertia leads to lower stresses
- shear flow does not vary with the thickness
- highest normal stress is at the point furthest to the neutral axis

13.1.1. Verification Through FEM

A finite element method (FEM) simulation verifies both the boom idealization and the Python code. For this, the *Solidworks Simulation* workbench is used. The FEM results contain the stress distribution which can be compared to the results from the previously written Python program. The simulation setup is split into three tasks. Firstly, the CAD file needed to be prepared, by removing the rounded fuselage interface. Secondly, the CAD file of the fixed-wing section was meshed. This was done with the mesher *Standard Mesh* using a solid mesh and a mesh element size of 10.5 mm. Thirdly, the distributed lift loads needed to be applied with a formula according to the coordinate system in the CAD part and the root chord had to be clamped rigidly.

Figure 13.2 shows the stress distribution. The distribution is less coarsely discretized than the Python program resolution because the latter only returns the maximum stress per element. However, both programs return the maximum stress in the upper skin panel of the center cell. The maximum stress magnitude of the FEM is 16% larger than the one calculated in Python. This is acceptable given the safety factor of 1.5. The difference can be explained by possible errors in both models, different underlying equations, and different assumptions. One such assumption is that the boom idealization does not assume distortion, whereas the FEM does.

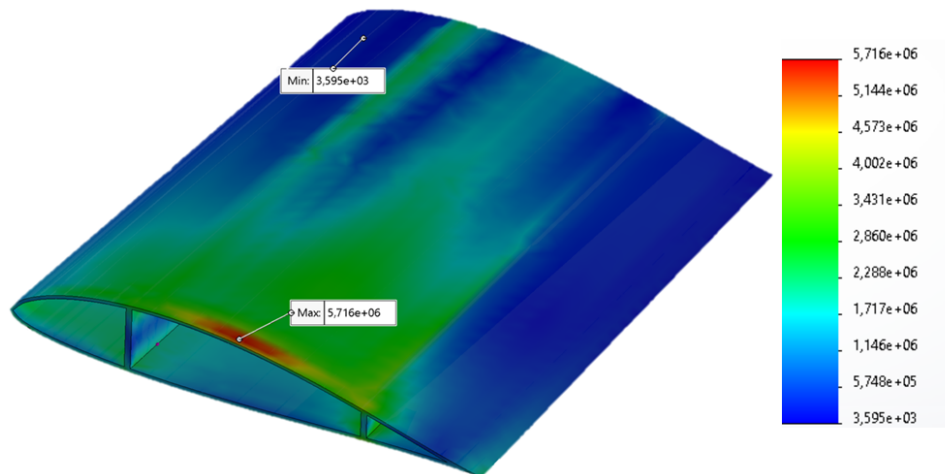


Figure 13.2: Stress distribution of the fixed wing section from finite element method analysis [Pa]

13.1.2. Drop Test

Ensuring that the design satisfies the drop test requirement (REQ-UAV- RAMS-006) can be checked with a Solidworks simulation. The simulation setup included the same steps as described in Subsection 13.1.1. However, meshing the total assembly with a solid mesh is computationally expensive and often, due to complex, high aspect-ratio elements impossible. Thus, the geometry had to be simplified. Eventually, only the fixed wing structure and an idealized fuselage remained and a mass inside the fuselage was added to achieve the same total weight as the real assembly. Despite the high elasticity of balsa wood, the drone will exceed the elastic strain range. The maximum achieved stress during the drop is 17.1 MPa, the material yield strength is 16.2 MPa and the ultimate strength is 25 MPa.

There are four options to deal with this. The fuselage thickness on the bottom can be increased, different materials can be used, a crumbling structure can be added, or it can be assessed that slight plastic deformation of the fuselage is not critical.

13.1.3. 3D Printing

The morphing structures can be 3D printed to validate both manufacturability and kinematic motion. Half of the tail morphing mechanism was printed, shown in [Figure 13.3](#). The CAD files had to be alternated for 3D printing. This included adding fitting margins, reducing the platelet length, and sectioning the part to print thin parts in an optimal orientation. The actuation bar only attaches to the three outer platelets, as the inner most platelet is not free to rotate.

The platelets, outer bracket, and actuation rod were FDM printed. This means the chosen printable liquid-crystal polymer can be used. Only the very small structures of the elevator bracket failed when FDM printing. Instead, it was printed with an SLA printer. Thus, this part has to be altered for the manufacturing requirement. Further, it could be demonstrated that the platelets reach the required actuation range and do not jam when moving the actuation bar.



Figure 13.3: Picture of the 3D printed tail mechanism of the Air-Guard drone

13.2. Payload

This section discusses the verification and validation of the payload subsystem. First the verification will be discussed, then the validation plans.

13.2.1. Verification of the Payload System

To test the range of the payload system, a Python code was used based on an analytically derived equation ([Equation 5.4](#)). To verify that the equation was implemented correctly, Desmos was used to simulate the outcomes ¹, and the same results were obtained. To verify that REQ-UAV-PERF-001, REQ-UAV-PERF-002, REQ-UAV-PAYL-002 and REQ-UAV-PAYL-003 ([Table 5.1](#)) have been met, the specification sheet of the parachute manufacturer was used ², in which compliance with these requirements can be found. Verifying REQ-UAV-PAYL-005 and REQ-UAV-PAYL-007 was done by designing the net in such a way that these requirements could also be met. The requirements regarding aerodynamic performance have been verified using Star-CCM+.

13.2.2. Validation of the Payload System

To ensure the payload system can fulfill its mission when the UAV has actually been built, it needs to be validated. The payload canister has been based on an existing solution built by OpenWorks engineering ³, which has already been proved to work. As the canister Air-Guard uses has been slightly altered, tests need to be performed in the future with a prototype, to ensure correct deployment. Additionally, the shooting structure and rails need to undergo thorough testing to ensure the pseudo-nose does not jam when it slides forward, and the shooting structure can provide the required impulse to the payload canister.

¹<https://desmos.com> [Accessed 24/05/2022]

²https://dronerescue.com/wp-content/uploads/2022/04/drs_10_specsheet.pdf [Accessed 24/05/2022]

³<https://openworksenineering.com/skywall-patrol/> [Accessed 23/05/2022]

13.3. Propulsion

This section will discuss how the propulsion subsystem, mentioned in [Chapter 8](#), was verified. Several methods have been used to verify that the calculations were implemented correctly. In addition, validation techniques that will have to be implemented are discussed.

13.3.1. Verification of the Propulsion System

Analytical calculations have been done to verify that the Python and Excel functions have been implemented correctly.

Since not everything could be analytically tested, unit and system tests were also created to verify this system. Additionally, the flight dynamics model was used to assess whether the given thrust data, combined with aerodynamics, let the drone achieve its intended performance requirements.

13.3.2. Validation of the Propulsion System

To validate whether the propulsion system was designed correctly, it ideally needs to be tested in real-life to compare the behavior to the simulated behavior. Performance tests will need to be performed in different flight conditions, such as during loiter or in dive. These can be done in a wind tunnel or using a prototype. In addition, the manufacturer of the engines provides thrust data which can be used to validate whether the calculations used in the flight dynamics model are correct.

13.4. Aerodynamics

Verification and validation of the aerodynamic department is crucial to the system, since these values are used in all other departments: the sizing of the structures, the flight dynamics model, the propulsion calculations and the performance analysis. The aerodynamic department verified OpenVSP with another CFD software and by comparing it to previous research from EPFL.

13.4.1. Comparing OpenVSP and Star-CCM+

Throughout the aerodynamic analysis of the Air-Guard drone, OpenVSP is extensively used to determine lift, drag, and moment coefficient under different flight profiles, and morphing conditions. This is particularly convenient, as this CFD tool makes use of the Vortex Lattice Method, which offers fast computing times, and relatively accurate results. To verify these, Star-CCM+ is used on a reference model of the Air-Guard drone. This CFD tool accurately predicts stall, separation, and turbulent flows using the SST k-omega model⁴. Comparing this CFD software on the same reference model, under the same flow conditions, allows for proper cross verification. An overview of the results is provided in the following [Table 13.1](#). For ranges close to $\alpha = 0^\circ$, it can be concluded that OpenVSP produces aerodynamic data with sufficient accuracy, as it produces results with a maximum observed difference of 12.5%. It is recommended to use the more advanced CFD software to also compute the aerodynamic coefficients for different angles of attack and states of morphing, such that all departments get more accurate data.

Table 13.1: Simulation results for OpenVSP and Star-CCM+ for $\alpha=0^\circ$

	ρ	V	μ	Cl	Cd
Unit	kg/m/s	m/s	Kg/m/s	-	-
OpenVSP	1.225	20	1.86E-5	0.088	0.021
Sar-CCM+	1.225	20	1.86E-5	0.095	0.024
	Delta			0.007	0.003

⁴https://www.cfd-online.com/Wiki/SST_k-omega_model [Accessed: 10/06/2022]

13.4.2. Validation by Comparing Aerodynamic Data with Similar Drones

Based on papers from EPFL [4] [45], aerodynamic coefficients and behavior can be compared against the results found there. While the UAVs are different, many aerodynamic coefficients are non-dimensionalized and trends in the aerodynamic behavior can be compared.

Lift and drag coefficients

Ajanic et al. used wind tunnel testing to measure the lift and drag coefficients for different states of morphing. Figure 13.4 compares the lift curve of the EPFL drone with the Air-Guard and Figure 13.5 compares the drag curves. The comparison in lift coefficient shows a clear similarity for the extended states. However, when looking at the retracted state there is a clear distinction in the lift coefficient which might be due to the airfoil being aligned with the flow in the OpenVSP model but not in real life. As mentioned in Subsection 6.3.1, the VLM method used for the openVSP calculations underestimates the viscous drag which can also be seen in Figure 13.5.

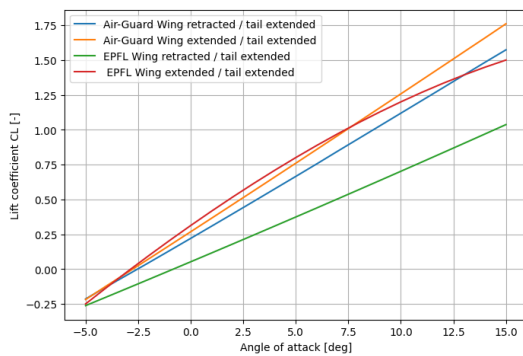


Figure 13.4: Lift curve in different morphing conditions for the EPFL, and Air-Guard Drone

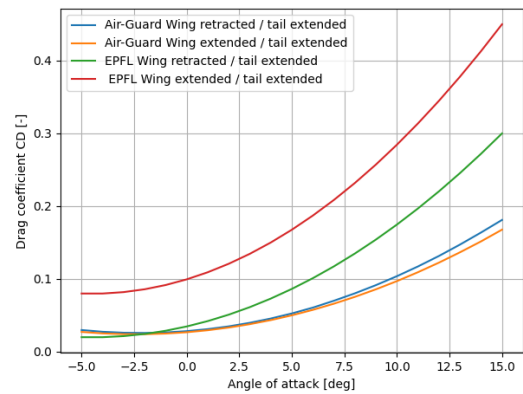


Figure 13.5: Drag curve in different morphing conditions for the EPFL, and Air-Guard Drone

Roll control due to morphing

Luca et al. analyzed the roll coefficient against the lift coefficient to compare it to ailerons (Figure 13.6). When doing this analysis for the Air-Guard, a similar trend can be observed. This is presented in Figure 13.7. The roll rate also shows linear behavior when increasing the C_L . Note that the actual models differ, which induces discrepancies, however, they still are in a similar order of magnitude.

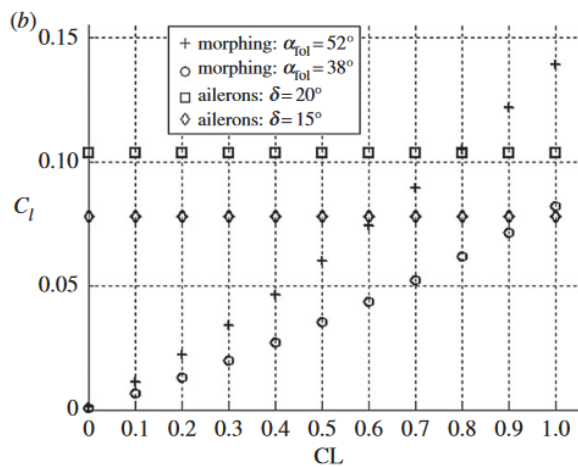


Figure 13.6: EPFL drone Roll coefficient as a function of lift coefficient for different morphing states [45]

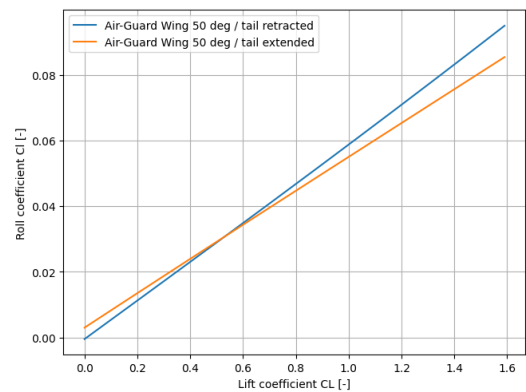


Figure 13.7: Roll coefficient as a function of lift coefficient for the Air-Guard drone

Stability and controllability due to morphing

Lastly, EPFL also presented data concerning the pitching moment coefficient with respect to different angles of attack and morphing states, as presented in Figure 13.8. A similar graph has been made for the Air-Guard, of which the results were presented in Figure 7.7. Since EPFL does not change its payload and has a different center of gravity position, the actual values cannot be compared but the trends can. In both cases, it is clear that morphing the wings forward makes the slope of the pitching moment curve more positive since the aerodynamic center moves forwards. Similarly, when morphing the tail outwards, stability increases again and the slope of the pitching moment curve gets more negative.

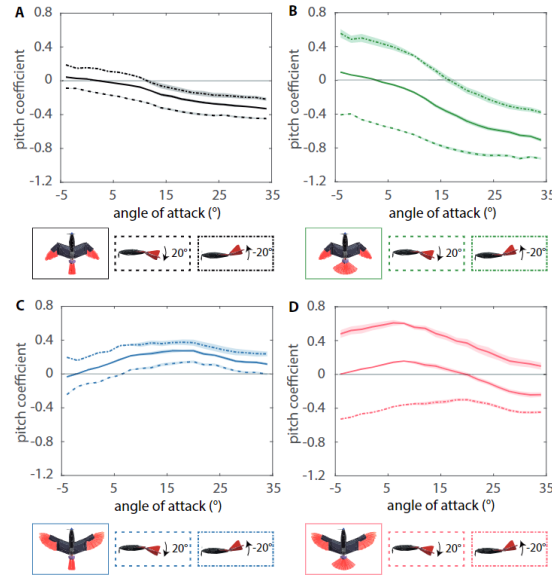


Figure 13.8: Pitching moment coefficient vs angle of attack for different morphing states of the Lishawk drone [4]

13.4.3. Validation by Wind Tunnel Testing

Currently, all verification and validation methods use openVSP simulations to compare with other data. However, to improve the validity of the design it is advised to use wind tunnel testing to get a more accurate estimate of the aerodynamic coefficients. This could be done by 3D-printing the surface of the drone and installing it in a wind tunnel to get the forces generated by the model. Also to get a real sense of the alula effects, wind tunnel testing and other methods such as digital particle image velocimetry needs to be performed to truly quantify its effects.

13.5. Flight Dynamics Model

This section will discuss the verification and validation of the flight dynamics model that was presented in Chapter 9.

13.5.1. Comparing the Linear Model with a Verified Model

To verify the linear flight dynamics model described in Section 9.1, it was compared with an existing verified model that could be found in the flight dynamics reader [40]. The stability derivatives from the Cessna Citation 500 were fed into the program to compare the eigenvalues that it would output. These were the same as the ones mentioned in the reader, with an accuracy greater than 1%, indeed verifying the model.

13.5.2. Verifying the Non-Linear Model

As the non-linear model is substantially more extensive than the linear model, verification was also carried out more extensively. The verification has been split up into code and calculation verification.

The nonlinear flight dynamic model has completely been set up in Matlab and Simulink. Code verification of the Matlab scripts was straightforward and was done using unit tests, subsystem tests, and system tests. As expected from extreme value testing the model becomes increasingly less reliable once the model exceeds an angle of attack of 12 degrees. In addition, the kinematic equations are based on Euler angles and hence include a singularity at a pitch angle of 90°. The Simulink models were slightly harder to code verify as they contain graphical models rather than code. Most of the verification was therefore done by inspection.

Similarly, for calculation verification, several unit and subsystem tests have been carried out. To facilitate calculation verification, the subsystems have been demarcated within the Matlab scripts and the Simulink models. Most outputs, such as the forces and moments generated by the engine and gravity were verified using hand calculations.

The greatest source of uncertainty lies with the aerodynamic model and the retrieval of the aerodynamic coefficients. This is mainly because of the lack of documentation of OpenVSP. For example, there is no clear description of how the aerodynamic coefficients are non-dimensionalized within OpenVSP, which led to uncertainty in how to exactly dimensionalize the coefficients. It was assumed that they followed the conventions mentioned in [40] and hence were dimensionalized in this manner.

To verify the correct implementation of aerodynamics, gravity and engine forces, data for a different aircraft was used. For this, the RCAM model was used ⁵. The characteristic motions of this aircraft are known, so once the aerodynamics and engine forces of this aircraft were implemented in the non-linear model, its eigenmotions could be compared to known eigenmotions from literature.

13.5.3. Validation of the Model

The intended purpose of the flight simulator is to analyze the dynamic behavior of the UAV and to assess its flight performance. The only manner to assess the ability of the flight simulator to perform its intended purpose is to build and fly the UAV or a representative model of it.

⁵<https://www.yumpu.com/en/document/view/38469129/the-research-civil-aircraft-model-rcam-garteur>

[Accessed: 20/06/2022]

14. Conclusion and Recommendations

The goal of this report was to present the results in the development of the counter unmanned aerial system (CUAS). Previously, the project plan was set up to cover the organizational and planning aspects of the project, and the baseline report was created to document requirements and project scope. In addition to this, a list of design options was made through the use of the design option tree. After this, the midterm report initiated the design phase of the project. In this report, the chosen configuration from the design trade-off entered the detailed design phase.

The detailed design was split up into 4 different main departments: Aerodynamics, structures, stability and control, electronics and morphing. These departments drove the detailed design choices for the drone.

Whilst designing the drone, sustainability has to be considered. As a result of this, the drone is powered 100% electrically. This energy is provided by the interchangeable battery positioned in the fuselage. In addition to this, 99% of the structural mass of the drone is recyclable.

The design of the fuselage was mainly driven by the structures department. It is roughly 1 meter long, 12 centimeters high, and 10.6 centimeters wide. The 4 fuselage spars and the skin encapsulate the components of the internal systems, such as the flight controller and the battery. The fuselage also houses the payload system. The payload consists of a capsule that holds a net and a parachute that is launched at the unlicensed drone to catch it. This is done through the use of a pneumatic system. As the payload is launched, the stability and control characteristics of the drone alter. To prevent becoming too unstable, the wings and tail are able to morph to counteract this instability.

Other than the benefits to stability, the morphing mechanisms are crucial to ensure that the drone is agile enough, to be able to chase the enemy drones. Thus, it is possible for the drone to be efficient in loitering by having a high aspect ratio, but also maneuverable when in attack mode by changing both the wing's and horizontal stabilizer's planforms. This is done through actuators applying a moment force on the morphing system. The morphing mechanism is composed of platelets that simulate feathers. These platelets are allowed to move over each other if necessary, or fan out. Through the changes in surface area of the wing and tail, the drone can become more maneuverable or more stable and efficient. For the wing, the surface area can differ up to 30% in both wings, they also have the ability to morph asymmetrically. The tail can increase up to 3 times its original retracted surface area. As a result of the configuration design, the drone can loiter for over 1 hour. Within this time, it will be able to fly 71 kilometers at sea level. This ensures that the Air-Guard can protect sensitive airspace against the threat of unlicensed drones.

As a reflection on the last 10 weeks, some minor problems delayed the progress of the design. This was mainly due to the extent of communication the team had between the departments. This meant that if one department altered the value of a certain parameter, it was not always communicated clearly. This led to certain calculations having to be performed multiple times. Aside from the communication, an extra obstacle that the group ran into came from the lack of time. Due to this, the group had to make concessions in the extent of detailed design for certain departments. This meant that there is a difference in the amount of detail that is provided for each system.

Recommendations

This report provides an overview of the detailed design of the systems of the drone. However, more research can be done to further optimize the design. The recommendations for further research are listed in bullet points below. The recommendations are divided into four sections; aerodynamics, payload, structures, and flight dynamics.

From structures point of view, there are some important actions that need to be taken. First, because of the late introduction in the design of the vertical tail and time constraints, it was impossible to make a detailed analysis and design of the tail's structure. This would be the next step from structures point of view. It is expected to be a simple design, with low weight and associated costs, as there is no rudder and the aerodynamics loads are relatively low. The Python code written for the fixed part of the wing can also be used for this. Next, a reiteration for the structural calculation is needed to check for the most recent aerodynamic loads. Thirdly, more analysis is needed for the joints of the structure, as not all the failure modes were considered, only the ones considered critical. Finally, the drop test requirement was not met. This can be dealt with by reinforcing the belly or adding a crumbling structure.

From the morphing point of view, four main recommendations are in place: determination of the rubber band

stiffness, the shape of the fairing around the morphing wing and tail, the shape of the platelets and finally the investigation into the implementation of additional degrees of surface morphing. Firstly, the rubber band stiffness has been estimated at this point. Further research could determine the stiffness of the individual rubber band that will optimize the reliability of the mechanism and the possible rate of morphing. In addition to this, the shape of the fairing around the morphing mechanisms have been inspired by a NACA airfoil. However, the exact shape and optimization of this is still to be included. This could improve the aerodynamic performance of the fairing. Moreover, the shape of the platelets can be researched into greater depth. As the platelets for the wing and tail are positioned at a different angle of attack, the shape can be optimized for this. Instead of using flat platelets, having a slight curvature or thin airfoil could aid performance. Lastly, the current morphing design focuses on morphing methods such as wing extension/retraction, tail spread, and tail deflection, however there exists multiple further degrees of morphing of both the wing and tail involving changes in dihedral angle and twist. These latter aspects of control surface morphing were not investigated in detail and their effects were not fully quantified, thus, further studies into these morphing concepts must be taken into account moving further such that the most effective combinations of surface morphing can be determined.

Bibliography

- [1] H. Detrick. Gatwick's december drone closure cost airlines \$64.5 million. *Fortune*, 2019.
- [2] A. Smout. Gatwick drone disruption cost easyjet nearly \$20 million. *Reuters*, 2019.
- [3] Dubai airport airspace closed due to 'unauthorised drone activity'. *The National News*, 2016.
- [4] E. Ajanic, M. Feroskhan, S. Mintchev, F. Noca, and D. Floreano. Bioinspired wing and tail morphing extends drone flight capabilities. *Sci. Robot.*, (5):eabc289, October 2020. doi: 10.1126/scirobotics.abc289.
- [5] E. Chang, L. Y. Matloff, A. K. Stowers, and D. Lentink. Soft biohybrid morphing wings with feathers underactuated by wrist and finger motion. *Sci. Robot.*, (5):eaay1246, January 2020.
- [6] H. Bao, B. Song, W. Yang, J. Xuan, and D. Xue. The progress of aerodynamic mechanisms based on avian leading-edge alula and future study recommendations. page 259, 2021. doi: <https://doi.org/10.3390/aerospace8100295Academic>.
- [7] S. Lee, J. Kim, H. Park, P. G. Jablonski, and H. Choi. The function of the alula in avian flight. *scientific report*, 5:9914, 2015. doi: 10.1038/srep09914.
- [8] C. Ge, L. Ren, P. Liang, C. Zhang, and Z. Zhang. High-lift effect of bionic slat based on owl wing. *Journal of Bionic Engineering*, 10(4):456–463, 2013. ISSN 1672-6529. doi: [https://doi.org/10.1016/S1672-6529\(13\)60243-7](https://doi.org/10.1016/S1672-6529(13)60243-7).
- [9] Yi Yang, A. Nambiar, N. Luxcey, F. Fonseca, and L. Amaral. Advanced Design Tools for Ocean Energy Systems Innovation, Development and Deployment. 2020.
- [10] Prof. dr. ir. M.J.L. van Tooren Ir. R.J. Hamann. Systems engineering & technical management techniques part ii, Jan 2006.
- [11] B. Penzenstadler and H. Femmer. A generic model for sustainability with process- and product-specific instances. *GIBSE '13: Proceedings of the 2013 workshop on Green in/by software engineering*, pages 3–8, March 2013. doi: <https://doi.org/10.1145/2451605.2451609>.
- [12] J. Sinke. Production of aerospace systems reader, 2022.
- [13] L. Romansky, M. Garrod, K. Brown, and K. Deo. How to measure inclusion in the workplace. *Harvard Business Review*, 2021.
- [14] International Trade Union Confederation. 2018 ituc global rights index. the world's worst countries for workers.
- [15] Economic sustainability: Definition, importance, and examples. *MaterClass*, 2022.
- [16] Seongjoon Park, Hyeong Tae Kim, Sangmin Lee, Hyeontae Joo, and Hwangnam Kim. Survey on Anti-Drone Systems: Components, Designs, and Challenges. *IEEE Access*, 9, 2021. doi: <http://dx.doi.org/10.1109/ACCESS.2021.3065926>.
- [17] Georgia Lykou, Dimitrios Moustakas, and Dimitris Gritzalis. Defending Airports from UAS: A Survey on Cyber-Attacks and Counter-Drone Sensing Technologies. *Sensors*, 20(12), 2020.
- [18] Mobile force protection program concludes with successful demonstration. *DARPA*, 2022.
- [19] G. Lykou, D. Moustakas, and D. Gritzalis. Defending airports from uas: A survey on cyber-attacks and counter-drone sensing technologies. *Sensors*, 20:3537, 06 2020. doi: 10.3390/s20123537.
- [20] B. Custers. *The Future of Drone Use: Opportunities and Threats from Ethical and Legal Perspectives*, volume 27. 01 2016. ISBN 978-94-6265-131-9. doi: 10.1007/978-94-6265-132-6.
- [21] Christian R. Bolander Christina Harvey, Lawren L. Gamble, Douglas F. Hunsaker, James J. Joo, and Daniel J. Inman. A review of avian-inspired morphing for uav flight control. *Progress in Aerospace Sciences*, 2022.
- [22] Group 26. Air-guard baseline report, 2022. Course AE3200 – Design Synthesis exercise (TU Delft).
- [23] What frequency do drones use? *Aerocorner*, 2020.
- [24] D. P. Raymer. *Aircraft design: A conceptual approach*. AIAA-education series, 2 edition, 1989.
- [25] M. Kenny. Gas gun dynamics. *European Journal of Physics*, 34(5):1327–1336, August 2013.
- [26] S. Lee, J. Kim, H. Park, P. G. J. ski, and H. Choi. The function of the alula in avian flight. *Sci. Rep.* 5, May 2015. doi: 10.1038/srep09914.
- [27] D. Liu, B. Song, W. Yang, X. Yang, D. Xue, and X. Lang. A brief review on aerodynamic performance of wingtip slots and research prospect. *Journal of Bionic Engineering*, 18:1255–1279, 2021. doi: <https://doi.org/10.1007/s42235-021-00116-6>.
- [28] A. Deperrois. About xflr calculation and experimental measurements. *XFLR5 Documentation*, 2009.

- [29] T. Shahid, F. Sajjad, M. Ahsan, S. Farhan, S. Salamat, and M. Abbas. Comparison of flow-solvers: Linear vortex lattice method and higher-order panel method with analytical and wind tunnel data. pages 1–7, 2020. doi: 10.1109/iCoMET48670.2020.9073909.
- [30] H. Bao, B. Song, W. Yang, Jianlin Xuan, and Dong Xue. The progress of aerodynamic mechanisms based on avianleading-edge alula and future study recommendations. *Aerospace2021*, page 295, october 2021. doi: doi.org/10.3390/aerospace8100295.
- [31] Aimy Wissa, Amy Han, and Mark Cutkosky. Wings of a feather stick together: Morphing wings with barbule-inspired latching. 07 2015. doi: 10.1007/978-3-319-22979-9_13.
- [32] T. H. G. Megson. *Aircraft Structures for Engineering Students*, volume 1. 03 2007. ISBN 978-0-75066-7395. doi: https://doi.org/10.1016/C2019-0-03113-5.
- [33] Ces edupack software, materials database. Granta Design Limited, Cambridge, UK, 2009.
- [34] S. Gantenbein, K. Masania, and W. et al. Woigk. Three-dimensional printing of hierarchical liquid-crystal-polymer structures. *Nature*, 561:226–230, 2018. doi: https://doi.org/10.1038/s41586-018-0474-7.
- [35] F. Oliviero. Requirement analysis and design principles for a/c stability & control (part 1), .
- [36] D. E. Hoak and R. D. Finck. *USAF stability and control datcom*. Global Engineering Documents, 1978.
- [37] F. Oliviero. Requirement analysis and design principles for a/c stability & control (part 2), .
- [38] W.B. Garnaer. Model airplane propellers, 2009.
- [39] D. P. Witkowski R. T. Johnson and J. P. Sullivan. Experimental results of a propeller/wing interaction study. *SAE International*, 100:121–130, November 1991.
- [40] J.A. Mulder, W.H.J.J. van Staveren, J.C. van der Vaart, E. de Weerdt, C.C. de Visser, A.C. in't Veld, and E. Mooij. *AE3212-I Flight Dynamics Lecture Notes*. 03 2013.
- [41] P. Lu, E. van Kampen, C. de Visser, and Q. Chu. Aircraft fault-tolerant trajectory control using incremental nonlinear dynamic inversion. *Control Engineering Practice*, 57:126–141, December 2016. doi: 10.1016/j.conengprac.2016.09.010.
- [42] I. Matamoros and C. C. de Visser. Incremental nonlinear control allocation for a tailless aircraft with innovative control effectors. *2018 AIAA Guidance, Navigation, and Control Conference*, 2018. doi: 10.2514/6.2018-1116.
- [43] International Civil Aviation Organization. *Air Traffic Management*, volume 16. 10 2016. ISBN 978-92-9258-081-0.
- [44] G. Lykou, D. Moustakas, and D. Gritzalis. Defending airports from uas: A survey on cyber-attacks and counter-drone sensing technologies. *Sensors*, 20(12):3537, 2020. doi: 10.3390/s20123537.
- [45] M. Di Luca, S. Mintchev, G. Heitz, F. Noca, and D. Floreano. Bioinspired morphing wings for extended flight envelope and roll control of small drones. *Interface Focus*, 7, 2017. doi: 10.1098/rsfs.2016.0092.

A. Requirements and Compliance Matrix

In this chapter, the requirements posted on the system and the drone itself will be presented. The identifier of each requirement is highlighted in a certain color. Green means that the requirement was fully met. Orange signifies that compliance with the given requirement cannot be reliably verified. Red then means that the requirement was not met. Finally, blue marks a requirement, which cannot be verified due to the way it was formulated. Justification of this compliance rating is then provided in the compliance matrix for all individual requirements.

Requirements Table

Requirement Identifier	Requirement
REQ-CUAS-OPER-002	The C-UAS shall be able to detect drones in the defined action area
REQ-CUAS-OPER-003	The C-UAS shall be able to protect the action area from the threat of enemy drones
REQ-CUAS-OPER-004	The C-UAS shall not conduct operations on airport runways unless specified by ATM
REQ-CUAS-OPER-005	The C-UAS shall not interfere with airport ground operations
REQ-CUAS-OPER-006	The C-UAS shall be able to differentiate between birds and drones
REQ-CUAS-OPER-007	The C-UAS shall be able to monitor enemy drone activity up to the point where it is immobilized
REQ-CUAS-OPER-008	The C-UAS communications shall not interfere with ATM communications
REQ-CUAS-OPER-009	The C-UAS shall have continuous/uninterrupted downlink from the UAV to the ground station
REQ-CUAS-OPER-010	The C-UAS shall have continuous/uninterrupted uplink from the ground station to the UAV
REQ-CUAS-OPER-011	The C-UAS shall be deployable at any airport
REQ-CUAS-OPER-012	The C-UAS shall communicate with ATM
REQ-CUAS-OPER-013	The C-UAS shall be able to differentiate between licensed and unlicensed drones
REQ-CUAS-OPER-014	The C-UAS shall be able to read drone licenses
REQ-CUAS-OPER-015	The C-UAS shall be able to transport captured drones to relevant authorities
REQ-CUAS-OPER-016	The C-UAS shall be capable of deploying atleast one UAV at all times
REQ-CUAS-OPER-017	The C-UAS shall continue to operate in rainy conditions
REQ-CUAS-OPER-018	The C-UAS shall monitor an area of at least 28 km^2
REQ-CUAS-STK-001	The C-UAS development costs shall not exceed 300,000 euros
REQ-CUAS-STK-002	The C-UAS operational cost shall not exceed 7000 euros/hour
REQ-CUAS-STK-003	The C-UAS maintence cost shall not exceed 50 euros per flight
REQ-CUAS-STK-004	The C-UAS shall demonstrate the effectiveness of bio-inspired morphing drones to combat unlicensed drones
REQ-CUAS-STK-005	The C-UAS system concept design shall be complete by the 20th of June 2022
REQ-CUAS-STK-006	The C-UAS development shall fall within the resources/expertise provided by TU Delft
REQ-CUAS-STK-007	The unit price of the UAV shall not exceed 5,000 euros
REQ-GS-OPER-001	The ground station shall provide charging capabilities for the UAV
REQ-GS-OPER-002	The ground station shall be able to perform maintenance work on the UAV
REQ-GS-OPER-003	The ground station shall have continuous uplink to ATM
REQ-GS-OPER-004	The ground station shall be able to provide an emergency cutoff
REQ-UAV-OPER-001	The UAV shall be able to autonomously return to the charging station if the state of charge of the battery is below 20%
REQ-UAV-OPER-001-A	The UAV shall transmit the position of the unlicensed drone to the other drones when the state of the charge of the battery is below 20% when in attack mode.
REQ-UAV-OPER-004	The UAV shall continuously downlink telemetry data to the ground station
REQ-UAV-OPER-006	The UAV shall be able to target unlicensed drones
REQ-UAV-OPER-008	The UAV shall be able to autonomously switch between operating modes mid flight when an unlicensed drone is detected

Compliance Matrix

Table A.1: Compliance matrix

Requirement Identifier	Compliance rationale
REQ-CUAS-OPER-002	System will use data from airport's detection systems
REQ-CUAS-OPER-003	To be proven by real world deployment
REQ-CUAS-OPER-004	Forbidden areas can be specified in flight plan
REQ-CUAS-OPER-005	Forbidden areas can be specified in flight plan
REQ-CUAS-OPER-006	Onboard computer software is to be designed
REQ-CUAS-OPER-007	Drone is equipped with camera and IR camera
REQ-CUAS-OPER-008	System communicates on different frequency than ATM
REQ-CUAS-OPER-009	Sufficient link budget and transmission power are provided
REQ-CUAS-OPER-010	Sufficient link budget and transmission power are provided
REQ-CUAS-OPER-011	Depends on design of ground station
REQ-CUAS-OPER-012	Ground station was not designed
REQ-CUAS-OPER-013	Onboard computer software is to be designed
REQ-CUAS-OPER-014	Not covered in the project
REQ-CUAS-OPER-015	Parachute design was used instead
REQ-CUAS-OPER-016	Fast-to-reload catapult is used for deployment of the UAV
REQ-CUAS-OPER-017	Watertight fuselage design together with water-resistant components
REQ-CUAS-OPER-018	Sufficient endurance and range performance
REQ-CUAS-STK-001	Ground station dev. costs not estimated
REQ-CUAS-STK-002	Ground station operational cost is to be determined
REQ-CUAS-STK-003	To be analyzed once failure rate of components is known
REQ-CUAS-STK-004	To be verified by flight test
REQ-CUAS-STK-005	Completed on 9th of June 2022
REQ-CUAS-STK-006	Design performed by TU Delft students
REQ-CUAS-STK-007	The unit price of the UAV is 2,391 euros
REQ-GS-OPER-001	Ground station was not designed
REQ-GS-OPER-002	Ground station was not designed
REQ-GS-OPER-003	Ground station was not designed
REQ-GS-OPER-004	Ground station was not designed
REQ-UAV-OPER-001	Energy needed for return is 13.2% of total capacity
REQ-UAV-OPER-001-A	Power needed for communication is sufficiently small
REQ-UAV-OPER-004	Sufficient link budget and transmission power are provided
REQ-UAV-OPER-006	UAV is equipped with IR and visual camera for this purpose
REQ-UAV-OPER-008	UAV is equipped with autonomous controller
REQ-UAV-OPER-009	To be verified by flight test
REQ-UAV-OPER-010	The drone is recharged by swapping the battery (<10 min)
REQ-UAV-OPER-011	UAV is equipped with autonomous flight controller

REQ-UAV-OPER-009	The UAV shall be able to follow a predetermined flight path until an unlicensed drone is detected
REQ-UAV-OPER-010	The UAV shall have a turn over time between flights of 30 minutes
REQ-UAV-OPER-011	The UAV morphing mechanism shall be able to autonomously morph depending on the flight regime
REQ-UAV-OPER-012	The UAV shall be able to be identified when operating at night
REQ-UAV-PERF-001	The minimum mass of drones that the UAV shall be able to immobilize shall be 0.5kg
REQ-UAV-PERF-002	The maximum mass of drones that the UAV shall be able to immobilize shall be 10 kg
REQ-UAV-PERF-003	The UAV shall be able to immobilize drones with a maximum speed of 31 m/s
REQ-UAV-PERF-004	The UAV shall be able to immobilize drones capable of sustaining a climbing rate up to 8 m/s
REQ-UAV-PERF-005	The UAV shall be able to immobilize drones with a maximum diameter of 1m
REQ-UAV-PERF-006	The UAV shall be able to operate in wind speeds of up to 15 m/s
REQ-UAV-PERF-007	The UAV shall have a minimum operating temperature of -10 deg C
REQ-UAV-PERF-008	The UAV shall have a maximum operating temperature of 40 deg C
REQ-UAV-PERF-009	The UAV shall have a maximum service ceiling of at least 5000m above sea level
REQ-UAV-PERF-011	The UAV shall have a minimum loiter time of 60 minutes
REQ-UAV-PERF-012	The UAV shall have a maximum climb rate of at least 12 m/s
REQ-UAV-PERF-013	The UAV shall have a maximum operating speed of 45 m/s
REQ-UAV-PERF-014	The UAV shall be able to withstand normal overloads of at least 8g
REQ-UAV-PERF-015	The UAV shall have pull over radius of less than 1m
REQ-UAV-PERF-016	The UAV shall have sharp turn radius of less than 1.5m
REQ-UAV-PERF-017	The UAV payload system shall have a maximum mass of 2kg
REQ-UAV-PERF-018	The UAV shall have a maximum take off distance of 5m
REQ-UAV-PERF-019	The UAV shall have a maximum landing distance of 5m
REQ-UAV-PERF-020	The UAV payload shall have a pointing accuracy of +/- 5 degrees
REQ-UAV-PERF-021	The UAV shall have a maximum mass of 10 kg
REQ-UAV-PERF-022	The UAV shall have a maximum landing distance of 15m in case of an emergency landing
REQ-UAV-PERF-023	The UAV shall be able to loiter for at least 60km
REQ-UAV-RAMS-001	The UAV shall be able to be located after system failure
REQ-UAV-RAMS-002	The UAVs subsystems shall be able to be replaced completely between flights if damages occur
REQ-UAV-RAMS-003	The UAV shall be able to be disassembled between flights for maintenance
REQ-UAV-RAMS-004	The morphing mechanism of the UAV shall be able to operate with at least 95% reliability
REQ-UAV-RAMS-005	The UAV shall have a maximum lifetime of 5 years or 2000 flight cycles depending on which is reached first
REQ-UAV-RAMS-006	The UAV shall be able to withstand a drop of 2m on concrete without any impedance on its capabilities
REQ-UAV-RAMS-007	The UAV shall comply with IP-03 certification
REQ-UAV-STAKE-001	The UAV shall have a maximum development cost of 10,000 euros
REQ-UAV-STAKE-003	The UAV shall adhere to the EASA drone regulations.
REQ-UAV-SUS-001	75% of the structural mass of the UAV shall be made of recyclable materials
REQ-UAV-SUS-002	The noise emissions of the UAV shall not exceed 90 dB
REQ-UAV-SUS-003	The UAV shall be 100% electrically powered
REQ-UAV-PAYL-001	The net deployment mechanism shall have a reliability of TBD %
REQ-UAV-PAYL-002	The parachute shall slow down the rogue drone to a maximum vertical speed of 4 m/s
REQ-UAV-PAYL-003	The parachute shall deploy within 5 seconds of net deployment
REQ-UAV-PAYL-005	The net shall expand to a size of 4 m ² after shooting
REQ-UAV-PAYL-006	The net gun shall have a range of 10m

REQ-UAV-PAYL-007	The net shall have a size of 2 m by 2 m
REQ-UAV-PAYL-008	The nose profile after payload ejection shall not induce static instability
REQ-UAV-PAYL-009	The nose shape after payload ejection shall not induce separation along any point on the fuselage and wing surfaces

REQ-UAV-OPER-012	UAV is equipped with GPS locator
REQ-UAV-PERF-001	To be verified by flight test
REQ-UAV-PERF-002	To be verified by flight test
REQ-UAV-PERF-003	To be verified by flight test
REQ-UAV-PERF-004	To be verified by flight test
REQ-UAV-PERF-005	To be verified by flight test
REQ-UAV-PERF-006	To be verified by flight test
REQ-UAV-PERF-007	To be verified by testing
REQ-UAV-PERF-008	To be verified by testing
REQ-UAV-PERF-009	Maximum ROC at 5000m a.s.l. is non-zero
REQ-UAV-PERF-011	Achieved loiter time is 62 minutes
REQ-UAV-PERF-012	Maximum rate of climb is 15.7m/s
REQ-UAV-PERF-013	Maximum operating speed is 48.4m/s
REQ-UAV-PERF-014	UAV was designed to operate up to 8.7g
REQ-UAV-PERF-015	To be verified by flight test
REQ-UAV-PERF-016	To be verified by flight test
REQ-UAV-PERF-017	Payload mass is 0.7kg
REQ-UAV-PERF-018	Stall speed is below 12m/s
REQ-UAV-PERF-019	Launch device is used for take-off
REQ-UAV-PERF-020	To be verified by flight test
REQ-UAV-PERF-021	The maximum mass of the UAV is 3.75kg
REQ-UAV-PERF-022	To be verified by testing (depending on type of emergency)
REQ-UAV-PERF-023	Achieved loiter distance is 71km
REQ-UAV-RAMS-001	UAV is equipped with GPS locator
REQ-UAV-RAMS-002	Taken into account in the design
REQ-UAV-RAMS-003	Taken into account in structural design
REQ-UAV-RAMS-004	To be verified by flight test
REQ-UAV-RAMS-005	To be verified by flight test
REQ-UAV-RAMS-006	The main wing would sustain damage in 2m drop
REQ-UAV-RAMS-007	To be assessed by relevant authorities
REQ-UAV-STAKE-001	Estimated development cost of the UAV is estimated at 98,000 EUR
REQ-UAV-STAKE-003	To be assessed by relevant authorities
REQ-UAV-SUS-001	99% of structural mass is recyclable
REQ-UAV-SUS-002	The noise emission is estimated below 50dB
REQ-UAV-SUS-003	The UAV is fully electrical
REQ-UAV-PAYL-001	Requirement was not specified
REQ-UAV-PAYL-002	Parachute slows down the drone to 5m/s
REQ-UAV-PAYL-003	Time delay to parachute deployment is adjustable
REQ-UAV-PAYL-005	Net expands to 4 m ²
REQ-UAV-PAYL-006	Achieved range is 15m
REQ-UAV-PAYL-007	Net dimensions are 2x2m
REQ-UAV-PAYL-008	Demonstrated by CFD simulations
REQ-UAV-PAYL-009	Demonstrated by CFD simulations

B. Functional Diagrams

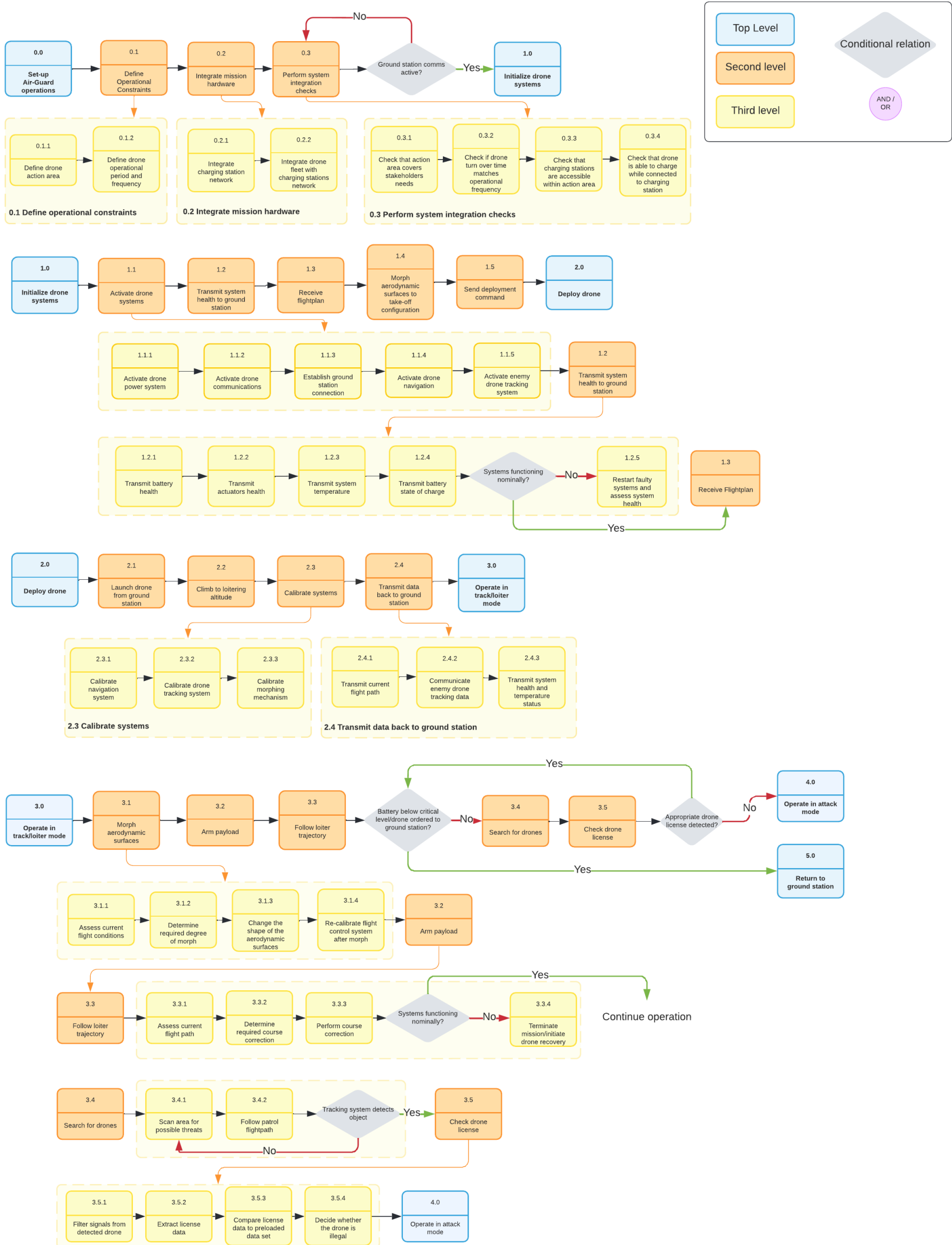


Figure B.1: Mission Functional Flow Diagram 1/2

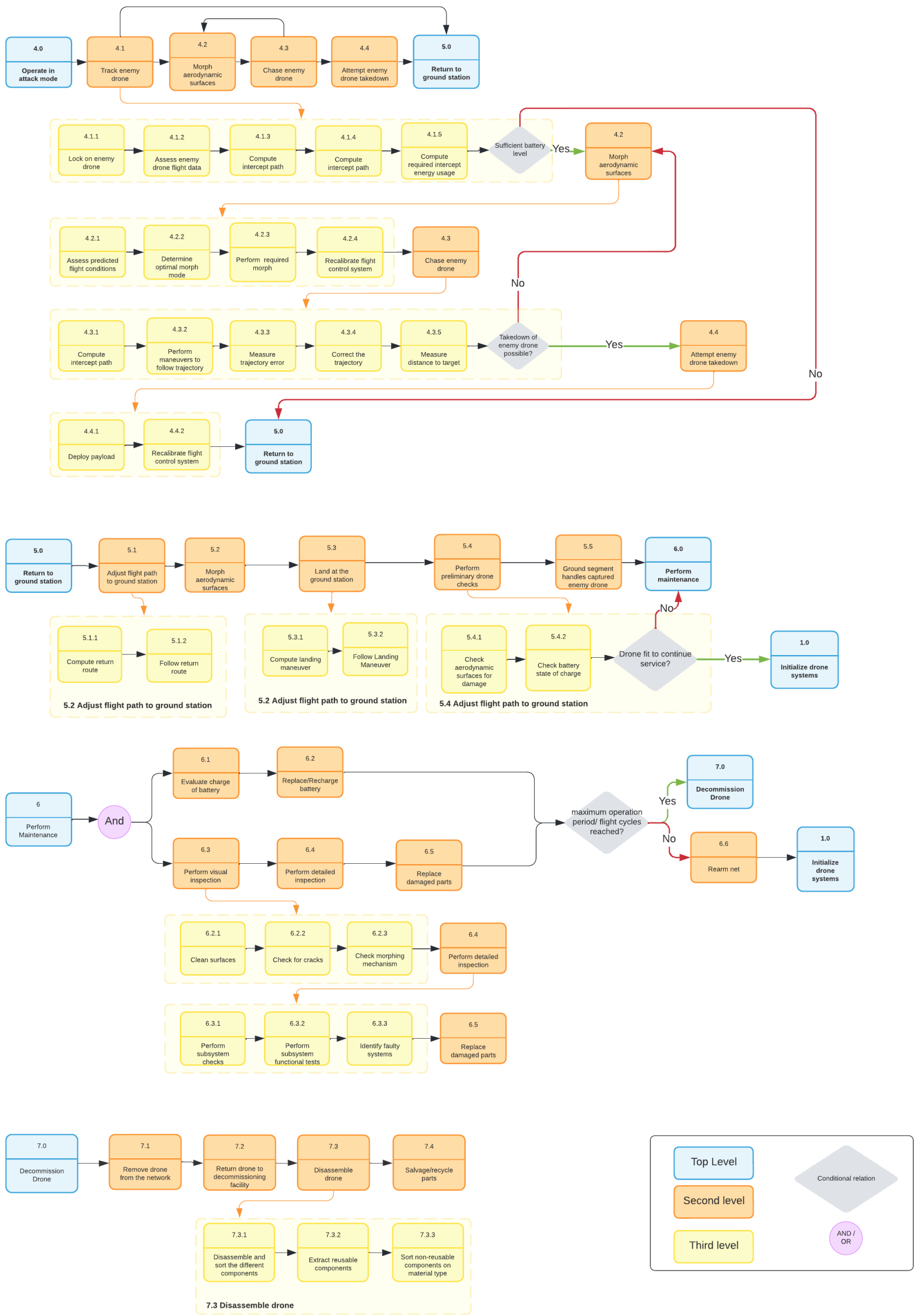


Figure B.2: Mission Functional Flow Diagram 2/2

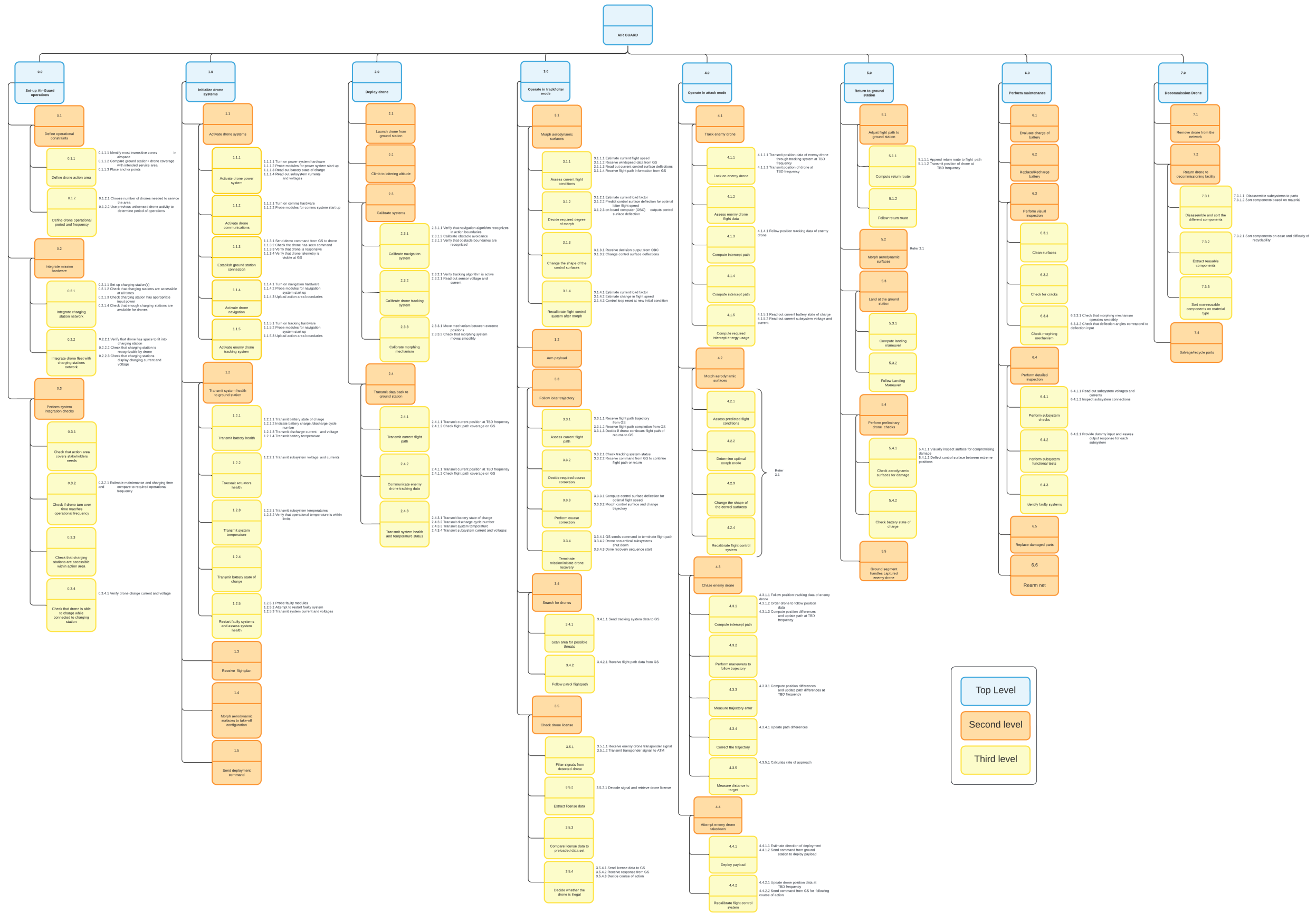


Figure B.3: Mission functional breakdown structure

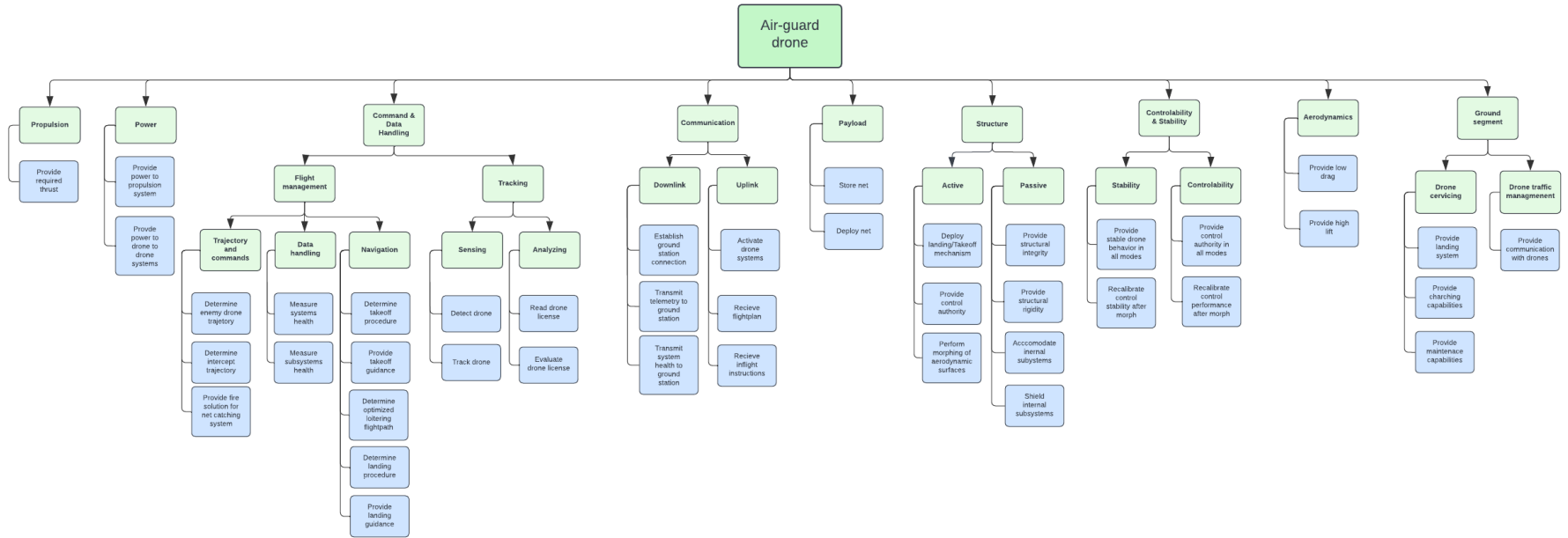


Figure B.4: Systems based functional breakdown